

Gold Nanoparticles in Polymeric Matrices for Biomedical Applications



Thesis submitted in accordance with the requirements of the University of
Liverpool for the degree of Doctor in Philosophy by

Malte Strozyk

Department of Chemistry - University of Liverpool
Bionanoplasmonic Group - CIC biomaGUNE

LIVERPOOL, OCTOBER 2017

"WEGE ENTSTEHEN DADURCH, DASS MAN SIE GEHT."

[FRANZ KAFKA]

Acknowledgements

First of all I would like to thank my supervisors Prof. Luis Liz-Marzán and Prof Mathias Brust for giving me the opportunity to do my PhD in their laboratories. They were patience and helpful throughout the 4 years even in complicated times and never stopped supporting me. Special thanks also belong to Prof Joerg Lahann and the responsible persons from the "HYMADE" project for giving me the opportunity to visit the University of Michigan (USA) for 4 month in Summer 2016.

I feel very lucky for the possibility of working in three different laboratories and countries and I felt very welcome everywhere. Just trying to mention all the people who helped me by its name would make me afraid of forgetting someone. In every laboratory I felt immediately comfortable and supported by everyone: the technicians, lab managers, platform managers, Post Docs and other PhD students. However I want to especially thank Dr. Fernando López-Gallego, Dr. Malou Henriksen Lacey, Dr. Susana Carregal-Romero and Dr. Dorleta Jimenez de Aberasturi for helping me extensively with my

practical work and the writing of the publications. Without them the work of this thesis would not have been possible. I would also specially thank Dr. Casper Kunstmann Olsen and Dr. Samuel Booth for helping me throughout the process of writing and for proofreading.

Last but not least I want to thank my family, all the new friends I made over the last years and my old friends, who stayed in contact with me even when countries started separating us, for their support and the time they spend with me. I feel thankful and happy for this life and I am looking forward for new (scientific) adventures with all of you!

List of abbreviations

ABTS - 2,2'-azino-bis(3-ethylbenzothiazoline-6-sulphonic acid)

AuNPs - Gold nanoparticles

AuNSs - Gold nanostars

CV - Crystal violet

A549 cells - Adenocarcinomic human alveolar basal epithelial cells

DAAO - D-amino acid oxidase

Doxo - Doxorubicin

DMEM - Dulbecco/Vogt modified Eagle's minimal essential medium

FBS - Fetal bovine serum

GOX - Glucose oxidase

GSH - Glutathione

HDF cells - Human dermal fibroblasts

HUVEC cells - Human umbilical vein endothelial cells

HRP - horseradish peroxidase

HUVEC cells - Human umbilical vein endothelial cells

IL-6 - Interleukin 6

IMiDs - Immunomodulatory imide drugs

LCST - Lower critical solution temperature

LbL - Layer-by-layer

LPS - Lipopolysaccharides

MTT - 3-(4,5-dimethylthiazol-2-yl)-2,5-diphenyltetrazolium bromide

PLGA - poly(lactic-co-glycolic acid)

PEGMA - Poly(ethylene glycol) methacrylate

pNIPAM - Poly(N-isopropylacrylamide)

Poma - Pomalidomide

SERS - Surface enhanced Raman spectroscopy

SERRS - Surface enhanced resonance Raman spectroscopy

Contents

1. Abstract	1
2. General Introduction	3
2.1. Overview of nanoparticle polymer hybrid materials	3
2.2. Synthesis of nanoparticle polymer hybrid materials	6
2.2.1. Polymeric matrices as AuNP supports	6
2.2.2. AuNPs embedded in thermoresponsive hydrogels	10
2.3. Optical properties of gold nanoparticles	17
2.4. Surface enhanced Raman scattering (SERS)	22
2.4.1. The Raman effect	23
2.4.2. Mechanism for SERS	25
2.4.3. Hot spots	28
2.4.4. Confocal Raman microscopy	30
2.5. Nanoparticle polymer hybrid materials for SERS	32
2.6. Nanoparticle polymer hybrid materials for drug delivery	38

3. Synthesis of gold/polymer hybrid materials	43
3.1. PEGMA hydrogels with in-situ grown gold nanoparticles . . .	44
3.1.1. Synthesis and polyelectrolyte coating	44
3.1.2. Physicochemical properties of coated nanogels	50
3.1.3. Thermoresponsive behavior	55
3.1.4. Conclusion	57
3.1.5. Experimental part	57
3.2. PLGA microstructures loaded with metal nanoparticles	59
3.2.1. Synthesis	60
3.2.2. Stability of compartments	62
3.2.3. Different shapes and composition	64
3.2.4. Conclusion	66
3.2.5. Experimental part	68
4. PEGMA nanogels as drug delivering tool	73
4.1. Introduction	74
4.1.1. Doxorubicin	75
4.1.2. Pomalidomide	77
4.2. Drug loading	80
4.2.1. Determination of loading and release	81
4.3. Drug release	82
4.3.1. Doxorubicin release	82
4.3.2. Pomalidomide release	83

4.3.3.	Calculation of release exponent	84
4.4.	Other stimuli	86
4.5.	Cellular uptake	91
4.5.1.	Intracellular degradation	94
4.6.	Intracellular drug release	96
4.6.1.	Laser stimulated intracellular drug release	97
4.6.2.	Intracellular pomalidomide release	99
4.7.	Conclusion	103
4.8.	Experimental part	104
4.8.1.	Loading with doxorubicin/pomalidomide	104
4.8.2.	Co-culture and live/dead staining	104
4.8.3.	Flow cytometry	105
4.8.4.	Transmission electron microscopy of cells	106
4.8.5.	LPS-induced IL-6 production from J774 cells	107
4.8.6.	Angiogenesis assays	108
4.8.7.	Pomalidomide-induced cell morphological changes	109
5.	Au-Polymer hybrid structures as SERS platforms	111
5.1.	Introduction	111
5.2.	PEGMA nanogels as SERS sensors for bioimaging	112
5.2.1.	Crystal violet as a Raman reporter	113
5.2.2.	Doxorubicin as Raman reporter	116
5.2.3.	In-Vitro imaging of crystal violet	119

Contents

5.2.4. In-Vitro imaging of doxorubicin	120
5.2.5. Conclusion	122
5.3. PLGA microgels for SERS imaging	123
5.3.1. Spatial resolution of PLGA microstructures	124
5.3.2. Bleaching experiment	125
5.3.3. Conclusion	127
6. Enzymatic catalysis	129
6.1. Principles of enzymatic catalysis	130
6.1.1. Enzyme kinetics	133
6.2. Introduction of ABTS as a measuring tool	136
6.2.1. Cascade reaction	141
6.2.2. Michaelis Menten constant	146
6.2.3. Introducing a competing enzyme	148
6.3. Catalysis in beads	149
6.4. Possible implementation of SERS	151
6.5. Conclusion	154
7. Conclusion and Outlook	157
A. XPS measurements	165
B. Publications and conference contributions	171
B.1. Publications	171

B.2. Conferences 172

References **173**

1 Abstract

Polymers and nanoparticles can be combined into a host of different materials with applications in a wide range of fields such as catalysis, biotechnology, or drug delivery. Even in the colloidal state, such composites may vary significantly, e.g. ranging from a single nanoparticle stabilized by a polymer shell to a polymeric carrier decorated with hundreds of nanoparticles. In this context this thesis will present a novel strategy to grow gold nanoparticles in-situ in thermoresponsive microgels for different applications. Their ability to be used as a drug delivery tool will be presented (Chapter 4) as well as their use as SERS platform (Chapter 5).

In the first experimental chapter the synthesis of thermoresponsive nanogels decorated with gold nanoparticles (AuNPs) is introduced, which are later on used as drug delivery tool and as SERS substrate. The second Au-polymer composite which is introduced is based on poly(lactic-co-glycolic acid) (PLGA). Using the electro hydrodynamic co-jetting process, we show that nanoparticles of different morphologies and sizes can be implemented in

1. Abstract

high quantities. We focus especially on gold nanostars, functionalized with a Raman active molecule to exploit the possibilities of using three dimensional SERS microscopy.

In the second experimental chapter the thermoresponsive nanogels were loaded with two different anti cancer drugs allowing for the ability to use them as drug delivery tool, with special emphasis on the influence of different polyelectrolyte coatings and the usage of laser light as heat source to externally stimulate the release of the drugs.

The third experimental chapter exploits the possibility of using both gold-polymer systems introduced previously as SERS substrates. The thermoresponsive nanogels are loaded with different Raman dyes imaging in solution as well as in-vitro imaging is conducted. Secondly, we exploit the PLGA-gold structures being combined with three dimensional SERS microscopy to show the potential of using these structures for advanced bioimaging.

In the last experimental chapter a versatile method to use Raman spectroscopy as tool to observe enzyme catalyzed reactions is presented. Hydrogen peroxide producing enzyme reactions are coupled in a cascade reaction to the enzymatic oxidation of a Raman detectable substrate, enabling real time monitoring of reaction kinetics. Smart designs of substrates could also lead to an advanced and universal system for the study of enzymatic reaction kinetics using SERS, which will be briefly discussed and introduced.

2 General Introduction

2.1. Overview of nanoparticle polymer hybrid materials

Composite materials comprise of the combination of various components with distinct compositions and properties, typically with the aim to achieve enhanced or even novel functionalities. In the most common configuration, one of the materials acts as a matrix, in which one or more other components are embedded. Even though most composite materials involve a bulk matrix containing dispersed nanosized particles, a particular class can be defined as "colloidal composites" or "composite colloids", in which the combination of matrix and embedded nanoparticles (NPs) are dispersed in a continuous dispersion medium (solvent). In such composite colloids, the nanoparticles provide physical properties of interest such as optical absorption or fluorescence, magnetic behavior or mechanical strength.^{1,2} The matrix on

2. *General Introduction*

the other hand may provide not only colloidal stability, but also further functionalization through suitable surface chemistry, controlled porosity, or responsiveness toward external stimuli, among other properties. The colloidal state, however, offers the opportunity to design composites comprising a colloidal carrier on which functional nanoparticles are adsorbed, which can then be further encapsulated within an external shell. Among the wide variety of materials combinations that can be used for the fabrication of composite colloids, plasmonic gold nanoparticles are of high interest with proposed applications in different fields like sensing, catalysis, energy conversion and stimulated drug delivery.³⁻⁶

The synthesis of gold nanoparticles (AuNPs) has seen huge progress since the well-known report by Turkevich et al. in 1951,⁷ in which citrate was used as reducing and capping agent. Although this method is still widely employed, scientists have achieved a degree of control and understanding of the reaction conditions, and a large library of AuNPs with different shapes and sizes is currently available.⁸⁻¹¹ Although AuNPs can be used as synthesized for certain applications, others require additional elements, which may be related to tailored assemblies or combination with different materials that can add additional functionalities and achieve combined unique properties. Among the large choice of materials to be used, polymers offer a wide variety of possibilities for combination with AuNPs in many different configurations resulting in improved hybrid materials - including composite colloids

2.1. Overview of nanoparticle polymer hybrid materials

- for specific applications. The implementation of functional groups with a strong affinity toward gold, the fine control over the chemical composition and the stability that polymers can provide, render them a versatile tool for implementation of hybrid composites. Additionally, polymers can provide functionalities other than colloidal and chemical stability, such as control over polarity, anchoring points for further functionalization, or as carrier systems or matrices to finely tune interparticle interactions.^{1,12}

In general, hybrid polymer particle systems can be composed of single NPs covered with a polymeric shell which in general provides high stability in aqueous media and anchor points for surface functionalization.^{13,14} Clusters of NPs may also be formed - whereby new properties are expected to arise from the interaction between multiple metal particles within a polymer matrix. A characteristic example would be the combination of nanoparticles embedded in a thermoresponsive microgel where temperature can be used to tune the collective localized surface plasmon resonances (LSPR).¹²

LSPRs are related to collective oscillations of the electron density in metal particles, as a response to an external electromagnetic field (light). In the case of AuNPs this resonance occurs at the visible and near IR wavelength ranges. AuNPs thus typically display an intense color due to absorbance in the visible region of the spectra, which is accompanied by a significant enhancement of the electric field at the NP surface (which decays rapidly within just a few nm away from the surface). Such enhanced electric fields

2. General Introduction

can affect the polarizability of molecules adsorbed on the nanoparticles, for example resulting in huge enhancements (by many orders of magnitude) of Raman scattering signals, which is known as surface enhanced Raman scattering (SERS). A more detailed description of the theory and nature of LSPRs and SERS is discussed in Section 2.4.

2.2. Synthesis of nanoparticle polymer hybrid materials

Gold-polymeric particles will form the basis of this thesis. In the following section different concepts for the synthesis of these composites are introduced. Since this thesis focuses on polymeric matrices as nanoparticle support, the introduction focuses on the variety of these systems. Other systems, such as particle-polymer assemblies are also popular research topics at the moment and are covered elsewhere.¹⁵⁻¹⁸

2.2.1. Polymeric matrices as AuNP supports

A common strategy is the incorporation of AuNPs on the surface of polymer beads or implemented in a matrix of a polymeric microstructure, which results in high loading of AuNPs on the polymeric superstructure. The aim of this concept is to establish a statistical distribution of AuNPs in order to develop new functionality such as optical responses and/or multitasking

2.2. *Synthesis of nanoparticle polymer hybrid materials*

systems ideal for applications like drug delivery and SERS, rather than focusing on a distinct number of attached particles or distinct pattern.¹ This allows straight forward synthesis methods and simultaneously a high density of AuNPs concentrated in a structure of not more than a few micrometers. The method of synthesis depends on the polymeric structure but usually follows the concept of particle attachment or in situ growth. The AuNP attachment is driven through electrostatic interactions and ligand exchange processes. In all cases it is important that the polymer is big enough to attach many AuNPs. In situ growth uses the polymeric structure as stabilizer followed often established synthesis methods of AuNPs.

AuNP decorated polystyrene beads

A simple but effective method to form hybrid systems is the decoration of polymeric microbeads with nanoparticles. A common polymer in such systems is polystyrene (PS), because of the low toxicity, high monodispersity of the beads and easy surface functionalization.¹⁹

Nanoparticles can be grown directly onto the beads in a two-step method: an initial seed deposition is followed by an overgrowth (Figure 2.1A).²⁰⁻²² Recently, to gain more control over the particle size and morphology, researchers deposited pre-synthesized gold nanostars (AuNSs) onto amine terminated polystyrene beads (Figure 2.1B-D).²³ AuNSs were stabilized with a small amount of PEG and attached to the surface of the PS beads due to the

2. General Introduction

affinity of the gold surface towards amino groups. Similar to that, Mir-Simon *et al.* functionalized PS beads with four alternating polyelectrolyte layers using the layer by layer (LbL) technique, followed by the deposition of gold and silver nanoparticles of different sizes via electrostatic interactions.²⁴ In both cases the attachment of NPs offers a better control over composition and nanoparticle morphology compared to the reported in-situ methods. For further application, especially the shape control is of huge interest to shift the optical properties towards lower energies in the visible spectrum.

The polymeric beads contribute mainly as stabilizing support to the system. PS beads decorated with AuNSs are stable in cell media and can be used for in-vitro experiments.²³ This is remarkable considering that prevention of aggregation of nanoparticles in cell media often requires further functionalization like silica coating, which itself complicates the synthesis steps significantly. Additionally PS beads confine a lot of nanoparticles in a small volume and can be used as imaging platform for in-situ cell imaging.

Layer-by-Layer derived AuNP carriers

A wide variety of AuNP carrier systems can be derived through the application of LbL techniques onto polymeric beads to achieve polyelectrolyte capsules and hollow silica capsules with defined optical properties. The synthesis of polyelectrolyte capsules was developed through pioneering work by Möhwald and co-workers in the late 90s.^{25,26} Starting with water

2.2. Synthesis of nanoparticle polymer hybrid materials

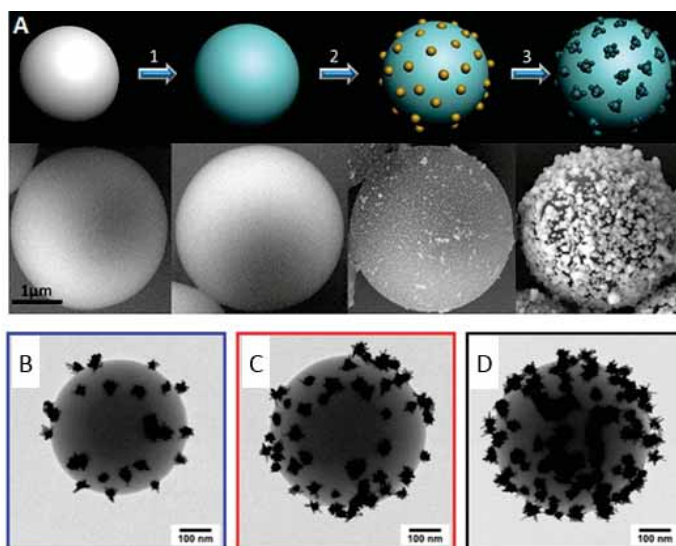


Figure 2.1.: A) Schematic representation of the seeded growth method to grow nanoparticles in situ on a PS bead and representative SEM pictures for each stage. B-D) TEM pictures of PS beads decorated with different amounts of pre-synthesized gold nanostars. Figure A reproduced with permission from ref.²⁰ Copyright 2012, American Chemical Society. B-D reproduced with permission from ref.²³ Copyright 2016, American Chemical Society.

soluble microbeads made out of melamin, subsequent polymer layers of opposing charge are deposited onto the surface of the beads. The thickness and physico-chemical properties are controlled by the nature of polyelectrolytes and the number of layers. Finally, the beads are dissolved and a hollow polymeric sphere resides. These systems can be further functionalized in many different ways. Amongst others, gold nanoparticles can be immobilized between the different layers of polymers to form complex systems with applications in catalysis, drug delivery and SERS.²⁷⁻³⁰

2. General Introduction

PLGA structures as AuNP carriers

Another attractive polymeric system uses poly(lactic-co-glycolic acid) (PLGA) as the base polymer. PLGA is widely used and is especially interesting for biomedical application as it is synthetically produced and yet FDA approved due to its biocompatibility and degradability.³¹ PLGA microstructures such as spherical particles, fibers or cylinders are commonly used to synthesize scaffolds for cell growth, as well as for biomedical applications such as drug delivery. Commonly, they are labelled with fluorescent dyes to monitor the degradation or cell uptake. In the specific case of electrohydrodynamically co-jetted polymer structures, additional functionalization in terms of multiple compartments can be implemented. This leads to more functionality and diversity for applications.³²

Recent work, which will be discussed in detail in this thesis, follows up the idea of implementing AuNPs into PLGA microstructures and showed that the method is not limited to small particles but instead even loading with anisotropic nanoparticles, such as stars is possible. The structures retain their functionality and different compartments.^{33,34}

2.2.2. AuNPs embedded in thermoresponsive hydrogels

A prominent type of hydrogels are thermoresponsive polymers which are extensively studied in this thesis. They form a highly porous polymer matrix

2.2. *Synthesis of nanoparticle polymer hybrid materials*

which allows either particle attachment on the surface or the incorporation of them inside the gel while keeping the NP surface accessible. When such thermosensitive polymers are formulated as sub-micron particles, they are called microgels and the phase transition leads to a sharp change in solubility upon heating. Although the reverse also exists, most thermosensitive polymers become more hydrophobic above the so-called lower critical solution temperature (LCST) and the value of which depends on polymer composition.^{1,35-37} In the case of hydrogels, this means that a sharp decrease in particle size occurs around the LCST, i.e. a transition from a swollen to a collapsed state. Probably the most popular thermosensitive polymer is poly(N-isopropylacrylamide) (pNIPAM), which displays an LCST that is independent of cross-linker concentration and other environmental parameters, rendering it very attractive for many applications.

Thermoresponsive microgels are commonly synthesized using the radical precipitation polymerization, which was first described by Chibante and Pelton for pNIPAM.³⁸ Above the LCST, the monomers will be dissolved whereas the newly formed polymers precipitate and under the right condition such as crosslinker concentration and surfactants, uniform and highly monodisperse microgels are formed. Several procedures have been reported for the synthesis of plasmonic nanoparticles embedded within crosslinked hydrogels,³⁹⁻⁴¹ which were proven useful for a wide range of applications, from catalysis, to drug delivery and sensing.⁴²⁻⁴⁴ As usual, the preparation

2. General Introduction

of a well-defined core-shell structure containing a single AuNP covered by a uniform pNIPAM shell, comprises a multi-step synthetic method, in which AuNPs are first synthesized with the appropriate size and shape, and subsequently functionalized so that they can be used as seeds for the uniform polymerization of the hydrogel around the AuNP core. Alternative methods in which nucleation and growth of AuNPs are carried out in situ, inside pre-made microgels, rarely result in the formation of a single nanoparticle per microgel, but invariably in multiple NPs with a certain size distribution and lack of morphological control. These systems can however still be of interest and are introduced later.

Single AuNP encapsulation in hydrogels

The preparation of single NPs covered with a uniform thermoresponsive polymer shell requires deposition of a primer layer on the surface of the NPs, so that polymerization and shell growth can be successfully implemented. As schematically shown in Figure 2.2, various approaches have been used for this initial step. Typically, CTAB stabilized AuNPs are first covered with a polystyrene layer, followed by pNIPAM polymerization which results in encapsulation of the particles.⁴⁶ The CTAB bilayer plays a crucial role, as its hydrophobic environment allows accumulation of styrene and divinylbenzene, and their polymerization into a thin layer of polystyrene, which is ultimately used as an anchor for further polymerization of the pNIPAM

2.2. Synthesis of nanoparticle polymer hybrid materials

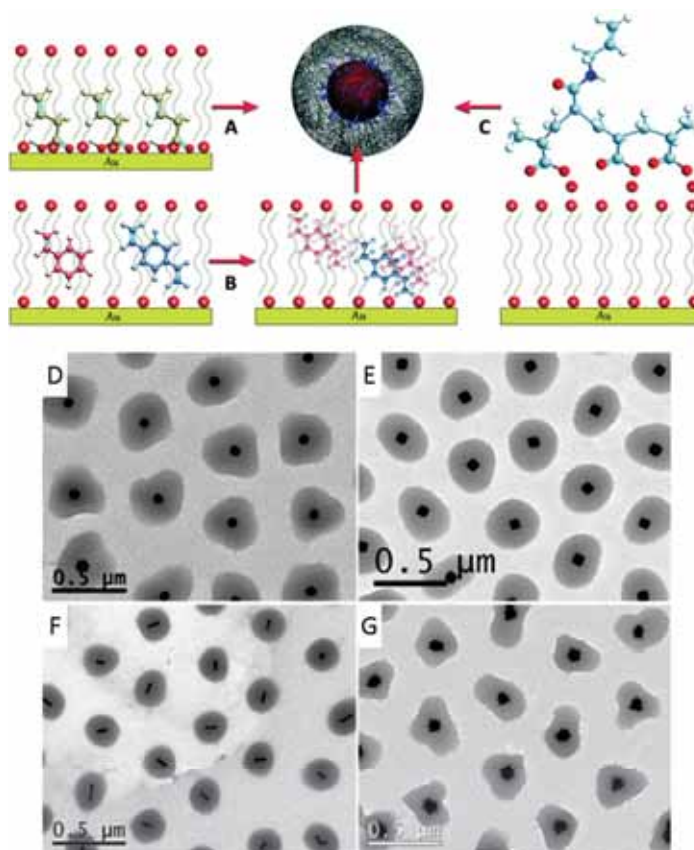


Figure 2.2.: Upper panel: Schematic representation of different approaches for surface functionalization with vinyl groups: butenoic acid (A), polystyrene and vinylbenzene (B) and LbL with allylamine (C). Lower panel: Representative TEM images of Au spheres (D), octahedra (E), nanorods (F) and nanostars (G), encapsulated with pNIPAM using the LbL method. Reproduced with permission from ref.⁴⁵ Copyright 2013, Royal Society of Chemistry.

shell (Figure 2.2B). This multi-step method is rather laborious and limited to particles covered by a CTAB bilayer. Therefore, more versatile approaches have been implemented, in which butenoic acid or a polyelectrolyte layer are used to surround AuNPs with the required vinyl anchor groups (Figure 2.2A,C). Butenoic acid can also accumulate within the CTAB bilayer and act as an anchor point with no need for an initial polymerization step (Fig-

2. General Introduction

ure 2.2A). Interestingly, butenoic acid can also be used as a mild reducing agent for the growth of Au NPs, so that it is present on the NP surface.⁴⁷ In the case of polyelectrolytes, the LbL technique can be used regardless of the AuNPs morphology.⁴⁸ A suitable polyelectrolyte pair, comprising polyacrylic acid functionalized with vinyl groups (Figure 2.2C) and poly(allylamine) hydrochloride, is selected to form a shell around the nanoparticles, which can be implemented on basically any pre-existing surface functionalization. TEM images in Figure 2.2D-G illustrate the successful encapsulation of gold spheres, octahedra, nanorods and nanostars, which were synthesized under different conditions and using different stabilizing agents, prior to the LbL-based encapsulation method.⁴⁸

Once the AuNPs have been functionalized, the polymerization of NIPAM is carried out following the usual precipitation polymerization method.⁴⁹ The monomers, including a crosslinker, are mixed with the particles and polymerized at a temperature above the LCST. Detailed studies showed that both the thickness of the pNIPAM shell and the pore size can be varied by changes in the crosslinker concentration and by addition of surfactants to the reaction mixture.⁵⁰ It should be noted that this is not a conventional seeded growth process where polymerization happens exclusively on the nanoparticles, but nucleation also occurs in solution, so that pure polymeric microgels (without gold cores) must be separated by centrifugation. The thermoresponsive shell around the AuNP core offers interesting properties

2.2. *Synthesis of nanoparticle polymer hybrid materials*

which have been demonstrated for a variety of applications. First of all, the diffusion of small molecules toward the AuNP surface can be altered by simple temperature changes, meaning that in the collapsed state (at temperatures above the LCST) molecules from the external solution can either have their progress towards the core hindered or may be entrapped and retained close to it.⁴⁴

Thermoresponsive hydrogels as a carrier matrix for AuNPs

In principle there are two different approaches reported in the literature: 1) assembly of pre-synthesized particles onto the hydrogel and 2) in situ growth of nanoparticles.

First protocols for a gold nanorod (AuNR) assembly on the surface of pNIPAM were established by Mathias Karg et al. and the group of Eugenia Kumacheva around the same time.^{1,51,52} In both cases pNIPAM microgels were copolymerized with a monomer containing carboxylic groups, e.g. methacrylic acid or allylacetic acid to obtain a negative net charge of the hydrogel. Similar to the PS beads, the positive charged particles assemble on the surface by electrostatic interactions. Figure 2.3A shows the result of LbL modified nanorods with a positive net charge on negatively charged pNIPAM hydrogels. More recent work by Lim et al. nicely shows the attachment of spherical citrate stabilized AuNPs of different sizes to allylamine copolymerized pNIPAM hydrogels.¹² Following a very accurate protocol, spherical

2. General Introduction

particles evenly attach onto the whole microgel and show remarkable optical properties.

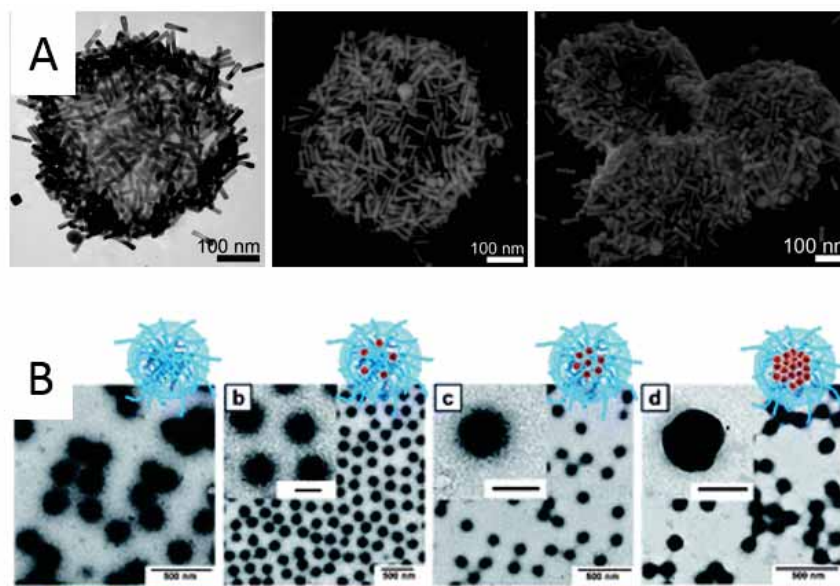


Figure 2.3.: A) TEM pictures of nanorod assembly onto pNIPAM microgels. (B) Scheme and TEM pictures of in situ grown nanoparticle onto PEGMA microgels below and above the LCST. C) Gold nanoparticles grown inside a vinyl caprolactam microgel which was copolymerized with acetoacetoxyethylmethacrylate. Acetoacetoxyethylmethacrylate inside the gel reduces the gold in situ without additional reducing agent. Figure A reproduced with permission from ref.¹ Copyright 2009, American Chemical Society. Figure B reproduced with permission from ref.⁵³ Copyright 2013, The Royal Society of Chemistry

Another interesting and different approach for the in situ growth was reported by the group of Andrij Pich.⁵³ They used thermoresponsive vinyl caprolactam and copolymerized it with acetoacetoxyethylmethacrylate (AAEM) and acetylic acid. Due to the faster conversion of AAEM, a core-shell like microgel is produced with AAEM mainly located in the core. The whole sys-

2.3. Optical properties of gold nanoparticles

tem is then able to slowly reduce gold and form clusters inside the microgel without further addition of a reducing agent. Figure 2.3B shows the TEM pictures of the particle growth at different concentrations of gold during the reduction. The exact mechanism is not yet understood but it's claimed that AAEM is accountable for the reduction.

In all systems the thermoresponsive behavior of the hydrogels were used to alter the optical properties of the hybrid material. Since the hydrogel collapses at temperatures higher than the LCST the surface plasmon interaction between the gold nanoparticles increases and a red shift can be observed (Section 2.3).

In this context this thesis will present a novel strategy to grow gold nanoparticles in-situ in thermoresponsive microgels for different applications. Their ability to be used as a drug delivery tool will be presented (Chapter 4) as well as their use as SERS platform (Chapter 5).

2.3. Optical properties of gold nanoparticles

Gold nanoparticles show a variety of intense colors depending on their shape and size. This phenomenon can be explained by a change of the interaction with an oscillating electromagnetic field when the size of the particle is lowered to dimensions smaller than the wavelength of the incoming light. Simply, the incoming light interacts with the free electron gas in the nanopar-

2. General Introduction

title and induces a coherent oscillation. This oscillation leads to a charge separation at the particle surface with respect to the cationic metal lattice and forms a dipole oscillation along the direction of the electric field of the electromagnetic wave. As for all oscillations, a resonance energy is present (Figure 2.4).

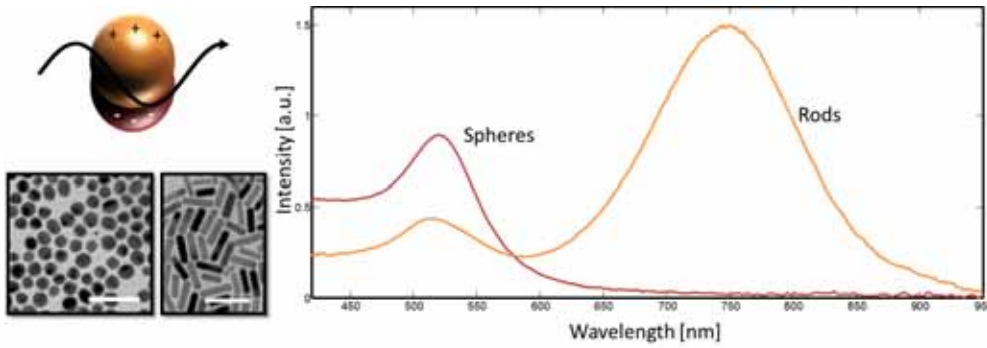


Figure 2.4.: Scheme of the oscillating electrons under electromagnetic irradiation and corresponding UV-vis spectra for spherical particles and rodshaped particles. Scale bar in both pictures is 100 nm.

In the early 20th century Gustav Mie and Richard Gans developed a solution to describe the extinction of spherical particles (Mie) and ellipsoidal particles (Gans) for particles under 20 nm.^{54,55} For bigger particles the theory loses accuracy and numerical methods (e.g. the boundary element method - BEM)⁵⁶ need to be implemented for the calculation of extinction spectra. However the extinction for small particles can be summarized with the following formula:⁵⁷

$$C_{ext} = \frac{24\pi^2 N_A a^3 \epsilon_m^{3/2}}{\lambda \ln(10)} \frac{\epsilon_i}{(\epsilon_r + 2\epsilon_m)^2 + \epsilon_i^2}. \quad (2.1)$$

2.3. Optical properties of gold nanoparticles

With C_{ext} as the extinction cross section, R as the gas constant, ε_m as dielectric constant of the surrounding medium, λ as the wavelength of the incoming light, ε_r and ε_i the real and imaginary part of the dielectric constant of the metal, ξ as the term to describe the aspect ratio and a is the radius. Hence the position of the extinction (localized surface plasmon resonance - LSPR) depends on the type of metal, the size and shape of the NPs and on the surrounding media, which is often used in sensing devices.⁵⁸⁻⁶⁰

The shape dependency of the extinction is shown in Figure 2.4. For a spherical gold nanoparticle the usual spectra contains one single plasmon peak whereas the rod shaped particles shows two peaks due to the anisotropy of the particle.

The first peak is due to the transversal mode (along the small side of the rod) and the second, broader peak is attributed to the longitudinal oscillations (along the long side of the rod) of the electrons. Other shapes, like triangles and stars show several plasmon peaks as well.^{61,62}

In terms of materials, silver and gold are mostly used since they show strong extinction cross sections in the visible light whereas for other metals the extinction is usually shifted to the UV regime.⁶³

Another important factor for the understanding of the optical properties of metal nanoparticles is the ratio between scattered and absorbed light. For small nanoparticles up to 20 nm absorption is dominant whereas the bigger the nanoparticles get, the bigger the fraction of scattered light. For example,

2. General Introduction

the extinction of an 80 nm sphere is composed of 50% scattered and 50% absorbed light.⁶⁴

The excited electrons of the LSPR quickly relax into their non-excited state and the energy is released as phonons which heat up the environment.^{65,66}

The different mechanism of plasmon relaxation and their contribution to photothermal properties are very complex and were intensively studied by Link and El-Sayed.⁶⁷ In this context, many studies were conducted to use the locally created heat around the particles for a variety of applications, such as biomedical application. Briefly, the heat can be used for photothermal therapy in the fight against cancer or to induce photothermal ablation of cells. In Chapter 4 we will use this effect to show enhance drug release from thermoresponsive nanogels upon NIR laser irradiation.

An important aspect for the understanding of plasmonic effects, especially in the case of polymer-gold hybrid materials and SERS systems is the interaction of nanoparticles in close proximity to each other. A simple case would be the assumption of two spherical gold nanoparticles with a size of 20 nm. We consider a case where they are separated by several 100 nm. The two particles are too far separated and show no interaction, thus the UV-vis will show one single plasmon peak, which can be attributed to a superposition of both single nanoparticles. As soon as the particles get closer to each other, the plasmons will interact with one another and different plasmon modes are created. Nordlander and co-workers developed an efficient method to

2.3. Optical properties of gold nanoparticles

characterize the interaction of nanoparticles called the plasmon hybridization method, which is adapted from molecular orbital theory.⁶⁸ It is a simple and intuitive way to interpret and foresee plasmon interaction between particles. For a dimer for example, it is predicted that two plasmons bands will arise upon interaction, depending on the polarization of the light. Transversal polarized light will show no coupling whereas longitudinal polarized light will interact and a bright plasmon at lower energies is generated together with a dark mode at higher energies. The extreme case of the dimers merging together will, in consequence, lead to a spectrum for rodshaped particles.^{68,69}

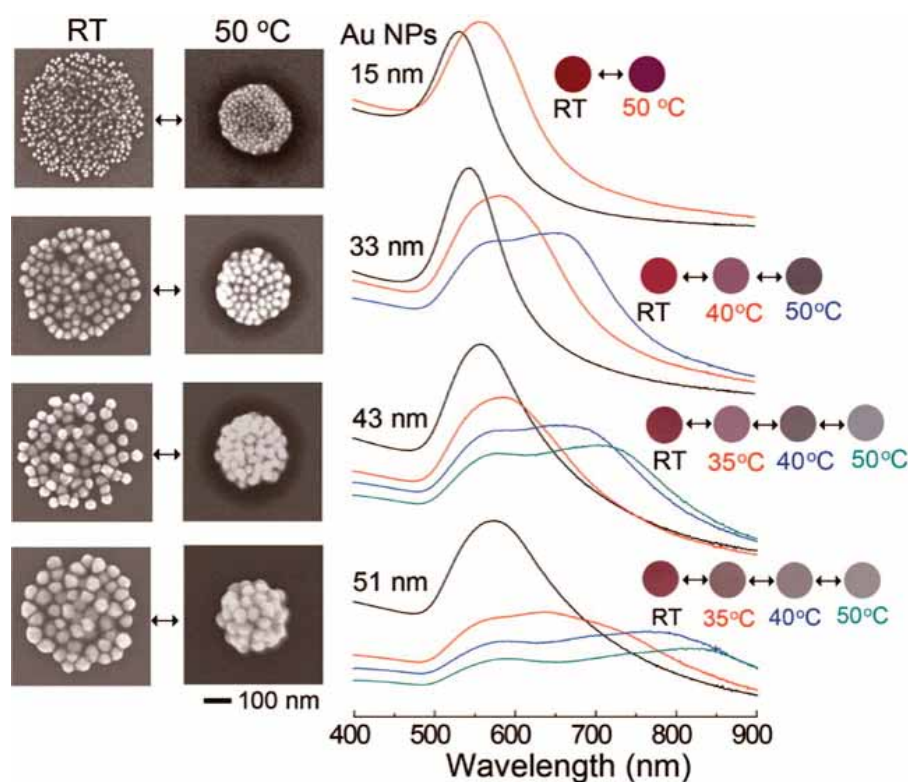


Figure 2.5.: SEM images pNIPAM microgels decorated with AuNPs of different sizes below and above the LCST. Additionally the corresponding UV-vis spectra are shown. Reproduced with permission from ref.¹² Copyright 2014, American Chemical Society.

2. General Introduction

As soon as more particles are close to each other the exact calculation gets more complicated but the basic effects stay the same. Lim and co-workers used pNIPAM microgels decorated with gold nanoparticles of different sizes.¹² Upon heating the polymer collapses and the particles get closer to each other, which then leads to plasmon coupling. Figure 2.5 shows how the effect of plasmon coupling and thermoresponsive polymers can be used in combination to accurately engineer the optical properties of a particle system.

2.4. Surface enhanced Raman scattering (SERS)

Experimental evidence for the surface enhanced Raman scattering (SERS) effect was first observed in 1974 by Fleischman and co-workers.⁷⁰ They observed an unusually high Raman intensity of pyridine adsorbed on a roughened silver electrode but initially suggested that the signal intensity was due to an increase in the concentration of pyridine. In 1977 Jeanmarie & Van Dyne and Albrecht & Creighton simultaneously showed that the concentration cannot be the reason for such a strong signal and discovered the SERS effect by suggesting a special interaction between the analyte and the metal surface.^{71,72}

The effect has been studied extensively during the last decades and tremendous progress was made in the proposals of mechanisms (as explained later),

2.4. Surface enhanced Raman scattering (SERS)

preparation of new and improved SERS substrates, and in the development of relevant applications to make use of the intense signal. Compared to other labeling and sensing methods like fluorescence or infrared spectroscopy, Raman is a non-invasive and possibly label free method which works in aqueous environments since water has a very low Raman cross section (opposed to IR). This has led to applications in different fields like biotechnology, biochemical sensing, biology and analytical chemistry.⁷³⁻⁷⁵

2.4.1. The Raman effect

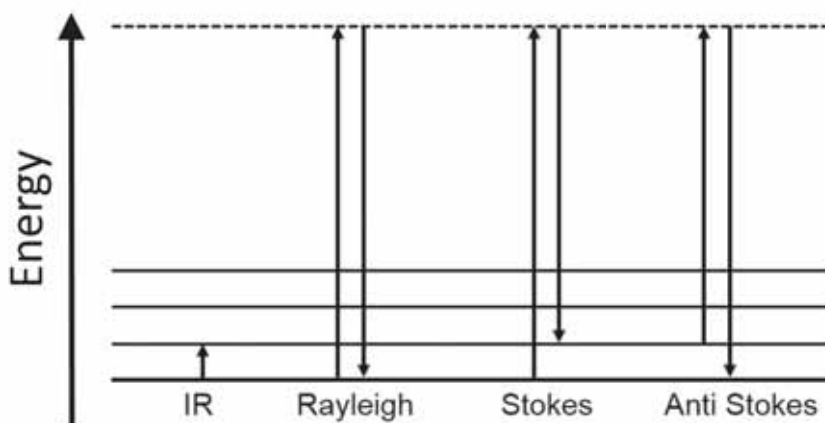


Figure 2.6.: Jablonski Diagram of the different scattering modes. Rayleigh scattering, Stokes Scattering and Anti Stokes Scattering. For comparison IR absorption is also shown.

C. V. Raman observed in 1928 a new type of scattered radiation upon the interaction of light with matter.⁷⁶ Next to elastic scattering (Rayleigh Scattering), matter shows a weak inelastic scattering where the frequency is shifted symmetrically around the initial frequency (ω_R) towards lower frequencies

2. General Introduction

(ω_S) and higher frequencies (ω_{AS}). Both cases are called Stokes and Anti-Stokes scattering, respectively, and are illustrated in Figure 3.4.

The frequency shift can be attributed to the energy of a vibrational state of the molecule. As shown in Figure 3.4, for Stokes scattering, the molecule is excited into a virtual state by the incident light and instead of the Rayleigh scattering process it decays into a state of less energy and the remaining energy is transferred to a vibrational state of the molecule. Anti-Stokes scattering works in the same way, in this case the electron is initially in an excited state. Following photon adsorption, the molecule passes through a virtual state into a lower energy state imparting the excess energy onto the emitted photon. Since the molecule is mainly populating the ground state at room temperature (Boltzmann distribution), the intensity of Stokes scattering is greater than the scattering of the Anti-Stokes.⁷⁷

The wavenumber of the Raman scattering response depends on the separation between vibrational energy states within the molecule and is independent of the intensity or wavelength of the incident light source. This means a single excitation wavelength, which has not to be in resonance with the molecule, is sufficient and the information is a spectrum similar to an infrared spectrum. In contrast to IR-spectroscopy, where the dipole moment is important for the activity of the vibration, a Raman active vibration needs to have a change in polarizability. For bonds with a strong dipole moment, hence a strong IR band, the polarizability is usually low. Whereas for bonds with a

2.4. Surface enhanced Raman scattering (SERS)

weak dipole moment, hence low IR activity, the polarizability is usually high and the vibrational states of the bond are Raman active. This explains also why water is Raman inactive but shows high activity in IR spectroscopy.

From an experimental viewpoint this enables a very simple system to detect a wide array of different molecules using a single excitation wavelength. Since the Raman spectrum acts as a fingerprint for a given molecule simultaneous detection of several molecules is also possible. A major disadvantage of Raman scattering is the low intensity or Raman cross-section for most molecules. The Raman cross-section (σ_R [m^2]) relates to the Raman scattering intensity of a given vibrational mode (P_R [W]) compared to the incident beam power density (S_o [Wm^2]). This is usually very low since just about every 10^6 - 10^8 photons are actually Raman scattered. Just a few compounds like azo-compounds or graphene show high Raman intensities. Having a roughened metal surface in close proximity however can increase the cross-section over several orders of magnitude and creates a feasible technique to detect molecules despite their low cross section⁷⁸

2.4.2. Mechanism for SERS

The mechanism behind the enhancement can be divided into two different categories, 1) the electromagnetic enhancement and 2) the chemical enhancement. The electromagnetic enhancement can be attributed to an effective field enhancement of electromagnetic waves close to the metal surface.

2. General Introduction

The intensity (I) of the Raman signal is proportional to the electric field of the incoming light $I \propto E_{in}^2$. The electric field, however, is drastically enhanced close to the surface of nanoparticles, due to the presence of surface plasmons. In consequence, the effective field (E_{Ef}) which interacts with the molecule is larger and thus the intensity enhanced. In the same way that the incoming electric field interacts with the nanoparticle surface, the resultant scattered light also interacts with the surface of the nanoparticles, leading to a further enhancement.

In summary, it can be concluded that the SERS intensity (I_{SERS}) for Stokes scattering depends as follows on the electric field:⁷⁹

$$I_{SERS} = |E_{in}(\omega_{in})|^2 |E(\omega_{in} - \omega_{vib})|^2, \quad (2.2)$$

considering that the vibrational energy is small with respect to ω_{in} the equation can be simplified as:

$$I_{SERS} = |E_{in}(\omega_{in})|^4. \quad (2.3)$$

This equation is known as the $|E|^4$ approximation and illustrates how much a small enhancement of the electric field will result in a huge enhancement of the SERS signal. This can be even better expressed by the enhancement factor (EF):

$$EF = \frac{I_{SERS}}{I_{RAMAN}} \quad (2.4)$$

2.4. Surface enhanced Raman scattering (SERS)

Considering for example an electric field enhancement of 10x, the resulting enhancement of the signal will already be 10000. In reality the enhancement factor is difficult to calculate and still controversially discussed because the intensity needs to be averaged per molecule in the sensing volume which is, in practice, hard to determine accurately using a normal optical microscope. The approximation is so far valid for all metal structures like rough surfaces and single nanoparticles. The best enhancement, however, is reached within junctions of nanoparticles (hot spots) where plasmon interaction is present. Within these junctions the electric field is drastically enhanced and good SERS results can be achieved.

It is important to notice that the electric field enhancement is a so called "near field effect" and thus dependent on the distance from the metal surface. The theory does not require adsorbance of the molecule but the presence in a certain sensing volume. The intensity (I_{SERS}) decreases roughly with r^{-10} . This illustrates how important it is for applications to engineer particle systems with hot spots of high electric field enhancement and at the same time good accessibility of the analyte.⁷⁹

Chemical enhancement takes an interaction between molecule and the substrate into account but is still not fully understood. It is believed that the interaction between the substrate and analyte changes the electronic structure in the analyte such as a change in the polarizability tensor of the molecule or the creation of new electronic states which can be in resonance with the

2. General Introduction

incoming light. Another possible mechanism could be a charge transfer between analyte and metal where an electron is transferred from the HOMO of the molecule to unoccupied states above the Fermi level of the metal.⁸⁰⁻⁸³ All cases however contribute little to the overall enhancement and the maximum chemical enhancement is believed to be a factor of 10^2 in very good cases.

2.4.3. Hot spots

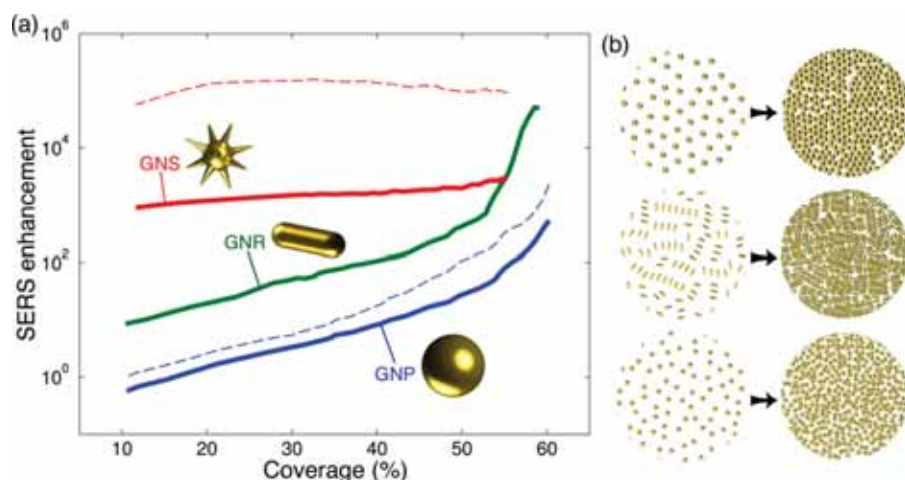


Figure 2.7.: a) SERS enhancement dependent on substrate coverage for nanoparticles with different morphologies at 785 nm excitation wavelength. The dashed lines represent excitation at 633 nm for GNP and 900 nm for GNS. b) Corresponding simulations of the surface coverage. Defects were taken into account for this study. Reproduced with permission from ref.⁸⁴ Copyright 2017, American Chemical Society.

In the section above it was briefly mentioned that the electric field enhancement is strongest if the molecule is present within junctions of particles (hot spots), but it is important to discuss this effect and the effect of particle shape on the SERS enhancement in more detail.

As an alternative to nanoparticle clusters or aggregates, anisotropic nanopar-

2.4. Surface enhanced Raman scattering (SERS)

ticles, in particular those displaying sharp edges, corners or tips, also exhibit high intrinsic electric field enhancement at specific regions, rendering them excellent substrates for SERS experiments, with no need for induced aggregation. Recently a lot of effort has been put into the creation of SERS system using gold nanostars (AuNS), since their sharp edges show huge enhancement and thus are suitable for single nanoparticle SERS systems in solution.^{18,62} In a recent study, Garcia de Abajo and co-workers, calculate the SERS enhancement of single nanoparticles with different shapes and their assemblies.⁸⁴ For a single particle or particles with little to no interaction (Figure 2.7) the SERS enhancement can be predicted by the nanoparticle shape, and the trend that nanoparticles with sharper edges give better enhancement is valid (nanostars > nanorods > nanospheres). The more complete the coverage the greater the plasmon interaction and, as stated in the previous section, the enhancement between the junctions of particles is bigger. For gold nanorods and spheres the enhancement increases significantly up to three orders of magnitude. However, for AuNSs the situation is more complicated, due to the interaction of the tips and some overlap upon assembly, the enhancement increases slowly and in some cases even a decrease of intensity can be observed if the coverage becomes dense enough.^{23,84}

2. General Introduction

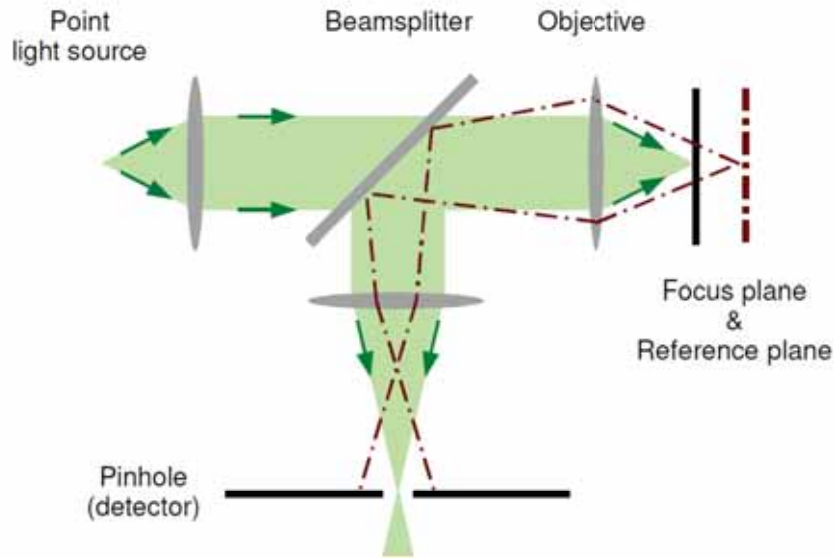


Figure 2.8.: Principle setup of a confocal microscope. Picture taken from Witec Manual

2.4.4. Confocal Raman microscopy

In confocal microscopy, a point light source, commonly a laser, is focused onto the sample and the reflected/scattered irradiation is focused back through a pinhole onto a detector. Figure 2.8 schematically illustrates the setup of a confocal microscope. Through focusing of the incoming and the outgoing signal, just the information of the focal point is recorded. The red, dashed lines indicate how the signal from points which are not in focus are excluded from detection. This technique offers increasing contrast and resolution. Spatial resolution in three dimensions can be observed and tomography-like measurements are possible. Especially for Raman microscopy, an increase in contrast by reducing the background signal holds

2.4. Surface enhanced Raman scattering (SERS)

huge advantage since commonly the Raman signal is often disturbed by fluorescence of the molecule or fluorescence of the sample substrate (glass). However, a confocal setup always decreases the signal intensity which is crucial for Raman spectroscopy since the Raman intensities are generally weak, compared to for example fluorescence intensities.⁸⁵

A crucial parameter for the confocality is the pinhole size. The pinhole has to be small enough to ensure confocal images have good lateral and in-depth resolution, whilst retaining sufficient signal intensity to enable Raman measurements. At the same time should it be chosen in a way that the overall intensity is still high enough to enable Raman measurements. Practically the pinhole size can be calculated using the following equation:

$$\frac{M}{NA} \geq \frac{\pi d_0}{2.5\lambda}, \quad (2.5)$$

with M as magnification, NA as numerical aperture, d_0 as pinhole diameter and λ as the wavelength of the incoming laser. If this equation is fulfilled, confocality is ensured. For an excitation with a 785 nm laser for example, using a 100x/0.9 objective a pinhole size of 50 μm is enough. An objective change to a 40x/0.6 already requires a 25 μm pinhole size.⁸⁵

2.5. Nanoparticle polymer hybrid materials for

SERS

In the case of SERS, polymeric systems are expected to comply some specific tasks besides improving stability or surface chemistry. A major aspect of successful SERS measurements is the creation of hot spots. A simple way to create hot spots involves inducing aggregation of the nanoparticles, usually by simply increasing the ionic strength in the colloidal solution. The resulting uncontrolled assembly of the nanoparticles leads to the formation of numerous junctions where a high electromagnetic field enhancement will originate from plasmon coupling (or plasmon hybridization), which are favorable for SERS measurements. Even though this approach is simple and effective, it suffers from a lack of control over the process, and consequently poor reproducibility of the SERS signal. Therefore, the ability to control or even direct the aggregation of particles and clusters is of high interest and polymers may play a key role in this direction.⁷³⁻⁷⁵

In both, the case of controlled aggregation and single particle SERS measurements, an additional crucial criterion needs be fulfilled to obtain a working SERS system. The analyte must be located at the hot spot, i.e. inside an interparticle gap or in close proximity to the nanoparticle surface. This can be challenging in many real systems, since the analyte molecules should display affinity for the Au surface and compete with the adsorbed surfactant

2.5. Nanoparticle polymer hybrid materials for SERS

or polymer, meaning that a suitable compromise between stabilization and SERS signal must be achieved. It is, however, possible to take advantage of this feature when devising SERS-encoded particles for imaging applications, by using a SERS active surfactant (SERS tag). This tag may either be adsorbed directly on the nanoparticle surface or as a thiolated SERS active molecule mixed with the selected surfactant. A polymer layer may be then used to stabilize the encoded particles, so that the surface is protected and isolated from the environment, to ensure a constant signal from the SERS code throughout the targeted application. A good example of efficient encapsulation of AuNSs covered with SERS active molecules in a polymer shell is the work by Jimenez de Aberasturi et al.¹⁸ In a two phase transfer step process, AuNSs are capped with different SERS tags and then stabilized with a polymer. These particles show high stability and a good SERS signal which makes them suitable for biological applications such as multiplexing and cell discrimination, with a high sensitivity and signal stability (Figure 2.9A-C). In the same line of application, the imaging quality and signal to noise ratio can be further improved by increasing the concentration of particles in the measurement volume, by either AuNP self-assembly on a polymeric superstructure or by implementation of additional functionalities, such as magnetic nanoparticles, and application of an external magnetic field.⁸⁶ A nice example which demonstrates this effect was shown by Serrano-Montes et al.,²³ where PS beads are decorated with AuNSs. This leads to increased

2. General Introduction

concentrations of AuNSs in a confined space, which in consequence enhances the SERS signal inside the cell drastically compared to the same concentration of AuNSs in solution as shown in Figure 2.9D-E.

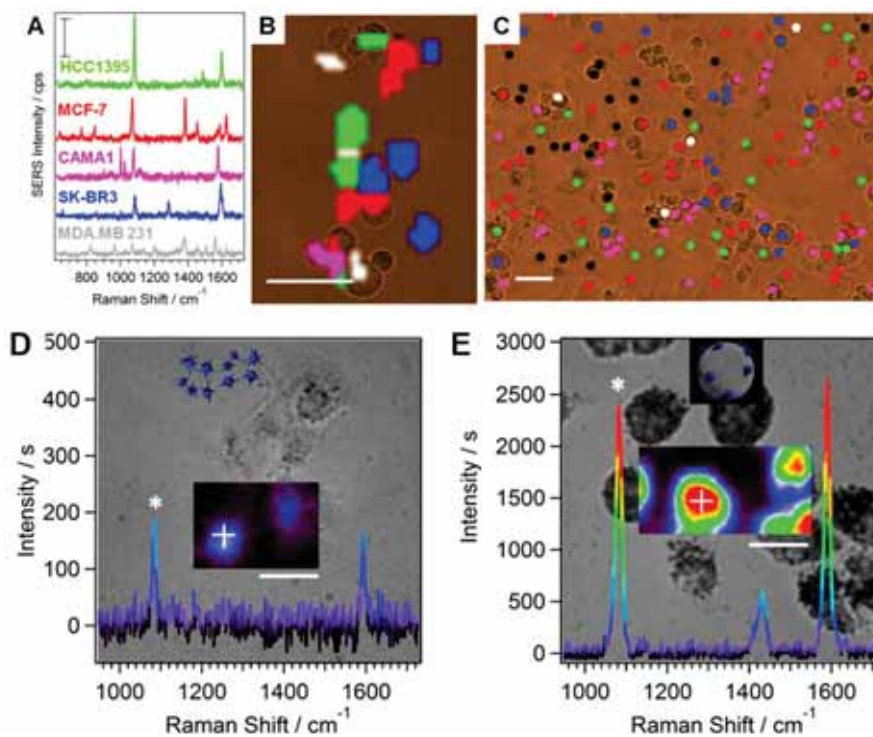


Figure 2.9.: Upper panel: Reference spectra of the difference SERS encoded nanoparticles in single cell cultures. B) and C) SERS spectra and particle assignment inside a cell co-culture. Reproduced with permission from ref.¹⁸ Copyright 2016, American Chemical Society

Lower panel: In one case the as a solution (D) and in the other case immobilized on PS beads (E). The intensity differs a lot showing an increased signal for the PS beads while keeping the AuNS concentration constant. Reproduced with permission from ref.²³ Copyright 2016, American Chemical Society

For ultrasensitive sensing applications, the gold surface must be accessible to the analyte, which may require the design of more complex systems, especially when using AuNPs in solution, as naked NP surfaces often lead to

2.5. Nanoparticle polymer hybrid materials for SERS

uncontrolled aggregation. Therefore, most sensing applications are based on nanoparticles deposited on solid substrates, where aggregation and colloidal stability are not of concern. In these systems, cleaning (e.g. by plasma etching) can be carried out after synthesis to make the AuNP surface accessible, while avoiding SERS signal contamination from residual impurities.⁸⁷⁻⁸⁹

Alternative strategies include the use of surface coating shells such as stimuli-responsive polymers, which not only protect the gold nanoparticles but also capture the analyte molecules and entrap them close to the AuNP surface. In the landmark publication on this topic, detection of 1-naphthol was demonstrated as an example (Figure 2.10).⁵⁰ Two different scenarios were tested to show that a swell-collapse transition is key for 1-naphthol detection. When the Au@pNIPAM particles were mixed with 1-naphthol solution at 4 °C, molecular diffusion could occur through the open structure of the swollen microgel, as reflected in a SERS spectrum with low intensity, but when the temperature was raised up to 60 °C (above the LCST), the polymer structure collapsed, analyte molecules were trapped and the SERS signal was enhanced. Interestingly, when the temperature was lowered back to 4 °C, the signal decreased again, indicating diffusion of 1-naphthol out of the microgel shell. In the second experiment, Au@pNIPAM particles and 1-naphthol were mixed at 60 °C, when the microgel was in the collapsed state, so that the pores were too small to allow molecular diffusion, as seen in a featureless SERS spectrum. As expected, an in situ cooling and heating cycle allowed 1-naphthol detec-

2. General Introduction

tion. This proof of concept experiment demonstrates the possibility of using these hybrid colloidal materials as substrates for generalized SERS detection in aqueous solution.

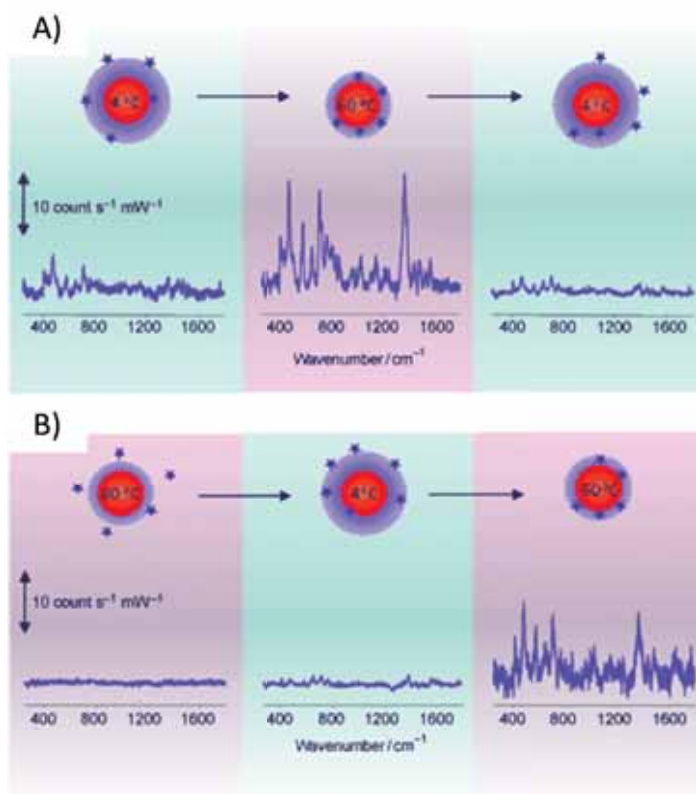


Figure 2.10.: SERS signal of 1-naphtol as a function of temperature and heating cycle. (A) Starting at 4°C, heating up to 60 °C and cooling down back to 4 °C. (B) Starting at 60 °C cooling down to 4 °C and heating up back to 60 °C. Reproduced with permission from ref.⁹⁰ Copyright 2009, Wiley-VCH.

In the context of the work contained within this thesis it is important to also mention the pioneering work by Kang et al. towards the in vitro monitoring of doxorubicin release.⁹¹ Briefly, particles were functionalized with PEG and doxorubicin was conjugated to the surface through a pH sensitive

2.5. Nanoparticle polymer hybrid materials for SERS

hydrazone linkage. The particles were incubated with cells and taken up via the endocytosis pathway. Due to the microenvironment, mainly the pH inside the endosomes, doxorubicin is released and monitored using SERS and fluorescence techniques (Figure 2.11). This work is a good example of a particle system designed to take advantage of the different environments inside cells to create a smart delivery system and shows especially how SERS can be used to gain more insights into the mechanism of drug release in cells.

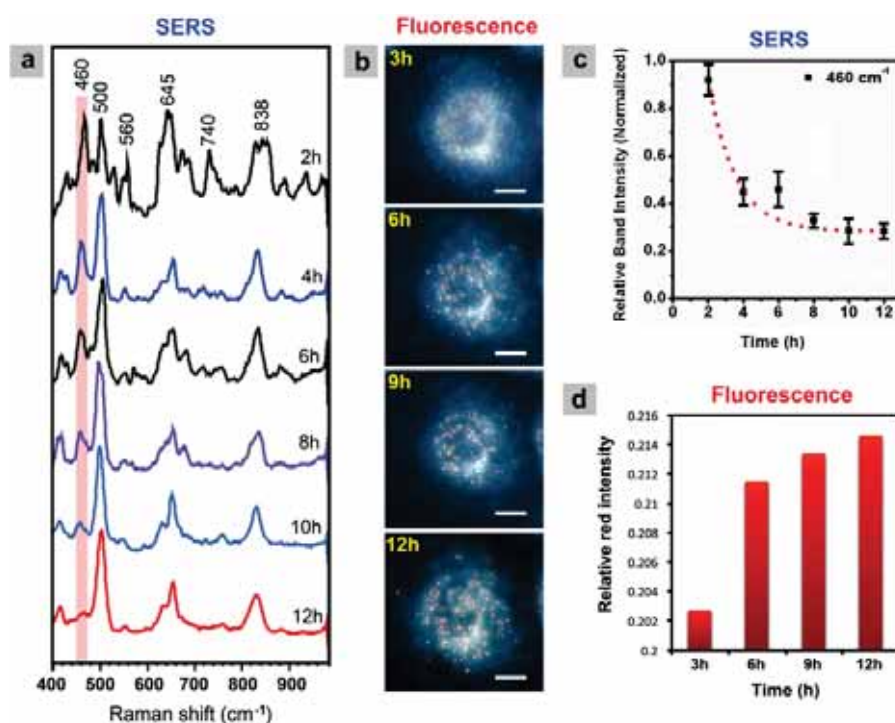


Figure 2.11.: (a) Real-time monitoring of the doxo release measured by SERS (a) and fluorescence (b). The scale bar is 10 μm. Decrease of normalized Raman band intensities over time at 460 cm⁻¹ (c) and the increase of the relative fluorescence intensity (d). Reproduced with permission from ref.⁹¹ Copyright 2013, American Chemical Society

2.6. Nanoparticle polymer hybrid materials for drug delivery

Drug delivery has become a major research topic in recent years. The idea is to improve drug efficiency of existing drugs while simultaneously reducing side effects. Incorporation of a drug, like doxorubicin, into more sophisticated responsive nanoparticle systems could help to tailor the accumulation in a desired part of the body. A common example is the delivery of chemotherapeutic drugs directly to the tumor while shielding the healthy cells from the drug. In a system which encapsulates the drug and is simultaneously functionalized with biomarkers to target specifically cancer cells, side effects could therefore be minimized. After targeting the desired cells in the first place, an ideal system would then release the drug to ensure an efficient treatment. Drug release can be either facilitated through stimulation of the cell, pH modification, an external stimulus like heat (burst delivery) or by slow degradation (continuous delivery) depending on the desired time period.⁹²⁻⁹⁴ Another idea for the encapsulation of drugs is to control the solubility of drugs. Most drugs are organic molecules which sometimes show low solubility in water, thus an encapsulating shell to improve solubility is key for convenient delivery through the blood of the patient or to overcome other biological barriers.⁹⁵

There are many different ways to face all the above mentioned challenges,

2.6. Nanoparticle polymer hybrid materials for drug delivery

including liposomes, silica shells, polymers or inorganic particles.⁹⁶⁻¹⁰⁰ This thesis will focus on thermoresponsive drug delivery tools. Thermoresponsive nanomaterials show a rapid change in their structure upon temperature change. In Section 2.2 thermoresponsive microgels were already introduced along with the concept of the LCST. Another example of thermoresponsive behavior would be the phase transition of lipids.^{42,96,101} The thermoresponsive behavior is used to encapsulate drugs and release them due to the change of the structure upon temperature change. Different strategies exist which may be used to utilize this process, such as a brief decrease in temperature (cryotherapy) leading to free diffusion of the drug.¹⁰² The more common way however is to induce a structural change upon heating and by that stimulate drug release. Currently liposomes show the most promising behavior and some systems have already reached clinical trials.¹⁰³

In this context, nanoparticle polymer hybrid materials show great potential for applications. The extra functionality of the metal nanoparticle can be used to locally produce heat and trigger the release of the drugs upon an external trigger. Put simply, the nanoparticles act as antenna for external irradiation and, by that, transform energy into heat and induce the phase transition of the polymer. Pelegrino and co-workers introduced a system of cubic magnetic nanoparticles functionalized with a thermoresponsive polymer.¹⁰⁴ The polymer intercalates doxorubicin in its swollen state but will release it once the temperature is raised above the LCST. An applied magnetic

2. General Introduction

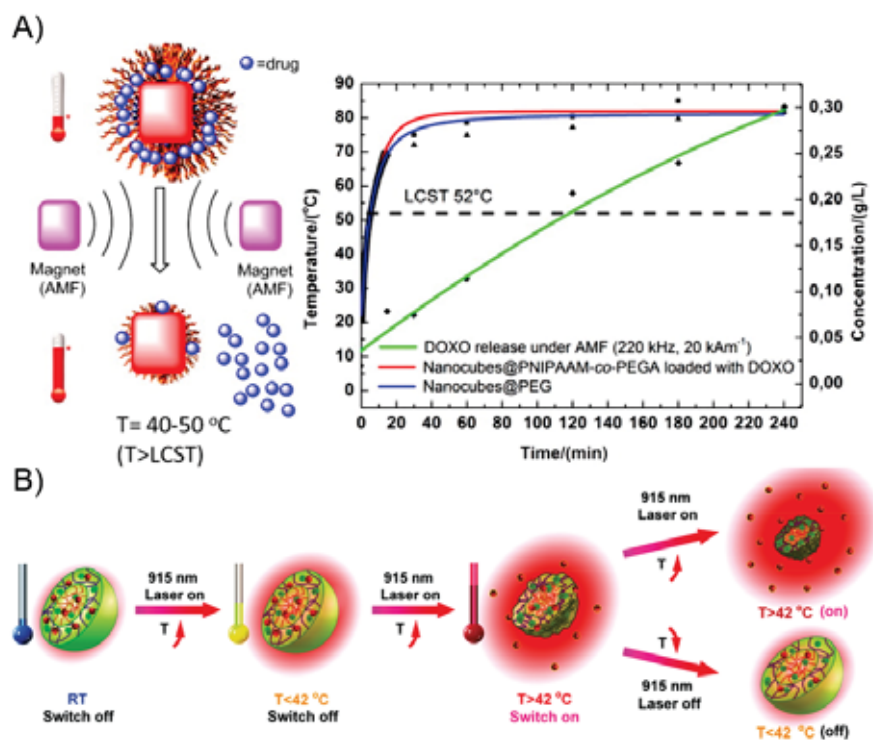


Figure 2.12.: A) Schematic representation of doxo loaded polymer coated magnetic nanocubes under the influence of an magnetic field. On the right, the temperature profiles of the particles under a influence of a magnetic field and the release profile of doxorubicin. B) Release scheme of the doxo loaded polymer-CuS hybrid particle under the influence of laser irradiation. Figure B reproduced with permission from ref.¹⁰⁴ Copyright 2015, American Chemical Society. Figure B reproduced with permission from ref.¹⁰⁵ Copyright 2016, Wiley VCH.

field induces local heat in the polymer due to the magnetic nanoparticles and the polymer collapses and doxorubicin is released (Figure 2.12A). A similar approach was used by Zhu and co-workers.¹⁰⁵ Instead of iron oxide cubes they implemented copper sulfide quantum dots in a thermoresponsive polymer. Again, as shown in Figure 3.2B, the quantum dots work as antenna and produce local heating under IR irradiation which leads to the collapse of the microgel and the release of the drug. Both cases are good examples of how

2.6. Nanoparticle polymer hybrid materials for drug delivery

the combination of inorganic nanoparticles and polymeric nanostructures lead to an increased complexity of the system which can be explored to enhance the efficiency of drug delivery systems. In this context this thesis will present a way to deliver two different drugs with different physical properties using a polymeric microgel with AuNPs. At the same time the use of a NIR laser is explored to externally trigger the release of doxorubicin.

3 Synthesis of gold/polymer hybrid materials

This chapter describes the synthesis and characterization of the polymer gold hybrid systems which will be used later on as drug delivery stems (Chapter 4) and SERS platform (Chapter 5). This chapter is resulted in two recently published papers.^{106,107}

In the first section the synthesis of AuNP-containing thermosensitive nanogels made out of polyethylene glycol methacrylate (PEGMA) is demonstrated. The nanogels will be covered with in-situ grown AuNPs and finally coated with two different types of polyelectrolytes to gain further functionality and stability.

In the second part the polymer is switched from PEGMA to PLGA and microstructures with incorporated nanoparticles are presented. Nanoparticles, especially gold nanostars (AuNSs) are transferred to organic media and coated with a Raman active molecule. These particles are then implemented

3. Synthesis of gold/polymer hybrid materials

in microstructures different shape and size using the electro hydrodynamic (EHD) co-jetting process.

3.1. PEGMA hydrogels with in-situ grown gold nanoparticles

The nanogels are made out of a thermoresponsive polymer on poly(ethylene glycol) methacrylate basis and have in situ grown gold nanoparticles attached to it.

The mechanism of the synthesis will be explored and the system tested on its thermoresponsive properties and general physicochemical properties. An extra polyelectrolyte layer gives further stability and makes the nanogels suitable for various applications, such as drug delivery tool or SERS platform. In Chapter 4, high drug loading abilities which lead to a highly versatile systems are shown in which drug release profiles can be controlled via polyelectrolyte coating and/or various external stimuli. On the other hand we focus on SERS imaging and the ability to load the microgel with a Raman active molecule to conduct in vitro cell imaging in Chapter 5.

3.1.1. Synthesis and polyelectrolyte coating

The thermoresponsive nanogels are formed by the well-established free radical polymerization method.^{2,108} PEGMA nanogels were chosen because

3.1. PEGMA hydrogels with in-situ grown gold nanoparticles

of their easy-to-tailor lower critical solution temperature (LCST), ranging from room temperature up to 90 °C,^{109,110} and because their monomer constituents are non-toxic.¹¹¹ These are two major advantages, as compared e.g. to the widely used poly(N-isopropyl acrylamide) (pNIPAM).^{112,113} In the second step of the synthesis, a surfactant-free method was used to incorporate AuNPs within the PEGMA nanogels, thereby avoiding potential toxicity of surfactants and keeping the AuNPs surface free to adsorb other molecules (Figure 3.1).

To this purpose, pre-made nanogels were immersed in a solution of H₂AuCl₄, followed by addition of a strong reducing agent, NaBH₄. The amino groups in the nanogels (present in the monomer 2-aminoethyl methacrylate hydrochloride) coordinate the gold precursor and small gold seeds of approximately 3 nm were formed upon NaBH₄ reduction. These seeds were subsequently grown by addition of H₂AuCl₄, sodium bromide and formaldehyde, which displays a pH-dependent reducing potential.¹¹⁴ Sodium bromide helped in controlling AuNP growth due to the formation of a gold bromide complex with higher stability as compared to free H₂AuCl₄. When the process was carried out, in the absence of either Au seeds or sodium bromide, nanogels were obtained with particle disparity, anisotropy and aggregation (Figure 3.2).

On the contrary, seeded growth produced nanogels with evenly distributed AuNPs with an average size of 23.2 ± 6.1 nm and a low proportion of anisotropic

3. Synthesis of gold/polymer hybrid materials

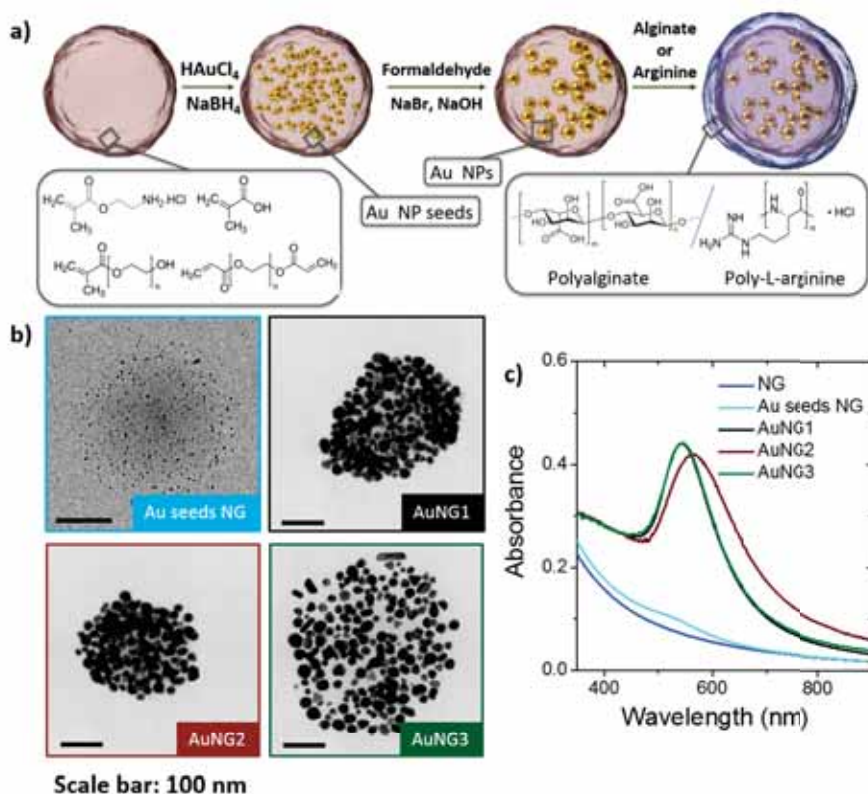


Figure 3.1.: a) Schematic representation of the in-situ growth of AuNPs in PEGMA nanogels. Small gold seeds were synthesized by reduction with NaBH₄. Further growth was realized by introducing the nanogels with seeds in a growth solution containing NaBr and formaldehyde at high pH. The obtained nanogels were finally wrapped with a layer of polyelectrolytes. b) Representative TEM pictures of the nanogels during the different growth steps, as labeled. c) UV-Vis spectra of the corresponding particle colloids. Reproduced with permission from ref.¹⁰⁶ Copyright 2017, American Chemical Society.

particles (Figure 3.3 and 3.4). The nanogels containing AuNPs displayed a localized surface plasmon resonance (LSPR) band centered at 540 nm (Figure 3.1), which is redshifted with respect to free AuNPs with similar sizes due to some anisotropy and plasmon coupling between the AuNPs in the gel. This two-step process allows a good level of control over the final AuNP size, which can range from 9 to 30 nm simply by tuning the amount of Au

3.1. PEGMA hydrogels with in-situ grown gold nanoparticles

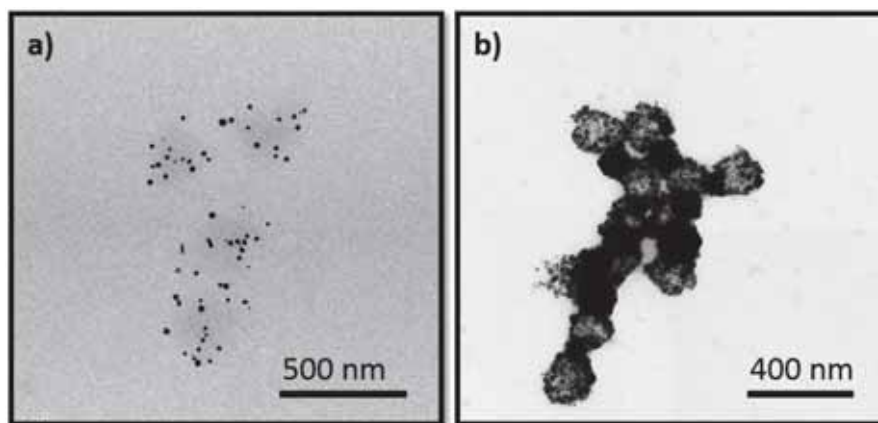


Figure 3.2.: a) TEM images of particles grown without initial seed growth step. b) Particles grown without NaBr in the second growth step. Reproduced with permission from ref.¹⁰⁶ Copyright 2017, American Chemical Society.

seed-loaded nanogels added to the growth solution (Figure 3.3).

PEGMA nanogels were subsequently wrapped with biodegradable and biocompatible polyelectrolytes by immersing AuNP-loaded nanogels in the appropriate polyelectrolyte solution followed by several washing steps to remove non-adsorbed polyelectrolytes. Samples with different surface compositions were named as follows:

- 1) AuNG1 had no coating,
- 2) AuNG2 was coated with poly-L-arginine and
- 3) AuNG3 was coated with polyalginate.

The influence of the two different coatings, i.e. the polypeptide poly-L-arginine and the polysaccharide polyalginate, on the physicochemical properties of the nanogels, and in detail their drug loading and release profiles for both Doxo and Poma was studied in Chapter 4.

3. Synthesis of gold/polymer hybrid materials

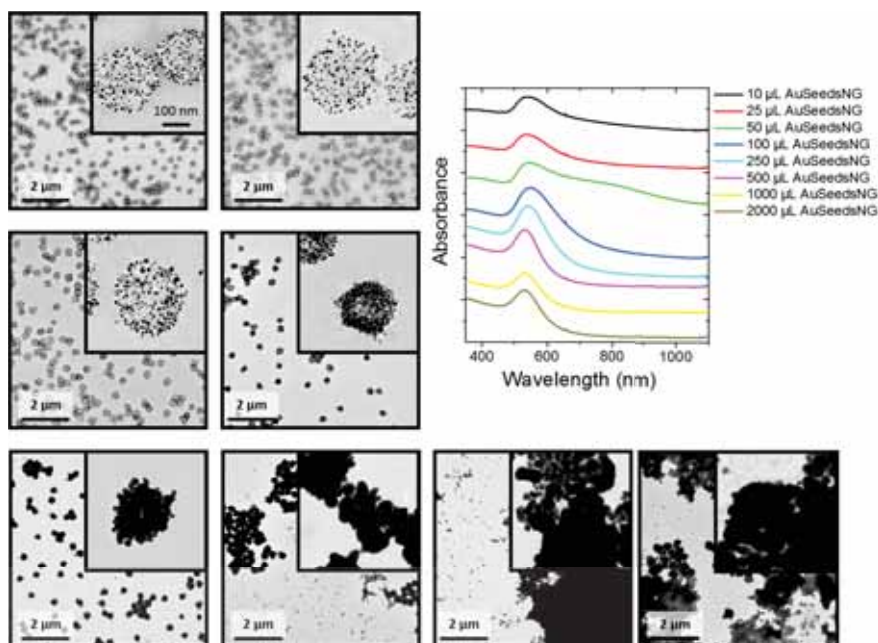


Figure 3.3.: TEM pictures and corresponding UV-vis spectra of AuNGs synthesized with different amount of seeds. Seed concentrations decreases from 2000 μL (top left TEM image) to 10 μL (bottom right TEM image). Lower AuSeedsNG concentration leads to bigger nanoparticles inside the gel (250-500 μL AuSeedsNG). At very low concentration secondary nucleation occurs and gold forms a shell around the nanogels (50-10 μL AuSeedsNG). In all cases the gold salt concentration in the growth solution was constant at 0.5 mM. Insets share all the same scale bar of 100 nm. Reproduced with permission from ref.¹⁰⁶ Copyright 2017, American Chemical Society.

Gold nanostar growth

Nanogels decorated with gold nanostars were grown adapting the synthesis developed by Kumar et al. (Figure 3.4).⁶² Briefly 10 mL DMF was mixed with 54.6 μL of 0.5 M HAuCl_4 . After 20 minutes different amounts of nanogels (acting as seeds) were added. At a constant gold salt concentration in the growth solution, the length of the tips was controlled by the amount of nanogels containing gold seeds (AuSeedsNG) added.

3.1. PEGMA hydrogels with in-situ grown gold nanoparticles

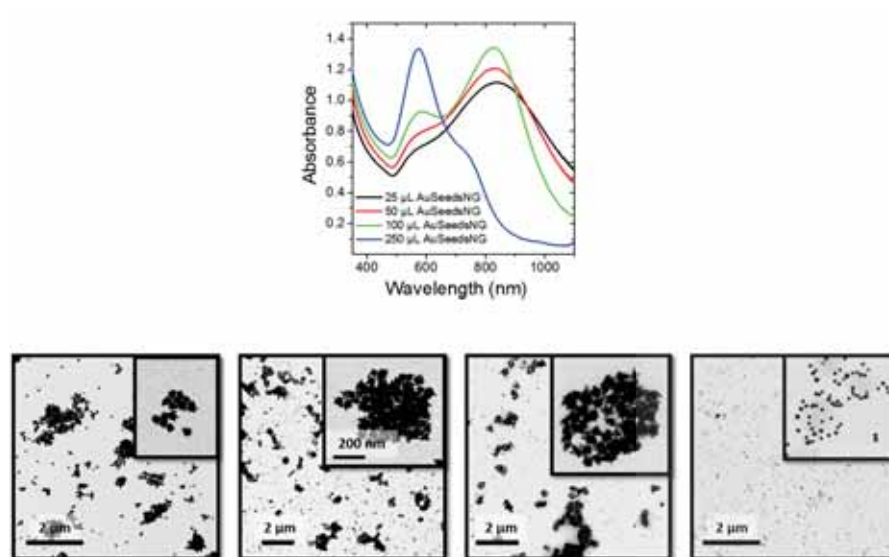


Figure 3.4.: Growth of nanostars inside nanogels. Higher HAuCl_4 :AuSeedsNG ratio leads to better defined tips. TEM pictures from left to right show nanostars grown with 20, 50, 100 and 200 μL seed solution respectively. The concentration of HAuCl_4 was kept constant at 2.75 mmol/L for all samples. Scale bar is 200 nm for all insets. Reproduced with permission from ref.¹⁰⁶ Copyright 2017, American Chemical Society.

The synthesis of nanostars instead of spherical nanoparticles is of interest to exhibit better absorbance in the near-IR range (biological window).¹¹⁵ However, the growth of nanostars within the nanogels has several drawbacks which need to be overcome prior applying such nanogels for applications in drug delivery or sensing which require long term stability. The first drawback is the use of polyvinylpyrrolidone (PVP) as surfactant during the synthesis, which makes the gold surface less accessible to adsorb molecules such as amino terminated drugs or Raman reporters. Another drawback is the low thermal stability of the Au nanostars. Figure 3.5 shows the UV-vis spectra of star-containing nanogels at different temperatures, evidencing no

3. Synthesis of gold/polymer hybrid materials

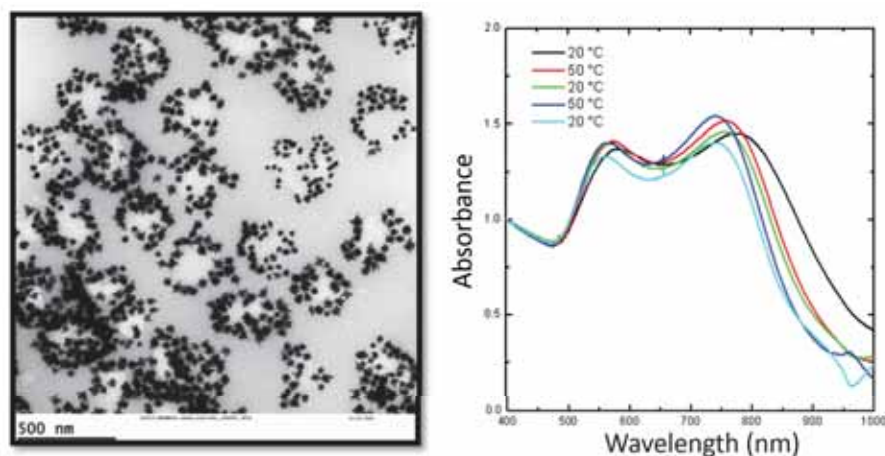


Figure 3.5.: Au Nanostar decorated PEGMA nanogels and evolution of their UV-Vis spectra under heating and cooling cycles. The change of the spectra is irreversible due to reshaping. Reproduced with permission from ref.¹⁰⁶ Copyright 2017, American Chemical Society.

reversibility and a blueshift of the LSPR, indicating reshaping.

3.1.2. Physicochemical properties of coated nanogels

The presence of the polyelectrolytes on PEGMA nanogels was confirmed by X-ray photoelectron spectroscopy (XPS), zeta potential, LSPR and particle size analysis. XPS data showed a clear decrease in the amount of Au on the nanogel surface between coated and non-coated nanogels (the experimental results and a small description can be found in the Appendix). Additionally, nitrogen was identified in sample AuNG2 due to the amino groups in poly-L-arginine, whereas AuNG3 showed a higher amount of oxygen due to the hydroxyl and carboxyl groups in polyalginate, as compared with AuNG1. Changes in zeta potential, LSPR and particle size were also observed, as

3.1. PEGMA hydrogels with in-situ grown gold nanoparticles

shown in Table 3.1.

Table 3.1.: Differences in elemental composition, LSPR, zeta potential (ξ) and hydrodynamic diameter (D_h) of the coated and non-coated PEGMA nanogels.

Sample	N (at.%)	C (at.%)	O (at.%)	Au (at.%)
AuNG1	0	64.3	24.8	10.9
AuNG2	11.1	56.3	27	5.6
AuNG3	0	46.9	49.6	3.5
Sample	LSPR (nm)	ξ (mV)	D_h (nm)	
AuNG1	544	-36.2 \pm 0.2	274.1 \pm 2.0	
AuNG2	567	40.9 \pm 0.3	223.8 \pm 1.4	
AuNG3	544	-34.5 \pm 0.8	292.1 \pm 4.4	

AuNG2 was found to become more compact upon polyelectrolyte addition, which in turn reduced the AuNP interparticle distance attached to the nanogels, resulting in stronger plasmon coupling and a LSPR red shift of 23 nm after functionalization (Figure 3.1). The decrease in overall nanogel size observed in AuNG2 is due to the strong electrostatic interaction between the negatively charged nanogels and the positively charged polyelectrolyte causing the formation of a polyelectrolyte-gel complex.¹¹⁶ In some cases if the molecular weight of the coating molecule is low enough they can even penetrate the nanogels and thus reducing the mesh size.¹¹⁷ In contrast, functionalization with the anionic polyalginate did not modify the LSPR but caused slight swelling of the nanogels, presumably due to the weaker interactions between polyalginate and the nanogels.

3. Synthesis of gold/polymer hybrid materials

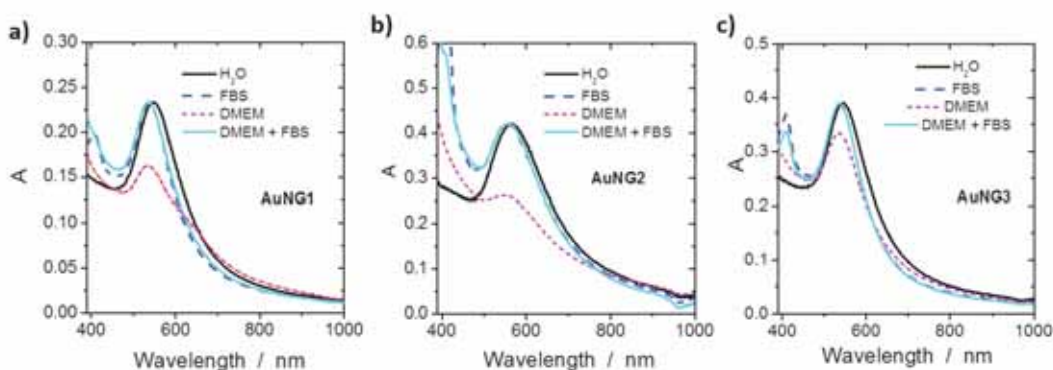


Figure 3.6.: UV-VIS spectra of PEGMA nanogels in different media. Reproduced with permission from ref.¹⁰⁶ Copyright 2017, American Chemical Society.

Colloidal stability

The colloidal stability was studied by measuring the LSPR of Au-decorated PEGMA nanogels in different media. Nanogels were incubated for 10 minutes with slow stirring in different media, as reported by Fleischer et al.¹¹⁸ The spectra of the different PEGMA nanogels in water, water containing 10% fetal bovine serum (FBS), DMEM cell culture media, and in 10% FBS supplemented DMEM cell culture media were measured. AuNG1 and AuNG2 clearly aggregated in DMEM cell culture media as the broadening of their plasmon band indicates in Figure 3.6. AuNG3 were in contrast more stable. No broadening of the plasmon band was noted upon incubation of the nanogels in FBS containing water or DMEM as the presence of protein adsorbed onto the surface stabilized the nanogels. Typically, incubation of AuNPs in FBS-containing media results in a red shift on the LSPR.¹¹⁹ However, in our case the presence of the protein produced blue shifts that corre-

3.1. PEGMA hydrogels with in-situ grown gold nanoparticles

sponded to 11, 5 and 7 nm for AuNG1, AuNG2 and AuNG3, respectively. Since nanogels are flexible nanostructures with AuNPs evenly distributed in their whole volume, the adsorption of FBS could affect the inter-particle distance affecting the LSPR and produces a blue shift.

During protein adsorption, the zeta potential of AuNPs is known to approach the zeta potential of the adsorbed protein.¹¹⁹ Indeed, the zeta potential of all PEGMA nanogels was observed to reach approximately -20 mV after incubation in FBS containing media, similar to previously reported zeta potential values of FBS coated AuNPs.¹²⁰ The values are included in Table 3.2.

Table 3.2.: Zeta potential values for AuNG1, AuNG2 and AuNG after incubation in different media.

Sample	Solvent	ξ (mV)
AuNG1	H ₂ O	-36.6±0.7
AuNG1	FBS in H ₂ O	-18.3±0.4
AuNG1	DMEM	-18.0±0.3
AuNG1	DMEM + FBS	-14.4± 0.2
AuNG2	H ₂ O	+46.3±0.6
AuNG2	FBS in H ₂ O	-18.4±0.4
AuNG2	DMEM	-8.1 ±1.9
AuNG2	DMEM + FBS	-18.4±0.4
AuNG3	H ₂ O	-32.7±1.2
AuNG3	FBS in H ₂ O	-17.1±0.7
AuNG3	DMEM	-19.8±0.7
AuNG3	DMEM + FBS	-17.5±0.9

3. Synthesis of gold/polymer hybrid materials

Degradation

We used TEM to analyze the effects of glutathione on the nanogels, at concentrations similar to those found in the intracellular environment. Glutathione at high concentrations (10 mM) partially degraded the nanogels (Figure 3.7), yet this was seen to depend on the polyelectrolyte coating. Nanogels without coating and with polyalginate coating show both detachment of gold nanoparticles and deformation of the polymeric structure. AuNG2 (poly-L-arginine coating) in contrast stayed stable over a week and showed no sign of degradation.

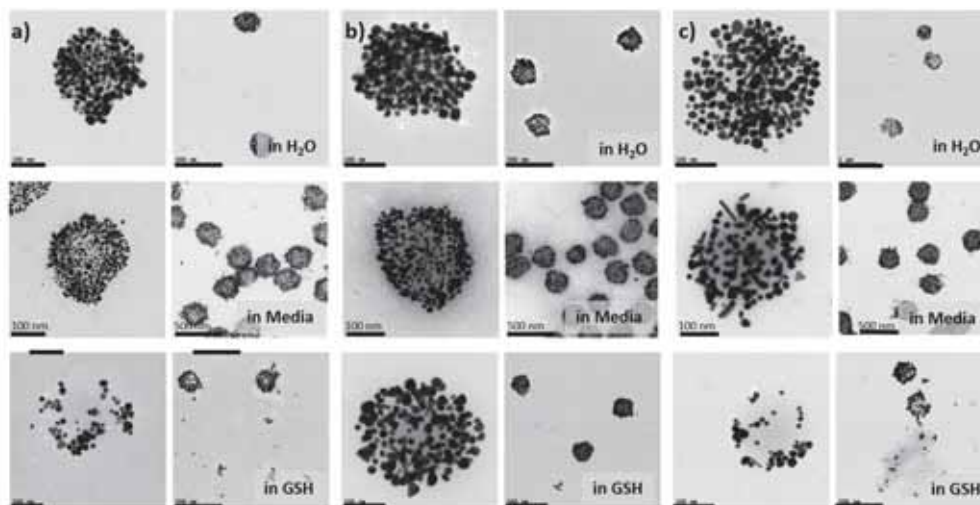


Figure 3.7.: AuNP loaded nanogels without coating (a) and with poly-L-arginine (b) and polyalginate coating (c) in water, cell media with 10% FBS-serum and glutathione (10 mM), after 1 week. Scale bar for close up pictures is 100 nm, for pictures with lower magnification 500 nm. Reproduced with permission from ref.¹⁰⁶ Copyright 2017, American Chemical Society.

3.1. PEGMA hydrogels with in-situ grown gold nanoparticles

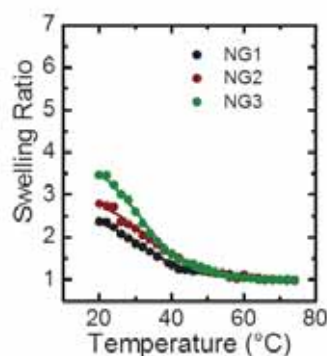


Figure 3.8.: Thermoresponsive behavior of nanogels (no Au NPs growth). Reproduced with permission from ref.¹⁰⁶ Copyright 2017, American Chemical Society

3.1.3. Thermoresponsive behavior

Bare nanogels displayed a LCST above 30 °C (Figure 3.8), measured by dynamic light scattering and the inclusion of AuNPs inside the nanogels did not hinder their ability to shrink or swell in response to heat changes (Figure 3.9). In contrast, we noted significant differences in the swelling ratios (Q) depending on the type of polyelectrolyte coatings. Q was defined as the ratio between the volume of the corresponding nanogels at a temperature T versus the volume at 70 °C.

$$Q = \frac{V(T)}{V(70^{\circ}\text{C})}. \quad (3.1)$$

Figure 3.9b illustrates the observed decrease in Q for coated PEGMA nanogels. The largest decrease of Q between coated and non coated nanogels was observed for AuNG2, which almost completely lost its thermoresponsiveness.

3. Synthesis of gold/polymer hybrid materials

This result is in agreement with the reduction in particle size upon coating with poly-L-arginine. Interestingly, the LCST increased from 32 °C in AuNG1 to 36 °C and 37 °C for AuNG2 and AuNG3 respectively, closer to physiologically relevant temperatures.

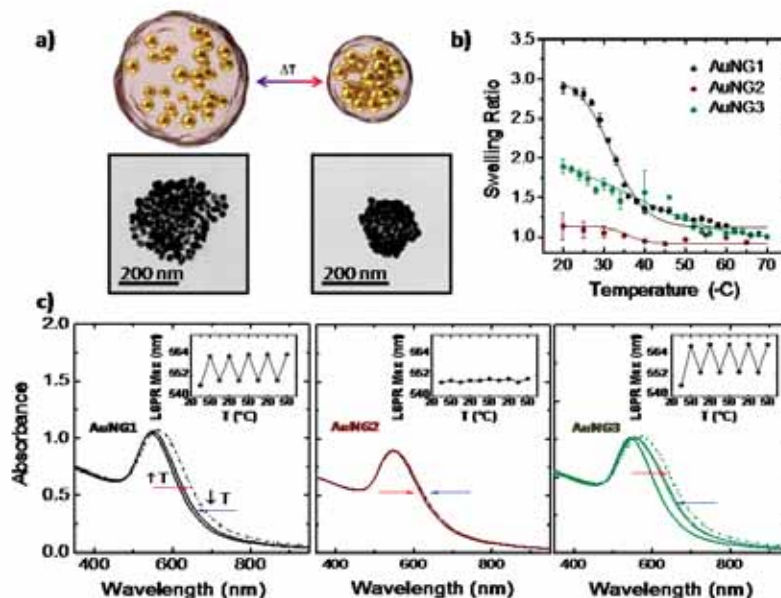


Figure 3.9.: a) Schematic representation of the shrinking process and representative TEM pictures in collapsed and swollen states. b) Dynamic light scattering monitoring of the swelling ratio in AuNGs. c) UV-Vis spectra of the nanogels, alternating at 20 °C and 50 °C, plotted as solid and dashed lines, respectively. The insets show the LSPR maxima during each cycle. Reproduced with permission from ref.¹⁰⁶ Copyright 2017, American Chemical Society.

These results were confirmed with UV-Vis spectroscopy. As expected, the thermoresponsive decrease in the volume of the nanogels led to smaller inter-particle distances and hence to a red shift and broadening of the LSPR band (Figure 3.9c). AuNG1 and AuNG3 behave similarly, with an approximate red shift of 14 nm between 20 and 50 °C. We verified the reversibility of the

3.1. PEGMA hydrogels with in-situ grown gold nanoparticles

shift by carrying out multiple heating/cooling cycles. The shift was fully reversible over 5 temperature cycles (Figure 3.9, inset). AuNG2, in contrast, shows no change of the LSPR, in accordance with the low Q value ($Q = 1.1$). Interestingly, the thermoresponsive behavior of coated PEGMA nanogels was observed to further change after encapsulation of drugs, in such a way that AuNG2 recovered its thermal responsiveness (Chapter 4).

3.1.4. Conclusion

In summary we synthesized a versatile multiresponsive nanogel system containing gold nanoparticles which will be further tested for the co-delivery of doxorubicin and pomalidomide and SERS imaging in Chapter 4 and 5 respectively. The gold nanoparticles inside the nanogels were synthesized in a new two-step method to ensure even particle distribution throughout the gel and surfactant-free synthesis. We studied two possible polyelectrolyte coatings to increase functionality: polyalginate and poly-L-arginine. These two coatings produced different modifications in the thermoresponsive behavior of the nanogels and other physicochemical properties that were characterized.

3.1.5. Experimental part

Milli-Q water (resistivity $18.2 \text{ M}\Omega \cdot \text{cm}$) was used in all experiments. Hydrogen tetrachloroaurate trihydrate ($\text{HAuCl}_4 \cdot 3\text{H}_2\text{O}$, $\geq 99.9\%$), di(ethylene glycol) methyl ether methacrylate, poly(ethylene glycol) methyl ether methacry-

3. Synthesis of gold/polymer hybrid materials

late, poly(ethylene glycol) diacrylate, 2-aminoethyl methacrylate hydrochloride, methacrylic acid, formaldehyde (37 wt%) and poly-L-arginine hydrochloride (mol wt >70,000) were all purchased from Sigma-Aldrich. Alginic acid (sodium salt) was obtained from Fisher Scientific. All glassware was washed with aqua regia, rinsed 3 times with Milli-Q water and dried before use.

Synthesis of poly ethylene glycol methacrylate nanogels

Nanogels were synthesized by purging a 300 mL Milli-Q water solution of 5.6 g (0.03 mol) di(ethylene glycol) methyl ether methacrylate, 2.4 g (0.008 mol) poly(ethylene glycol) methyl ether methacrylate, 160 mg (0.003 mol) poly(ethylene glycol) diacrylate, 297 mg (0.0035 mol) methacrylic acid and 576 mg (0.0035 mol) 2-aminoethyl methacrylate hydrochloride with argon for an hour at 70 °C. The reaction was then started by adding 120 mg (0.0004 mol) of 2,2, azobis(2methylpropionamidine)dihydrochloride dissolved in 2 mL of degassed Milli-Q water and run for 12 hours at 70 °C.

Synthesis of AuNP decorated nanogels

After washing via centrifugation, 10 mL of nanogels were incubated with 50 μ L 0.1 M HAuCl_4 overnight before reduction of the gold occurs with addition of 100 μ L 0.1 M NaBH_4 solution. Small gold domains of about 3-4 nm were formed and stabilized by the amino group of 2-aminoethyl

3.2. PLGA microstructures loaded with metal nanoparticles

methacrylate hydrochloride. The nanogels were used as seeds for the growth of bigger gold particles without further purification. Further growth of AuNP was carried out with formaldehyde under basic conditions. A 100 mL growth solution with a final concentration of 1 mM HAuCl_4 , 5 mM NaBr and different amounts of seeds was prepared followed by the addition of 500 μL formaldehyde solution (37 wt%). The reduction was finally started by changing the pH to 11 through the addition of 750 μL 1 M NaOH. The reaction was very slow due to the more stable gold-bromide complexes. After 15 minutes a color change was observed but the reaction was allowed to run overnight before particles were carefully washed via centrifugation and characterized (TEM and UV-Vis spectroscopy). By simply varying the amount of seeds, AuNPs with different sizes were obtained.

3.2. PLGA microstructures loaded with metal nanoparticles

In this part the synthesis of PLGA-metal nanoparticle hybrid materials using EHD co-jetting is introduced. Anisotropic gold nanoparticles (AuNSs) labeled with different SERS active molecules were embedded in different compartments of different polymeric structures (particles and fibers), and 3D-SERS imaging was used to monitor the distribution of the particles inside the polymer. We propose that these advanced hybrid materials offer

3. Synthesis of gold/polymer hybrid materials

significant advantages over other existing materials for use in bioimaging.

3.2.1. Synthesis

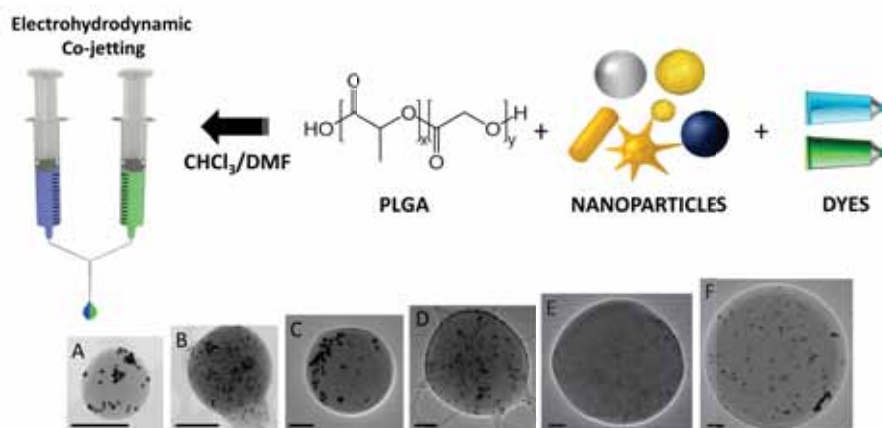


Figure 3.10.: Fabrication of multicompartmental hybrid particles using electrohydrodynamic co-jetting. The size of the particles can be controlled by using different polymer molecular weights and varying solvent ratios, solvent polymer concentrations and composition. Images in A-F are representative for particles of different sizes and compositions. PLGA molecular weight was varied from 17 kDA (A,B) through 40 kDA (C,D) up to 50-75 kDA (E,F). These examples show various configurations with two (A,C-F) or three compartments (B), containing AuNs (A-F) and iron oxide nanoparticles (B). The particles also contain Poly[(*m*-phenylenevinylene)-*alt*-(2,5-dihexyloxy-*p*-phenylenevinylene)] as blue dye and Poly[tris(2,5-bis(hexyloxy)-1,4-phenylenevinylene)-*alt*-(1,3-phenylenevinylene)] as green dye, in different compartments. All scale bars are 500 nm. Reproduced with permission from ref.¹⁰⁷ Copyright 2017, American Chemical Society.

The preparation of hybrid multicompartmental PLGA-plasmonic microparticles is schematically illustrated in Figure 3.10. Nanoparticles synthesized in aqueous media were transferred into CHCl_3 following a protocol previously reported.¹²¹ A Raman active molecule was used as surfactant during this process to obtain highly stable SERS-Tags. The resulting particle suspension

3.2. PLGA microstructures loaded with metal nanoparticles

was mixed with various amounts of PLGA and different fluorescent dyes: ((Poly[(m-phenylenevinylene)-alt-(2,5-dihexyloxy-p-phenylenevinylene) as blue dye or Poly[tris(2,5-bis(hexyloxy)-1,4-phenylenevinylene)-alt-(1,3-phenylenevinylene)] as green dye. Gold nanostars were specifically selected for most of the experiments due to their strong absorbance in the NIR range and their outstanding performance as SERS-Tags, to conduct 3D SERS measurements as it was further investigated in Chapter 5. The Raman active molecules biphenyl-4-thiol (4-BPT) and 2-naphtalene-thiol (2-NAT), were used as ligands due to their strong binding affinity to gold surfaces and their characteristic and easily distinguishable Raman signals. The final particle size is influenced by the solvent composition and the molecular weight of PLGA.¹²² When using 17 kDa PLGA and 70:30 CHCl₃:DMF, particles of 600-800 nm were obtained, whereas 40 kDa PLGA in 70:30 CHCl₃:DMF yielded particles of 1-2 μm , and using 50-75 kDa PLGA and solvent ratios between 70:30 and 97:3 CHCl₃:DMF, particles between 3-8 μm can be produced.

For EHD co-jetting, the polymer/particle/dye mixtures were flown in a laminar regime through parallel mounted metallic needles at 0.2 mL per hour. After a stable droplet was formed at the interface of the polymeric solutions, a voltage was applied between the droplet and a collector plate. The voltage created a polymeric jet from the tip of the droplet towards the collector and was sufficiently high to induce break-up of the jet into individual particles. Transmission electron microscopy (TEM), scanning

3. Synthesis of gold/polymer hybrid materials

electron microscopy (SEM) and fluorescence microscopy studies demonstrate that particles evenly formed over a large area (Figure 3.11).

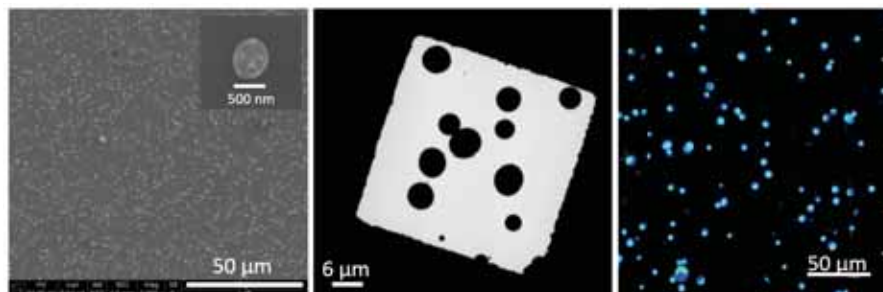


Figure 3.11.: Large scale images of bicompartmental nanoparticles with two different Raman labeled Au NSs and two different dyes (blue and green) characterized by (A) SEM (B) TEM and (C) fluorescence confocal microscopy. Reproduced with permission from ref.¹⁰⁷ Copyright 2017, American Chemical Society.

3.2.2. Stability of compartments

PLGA hybrid microgels showed high particle loading, regardless of the type of plasmonic particles used in the synthesis, as observed in TEM images (Figure 3.10). However, TEM images alone could not resolve the different compartments within the particles. Therefore, the inner distribution and the preservation of the different compartments after synthesis was characterized by means of fluorescence imaging (with blue and green dyes) and SERS imaging (with two different SERS-encoded AuNS).

Once synthesized, polymeric particles were embedded in a ProLong®gold matrix between two coverslips and initially examined by confocal fluorescence microscopy (Figure 3.11 and 3.12). For SERS measurements, the par-

3.2. PLGA microstructures loaded with metal nanoparticles

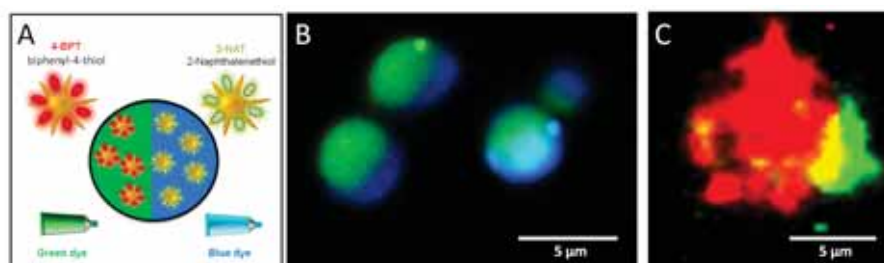


Figure 3.12.: (A) bicompartmental PLGA (40 KDa) particles containing 30 nm AuNSs labeled with 4-BPT and a green dye in one compartment, and AuNSs labeled with 4-BPT and a blue dye in the other compartment. (B) Fluorescence image of $\sim 4 \mu\text{m}$ particles showing that the dyes and hence the compartments are separated and distinguishable. (C) SERS mapping of a $\sim 7 \mu\text{m}$ particle, also showing two compartments. The signals from 4-BPT (red) and 2-Nat (green) are spatially separated. Reproduced with permission from ref.¹⁰⁷ Copyright 2017, American Chemical Society.

ticles were immobilized on a quartz glass slide to avoid the fluorescence background from standard glass and then examined under a WITEC confocal Raman microscope using a 785 nm diode laser as the excitation source. As a reference, we used the Raman bands at 1275 cm^{-1} for 4-BPT (C-C ring stretch) and 1375 cm^{-1} for 2-NAT (C-C ring stretch), so that the characteristic bands of both Raman reporters could be clearly distinguished (Chapter 5). In Figure 3.12 both fluorescence and SERS images indicate the stability and conservation of the two initial compartments. Interestingly, no interference from the fluorescent dyes was observed, and as a result the shape of the compartments was clearly resolved with both techniques. The SERS images also allowed for differentiation of the compartments, but in contrast to fluorescence imaging, the SERS signal is not evenly distributed throughout the entire particle. This is due to the distribution of AuNSs, which, in contrast

3. Synthesis of gold/polymer hybrid materials

to the dyes, do not fill the complete volume of the PLGA compartments, resulting in a distinct pattern with islands of higher intensity in the SERS maps (For more information on the the spatial distribution examined by SERS measurements see chapter 5).

3.2.3. Different shapes and composition

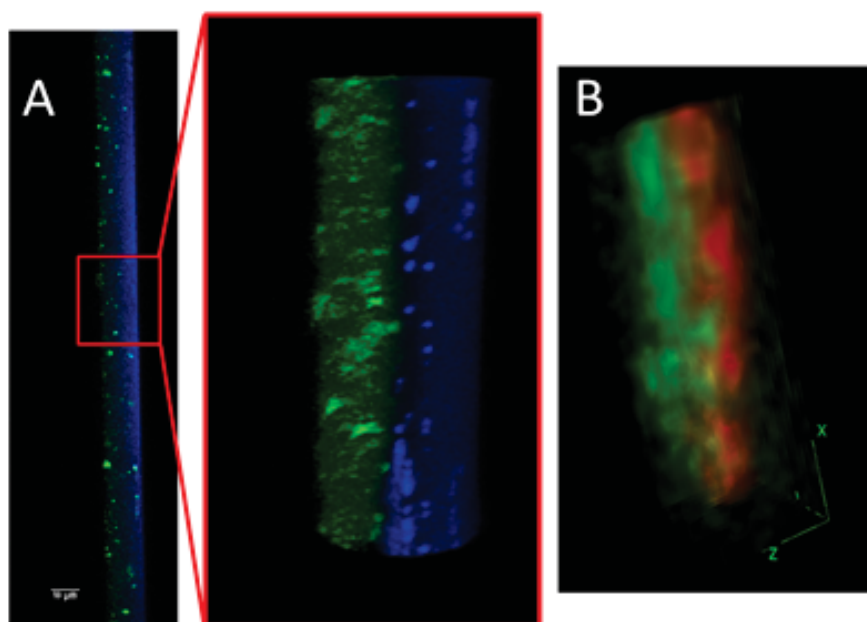


Figure 3.13.: Examples of PLGA-based bicompartamental fibers prepared by electrohydrodynamic co-jetting and analyzed by fluorescence imaging (A) and SERS mapping (B). Reproduced with permission from ref.¹⁰⁷ Copyright 2017, American Chemical Society.

Since PLGA electrospun nanofibers have been reported as scaffolds for cell or tissue growth,¹²³ we explored the possibility to synthesize PLGA fibers containing AuNS, while preserving their bicompartamental structure (Figure 3.13). We thus prepared fibers with a diameter of 10 μm , i.e., twice as large as

3.2. PLGA microstructures loaded with metal nanoparticles

the particles above, which is likely to facilitate the resolution of the different compartments. SERS imaging indeed showed a distinct separation between the compartments filled with 4-BPT coated AuNSs and 2-NAT coated AuNSs (Figure 3.13). Furthermore to demonstrate the universal character of our synthesis protocol, the obtained fibers were cut to obtain cylinders with different lengths (Figure 3.14). Embedding them in a Tissue-Plus[®] matrix and using a cryosectioning instrument, it was possible to fabricate these cylinders while keeping the two compartments stable.¹²⁴ Cylinders are of interest since the shape of particles plays an important role in the modulation of cell uptake, as reported elsewhere.¹²⁵

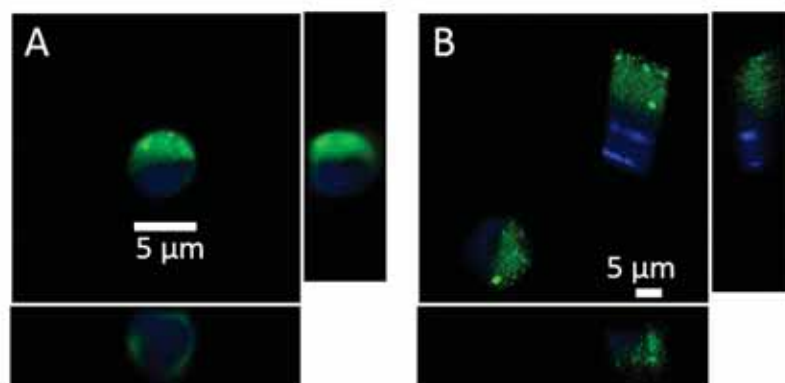


Figure 3.14.: Additional particles can also be produce. Fluorescence images of (A) Particles including COOH in their surface to be modified with antibodies or other molecules (30% of 5.9 kDa of PLGA with COOH added) and (B) Cylinder shaped particles: Synthesized fibers can be cut to obtain cylinders of different sizes. Reproduced with permission from ref.¹⁰⁷ Copyright 2017, American Chemical Society.

In order to explore the full universality of the method, polymeric particles containing SERS-encoded 30 nm AgNPs and 40 nm iron oxide particles (Figures 3.15) were synthesized. AgNPs are ideal for SERS measurements

3. Synthesis of gold/polymer hybrid materials

at a laser wavelength around 500-600 nm, whereas magnetic nanoparticles could be used to separate/collect the hybrid particles by magnetophoresis. In an additional experiment, the PLGA surface was functionalized with carboxylic groups, by adding 30 % of 5050DLG1 polymer (5.9 KDa) to the initial PLGA/AuNSs mixture (Figure 3.14). For subsequent experiments these can be useful as anchor points for further (bio)functionalization, e.g. with antibodies.

3.2.4. Conclusion

We have introduced a universal method for the synthesis of PLGA microgels of different sizes and shapes, loaded with dyes and metal nanoparticles with distinct electromagnetic properties. These particles offer a wide range of potential applications, in particular for biomedical imaging. In Chapter 5 the compartmental structure is examined using three dimensional SERS and ultimately it will be demonstrated that the SERS signal from embedded AuNS, in contrast to that from fluorescent dyes, is not affected by exposure to UV illumination and therefore offers the possibility for long-term imaging experiments. Since PLGA is a biocompatible and degradable polymer, potential applications of these hybrid materials can be foreseen, for example in form of combined drug delivery/imaging devices. In particular, microfibers functionalized with AuNS may allow us to obtain new insights in the role of implanted scaffolds in regenerative medicine.

3.2. PLGA microstructures loaded with metal nanoparticles

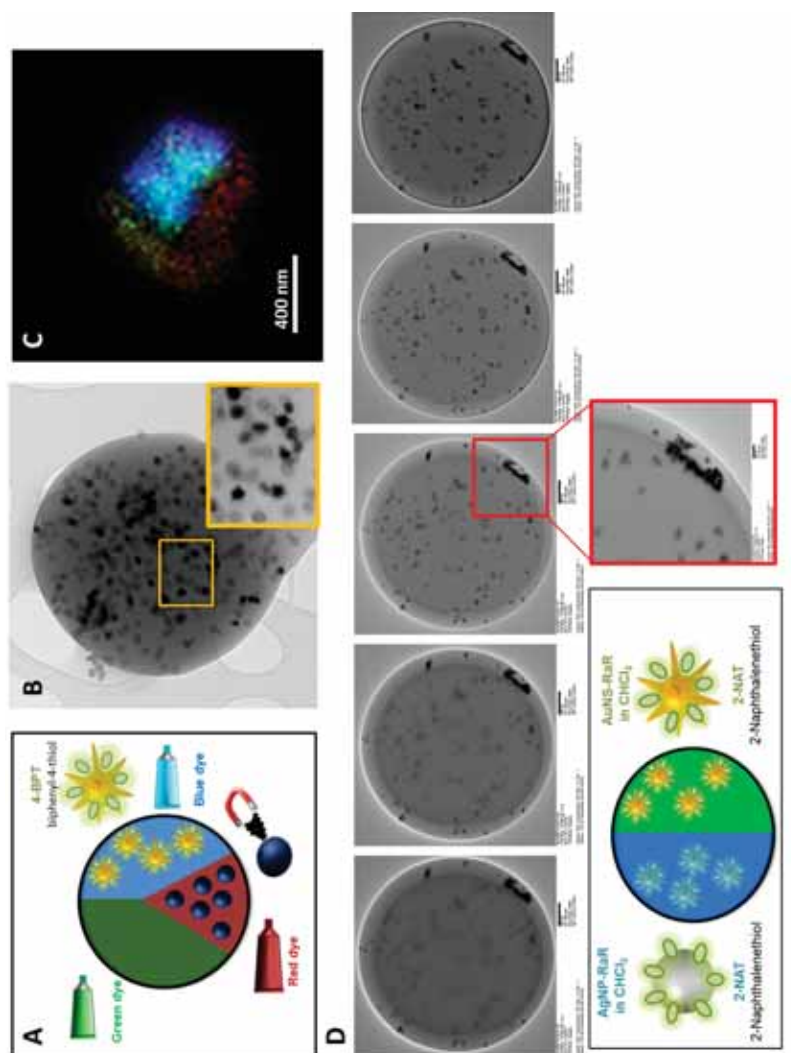


Figure 3.15.: (A) ~ 500 nm tricompartmental PLGA (17 KDa) particles containing 30nm AuNSs labeled with 4-BPT together with a blue dye in one compartment, 40 nm iron oxide nanoparticles with a red dye in a second compartment and a green dye in a thirds compartment. (B) TEM image where both nanoparticles can be observed. (C) Fluorescence image showing the three compartments differentiated by the 3 dyes. (D) Bicompartmental PLGA (55-75 KDa) particles $\sim 8 \mu\text{m}$ containing 30 nm AgNPs labeled with 2-NAT together with a blue dye in one compartment and 30 nm AuNSs labeled with 2-NAT and with a green dye in a second compartment are shown. TEM images at different focus confirm that particles are embedded onto the PLGA particles and not only at the surface. Reproduced with permission from ref.¹⁰⁷ Copyright 2017, American Chemical Society.

3. Synthesis of gold/polymer hybrid materials

3.2.5. Experimental part

Materials: Milli-Q water (resistivity $18.2 \text{ M}\Omega \cdot \text{cm}$) was used in all experiments. Hydrogen tetrachloroaurate trihydrate ($\text{HAuCl}_4 \cdot 3\text{H}_2\text{O}$, $\geq 99.9\%$), sodium citrate tribasic dihydrate ($\geq 98\%$), silver nitrate (AgNO_3 , $\geq 99\%$), L-ascorbic acid (AA, $\geq 99\%$), O-[2-(3-mercaptopropionylamino) ethyl]-O-methylpolyethylene glycol (PEG-SH, MW 5,000 g/mol), 2-naphthalenethiol (2-NaT, 99%), biphenyl-4-thiol (4-BPT, 97%), Chloroform (CHCl_3 , $\geq 99.8\%$) 17 kDa PLGA, 40 kDa PLGA and 50-75 kDa PLGA were purchased from Sigma-Aldrich. 5050 DLG 1A polymer (#LX00560-130) has purchased from Lakeshore Biomaterials. ProLong gold matrix was purchased from ThermoFisher scientific. Quartz microscope slides were from Electron microscopy (#72250-01). 5 nm AuNPs and 40 nm iron oxide nanoparticles were purchased from Ocean Nanotech LLC. For EHD co-jetting a syringe pump (Fisher Scientific Inc., USA) and a power supply (DC voltage source, Gamma High Voltage Research, USA) was used. All glassware was washed with aqua regia, rinsed 3-fold with Milli-Q water and dried before use.

Synthesis of gold nanostars

AuNSs were prepared using a seed-mediated growth method. Adding 5 mL of 34 mM citrate solution to 95 mL of boiling 0.5 mM HAuCl_4 solution under vigorous stirring and leaving boiling for 15 min seed particles are formed. 50 nm AuNSs with LSPR maximum at 750 nm were prepared adding 2.5

3.2. PLGA microstructures loaded with metal nanoparticles

mL of the citrate-stabilized seed solution to 50 mL of 0.25 mM HAuCl₄ solution (with 50 μ L of 1 M HCl) in a 100 mL glass erlenmeyer flask at room temperature under moderate stirring. Quickly, 500 μ L of 3 mM AgNO₃ and 250 μ L of 100 mM ascorbic acid were added simultaneously. The resulting AuNSs solution was mixed with 410 μ L of PEG-SH 0.1 mM stirred for 15 min and washed by centrifugation at 1190 g, 25 min, 10 °C redispersing them in water.

Synthesis of silver nanoparticles

A modified protocol was used based on a previously reported approach to prepare 30 nm AgNPs. 250 mL of Milli Q water was heated under magnetic stirring. 4 mL of trisodium citrate (0.1 M) and 0.32 mL of ascorbic acid (0.1M) were added to the boiling water. Then 0.93 mL of AgNO₃ (0.1M) was added leaving 1 h boiling under stirring. Then the solution was cooled down and stored in the fridge.

Phase transfer of plasmonic nanoparticles

All the plasmonic particles were pre-stabilized with PEG (O-[2-(3-mercaptopropionylamino) ethyl]-O'-methylpolyethylene glycol), and subsequently transferred from water into CHCl₃ by vigorously stirring the colloids with a CHCl₃ solution of the hydrophobic Raman active molecules. Both phases were mixed overnight, so that the particles slowly diffuse from the aqueous

3. Synthesis of gold/polymer hybrid materials

into the organic phase. Afterwards the aqueous phase is discarded and the organic phase centrifuged several times to remove excess of free ligand.

Bicompartmental PLGA particles

Bicompartmental PLGA particles were synthesized using 50-75 kDA PLGA (#430471 Aldrich) and a solvent ratio of 97:3 for CHCl₃ and DMF. Briefly, in compartment (I) 0.0405 g of PLGA were mixed with 235 μ L of green dye (1mg/mL in CHCl₃) and 485 μ L of SERS-Tag (4-BPT) AuNSs [Au(0) =3mM] in CHCl₃ and 15 μ L DMF. Compartment (II) was prepared mixing 0.0405 g of PLGA with 235 μ L of blue dye (1mg/mL in CHCl₃) and 485 μ L of SERS-Tag (2-NAT) AuNSs [Au(0) =3mM] in CHCl₃ and 15 μ L DMF.

Bicompartmental Fibers: Using a 50-75 kDA PLGA (#430471 Aldrich) and a solvent ratio of 97:3 for CHCl₃ and DMF 10 μ m fibers where obtained. In compartment (I) 0.15 g of PLGA were mixed with 54.55 μ L of green dye (1mg/mL diluted in CHCl₃) and 350 μ L of SERS-Tag (4-BPT) AuNSs [Au(0)=3mM] in CHCl₃ and 15 μ L DMF. Compartment (II) was prepared mixing 0.15 g of PLGA with 54.55 μ L of blue dye (1mg/mL in CHCl₃) and 350 μ L of SERS-Tag (2-NAT) AuNSs [Au⁰=3mM] in CHCl₃ and 15 μ L DMF.

Bicompartmental Cylinders

Bicompartmental fibers were deposited aligned in a tissue cryomold and embedded in a Tissue-Plus®matrix. Then they were stored at -4°C for 24h

3.2. PLGA microstructures loaded with metal nanoparticles

after being cut using a Leica 3050S cryostat cryosectioning instrument. The obtained different slides were collected in falcon tubes and washed several times centrifuging them with water. Cylinders of 2, 5 and 10 μm were obtained defined by the cutting plane size.

4 PEGMA nanogels as drug delivering tool

In this chapter the previously introduced AuNP-containing thermosensitive nanogels are tested as platforms for the co-delivery of doxorubicin (Doxo) - a cytotoxic agent - and pomalidomide (Poma) - an anti-angiogenic and immunomodulatory agent. It will be shown that these drug delivery systems are preferentially cytotoxic to cancer cells in vitro, while also being efficient at inhibiting angiogenesis in tube-formation assays in vitro. Nanogels are a highly versatile system in which drug release profiles can be controlled via polyelectrolyte coating and/or various external stimuli, showing good biocompatibility and biodegradation in vitro. The final nanogels thus offer a stable platform that can be prepared by straightforward production methods and used to deliver several drugs, with both hyperthermia and photothermal ablation therapy characteristics. This chapter resulted in a recent publication.¹⁰⁶

4.1. Introduction

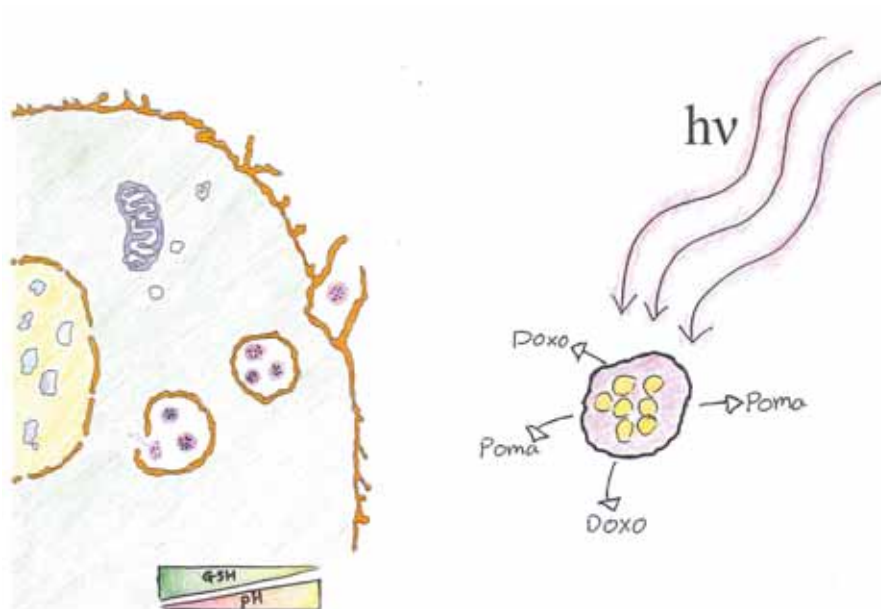


Figure 4.1.: Scheme of action for the application of the PEGMA nanogels as stimuli responsive drug delivering tool

Two different drugs with different physicochemical behaviour and different therapeutics effect were chosen to test the PEGMA nanogels (presented in Chapter 3) as a drug delivery tool. The idea is to take advantage of the properties of the nanogel and its porous structure which can act as cavity for drugs and the thermoresponsive behaviour combined with the gold nanoparticles to create a photothermal drug delivery system. Figure 4.1 shows an illustration of the scheme of action. After cell uptake of drug-loaded nanogels, the nanogels are exposed to various changes in the chemical surroundings. These changes, in combination with external heat, cause an increased release of the drugs and a therapeutic effect can be observed.

In the first step the efficacy of drug loading and release will be investigated followed by an ex vitro study of the release mechanism and the influence of other stimuli present in the cell, such as changes in the pH and glutathione concentration ([GSH]). In the second step the particle uptake in different cell lines is tested and finally the release of the two drugs (Doxo and Poma) confirmed.

4.1.1. Doxorubicin

Doxorubicin is a clinically established and a FDA approved anti cancer drug for several decades now and widely known as one of the most potent chemotherapeutic drugs on the market.¹²⁶ The major drawback is the non-selectivity which results in high side effects and demands a way to work around, for example by using carrier systems. One way, which is already in clinical use is the combination of Doxo with liposomes to form a more stable carrier.¹²⁷ Another idea would be the use of hydrogels as presented in this chapter.

Physical properties

Doxo is a polar molecule (Figure 4.2a) and has a high water solubility up to 50 mg/mL. The main part is formed by a tetracyclic ring with adjacent quinone-hydroquinone groups. The second major component is a sugar moiety, comprised of a 3-amino-2,3,4-trideoxy-L-fucosyl, attached to one of the rings by a glycosidic bond. Usually it is purchased as the hydrochloride

4. PEGMA nanogels as drug delivering tool

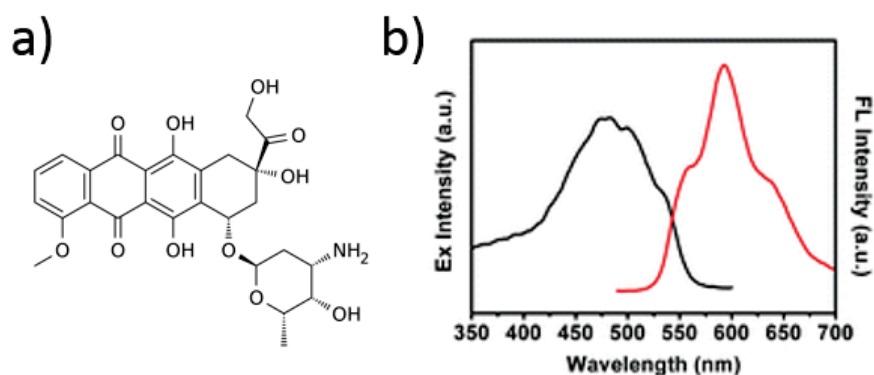


Figure 4.2.: a) Structure of doxorubicin. b) Excitation (black) and emission (red) spectra of doxorubicin under excitation at 470 nm. Figure B reproduced with permission from ref.¹²⁸ Copyright 2016, Royal Society of Chemistry

and then dissolved in water or buffer and stable in the fridge for several months, which is an exceptional stability for a drug. Next to its water solubility and high stability, Doxo shows intrinsic fluorescence properties. Figure 4.2b shows the excitation spectra and the emission under excitation at 470 nm.¹²⁹

For imaging applications the intrinsic fluorescence simplifies the experiment often, since Doxo can be observed in the fluorescence microscope without further labeling. Those characteristics, the high activity as anti cancer drug and the wide range of literature available for comparisons are responsible for its wide use amongst proof of concept works and as drug to in-vitro test novel drug delivery systems.

Mechanism of action

Free Doxo enters cells through passive diffusion and accumulates in the nucleus of the cell. The main cytotoxicity results through the binding of Doxo to several molecular targets such as topo isomerase enzymes which ultimately prevents proliferation of the cell. Beside that, Doxo also binds directly to DNA and RNA and inhibits the polymerase of them which leads to an inhibition of cell replication and cell death.¹²⁶

4.1.2. Pomalidomide

Pomalidomide (Poma) became tragically famous in the last century as it is a derivative of thalidomide which was sold to combat nausea under the trade name Contergan. Contergan led to birth defects of several thousands of children all around the world during the middle of the 20th century. Because of this scandal thalidomide and its derivatives vanished from the market and were just recently re introduced to the market as a drug for the treatment of multiple myeloma, a cancer of plasma cells. In this context it was discovered that Poma has immunomodulatory antiproliferative and anti-angiogenic effects.¹³⁰⁻¹³²

4. PEGMA nanogels as drug delivering tool

Physical properties

In contrast to Doxo, Poma is nonpolar and hardly soluble in water (1mg/mL) and therefore needs to be dissolved in nonpolar solvents like DMSO (54 mg/mL). The molecule (Figure 4.3) consists of two main components, a phthalimide compound, connected with a dioxo-piperidine over the nitrogen. The difference between thalidomide and pomalidomide is a further amino group in the third position of the ring structure. Both molecules have a stereocenter and will racemise automatically due to the reactive hydrogen at the stereocenter. There have been few reports on the physical properties of Poma. Poma is not fluorescent and absorbs in the UV.

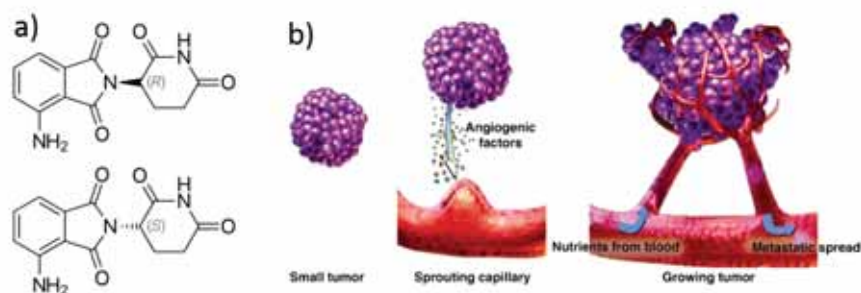


Figure 4.3.: a) Structure of Pomalidomide. b) Schematic representation of Angiogenesis. Picture taken from <http://www.angioworld.com/DominiqueGarrel.html>, October2017.

Immunodulatory effect

Poma belongs with Thalidomide and other analogs to the class of immunomodulatory imide drugs (IMiDs).¹³³ These drugs were found to have a stimulatory effect on the immune system, potentially helping the anti cancer immune

response. In a later section (Section 4.6.2) we take advantage of this effect and test LPS stimulated macrophages on their expression of Interleukin 6 (IL-6). IL-6 is a pro-inflammatory cytokine and expressed by T-cells or macrophages. In the human body it acts as an mediator of fever or the acute phase response.^{130,133}

Angiogenesis

IMiDs have also been shown to have anti angiogenic properties since they reduce the production of proangiogenic factors such as vascular endothelial growth factor and fibroblast-like growth factor. Angiogenesis describes the formation of new blood vessels. Upon chemical signaling by the prior mentioned factors endothelial cells will migrate and differentiate to form new blood vessel or repair them (Figure 4.3b).¹³⁴ In the presence of anti angiogenic drugs this process is suppressed which is important to fight cancer. Cancer needs to produce blood vessels for nutrition and oxygen supply to grow over a critical size of a few millimeters.¹³⁴ Ultimately hindrance of angiogenesis by IMiDs could help to slow tumor growth and tumor spreading throughout the body by cutting off the supply rather than attacking the tumor cell itself. In combination with a chemotherapeutic drug, IMiDs form a very promising tool to fight cancer. Currently Doxil, a liposomal doxorubicin carrying NP system, which has been combined with dexamethasone and pomalidomide, is such a combination and is currently in clinical trials to treat Multiple

4. PEGMA nanogels as drug delivering tool

Melanoma (MM) cancer (NCT01541332 from www.clinicaltrials.gov).

4.2. Drug loading

Drug loading was achieved by immersing AuNP decorated PEGMA nanogels in an aqueous solution of drugs (0.125 mg/mL) in basic conditions, and quantified by the decrease of drug concentration in solution after loading. After the immersion in the drug solution, the nanogels were wrapped with two different polyelectrolytes as described in Chapter 3 and tested on their different behaviours as drug delivery tool. As a reminder, nanogels without wrapping are called AuNG1, nanogels with poly-L-arginine AuNG2 and nanogels with alginate are named AuNG3.

The maximum loading of Doxo was 0.33 mol/mg(Au) for AuNG1 and AuNG3, and 0.30 mol/mg(Au) for AuNG2. Even though it is desirable, the concentration of AuNGs in solution could not be determined. Because of that the loading was measured with respect to the gold concentration. The gold concentration was adjusted to be the same by measuring it with ICP-MS. The encapsulation of Poma was less efficient with only 0.025 mol/mg(Au) for AuNG1, 0.019 mol/mg(Au) for AuNG2 and 0.020 mol/mg(Au) for AuNG3. The entrapment of drugs was possible due to attractive interactions between Au decorated PEGMA nanogels and Poma and Doxo. Both electrostatic interactions and hydrogen bonding may be involved in the loading of the

nanogels, due to the presence of carbonyl and ester groups in the nanogel and amino groups in both drugs.¹³⁵ In fact, a change in the zeta potential of the nanogels toward more positive values after drug encapsulation was observed, as previously reported for similar nanogels.¹⁰⁵

4.2.1. Determination of loading and release

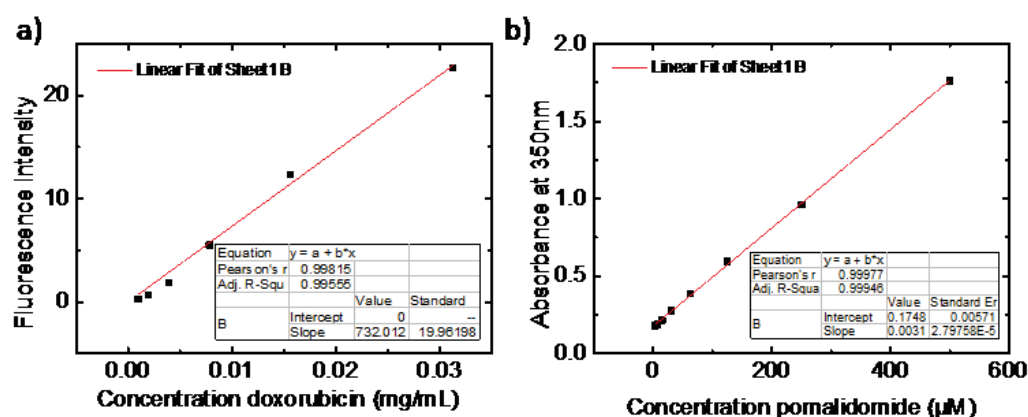


Figure 4.4.: Typical calibration curves for doxorubicin (a) and pomalidomide (b). Reproduced with permission from ref.¹⁰⁶ Copyright 2017, American Chemical Society.

To quantify the maximum loading, supernatants were collected and the amount of drugs quantified with fluorescence (Doxo) or absorbance (Poma) measurements. Typically 70 μ L of the supernatant was analyzed using a 96 well plate and a Varioskan flash (Thermo scientific) plate reader with an individual calibration curve for each plate (Figure 4.4). On the basis of the calibration curve, the exact amounts of drug in the supernatants were calculated. The loading was then determined by subtraction of the amounts in the supernatants from the initial amount added to the particles.

4.3. Drug release

Release was measured in a similar way: the particles were incubated under the desired conditions, then centrifuged at 12000 rpm for 10 minutes and the concentration of the drug in the supernatant was measured with a plate reader as described above.

4.3.1. Doxorubicin release

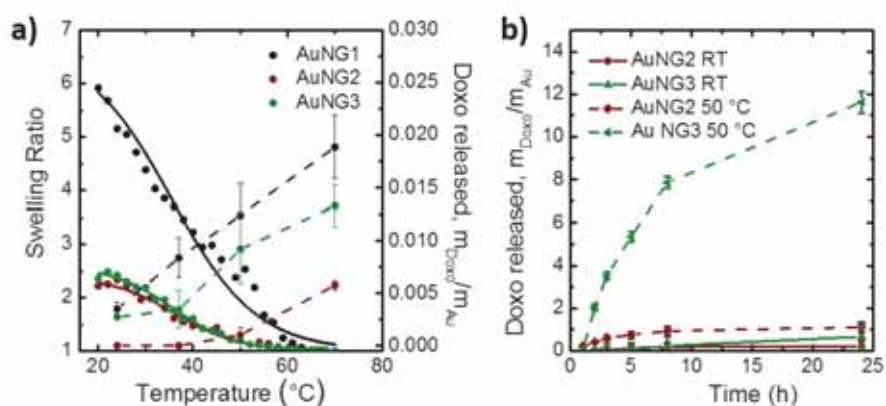


Figure 4.5.: Increased release of Doxo (a) and Poma (b) between intracellular ($pH=5.5$, $[GSH]=5$ mM) and extracellular conditions ($pH=5.5$, $[GSH]=1$ μM) with no trigger (control), heat and Laser. Reproduced with permission from ref.¹⁰⁶ Copyright 2017, American Chemical Society.

Figure 4.5 shows the influence of polyelectrolyte presence on Doxo release from PEGMA nanogels, as a function of increasing temperature. Both polyelectrolytes shifted the thermal release to temperatures above 37 $^{\circ}C$, as compared to the non-coated AuNG1 (Figure 4.5a). However, poly-L-arginine (AuNG2) hindered more the uncontrolled leakage of Doxo from the nanogel compared to polyalgininate (AuNG3), but also made PEGMA nanogels less

4.3. Drug release

efficient at thermally triggered release. This is shown in figure 4.5b, where an 18-fold increase for AuNG3 but only a 5-fold increase for AuNG2, of released Doxo between room temperature and 50 °C is observed.

We believe that the polyelectrolyte coating is wrapped around the particles with varying density and most likely porosity. Hence leakage is hindered and slowed down but not completely avoided and at the same time the release of the drugs upon shrinkage of the nanogels modulated. Poly-L-arginine seems to be more densely attached and reduces leakage and at the same time makes the release more sensitive to temperature changes. The overall release however is reduced as well compared to alginate.

4.3.2. Pomalidomide release

Pomalidomide (Poma) shows slightly different release properties, as compared to doxorubicin. Figure 4.6 shows the release of pomalidomide over a time span of 24 hours at room temperature and at 50 °C. The release of pomalidomide from AuNG3 (polyalginate coating) shows a trend similar to Doxo, with higher temperature causing more release. In contrast, pomalidomide release from AuNG2 (poly-L-arginine coating) is not significantly influenced by temperature.

4. PEGMA nanogels as drug delivering tool

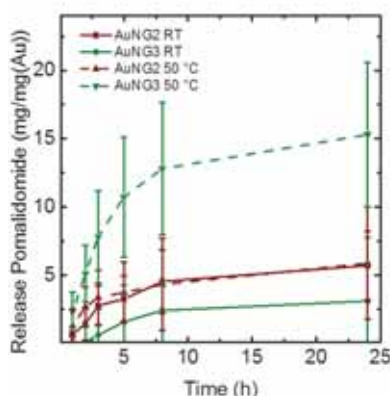


Figure 4.6.: Release of pomalidomide over time at room temperature and 50 °C, monitored over 24 h. Reproduced with permission from ref.¹⁰⁶ Copyright 2017, American Chemical Society.

4.3.3. Calculation of release exponent

Peppas and co-workers developed a simple model to determine the mechanism of release and to distinguish between diffusion controlled release and a mixture of diffusion and other release mechanisms:¹³⁶

$$\frac{M_t}{M_\infty} = kt^n, \quad (4.1)$$

M_t and M_∞ are the amount of released drug at time t and after infinite time, respectively; k is a structural factor and n is the release exponent. According to the model, the value of n gives information of the mechanism behind the release. For a spherical particle system, a value of $n < 0.43$ means pure diffusion-controlled release according Fick's second law of diffusion. A value between $0.43 < n < 0.85$ means anomalous diffusion. This is a result of a superposition of diffusion-controlled release and other mechanisms. At values

of $n > 0.85$, the zero order regime is entered (case-II transport).

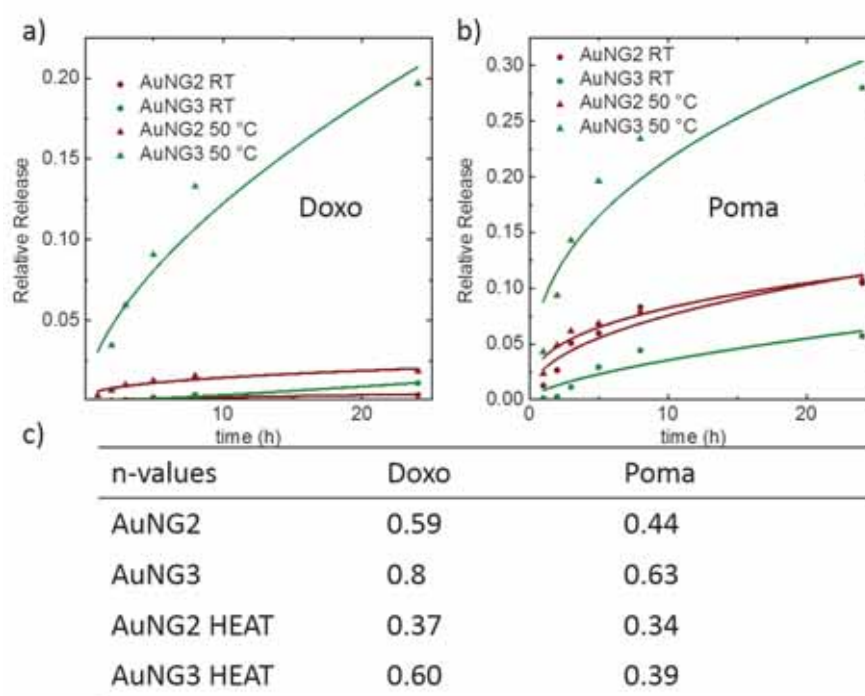


Figure 4.7.: Relative release of doxorubicin (a) and pomalidomide (b) over time at room temperature and at 50 °C. The lines are the corresponding fitting curves according to Peppas model. Table (c) shows the values extracted from the fit for the release exponent (n). Reproduced with permission from ref.¹⁰⁶ Copyright 2017, American Chemical Society.

In our case, all nanogels show n values within the regime of anomaly and sometimes slightly below that (Figure 4.7). The model is just a simple law which has to be viewed with caution. However, the law shows for our particles that a temperature change for both drugs does not change the mechanism significantly. If so, the diffusion regime is entered. Besides the temperature change we were interested if there is a difference between Poma and Doxo, as they show different polarities. Both drugs stay more or less inside the regime of anomaly indicating a superposition of different mechanisms. Based on

4. PEGMA nanogels as drug delivering tool

these results (Figure 4.7), no difference in the mechanism of release can be identified.

4.4. Other stimuli

Near-infrared (NIR) light, glutathione (GSH) and pH were also confirmed to trigger the release of drugs from AuNP decorated PEGMA nanogels, via different mechanisms (Figure 4.8a-c). The interaction of NIR light with AuNPs inside the nanogels led to shrinkage and in turn remotely controlled release of drugs due to the photothermal effect. Upon continuous NIR illumination (808 nm, 8.3 W/cm²), an initial increase in both the recorded temperature and Doxo release were noted, followed by a plateau in both measurements after ca. 10 minutes (Figure 4.8a).

The mechanism of drug release triggered by heating (including NIR light irradiation) and subsequent nanogel shrinkage can be related to the removal of hydrogen bonding between the drugs and the nanogel itself, but also to the decrease in the radius of the nanogel and shortening of the diffusion path for entrapped drugs.

GSH was also found to enhance drug release from AuNP decorated PEGMA nanogels. This trigger is of interest for intracellular drug delivery since its concentration is over 200 fold higher within cells (0.2-10 mM) than in the extracellular environment (2-20 μ M).^{137,138} To compare the GSH triggered

Doxo release with that induced by heating, we used the SERS intensity of Doxo molecules close to the gold surface. SERS of AuNG3 (as example) nanogels after incubation with GSH, after heating and after both heating and GSH incubation were measured, and the signals were compared to the corresponding fluorescence intensity of Doxo in the supernatant from the nanogel. A more detailed description of the SERS experiments can be found in Chapter 5. Figure 4.8b shows that both GSH and heat triggered the release of Doxo from the nanogel, and both triggers, acting in synergy, released 1.8 times more than the sum of the two triggers separately (30 min incubation time, $T = 50\text{ }^{\circ}\text{C}$, $[\text{GSH}] = 5\text{ mM}$). The presence of Doxo was monitored using the characteristic SERS peak at 1420 cm^{-1} (corresponding to the C-O-H and C-H bending mode). Upon application of both T increase and GSH, the Doxo signal vanished faster than by only heating, showing the influence of [GSH]. The release mechanism of GSH could be related to ion displacement,¹³⁹ since it is known that GSH adsorbs onto AuNPs and polymers and can trigger this kind of release mechanism intracellularly.^{140,141}

In addition, we observed degradation and disassembly of the Au decorated PEGMA nanogels, both after GSH exposure in solution and in in vitro experiments, which would subsequently enhance drug release (See 3.1.2).

pH changes affect hydrogen bonding,¹⁴² as well as charges on amino and carboxylic groups in the nanogels. As pH is also known to considerably decrease during the endocytotic pathway in cells, we studied the effect of

4. PEGMA nanogels as drug delivering tool

pH on the release of Doxo from the nanogels. By exposing AuNG3 to pH 7.4 or pH 5.5, values that are representative of the extracellular and intracellular environment respectively, we noted a 2-fold increase in Doxo release. Additionally, the increased Doxo release at low pH was more pronounced in the presence of GSH at the usual concentrations in the intracellular environment (Figure 4.8c).

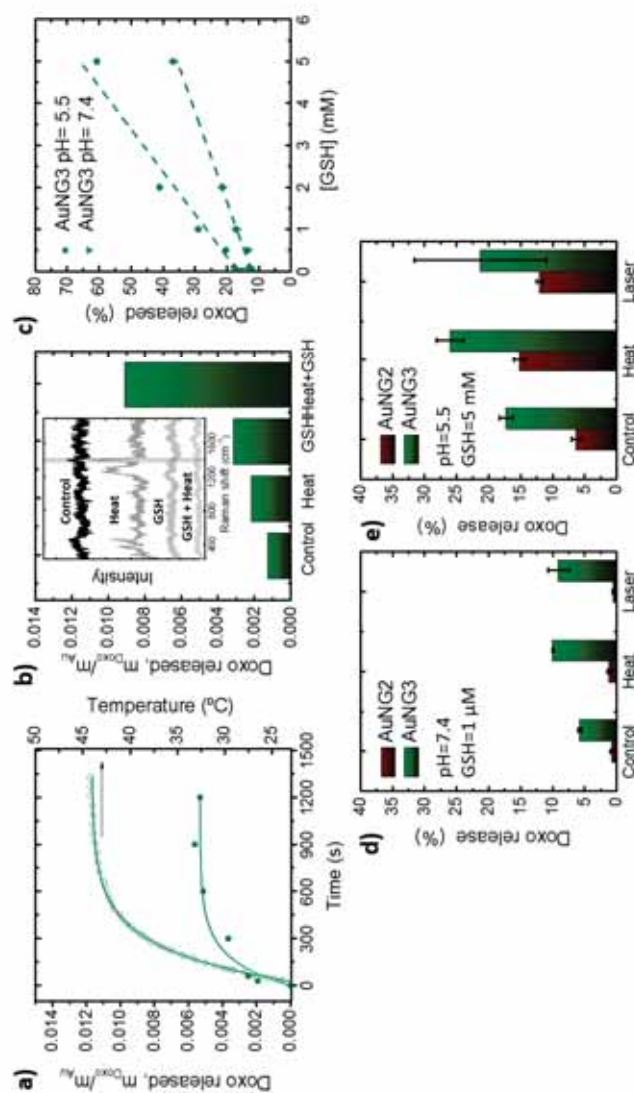


Figure 4.8.: a) Temperature increase (open circles) of AuNG3 solution under NIR illumination (808 nm, 8.03 W/cm²) and the corresponding doxorubicin release (filled circles). b) Doxo release from AuNG3 upon heating and/or GSH addition and corresponding SERS spectra (inset). SERS spectra were recorded in solution at a concentration of 5 μg/mL(Au), $P_{laser}=12\text{mW}$ for 633 nm and $t_{int}=20\text{s}$ with a 10x objective (NA=0.35). The assigned band at 1420 cm⁻¹ is highlighted with a gray background. c) pH influence on the release of Doxo at different [GSH]. d,e) Summary of the different Doxo release efficiencies comparing the delivery at room temperature (control) versus the delivery upon the application of external stimuli, NIR light and heat (50 °C) in solutions mimicking the extracellular (d) and intracellular environment (e). Reproduced with permission from ref.¹⁰⁶ Copyright 2017, American Chemical Society.

4. PEGMA nanogels as drug delivering tool

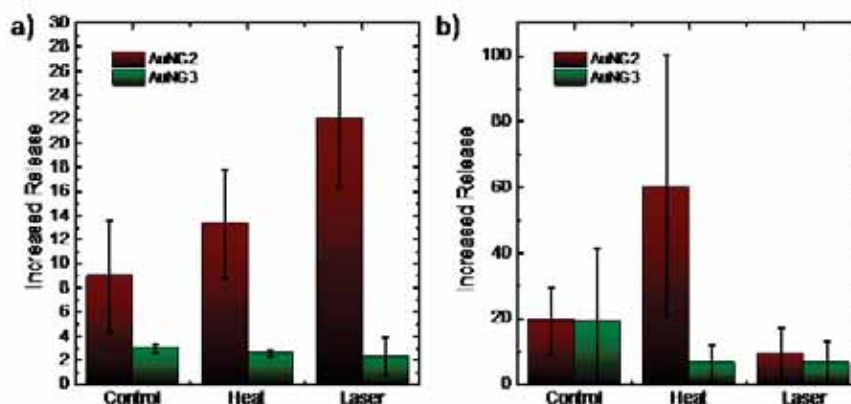


Figure 4.9.: Increased release of Doxo (a) and Poma (b) when moving from extracellular environment (pH=7, [GSH]= 1 μ M) to intracellular environment (pH=5.5, [GSH]= 5 mM) under the influence of no trigger (control), heat and laser illumination. Reproduced with permission from ref.¹⁰⁶ Copyright 2017, American Chemical Society.

We subsequently compared how all the aforementioned triggers can affect drug release in an environment mimicking both extracellular and intracellular conditions. Figure 4.9a shows that intracellular conditions enhance Doxo release induced by both heat and NIR illumination. Moreover, the polyelectrolytes on the nanogels surface caused significantly different drug release profiles, AuNG2 being more efficient in avoiding drug leakage, whereas all triggers enhanced drug release from AuNG3. We therefore conclude that AuNG3 appears to release higher amounts of Doxo, yet AuNG2 releases the same drug in a more controlled way under the effect of different triggers (Figure 4.9a). A similar study was carried out for the release of Poma (Figure 4.9b). In this case, release was more significantly affected at intracellular conditions (high [GSH] and low pH) than by the application of external

stimuli. AuNG2 were more efficient in releasing Poma than AuNG3 and uncontrolled leakage was similar for both types of nanogels. The different release profiles shown in our work are key when selecting the appropriate carrier for a specific drug that could demand a faster release or which is very toxic and should be only released at the target cells.

4.5. Cellular uptake

Polyelectrolyte shells on AuNG2 (poly-L-arginine) and AuNG3 (polyalginate) were shown to affect nanogel uptake by both cancer and non-cancer cells, due to the different composition and surface charge of the nanogels. Taking into consideration that the increased metabolic activity of cancer cells compared with non-cancer cells can be exploited to improve nanogel uptake,¹⁴³⁻¹⁴⁵ we conducted a co-culture of HeLa cancer cells with healthy human dermal fibroblasts (HDF) to determine the differences in nanogel endocytosis. Using fluorescence microscopy and TEM we observed higher levels of endocytosis for AuNG2, as compared to AuNG3 (Figure 4.10).

Flow cytometry determined the levels of AuNG2 and AuNG3 uptake in this co-culture, measured 24 h after a short 2 h incubation. The percentages of HDF cells positive for Doxo (used as a fluorescent label) were 75.6% and 33.7% for AuNG2 and AuNG3 nanogels, respectively, whereas the percentage of HeLa cells positive for Doxo were 99.4% and 75.6% for AuNG2 and

4. PEGMA nanogels as drug delivering tool

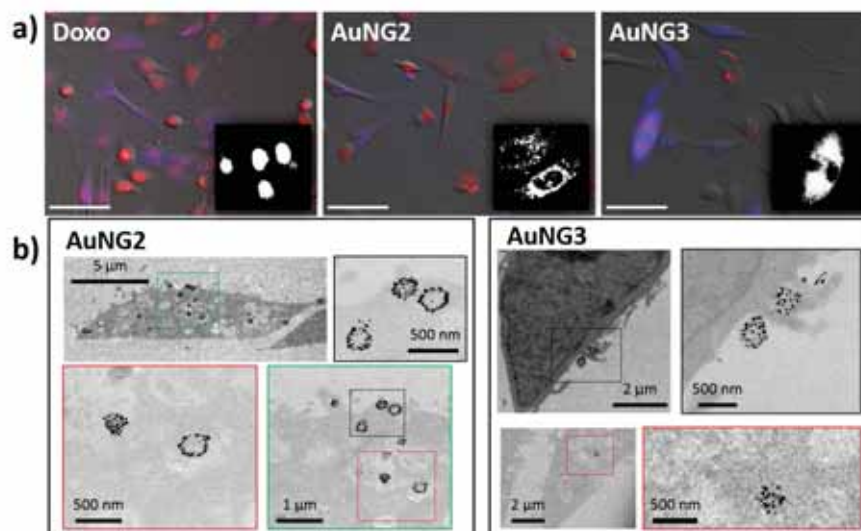


Figure 4.10.: a) Cellular uptake of free Doxo, AuNG2 and AuNG3 nanogels. A co-culture of HeLa (unstained) and HDF (blue stained) cells were exposed to Doxo and Doxo containing AuNG2 and AuNG3 for 2 h and uptake visualized using Doxo fluorescence (shown in red in main images or in white in inserts for clarity). Clear nuclear (left image) or endosomal staining (middle and right images) is seen after free or nanogel delivered Doxo, respectively. Scale bars are 100 μm. b) TEM images of HeLa cells exposed to AuNG2 and AuNG3 for 2 h and then processed the following day for TEM imaging. Magnified photos are shown in color coded boxes. Reproduced with permission from ref.¹⁰⁶ Copyright 2017, American Chemical Society.

AuNG3, respectively. This shows significant differences in cell specificity which can indeed be ascribed to the enhanced metabolic rates of cancer cells, as well as increased levels of AuNG2 uptake compared to AuNG3 due to the overall cationic charge of the AuNG2 system. Cationic nanoparticles and also molecules with overall positive charges (e.g cell penetrating peptides) are well known to associate with cell membranes to higher levels than their anionic counterparts. As expected, incubation of cells (both cancerous and healthy) with free Doxo resulted in rapid nuclear localization, whereas Doxo

4.5. Cellular uptake

containing AuNG2 and AuNG3 were localized in endosomes (Figure 4.10). Similar results were obtained with breast cancer MCF-7 cells (Figure 4.11), in agreement with previous studies.¹⁴³ Results also show the nontoxic and inert effects of the nanogel formulations without doxorubicin and pomalidomide drugs, with or without poly-L-arginine or polyalginate coatings, on various cells. However, such increased levels of uptake in cancer cells did not correlate with higher drug release in vitro as it is shown in section 4.6. We also confirmed that long term exposure to unloaded nanogels does not cause any increased cell death (Figure 4.11).

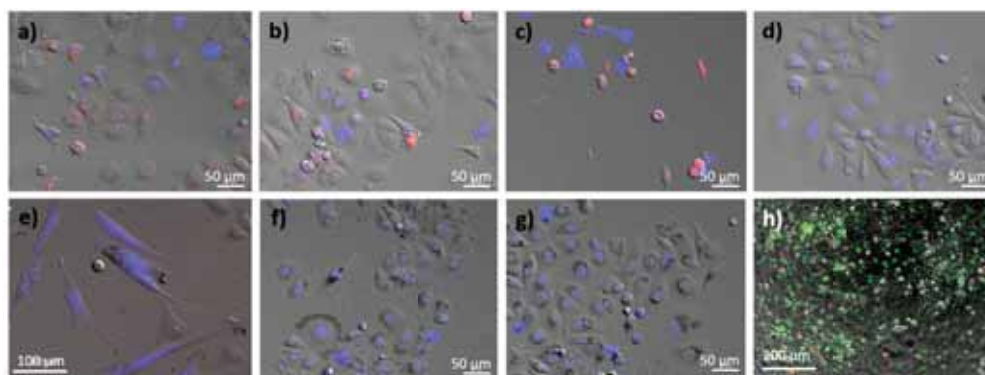


Figure 4.11.: MCF-7 breast cancer cells showing uptake of AuNG2 (a) and AuNG3 (b). Doxo (shown in red) is not released at this time, and therefore little to no cytotoxicity is observed. Free doxorubicin (c) causes high levels of cell death. Untreated control cells are shown in (d). Cells are DAPI stained. Scale bar is 50 μm . e) HeLa and HDF (stained blue) co-culture exposed to non-coated nanogels for 2 h; f) MCF-7 cells exposed to poly-L-arginine nanogels (AuNG2, without drugs) for approximately 18 h, and stained with DAPI. g) MCF-7 cells exposed to polyalginate nanogels (AuNG3, without drugs) for approximately 18 h, and stained with DAPI. h) Live/Dead staining of a HeLa and HDF cell co-culture exposed to non-coated nanogels for 2 h and then left for 4 days, with live cells imaged in the green fluorescence channel and dead cells using red fluorescence. Reproduced with permission from ref.¹⁰⁶ Copyright 2017, American Chemical Society.

4. PEGMA nanogels as drug delivering tool

4.5.1. Intracellular degradation

We were interested about the long term stability of the nanogel inside cells. Nanogel degradation would favour drug delivery and can indeed be observed inside cells (Figure 4.12). AuNG2 remain relatively unaffected even after 1 week of incubation in cells, whilst AuNG3 shows a high degree of degradation and AuNP detachment (Figure 4.12). In both cases, aggregated AuNPs without polymer can occasionally be found.

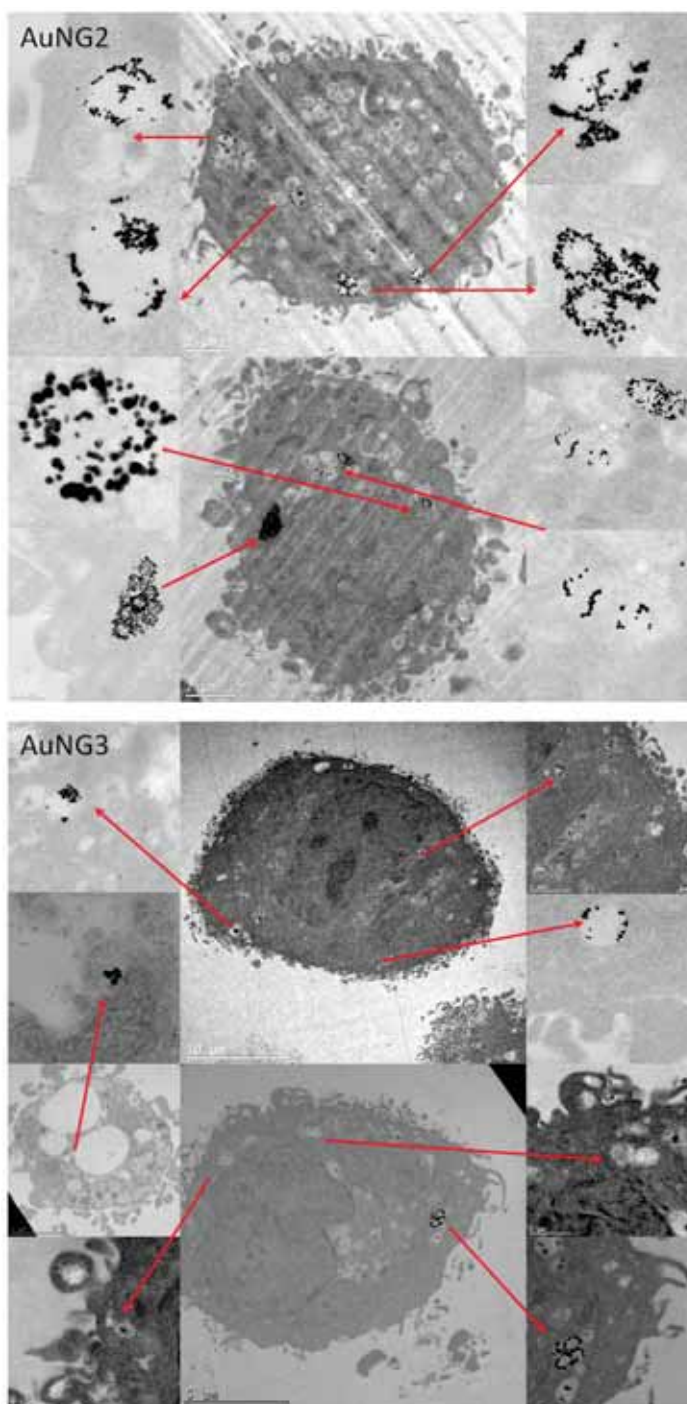


Figure 4.12.: TEM pictures showing AuNG3 and AuNG2 nanogel degradation inside cells after one week incubation time. HeLa cells were incubated with AuNGs for a week, followed by fixation, staining and embedding in a raisin. The pictures shows cross sections of thinly sliced cells with nanoparticles inside. The enlarged pictures highlight the presence of the nanogels. Reproduced with permission from ref.¹⁰⁶ Copyright 2017, American Chemical Society.

4.6. Intracellular drug release

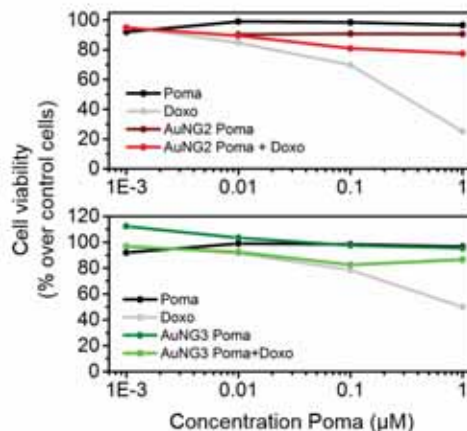


Figure 4.13.: Cell viability of HeLa cells after incubation with different Poma concentrations. Cells were incubated with free Poma, free Doxo (same concentrations as the corresponding Doxo loaded AuNGs contained) and AuNG loaded with Poma alone and Doxo plus Poma. Cell viability was measured ca. 24 h later using the MTT assay. Reproduced with permission from ref.¹⁰⁶ Copyright 2017, American Chemical Society.

The effect of the two drugs Poma and Doxo was measured separately because they affect cells through different molecular mechanisms. We first verified that the increased levels of AuNG-PEGMA nanogel uptake by cancer cells compared to non-cancer cells resulted in downstream cell death. As seen in Figure 4.10 and 4.14, whilst free Doxo resulted in cell death of both cancer and non-cancer cells in the co-culture system, exposure to Doxo-containing AuNG2 and AuNG3 was predominantly cytotoxicity to cancerous HeLa cells whilst HDF cells remained viable.

The presence of Poma within the nanogels was verified as not inducing any cytotoxic effects at the given concentration (Figure 4.13). The high levels of

4.6. Intracellular drug release

cytotoxicity noted in HeLa cells was slow, occurring ca. 4 days after the initial exposure of the cells to the AuNG-PEGMA nanogels. We investigated the ability of MCF-7 breast cancer cells to uptake AuNG2 and AuNG3 (Figure 4.11). Like the results noted for HeLa cells, both AuNG2 and AuNG3 are taken up by cells but do not display toxicity, unlike free Doxo (Figure 4.11c), due to the slow release by this system.

4.6.1. Laser stimulated intracellular drug release

In the next step, we subsequently investigated the use of NIR light as a method to improve Doxo release and subsequent cell death, compared to non-illuminated controls. HeLa cells were exposed to Doxo-containing AuNG2 and AuNG3, or non-Doxo control nanogels (AuNG*) for ca. 12 h, followed by illumination with an 808 nm diode laser at 16 W/cm² for 20 minutes. Cell viability was measured the following day using the MTT assay. NIR-light illumination of HeLa cells incubated with AuNG-PEGMA nanogels resulted in a significant decrease in the viability over the non-illuminated cells (Figure 4.14). Non-Doxo loaded nanogels (AuNG*) were used as second control, showing that it was possible to induce hyperthermia with AuNP-PEGMA nanogels, which is interesting for combined therapy as previously reported for other drug delivery systems.¹⁴⁶ However, we verified that there exists an enhancement of Doxo release under NIR light illumination *in vitro* when lower power densities are applied, thereby avoiding hyperthermia (Figure

4. PEGMA nanogels as drug delivering tool

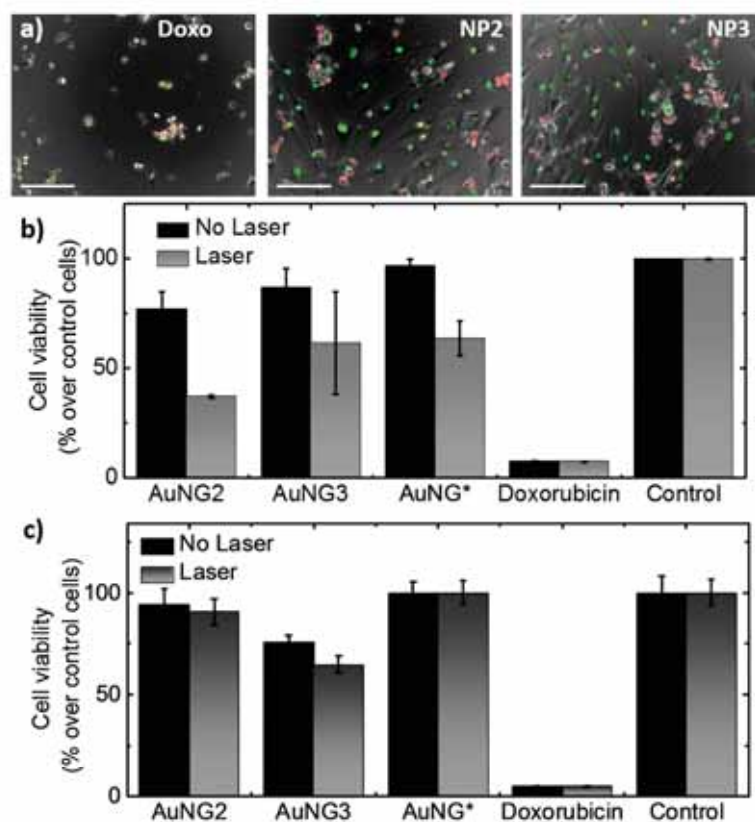


Figure 4.14.: a) Live/Dead staining of HeLa/HDF co-cultures, ca. 4 days post initial exposure to free Doxo, or Doxo-containing AuNG2 and AuNG3. Live cells show green-channel fluorescence whilst dead cells uptake propidium iodide and are positive for red channel fluorescence. The predominant live population (green) are HDF cells which can be identified by their characteristic shape, whereas HeLa cells are the majority "dead" population. Scale bars are 200 μm . b) NIR-laser induced hyperthermia and photo-thermal-induced cytotoxicity of HeLa cells and c) cell viability of HeLa cells after lower NIR-laser irradiation without hyperthermia, showing exclusively enhanced drug release through NIR irradiation. Reproduced with permission from ref.¹⁰⁶ Copyright 2017, American Chemical Society.

4.14b,c). Cells were incubated with free Doxo, Doxo-containing AuNG2, Doxo containing AuNG3 or AuNG nanogels without drug, for ca. 18h, followed by laser irradiation. In this case cell viability was measured ca. 24 h later using the MTT assay (mean of triplicate wells \pm SD). Laser illumination

4.6. Intracellular drug release

was carried out with an 808 nm diode Laser with 0.4 cm spot size, therefore illuminating the whole well of the 96-well plate ($t=20\text{min}$, $p=12\text{W}/\text{cm}^2$).

4.6.2. Intracellular pomalidomide release

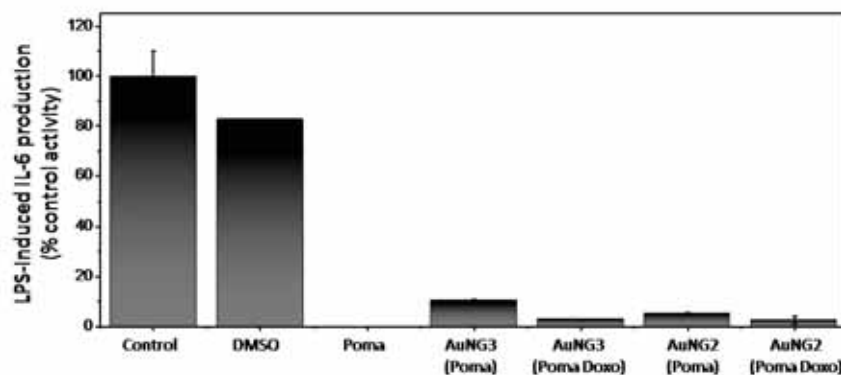


Figure 4.15.: Pomalidomide mediated inhibition of LPS-induced IL-6 from J774 murine macrophages. DMSO was also included as a solvent control, at the same final concentration as present in free Poma. Reproduced with permission from ref.¹⁰⁶ Copyright 2017, American Chemical Society.

The drug Poma has been shown to be highly efficient at inhibiting angiogenesis, in addition to a wide variety of immune system modifying effects such as the inhibition of cytokine production in LPS-stimulated peripheral blood mononuclear cells (PBMCs), thereby placing it in the group of immunomodulatory drugs (IMiDs) (Section 4.1.2) We took advantage of these immunomodulatory effects as a method to verify that Poma remained active after release from AuNG nanogels. In order to do so we exposed LPS-stimulated J774 murine monocyte-macrophage cells to AuNG2 and AuNG3,

4. PEGMA nanogels as drug delivering tool

containing Poma alone or Doxo and Poma, and determined the levels of IL-6 cytokine produced. Compared to non-exposed controls, IL-6 levels were reduced by 90%, similar to exposure to free Poma (Figure 4.15). No significant differences in the ability of AuNG2 and AuNG3 to inhibit LPS-induced IL-6 were observed, nor did the presence of Doxo in the formulations hinder Poma.

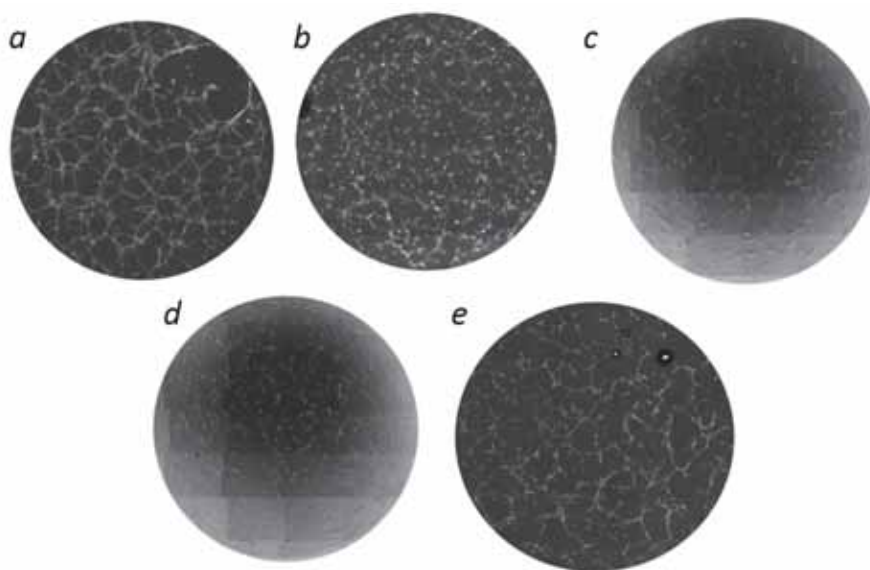


Figure 4.16.: a) The angiogenesis tube formation assay shows the ability of HUVEC cells to grow vessel-like interconnecting networks through the aid of growth factors present in the underlying gel. In cases where no nanogels were applied (a), established tube formation is seen within 6 h, yet with HUVEC cells pre-incubated with AuNG2 (c), or AuNG3 (d), or HUVEC cells incubated with free pomalidomide (b), poor or no tube-formation is seen. Control experiment with AuNG without coating and Poma show tube formation similar to no Poma (a). Each image (circle) is 4 mm in diameter DIC microscope image showing the whole well. Reproduced with permission from ref.¹⁰⁶ Copyright 2017, American Chemical Society.

We next investigated the ability of Poma containing nanogels to inhibit angiogenesis in an in vitro tube formation model. Due to the short time span of the

4.6. Intracellular drug release

assay ("tubes" form within hours and cells die naturally at approximately 24 h post planting), we pre-incubated HUVEC cells with Poma-containing nanogel formulations overnight, and the following day we planted the nanogel-containing HUVEC cells on the tube-inducing gel support. Figure 4.16 shows the effective inhibition of tube formation when healthy HUVEC cells, otherwise capable of tube formation, were pre-incubated with both Poma-containing AuNG2 or AuNG3, at a concentration equivalent to 10 μ M. On the contrary, HUVEC cells pre-incubated with Au decorated PEGMA nanogels without Poma were able to form tubes (Figure 4.16)e, as expected. In addition to Poma effects on HUVEC cells when grown under angiogenesis-stimulating conditions, the cell surface area and the aspect ratio (AR) of HUVEC cells were significantly reduced upon exposure to Poma-containing nanogels when grown under "normal" tissue culture conditions (Figure 4.17). IMiD compounds have been shown to activate GTPases, enzymes which are responsible for cellular cytoskeleton reorganization, cellular differentiation and movement.¹⁴⁷ In fibroblasts, Poma has been shown to induce formation of actin stress fibers,¹⁴⁷ and changes of cell area and aspect ratio have been documented upon exposure of cells to both anti- and pro-angiogenic molecules.^{148,149} Considering that the production of pro-angiogenic molecules such as VEGF and bFGF is inhibited by a cascade of signaling pathways due to pomalidomide's ability to down-regulate cell adhesion molecules and reduce VEGF, bFGF and IL-6 secretion,¹³⁰ it is

4. PEGMA nanogels as drug delivering tool

reasonable to assume that Poma will affect cell surface area. Exposure of HUVEC cells to Poma-containing nanogels resulted in a decrease in cell size, reducing the surface area by 30-60% of the original value. The decrease in cell surface area and aspect ratio was more pronounced for Poma-containing AuNG2 than for AuNG3, which can be correlated with an enhanced cell uptake of these nanogels, but also with the higher degree of Poma release observed in solution. Interestingly, we did not observe any similar effects upon exposure of HUVEC cells to free Poma, which suggests that these IMiD mediated changes in cell morphology are highly dependent on exposure time and subsequent Poma release from nanogel formulations.

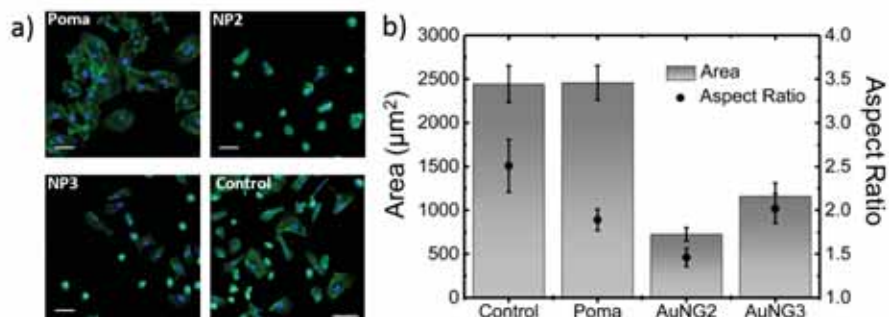


Figure 4.17.: HUVEC cells incubated with free Poma, AuNG2, AuNG3 or AuNG without Poma (control) for 4 h at a final Poma concentration of 10 µM. Cells were washed, fixed and stained with DAPI and AF488-phalloidin to show the nucleus and actin fibers respectively. Scale bars are 50 µm. c) Area and aspect ratio (AR) of cells described in (b), measured using ImageJ from at least 30 cells from 3 separate images. Mean + SD is shown. Reproduced with permission from ref.¹⁰⁶ Copyright 2017, American Chemical Society.

4.7. Conclusion

It was shown that the AuNGs presented in Chapter 3 are a versatile drug delivery system. The leakage of drugs was reduced by wrapping the nanogels with a polyelectrolyte shell. We studied two possible coatings: polyalginate and poly-L-arginine. These two coatings produced different modifications in the thermoresponsive behavior of the nanogels and other physicochemical properties that were characterized and influenced first, the stimuli responsive release of the two drugs and second, their interaction with cells and their drug delivery in vitro. We showed that pH, glutathione concentration, heat and NIR-light can all trigger the release of drugs in an extent that was dependent on the chemical nature of the drug and the coating polyelectrolytes. Both coated nanogel systems showed enhanced uptake by cancer cells compared to non-cancer cells, due to their enhanced metabolism, but more specific uptake in cancer cells was seen for nanogels coated with positively charged polyalginate. Taking this into account and considering: 1) both polyelectrolyte coated PEGMA nanogels have low leakage and show a slow drug release profile, 2) the cytotoxic doxorubicin is released more efficiently by a remote controlled trigger (light) from AuNG3 than AuNG2 nanogels and 3) the release of pomalidomide was effective for the two nanogel formulations, we can conclude that polyalginate coated PEGMA nanogels can be considered as the more convenient drug delivery system for the remote controlled co-delivery of doxorubicin and pomalidomide.

4.8. Experimental part

4.8.1. Loading with doxorubicin/pomalidomide

Nanogels were loaded with drugs prior further functionalization with the polyelectrolyte by immersing them in solutions of Doxo and/or Poma with a final concentration of 0.125 mg/mL of each drug and a pH adjusted to ca. 8. The nanogels were incubated overnight and the addition of the polyelectrolyte layer was carried out without further purification.

4.8.2. Co-culture and live/dead staining

Human dermal fibroblast (HDF; Invitrogen) cells were stained in suspension for 1 h, 37 °C, using Cell Tracker Blue CMF2HC (Invitrogen) at a final dilution of 1/100 in FBS free DMEM. Cells were washed and mixed 1:1 with unstained HeLa cells (a gift from Prof. Charles Lawrie, Biodonostia) and plated at a final cell number of 1×10^4 cells/well in a 96-well plate (Ibidi μ -plate 96-well). The following day media was replaced with doxorubicin (4 μ g/mL; Sigma Aldrich) and nanogel solutions (diluted 1/25, equivalent to 4 μ g/mL doxorubicin), 200 μ L/well. PEGMA nanogels were incubated with cells for 2.5h, followed by washing with warm PBS (10 mM, pH 7.4) and replacement of the medium. Images were taken at various time points, after removal of nanogel solutions, using a 20x objective with DIC contrast and red and blue fluorescence channels for doxorubicin and Cell Tracker Blue (HDF cells)

fluorescence respectively. A Zeiss Cell Observer microscope with AxioVision software was used.

The same cultures were used to analyze cell viability using Live/Dead (Abcam) staining after ca. 96 h. Media was replaced with 150 μ l of warmed staining buffer containing 1/1000 dilutions of both "live" and "dead" fluorophores. Cells were left at 37 °C for 15 min and then imaged using a 10x objective with phase contrast and green and red fluorescence channels for "live" and "dead" staining respectively. Due to the late timepoint, HDF cells were no longer positive for Cell Tracker Blue and therefore visual comparison of cell morphology alone was used to differentiate between dead cell populations. A Zeiss Cell Observer microscope with AxioVision software was used.

4.8.3. Flow cytometry

Human dermal fibroblast cells were stained in suspension for 1 h, 37 °C, using Cell Tracker Blue CMF2HC at a final dilution of 1/100 in FBS free DMEM. Cells were washed and mixed 1:1 with unstained HeLa cells and plated in a 24-well plate at 5×10^4 cells/well. The following day media was replaced with doxorubicin (4 μ g/ml) and nanogel solutions (diluted 1/25, equivalent to 4 μ g/ml doxorubicin), 500 μ L/well. PEGMA nanogels were incubated with cells for 2h30, followed by washing with warmed PBS (10 mM, pH 7.4) and replacement of the media. The following day cells were

4. PEGMA nanogels as drug delivering tool

lifted up using trypsin-EDTA and washed twice with ice-cold PBS. Samples were analysed in 1 % BSA/PBS on a BD Canto II flow cytometer using compensation. Cells were gated using the Pacific Blue channel (HeLa vs. CMF2HC-stained HDF cells), and then the % of doxorubicin positive cells measured in the PE channel. Cell viability; irradiation experiments HeLa cells were plated in a 96-well TC-treated transparent plate at 5×10^4 cells/mL, 100 μ L/well. The following day media was replaced with doxorubicin (4 μ g/mL) and NP solutions (diluted 1/25, equivalent to 4 μ g/mL doxorubicin), 100 μ L/well. NPs were left overnight with cells (approx 18 h) followed by replacement of the cell media. Individual wells were irradiated using a 808 nm fiber coupled laser diode with a maximum power of 4 W (Lumics). The spot size was chosen to illuminate the whole well at once (0.4 cm in diameter) and the power and time was adjusted to obtain the desired power density used for the experiments. The following day cell viability was analysed using the MTT assay (Roche) and absorbance measured at 550 nm, showing both non-irradiated and irradiated wells.

4.8.4. Transmission electron microscopy of cells

HeLa cells were grown in 60 mm diameter tissue culture treated petri dishes, 1×10^6 cells/3 mL/dish. The following day, nanogels were added at a final dilution of 1/50, 3 ml/dish. PEGMA nanogels were incubated with cells for 2 h, followed by washing with warm PBS and replacement of the medium.

4.8. *Experimental part*

The day after, cells were fixed in the dish using 2 % formaldehyde/2.5 % glutaldehyde in Sorensens buffer (initial fixation of 10 min at rt, followed by secondary fixation with fresh solution for 2 h at 4°C). Fixative was removed and cells washed using cold Sorensens buffer. A cell scrapper was used to bring the cells into suspension. Cells were embedded in 2% agar, followed by further fixation and staining with a 1% osmodium tetraoxide solution for 1h on ice. Samples were washed with Sorensens buffer and then water, and dehydrated in an ethanol series, followed by 2 final pure ethanol and then pure acetone washes. Samples were embedded in Spurr's resin and polymerized overnight at 65 °C. One hundred nm slices were cut using an ultramicrotome and viewed using TEM (JEOL JEM-1400PLUS , 40kV - 120kV).

4.8.5. LPS-induced IL-6 production from J774 cells

J774 macrophages were plated in a normal tissue culture treated 96-well plate at a concentration of 2×10^5 cells/ml, 100 μ L/well. The following day half the wells were pre-treated with LPS (Sigma Aldrich) at a final concentration of 1 μ g/ml, 100 μ L/well. After 1 h of LPS-stimulation, a further 100 μ L of NPs (1/5 diluted, equivalent to a final pomalidomide concentration of 10 μ M) were added. Controls including free pomalidomide (a final pomalidomide concentration of 10 μ M), DMSO (final dilution of 1/5000 equivalent to the volume present in 10 μ M pomalidomide), and pomalidomide free NPs were

4. PEGMA nanogels as drug delivering tool

included. The final volume was 200 μl /well. Cells were incubated for 24 h, following which supernatants were removed and frozen for subsequent IL-6 analysis. Supernatants were analysed for IL-6 using standard sandwich ELISA with TMB substrate detection.

4.8.6. Angiogenesis assays

Human umbilical vein endothelial cells (HUVEC) were plated in a normal tissue culture 96-well plate at 1×10^6 cells/ml, 100 μL /well. The following day nanogels were added at a final concentration equivalent to 10 μM pomalidomide. Cells were incubated with PEGMA nanogels for 2 h, followed by washing with warmed PBS and replacement of the media. The following day 10 μL of Geltrex (Invitrogen) was placed in the lower wells of an angiogenesis slide (Ibidi μ -slide Angiogenesis) and left to solidify at 37 °C for approximately 30 min. HUVECs, previously incubated with nanogels, were uplifted using Trypsin-EDTA (Invitrogen), counted, and adjusted to 2×10^5 cells/ml. Fifty μL of cells were added to each well (1×10^4 cells), taking care not to disturb the gel. Control wells without nanogel pre-incubation and with direct pomalidomide (10 μM) incubation were included. Cells were imaged approximately 6 h post seeding with a Zeiss Cell Observer microscope equipped with a x10 objective with phase contrast. AxioVision software with the "Mosaix" application was used to image the whole well (4 mm diameter).

4.8.7. Pomalidomide-induced cell morphological changes

HUVEC cells were plated in a 96-well plate (Ibidi μ -plate 96-well) at a concentration of 4×10^4 cells/well, 200 μ L/well. The following day media was replaced with the corresponding nanogel solution, 200 μ L/well, at a final concentration equivalent to 10 μ M pomalidomide. Pomalidomide-free nanogels at an equivalent concentration, and pomalidomide alone were also included. After 4 h, wells were washed with warmed PBS and fixed using a 4% formaldehyde solution in PBS. Cells were stained using DAPI (Invitrogen) and AF488-phalloidin (Invitrogen) to show the nucleus and actin fibers respectively. Images were taken using an EC Plan-Neofluar x40 oil objective with DIC contrast and filters for green (AF488-phalloidin actin staining), red (doxorubicin staining) and blue (DAPI nuclear staining) fluorescence. Cell area and aspect ratio (AR) values were calculated using ImageJ, analyzing 10 cells from 3 separate compound images composed of 9 tiles (in total ca. 30 cells/formulation).

5 Au-Polymer hybrid

structures as SERS platforms

5.1. Introduction

In this chapter both of the polymer-gold hybrid materials, presented in Chapter 3, are tested for their ability to be used as surface enhanced Raman spectroscopy (SERS) system for different kinds of application.

The chapter is divided in two sections. In the first section polyethylene glycol based (PEGMA) nanogels are tested with two different Raman reporter: crystal violet (CV) and doxorubicin (Doxo). Both are tested in solution, then Doxo is used to explore the thermoresponsive behavior of the nanogels as it was introduced in Chapter 3 in context of SERS measurements. Finally the nanogels are used for in-situ imaging of cells. The AuNGs discussed throughout this chapter were free of any polyelectrolyte coating.

The second part focuses on the PLGA microstructures. They contain SERS

5. *Au-Polymer hybrid structures as SERS platforms*

encoded gold nanostars (AuNSs) and it will be demonstrated that three dimensional confocal SERS microscopy can be used to show compartmentalization of the particles and to recreate the three dimensional structure of the polymeric superstructure. Finally we compare fluorescence and SERS signals over time to show that for possible long term exposure experiments, the SERS system would be favorable since the signal does not vanish. The work of the second part resulted in a recent publication.¹⁰⁷

5.2. PEGMA nanogels as SERS sensors for bioimaging

The PEGMA nanogels (AuNGs) presented in the previous chapters were tested as sensors for SERS measurements since the capability of the nanogel to act as a scavenger for small molecules and entrap them close to the nanoparticle surface is interesting for sensing applications. Due to the thermoresponsive nature of the polymer there is also the possibility to trigger the signal intensity externally. At temperatures above the LCST the nanogel will collapse and so the inter-particle distance is reduced which will ultimately lead to the creation of more "hot spots".¹⁵⁰

First we will present some SERS data of the microgel in solution and explore the ability to alter the SERS signal with temperature using CV and Doxo as Raman reporter. Additionally the particles were tested for SERS imaging of

5.2. PEGMA nanogels as SERS sensors for bioimaging

cells using CV as Raman reporter and the release of Doxo will be monitored in-vitro.

SERS spectra were recorded using a Renishaw InVia Raman microscope equipped with two Peltier-cooled CCD detectors, a Leica microscope and a gratings of 1200 lines/mm and band-pass filter optics. Solution measurements were carried out in small glass vials using 300 μ L samples and a 10x/0.25 objective. SERS measurements in cells were carried out in static mode using a 40x/0.8 water immersion objective. The exact power and integration times are stated explicitly in the main text since they varied depending on the Raman reporter.

5.2.1. Crystal violet as a Raman reporter

In the initial set of Raman experiments, the influence of nanoparticle size and excitation wavelength on the signal intensity was investigated. AuNGs with three different AuNP sizes (\approx 12 nm, \approx 18 nm, \approx 25 nm) were chosen and incubated with a 1 μ M CV solution for at least 2 hours. CV is a well studied Raman active molecule with a high affinity towards gold surfaces due to amino groups present and a high Raman cross section due to its symmetry. At the same time CV has an absorption maximum at around 633 nm which enhances the signal further when the excitation wavelength simultaneously excites the molecule. This effect is known as resonance Raman spectroscopy.¹⁵¹ Accordingly a SERS measurement of CV using an

5. Au-Polymer hybrid structures as SERS platforms

excitation wavelength of 633 nm should be referred to as surface enhanced resonance Raman spectroscopy (SERRS) to highlight that both resonance of the molecule and enhancement of the nanoparticle contribute to the intensity of the signal.^{152,153}

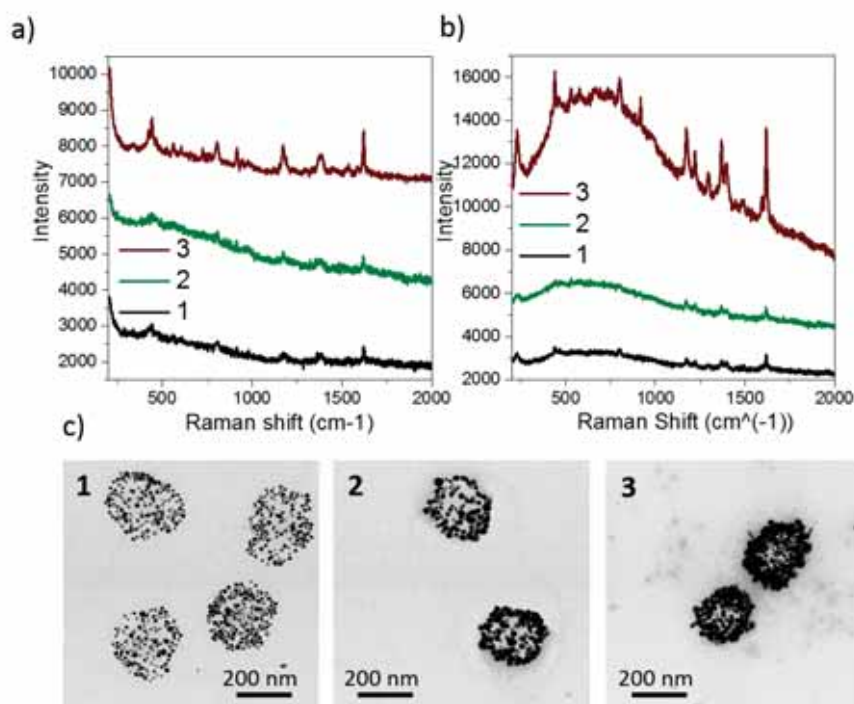


Figure 5.1.: a) SERS spectra of CV using 633 nm excitation wavelength (1.19 mW) for nanogels with different sized AuNPs of ≈ 12 nm (1), ≈ 18 nm (2), ≈ 25 nm (3). b) SERS spectra of CV using 785 nm excitation wavelength (19.4 mW) for nanogels with different sized AuNPs. c) Representative TEM pictures of nanogels used for this experiment

In this context we used AuNGs of the same concentration and measured the Raman spectrum with both a 633 nm and a 785 nm laser. For all measurements the typical CV Raman spectrum was observed with high intensities at 438 cm^{-1} , 1298 cm^{-1} and 1618 cm^{-1} . The exact concentration of the AuNG systems was challenging to keep the same for the different nanogels. In

5.2. PEGMA nanogels as SERS sensors for bioimaging

this case, the concentration of the polymeric nanogel before the synthesis of the AuNPs was the same and was kept constant during all the experiments to assume the same amount of nanogels for each sample, each containing different sized AuNPs.

The general trend shows that larger particles produce a higher intensity SERS response for both excitation wavelengths (Figure 5.1). This is an expected trend considering that for a constant amount of nanogels, roughly the same amount of AuNPs, but with different sizes, are present in solution. The bigger particles have a bigger surface area and better inter-particle interaction to promote a better SERS signal.

The excitation power for the 633 nm and the 785 nm laser was 1.19 mW and 19.4 mW, respectively (exposure time: 10s, dynamic grating range 200-2000 cm^{-1}). This difference makes it impossible to give a detailed comparison between the efficiency of the SERS signal depending on the excitation wavelength. The SERS intensity (I) scales theoretically with the fourth power of the incoming electric field intensity (E) at lower excitation wavelength in the green or blue region.⁷³ The intensity additionally depends on the distance of the molecule to the surface and of course the setup of the microscope. However comparing the SERS intensities of the different excitation wavelength shows that the 633 nm excitation wavelength is better suited for this particle system.

5. Au-Polymer hybrid structures as SERS platforms

5.2.2. Doxorubicin as Raman reporter

Since Doxo was used as a drug to show stimulated drug delivery in Chapter 4, we were also interested to follow Doxo using SERS.

A part of this section was already discussed in Chapter 4 to explain the release mechanism but this section will emphasize, in more detail, the SERS experiments and the information they contain. Doxo is a complex molecule but offers enough polar groups to show affinity towards gold surfaces and aromatic systems which are known to have a good Raman cross section (Structure is shown in section 4.1.1).

The nanogels were immersed in a 0.125 mg/mL solution of doxorubicin and the SERS spectrum was measured in solution (Figure 5.2). The spectrum shows the Raman vibrational bands typical for Doxo at 460 cm^{-1} , 1250 cm^{-1} and 1650 cm^{-1} corresponding to C=O deformation, C-O-H, C-H bending and C=O stretching vibrations, respectively.⁹¹ It should be noted that the SERS spectrum was recorded in solution using a 633 nm excitation wavelength with 6.3 mW power and an integration time of 40 s. These conditions are considered to be quite harsh for SERS experiments. They produce a clear signal in aqueous solution however in more complex systems, for instance in-vitro experiments, the low responsiveness will add measurement complications as shown in Section 5.2.3.

Glutathione (GSH) can replace Doxo on the surface of the AuNPs and, due to the higher affinity of thiol groups towards the surface of AuNPs, will even-

5.2. PEGMA nanogels as SERS sensors for bioimaging

tually cause a release of Doxo as we explained in Chapter 4. We monitored the Raman signal and the fluorescence before and after incubation with GSH. Molecules close to the surface have quenched fluorescence but high SERS intensities whereas molecules in solution show the opposite behavior. Their contribution to the SERS signal is low and the fluorescence intensity will increase. Upon addition of GSH the exact same behavior is observed (Figure 5.2). GSH replaces the Doxo at the surface and the fluorescence increases. At the same time the SERS signal decreased to a point where it almost vanished, indicating that Doxo was replaced on the AuNPs surface. Alongside explaining part of the release mechanism, this example shows how important the affinity between the surface and the analyte is in SERS measurements and indicates the potential benefit of correlating fluorescence and SERS data in order to gain information about drug delivery systems.

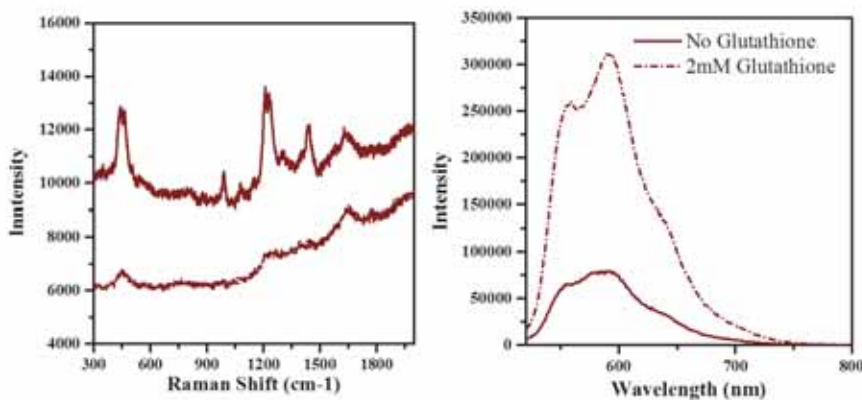


Figure 5.2.: SERS spectra and corresponding fluorescence spectra of Doxo without GSH and in a 2 mM GSH solution.

5. Au-Polymer hybrid structures as SERS platforms

Temperature dependence of SERS signal

The same system was tested on its ability to use the thermoresponsive behavior of the AuNGs to alter the SERS signal. In theory and according to other publications, the SERS signal should increase once the AuNGs are heated above the LCST.^{150,154} Thus we measured the SERS signal of Doxo in solution at RT and at 42 °C. Figure 5.3a shows that the signal increases upon heating. However the effect is not reversible which is interesting since the plasmon shift of the AuNGs is fully reversible over several cycles (Figure 5.3b). One explanation could be that the SERS intensity is not involving all of the particles but can rather be influenced significantly by just a few aggregates. These aggregates may be irreversible but will not be seen in the UV-vis spectrum which is in contrast an ensemble measurement where small changes are averaged out. To our knowledge there is just one paper which shows a reversible SERS spectrum upon heating, other systems which are more similar to ours do not show reversibility of the SERS signal either.¹⁵⁰

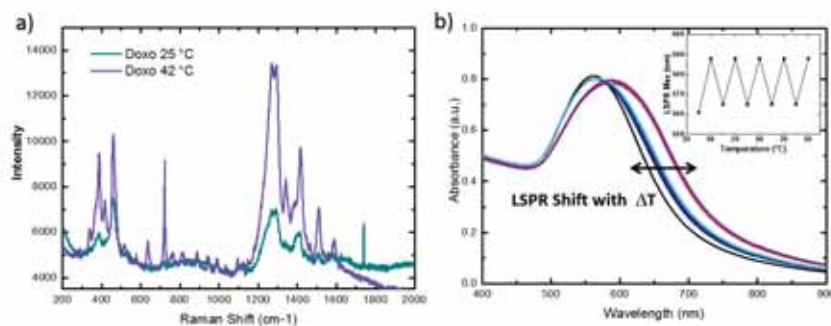


Figure 5.3.: a) SERS spectra of Doxo below and above the LCST of the PEGMA nanogels b) UV-vis spectra of the corresponding nanogel at RT and 50 °C. The inset shows the LSPR maxima during each cycle

5.2.3. In-Vitro imaging of crystal violet

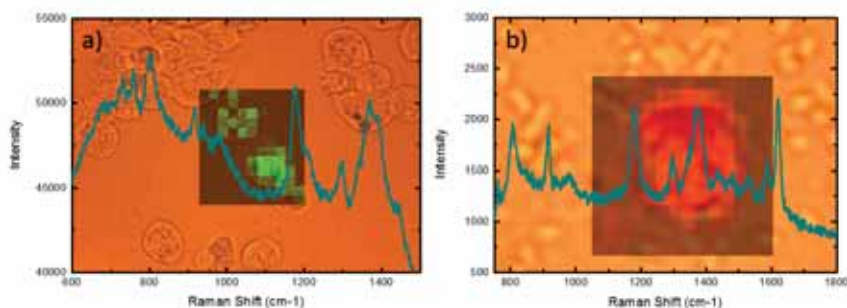


Figure 5.4.: SERS mapping and a representative spectrum of J774 macrophages (a) and A594 cells (b) incubated with CV loaded nanogels. The contour plot was created using the SERS intensity at 1175 cm^{-1} .

We first used CV loaded nanogels to examine the possibility of intracellular SERS measurements since the SERS intensities of the nanogels in solution were higher than for Doxo. For the measurement J774 macrophages (Figure 5.4a) and A549 cells (Figure 5.4b) were incubated with CV loaded nanogel for 3 hours and then washed three times. Afterwards the cells were examined under the Raman microscope using a 633 nm laser of roughly 5 mW and an integration time of 1 s. Figure 5.4 shows a contour plot of the peak intensity at 1175 cm^{-1} and a representative spectrum. In both cases the CV spectrum could be resolved and the cell was showing an even signal throughout the whole area, indicating that these particles with the right Raman reporter can be used as imaging device.

5. *Au-Polymer hybrid structures as SERS platforms*

5.2.4. **In-Vitro imaging of doxorubicin**

A more complex experiment was carried out to see if SERS and fluorescence microscopy can be correlated and used to monitor the release of Doxo in-vitro. Therefore we co-imaged AuNGs inside cells with SERS and fluorescence microscopy at two different time points to follow the release over time. A549 cells were incubated for 3 hours with Doxo loaded AuNGs and washed three times to avoid the release of any nanogel which was not taken up by the cells. The SERS signal and fluorescence were then measured and the cells stored for another 6 hours until a second measurement was carried out.

Directly after incubation and washing, a signal, similar to Doxo (Section 5.2.2), could be observed. The signal to noise ratio was very low and thus demanded long exposure times and high laser power (633 nm, 10 s, 10 mW). The 633 nm laser was necessary to obtain a signal of Doxo in all systems but has the major drawback of stimulating auto fluorescence of the cells. Thus the background is high and the spectrum can not be explicitly attributed to Doxo (Figure 5.5). However, a clear distinction between inside and outside of the cell can be made. Corresponding fluorescence microscopy also shows that Doxo is present inside the cells. After 6 hours of further incubation and potential Doxo release, the same measurements are repeated. The SERS spectra of Doxo can no longer be resolved leaving only the high fluorescence background. This indicates less Doxo close to the surface of the AuNPs. Fluorescence microscopy at the same time shows higher intensities

5.2. PEGMA nanogels as SERS sensors for bioimaging

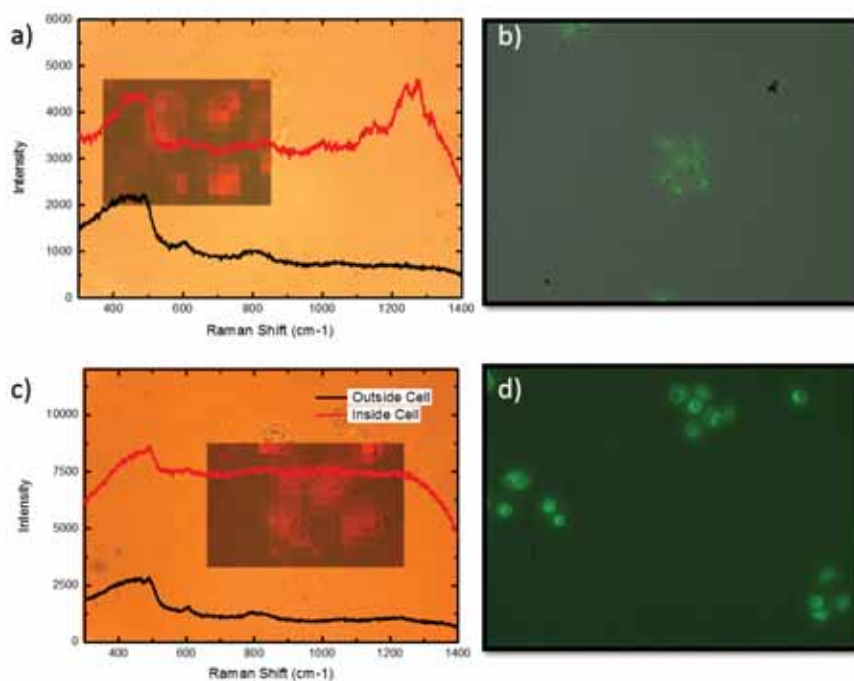


Figure 5.5.: Intracellular and extracellular SERS spectra of A549 cells incubated with Doxo loaded nanogels after 3 hours of incubation (a) with the corresponding fluorescence microscopy picture (b). The same measurement was repeated after 6 hours and the SERS spectra (c) and fluorescence microscopy pictures were taken (d). In both cases is the contour plot created by using the SERS intensity at 1250 cm⁻¹. It has to be mentioned that the difference in signal is most likely due to a change of the background and not due to a different SERS intensity of Doxo.

when compared with the first measurement, which indicates release of Doxo as well. In conclusion it can be stated that doxorubicin can be imaged with SERS and correlated with fluorescence microscopy allowing qualitative, time resolved measurements in-vitro. However the system does not show a signal which is intense enough to monitor certain peaks over time nor is there a quantitative conclusion possible regarding the amount of released Doxo.

5.2.5. Conclusion

It was demonstrated that the AuNGs are not just an efficient drug delivery system (Chapter 4) but can also be used as a SERS platform for solution based SERS measurements. Common Raman reporters such as CV can be detected when particles are simply immersed in a solution down to at least 1 μM concentrations. Lower concentrations may be possible but require extreme measuring conditions. Furthermore it was shown that Doxo can be detected using SERS spectroscopy as well. In a follow up study the effect of GSH was tested. Due to the strong thiol bond between GSH and the gold surface, GSH should replace the Doxo on the gold surface and lead to a decrease of the SERS signal whilst the fluorescence of Doxo will increase. Indeed, this effect was observed and shows nicely how fluorescence and SERS can be used as combined imaging techniques to gain insight about drug delivery mechanisms (Chapter 4).

Ultimately, the particles were tested on intracellular SERS measurements. For both Raman reporters (CV, Doxo) the signal could be detected inside cells and an imaging process would be possible. But it has to be noticed that desired monitoring of the Doxo release was not feasible due to the need for high laser powers, long exposure times and the low signal to noise ratio.

5.3. PLGA microgels for SERS imaging

In the second part of this chapter we examined the previously synthesized, two compartmental PLGA microgels using confocal Raman spectroscopy. 3D-SERS imaging offers powerful and complementary possibilities, it is still fairly undeveloped due to its complexity, as the weak nature of the Raman signal and its complicated scattering behavior requires a suitable compromise between the optimum pinhole size for confocality whilst maintaining a sufficiently high signal intensity.¹⁵⁵ Recently a few groups developed substrates to demonstrate Raman imaging with high spatial resolution in 3D.^{156–158} Promising applications for 3D SERS imaging would be, for example, related to monitoring of implanted scaffolds, so as to control their degradation over time, in combination with tissue growth. This is commonly done using mostly invasive methods such as histology which do not allow continuous monitoring, while non invasive methods such as fluorescence microscopy are often limited by penetration depth, sensitivity and long term stability and photobleaching.^{159,160} Photobleaching will be examined in the second part and compared to fluorescence microscopy.

SERS measurements (except bleaching experiment) were carried out using a WITec Alpha 300RS microscope with a 100x0.85 objective, a 600 g/mm diffraction grating and a 785 nm laser source with a power of about 7 mW.

5.3.1. Spatial resolution of PLGA microstructures

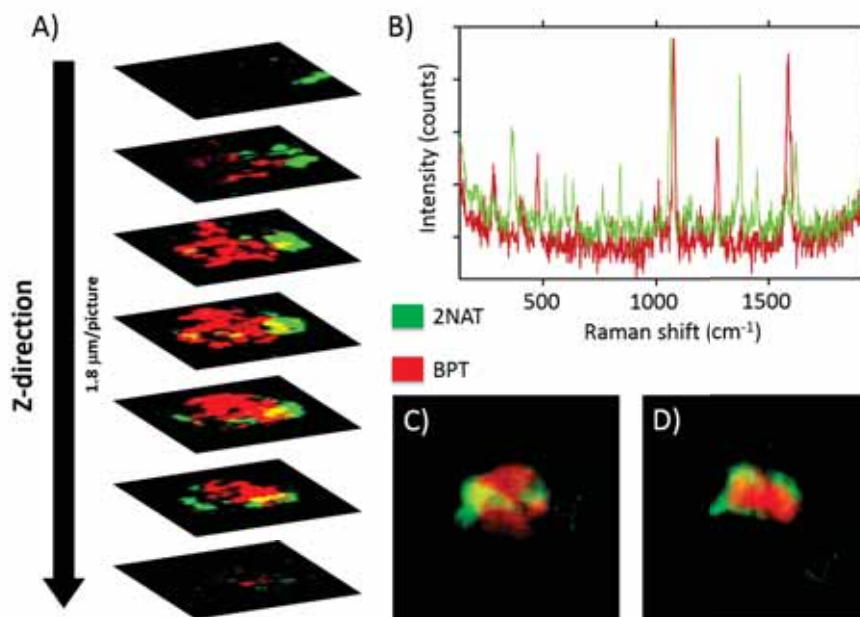


Figure 5.6.: Three-dimensional confocal Raman imaging of a single microgel particle. A) Z-stack showing the existence of separated compartments and the distribution of SERS labeled AuNSs within the particle. (B) Representative SERS spectra of BPT (red) and 2-NAT (green). The peaks marked with * indicate the specific signals used for mapping. (C,D) Three-dimensional reconstruction of the particle from two different perspectives. Reproduced with permission from ref.¹⁰⁷ Copyright 2017, American Chemical Society.

The 3D distribution of SERS-encoded AuNSs inside the microgel particles was examined with high resolution confocal Raman microscopy. We selected a 100%/0.9 objective with a 50 μm pinhole that best met our requirements.¹⁵⁵ One particle was scanned over a volume of $14 \times 14 \times 20 \mu\text{m}^3$ ($40 \times 40 \times 35$ points per line), with an integration time of 40 s per line (785 nm laser, 7 mW). The observed signal-to-noise-ratios were in general very high and the spectra for both Raman tags were well resolved under these scanning conditions (Figure

5.6). A series of slices (in z-direction) were imaged, in which both SERS tags (2-NAT, 4-BPT) spatially separated in different compartments could be resolved. Even though some degree of overlap (yellow-orange color) was observed, the compartments were found to be well separated from each other in most cases. Additional 3D reconstructions (Figure 5.6 C,D) confirm these results and suggest that the compartments are not perfect hemispheres but rather have a "tennis ball" like structure, where both compartments are wrapped around each other. In conclusion, we show that the SERS labeled AuNSs are present throughout the microgel and their distribution can be resolved by means of confocal Raman microscopy. This three-dimensional reconstruction especially helps to achieve information about nanoparticle distribution, which is not possible by conventional SERS measurements.

5.3.2. Bleaching experiment

Long term stability is a key advantage of SERS as compared to fluorescence and can be exploited in labeled scaffolds or microgels as imaging tools in nanomedicine. During long term experiments, the particles are exposed to a number of factors that lead to degradation and bleaching of organic molecules. The environment used for in-vitro and in vivo experiments is chemically aggressive, with the presence of redox active molecules, enzymes, highly reactive radicals and pH changes.¹⁶¹⁻¹⁶³ Additionally, exposure to light during microscopy observation leads to photobleaching of organic

5. Au-Polymer hybrid structures as SERS platforms

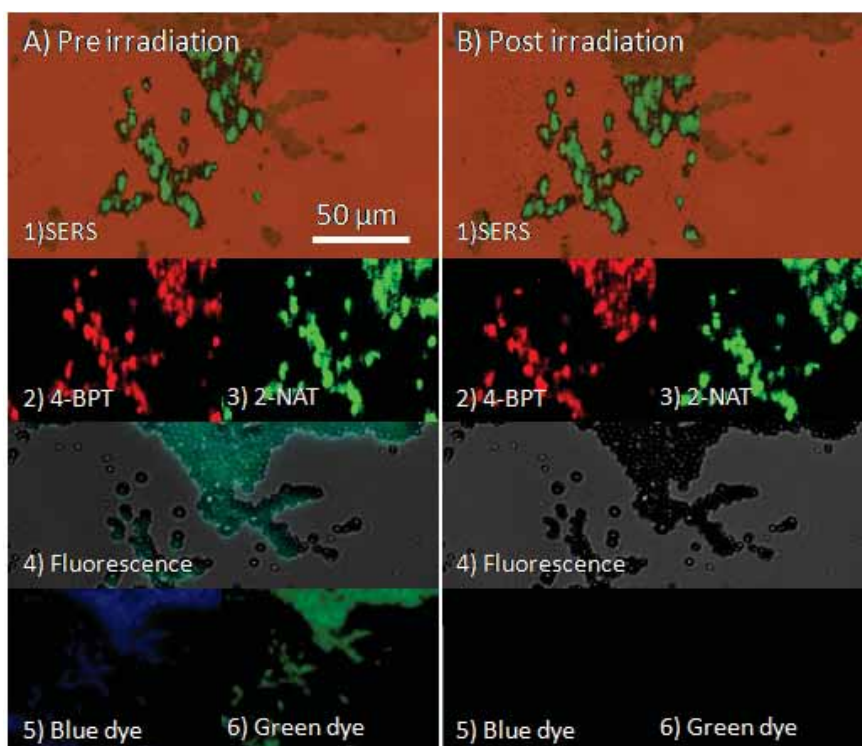


Figure 5.7.: A large number (>100) of bicompartmental particles were immobilized on a glass substrate and both SERS and fluorescence signals were measured before (a) and after (b) exposing them to UV-light. Images 1-3 show that the SERS signal from both 4-BPT and 2-NAT SERS tags show no difference over time and remain active upon irradiation. The fluorescence signals of both blue and green dyes (4-6) however vanish after UV light exposure due to bleaching of the dye molecules. Reproduced with permission from ref.¹⁰⁷ Copyright 2017, American Chemical Society.

dyes.¹⁶⁴ We analyzed the effect of photobleaching on our hybrid materials by measuring fluorescence and SERS signals from a large number of particles (>100) before (Figure 5.7) and after (Figure 5.7) UV-irradiation for 30 minutes. The microgel suspension was dropcasted on a quartzglass slide and a SERS map was measured using a Renishaw inVia Raman microscope equipped with a 1024x512 CCD detector using 785 nm excitation source and a 1200 g/mm diffraction grating. Measurements were carried out using a 100x0.85

5.3. PLGA microgels for SERS imaging

objective in Streamline mode with 2.1 mW laser power and an exposure time of 3.58 s. The slide was transferred to a Zeiss Cell Observer microscope where first fluorescence pictures under 20x magnification were taken and then the LED diodes were used to illuminate the sample. Overall the samples were illuminated for 30 minutes with the 470 nm and 530 nm LEDs with a power of 11.6 mW and 2.3 mW respectively. Afterwards fluorescence pictures and SERS measurements were repeated and processed under the exact same conditions like before. Prior to irradiation, the samples displayed fluorescence and SERS signals throughout the whole field of view. In contrast, after irradiation, the fluorescence signal completely vanished, while the SERS signals remained basically unaltered. This experiment clearly illustrates the degradation of the dye over time upon exposure to light, whereas the SERS tags remain stable and active, in a demonstration that SERS is an attractive tool for long term (bio)imaging experiments.

5.3.3. Conclusion

We demonstrated that SERS encoded AuNSs encapsulated within polymer microgels can be used to resolve and reconstruct the shape of particles or fibers. Importantly, dyes present inside the gel do not interfere with the SERS signal or create a background. Finally, an important outcome of this study is the demonstration that the SERS signal from embedded AuNSs, in contrast to that from fluorescent dyes, is not affected by exposure to UV illumination

5. Au-Polymer hybrid structures as SERS platforms

and therefore offers the possibility for long-term imaging experiments. Since PLGA is a biocompatible and degradable polymer, potential applications of these hybrid materials can be foreseen, for example in form of combined drug delivery/imaging devices. In particular, microfibers functionalized with AuNSs may allow us to obtain new insights in the role of implanted scaffolds in regenerative medicine.

6 Enzymatic catalysis

The final results chapter of this thesis contains work conducted in collaboration with Dr. Fernando López-Gallego from CICbiomaGUNE about enzyme catalyzed reactions. We developed a versatile cascade reaction to study enzyme kinetics through Raman spectroscopy. Enzyme reactions producing H_2O_2 as a by-product are coupled to the oxidation of 2,2'-azino-bis(3-ethylbenzothiazoline-6-sulphonic acid) (ABTS) which is catalyzed by horse radish peroxidase (HRP) in the presence of H_2O_2 . ABTS offers an intense color and Raman signal which makes it suitable to follow reactions in real time enabling calculation of the enzyme kinetics.

First, the HRP/ABTS reaction was examined as a function of pH, hydrogen peroxide and enzyme concentration to determine the reaction conditions for the follow up reaction cascade. Secondly, the second enzyme (oxidase) was introduced in order to initiate a reaction cascade, again using ABTS as the analyte. The oxidase produces H_2O_2 as a by-product which is subsequently utilized by HRP to oxidize ABTS. This process enables us to examine the

6. *Enzymatic catalysis*

kinetics of the HRP enzyme reaction. Thirdly, a catalase (CAT), a H_2O_2 consuming enzyme, is also introduced to the system to inhibit the reaction of HRP by competing for the hydrogen peroxide.

Finally, we immobilized the H_2O_2 producing and consuming enzymes in agarose beads and used Raman mapping to study how the spatial organization of the immobilized multi-enzyme systems influences in the kinetics of the reaction cascade.

6.1. Principles of enzymatic catalysis

Enzymes are very specific protein based catalysts which are used by nature to create complex and stereo-specific molecules under mild conditions. In contrast to conventional organic synthesis methods complex molecules can be formed at a high turnover rate in a mild pH buffer solution at room temperature.^{165,166}

In organic synthesis, enzymatic catalysis is often referred to under the more general term, biocatalysis, which covers the whole spectrum of natural catalysts such as whole cells, bacteria, plant extracts and purified enzymes.¹⁶⁷

Aside from fermentation, which has been used by human beings for thousands of years, enzyme catalysis marks one of the first examples of the manipulation of plants or microorganisms to synthesize organic compounds. First conducted over a century ago this marked a step change as a more

6.1. Principles of enzymatic catalysis

scientific and analytical approach was utilized. For example, the synthesis of (R)-mandelonitrile from benzaldehyde and almonds, or the usage of penicillin G acylase to make semi-synthetic antibiotics.^{168,169} Over time the knowledge acquired for enzyme purification and mechanisms of enzyme catalysis, was used to extend the pool of reactions from natural based products to purely synthetic compounds and intermediates for organic synthesis. For example, nitrile hydratase was extracted from cells and used to hydrate acetonitrile to acrylamide, as seen in polymer synthesis.¹⁷⁰ Today, elaborate screening and protein engineering has led to the next step of biocatalysis, where proteins are specifically designed to improve their activity and selectivity in order to withstand certain reaction conditions and to be used under non-natural reaction conditions for synthesis and even in cascades of several coupled enzymatic reactions.¹⁷¹ The spectrum of different enzyme classes which are mainly used nowadays include oxidases (as used in this thesis), lipases, esterases and proteases.^{172,173}

One challenge for the implementation of biocatalysis in organic synthesis is to gain a deeper understanding of the mechanism and the kinetics behind the reaction. For this purpose, a plethora of different techniques have been developed based on chromatography, mass spectrometry and spectroscopy, including fluorescence, IR, UV-vis and Raman.¹⁷⁴⁻¹⁷⁸ Fluorescence for example works in the study of a quenched fluorophore which is cleaved by the enzyme and leads to emission, to give just one example. An example of the

6. *Enzymatic catalysis*

potential of Raman spectroscopy can be found in the work of Graham and co-workers who utilized SERS as a sensing tool.¹⁷⁹ AgNP aggregates were used for the detection of a SERS active dye, with the dye being bound to a substrate, allowing for cleavage by lipases. Without the enzyme the dye does not interact with the AgNPs, however, upon enzymatic cleavage the dye may undergo free diffusion and interact with the AgNPs leading to an observable SERS response. In this work, several enzymes have been tested, showing that the proposed system is a fast and highly sensitive screening device to examine enzyme activity.

To increase stability and handling, enzymes are often encapsulated in polymeric particles, such as agarose beads.¹⁸⁰ Many industrial applications of enzyme reactions demand ways to increase enzyme stability, but also to simplify enzyme recycling and biocatalyst loading.¹⁸¹ With immobilization, enzyme kinetics will change and phenomena like mass transport and immobilization yield require an adaption of reaction conditions and extensive characterization.^{181,182} In this setup of immobilized enzymes special interest is given to measurements with spatial resolution. Again, fluorescence can be observed under a microscope but Raman microscopy offers a spectral acquisition for single points in the field of view, thus offering the possibility of gaining quantitative data for two (maybe even three) spatial dimensions. In this chapter we want to explore this possibility and work towards a spatially resolved quantitative measurement of enzyme activity.

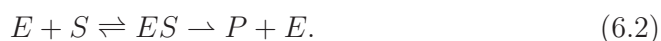
6.1.1. Enzyme kinetics

Enzyme kinetics can be grouped into reactions either with or without inhibition. In both cases, the rate of the reaction (ν), that is the change of product concentration ([P]) over time (t), depends on a simple mathematical formula which takes into account that the rate of the reaction depends on the concentration of the substrate itself:

$$\nu = \frac{d[P]}{dt} = a \left(\frac{1}{1 + \frac{b}{[S]}} \right). \quad (6.1)$$

The equation leads to a hyperbolic dependence of the rate compared to [S] where “a” defines the maximum of the curve and “b” is the point where [S]=1/2a. The exact values and their meanings are defined by the conditions of the catalytic reaction.

The simplest possible form of an enzyme reaction was first described by the German biochemist Leonor Michaelis and the Canadian Maud Menten. It describes the process where a substrate (S) interacts with an enzyme (E) forming a steady state (ES). The reaction is as follows:



The substrate forms a complex with the enzyme which is reversible, both reaction rates are defined by reaction rate constants, k_1 and k_{-1} , for the formation and the disintegration of ES respectively. Once the complex is

6. Enzymatic catalysis

formed another reaction towards the product (P) and E will compete with the disintegration, this reaction is defined by k_p . Through simple algebra, the reaction rate can be calculated and “a” and “b” can be expressed as the following:

$$a = k_p[E_0] = V_{max} \quad (6.3)$$

$$b = \frac{k_{-1} + k_p}{k_1} = K_M, \quad (6.4)$$

with $[E_0]$ being the initial enzyme concentration. The factors are commonly referred to as V_{max} and the Michaelis Menten constant (K_M). Substitution of “a” and “b” in to equation 6.1 is displayed in Figure 6.1 and assembles to:

$$\nu = V_{max} \frac{[S]}{K_M + [S]}, \quad (6.5)$$

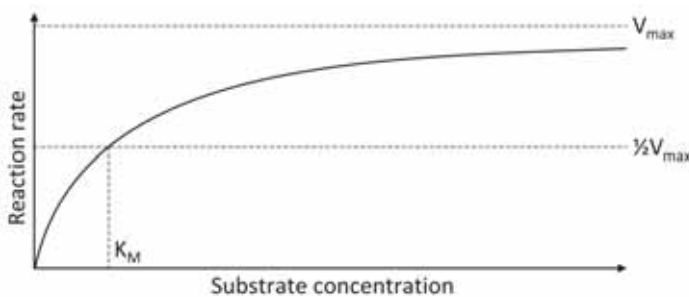


Figure 6.1.: A Michaelis Menten curve for the reaction rate (ν) against the substrate concentration

On closer inspection, the equation depends on the relative sizes of K_M and

6.1. Principles of enzymatic catalysis

[S]. If [S] is significantly smaller than K_M the equation can be simplified and a linear dependency is formed.

For the opposite case, when [S] is significantly bigger than K_M the equation can be simplified, showing that the reaction will become a zero order reaction where the rate does not depend on [S] anymore:

$$\text{For: } [S] \ll K_M \rightarrow \nu = \frac{V_{max}}{K_M}[S], \quad (6.6)$$

$$\text{For: } [S] \gg K_M \rightarrow \nu = V_{max}. \quad (6.7)$$

Especially within the first case, low substrate concentrations can be used to determine ν for different substrate concentrations [S] through linear regression. Once different reaction rates are calculated the Michaelis Menten constant can be fitted. A very elegant way is by use of the Lineweaver and Burk method, which reorders equation 6.1 to a linear expression:

$$\frac{1}{\nu} = \frac{K_M}{V_{max}} \frac{1}{[S]} + \frac{1}{V_{max}}. \quad (6.8)$$

If an inhibitor is present in the reaction solution, the equation is modified according to the type of inhibition. Different types of inhibition are: competitive inhibition, uncompetitive inhibition, non-competitive inhibition and mixed inhibition. Each type is defined by the interaction of the inhibitor with the substrate/enzyme. In the case of the competitive inhibition, the

6. Enzymatic catalysis

inhibitor forms a complex with the enzyme, thus reducing the effective free enzyme condition for the substrate. In this case K_M will increase but V_{max} will remain unchanged. For the uncompetitive inhibition the inhibitor forms a complex with the enzyme and substrate, resulting in K_M decreasing and V_{max} decreasing. When the inhibitor binds to the enzyme and reduces the activity without altering the affinity of the enzyme for the substrate, it is commonly called non-competitive binding. In this case for the non competitive binding the inhibitor binds to a different cavity of the enzyme, while in the competitive binding both inhibitor and substrate compete for the same binding site. In the last case of mixed inhibition which is the most complex case, the inhibitor binds to the enzyme and by that reduces the activity and the affinity of the enzyme towards the substrate.

6.2. Introduction of ABTS as a measuring tool

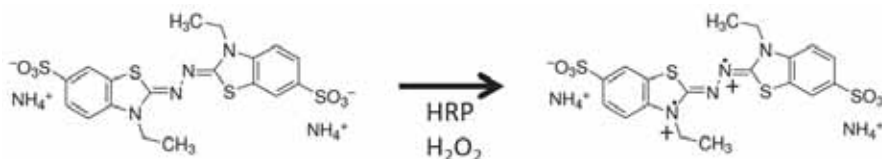


Figure 6.2.: Structural change of ABTS in presence of HRP and hydrogen peroxide.

Initially, the properties for the enzymatic reaction of ABTS are investigated in isolation to find conditions (pH, [HRP]) where the reaction rate is independent of the ABTS concentration (Equation 6.7). Under these conditions

6.2. Introduction of ABTS as a measuring tool

it is ensured that in the follow up experiments, where the reaction ABTS is coupled with GOX or DAAO, the kinetics are solely dependent on the conditions of the first reaction.

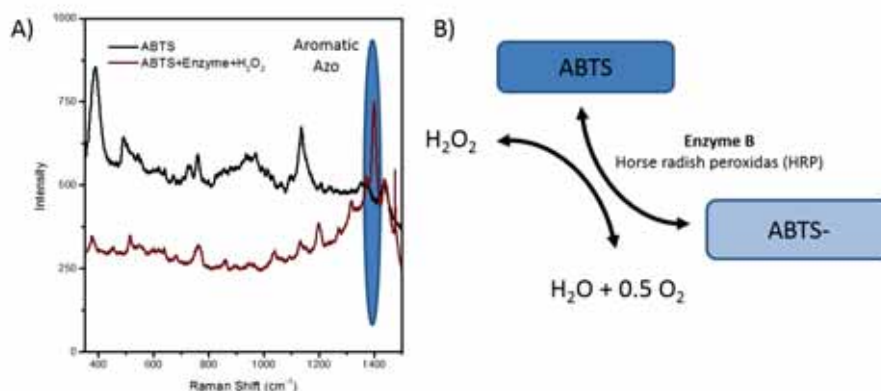


Figure 6.3.: a) Experimentally derived Raman spectrum of ABTS before and after the reaction (785 nm excitation wavelength). b) Scheme for the enzymatic reaction of ABTS

Figure 6.3 shows a schematic representation of the reaction under investigation. As mentioned, HRP will oxidize ABTS in the presence of H₂O₂ and two electrons are transferred. The detected analyte ABTS forms an anion (ABTS*, Figure 6.2) under oxidation which contains an aromatic azo compound. This compound shows a strong resonance Raman signal at 1400 cm⁻¹ ($\nu(\text{N}=\text{N})$) and can be used to detect the activity of enzymes (Figure 6.3).¹⁸³

The enzyme concentration was varied while the other factors were kept constant: 0.1 mg/mL ABTS, 10 mM H₂O₂ and pH 6. In Figure 6.4 the time curves of the ABTS* concentration are plotted, indicating the dependence on the HRP concentration. For all reported experiments in this chapter a Renishaw Raman microscope was used with a 785 nm laser at 10% laser

6. Enzymatic catalysis

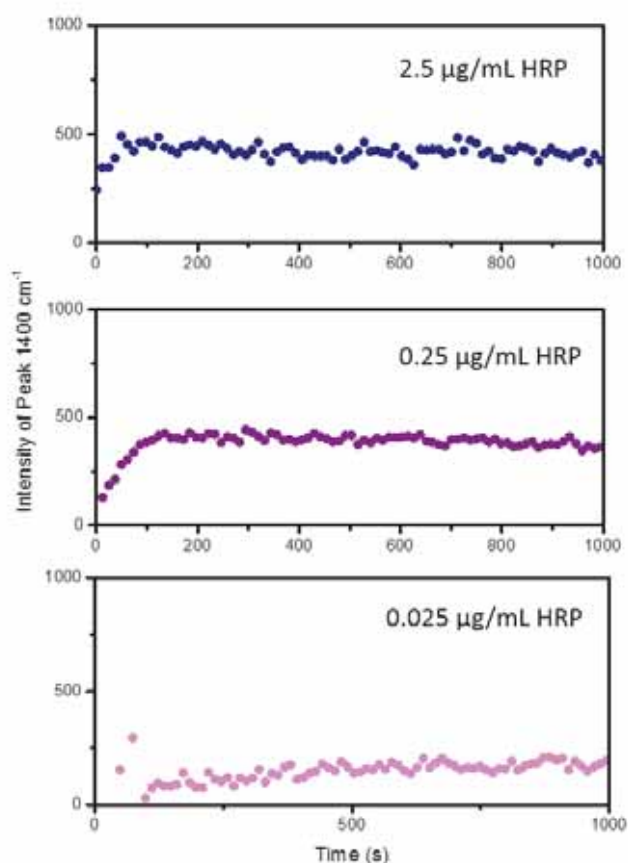


Figure 6.4.: Time dependent Intensity of ABTS under different HRP concentrations.

(17.8 mW) power and 10x magnification. For the lowest HRP concentration (0.025 $\mu\text{g}/\text{mL}$) there is almost no change of signal over a time span of 15 min, meaning that the enzyme concentration is too low to show a significant conversion within this time span. Increasing the concentration to 0.25 $\mu\text{g}/\text{mL}$ shows an increase of the signal within the first 2 min (500 counts) and remains stable for the rest of the measurement. The highest concentration tested (2.5 $\mu\text{g}/\text{mL}$) reached the maximum of 500 counts within less than a minute. In

6.2. Introduction of ABTS as a measuring tool

fact the reaction rate was high enough that the initial increase of the signal was not recorded, due the delay of enzyme addition and start of the reaction. Since the aim is to achieve a very fast reaction of ABTS, we fix the enzyme concentration for the following reactions to $2.5 \mu\text{g}/\text{mL}$.

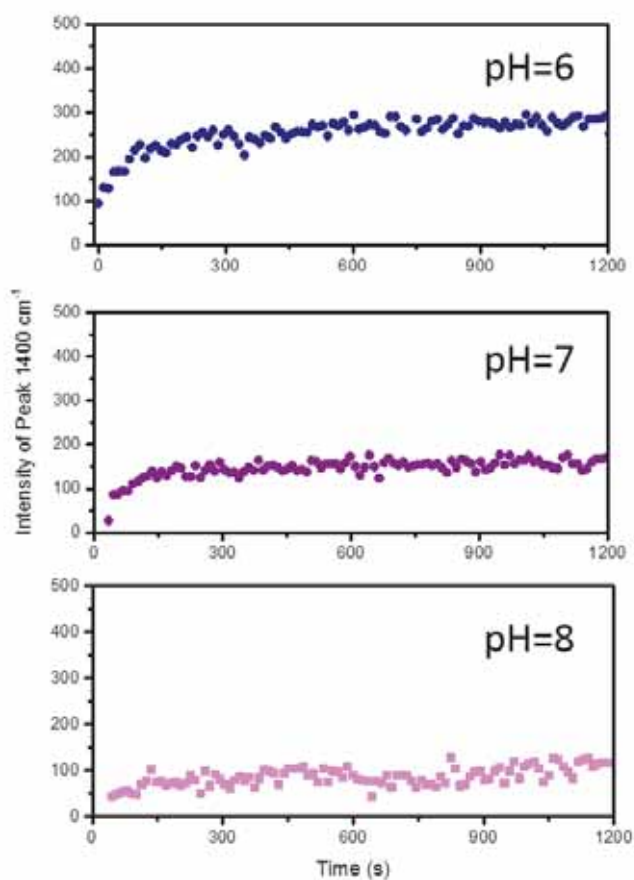


Figure 6.5.: Time dependent intensity of ABTS* at different pH's under otherwise constant conditions: $0.1 \text{ mg}/\text{mL}$ ABTS, 10 mM H_2O_2 , $2.5 \mu\text{g}/\text{mL}$ HRP.

The next set of experiments were conducted to examine the influence of pH on the reaction. According to literature, the enzyme activity decreases

6. Enzymatic catalysis

with rising pH.¹⁸⁴ Indeed, this trend was verified for our system as shown in Figure 6.5l. The activity was examined at a pH of 6, 7 and 8, showing a decrease in activity with increasing pH. At pH 8 the reaction is almost completely suppressed within the first 17 minutes, showing a negligent change in intensity. The pH was therefore fixed at a pH of 6 to enable fast reaction kinetics.

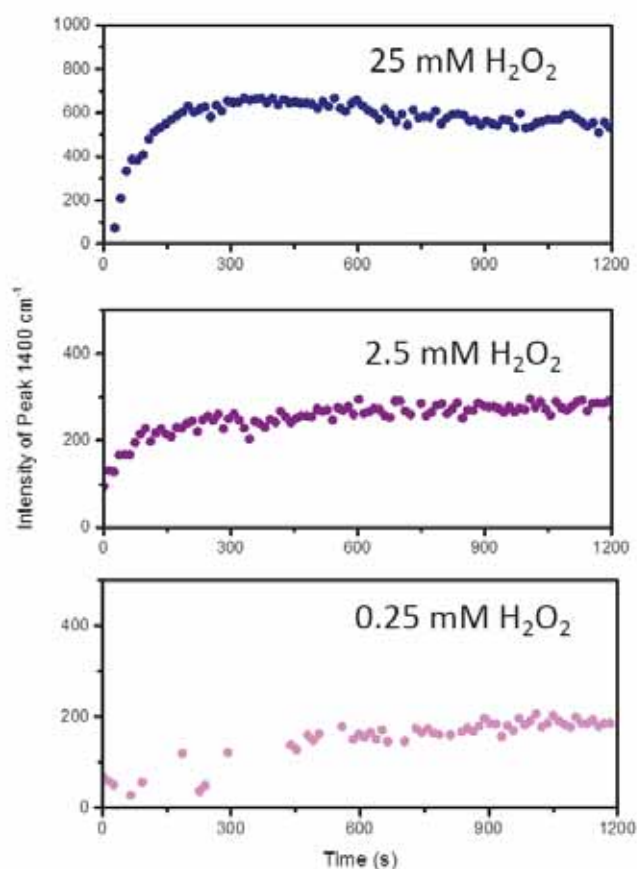


Figure 6.6.: Time dependent intensity of ABTS* at different H₂O₂ concentrations under otherwise constant conditions: 0.1 mg/mL ABTS, pH 6, 2.5 μg/mL HRP.

In a last set of experiments, before we move on to cascade reactions, the

6.2. Introduction of ABTS as a measuring tool

concentration of H_2O_2 was varied. A decrease of H_2O_2 will lead to a decrease of the reaction rate, if the concentration of H_2O_2 is low enough it should lead to an decrease of the overall intensity. Indeed this was observed as shown in Figure 6.6. The time until the intensity reached its maximum increased from about 3 minutes to more than 10 min for the lowest concentration. The overall intensity decreases as well for the lowest concentration (0.25 mM).

6.2.1. Cascade reaction

The conditions for the reaction were fixed at 0.1 mg/mL ABTS, pH 6 and 2.5 $\mu\text{g}/\text{mL}$ HRP throughout the following experiments. These conditions ensure that the measured kinetics depend only on the first reaction since the enzymatic reaction with HRP and ABTS will be fast enough to be considered instantaneous.

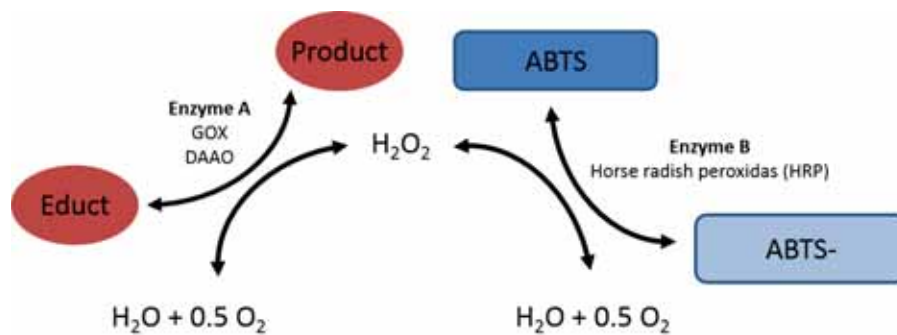


Figure 6.7.: Schematically presentation of a cascade reaction using a first enzyme (GOX, DAAO) with a substrate to produce H_2O_2 which is then reacting with HRP and ABTS to form ABTS*. In our case the educt will be glucose, but in principle other substrates can be used.

Figure 6.7 shows a scheme of the reaction cascade. In this thesis, two differ-

6. Enzymatic catalysis

ent enzymes (GOX and DAAO) and two different substrates (glucose and D-alanine respectively) will be investigated. The general method however, can be extended to every enzyme reaction where H_2O_2 is produced. In the reaction cascade the substrate will be oxidized in the presence of the enzyme and H_2O_2 is produced in-situ. This will subsequently react with ABTS and HRP and thus under reaction conditions where the HRP reaction is considered instantaneous, the reaction rate of the first reaction can be monitored. In the first set of experiments, different concentrations of glucose were reacted with GOX ($2.5 \mu\text{g}/\text{mL}$) and the change in intensity was measured by Raman spectroscopy. A series of 7 different glucose concentrations were tested examining the variation in signal intensity (Figure 6.8). For high concentrations the reaction is almost instantaneously complete and does not differ, which indicates that at these substrate concentrations, the reaction rate is not dependent on the substrate concentration itself (Equation 6.7). At these concentration we are high above K_M and work under saturation which means at V_{max} . For the lower concentrations, the rate of the reaction is lower showing a linear increase in intensity with time over the course of the experiment.

The same set of experiments was done using DAAO ($2.5 \mu\text{g}/\text{mL}$) as the enzyme with D-alanine as the substrate (see Figure 6.9) and the same trend can be observed, although even for high concentrations the reaction is significantly slower. This indicates that the activity of DAAO compared to GOX

6.2. Introduction of ABTS as a measuring tool

is significantly lower. Reasons for this could be a lower activity of DAAO as an enzyme. Other possible reasons for the difference in enzyme behavior such as variation between batches as the enzyme is isolated from bacteria, whilst age and storage can also be significant. This means it is difficult to make any general conclusions towards the enzyme activity. Throughout the experiments all enzymes were kept on ice to ensure their conservation but activity will still decrease over time. However, we showed that Raman spectroscopy of ABTS* can be used to measure the activity of enzymes of different nature and specificity for different substrates.

6. Enzymatic catalysis

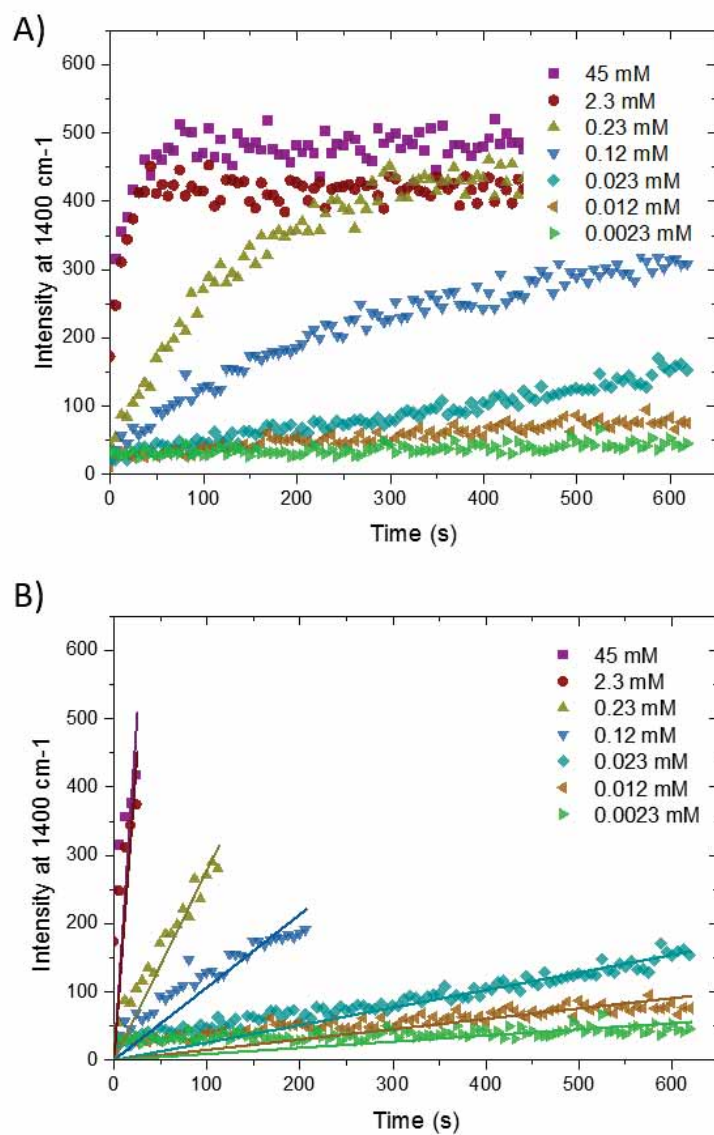


Figure 6.8.: A: Intensity of ABTS* over time at different glucose concentrations with GOX as the enzyme. B: From each dataset the first data-points where the increase of ABTS* is linear are separated. These data points follow a linear fit and can be used to determine the specific reaction rate for each glucose concentration.

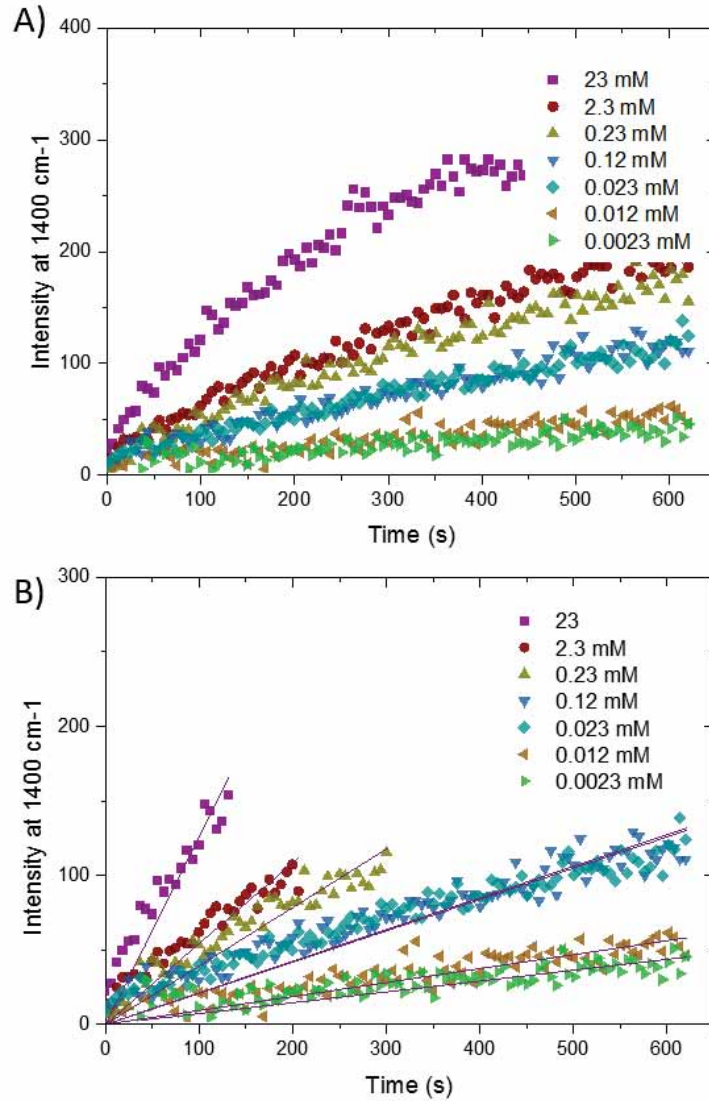


Figure 6.9.: A) Intensity of ABTS* over time at different XX concentrations with DAAO as the enzyme. B) From each dataset the first data-points where the increase of ABTS* is linear are separated. These data points follow a linear fit and can be used to determine the specific reaction rate for each glucose concentration.

6. Enzymatic catalysis

6.2.2. Michaelis Menten constant

The datasets derived in the last section as well as the linear fitting (Figure 6.8B and 6.9B) can be used to calculate the Michaelis Menten constant. Since the signal intensity corresponds to the turnover of H_2O_2 , and thus of glucose, a linear fit corresponds to the reaction rate, e.e.

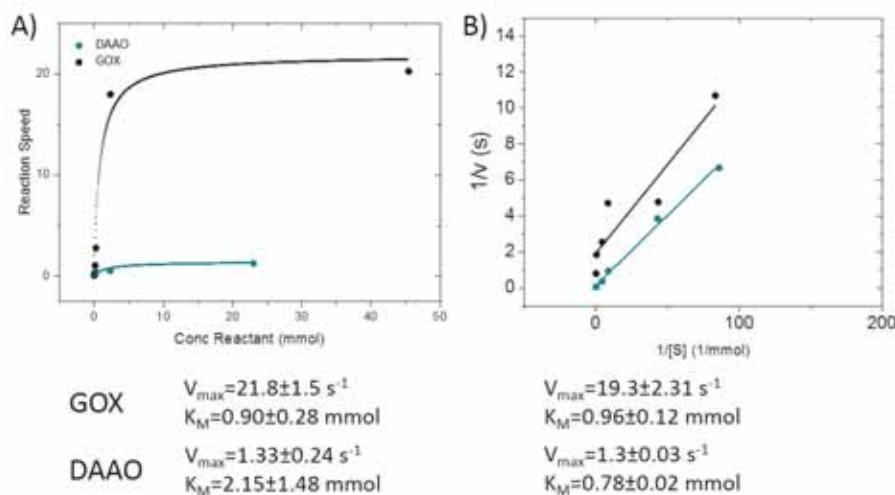


Figure 6.10.: A) Michaelis Menten plot with corresponding fitting values for V_{max} and K_M . B) Lineweaver Burk plot with corresponding values for V_{max} and K_M .

The values for V_{max} and K_M are shown in Figure 6.10 including the plotted data. Values for V_{max} are similar for both methods and show good agreement with the plots. For the enzyme GOX the value lies around 20 s^{-1} and for DAAO it is about 15 times lower at 1.3 s^{-1} . As mentioned before, by analyzing the rough data, the enzyme activity of DAAO is lower than GOX. The value of V_{max} is also plausible considering the maximum reaction rate in Figure 6.10 A, which is about 21 s^{-1} and 1.3 s^{-1} for GOX and DAAO respec-

6.2. Introduction of ABTS as a measuring tool

tively. A small discrepancy can be found when the two fitting parameters are compared for the K_M value. For GOX the value is in both cases around 0.9 mmol but for DAAO the value is 2.15 mmol using the Michaelis Menten fit and 0.78 mmol using the Lineweaver Burk method. K_M is similar for both enzymes, even though a 15 times higher V_{max} was measured. This means that binding of the substrate is similar but the transition state is not formed so rapidly in DAAO compared to GOX.

A direct comparison of these values with the literature is complicated since many factors, like the cascade reaction, the specific enzyme, the concentration and temperature all play a role. A closer look at the enzyme database BRENDA reveals how much the Michaelis Menten constants can vary for each enzyme and substrate.¹⁸⁵ For the oxidation of D-glucose with GOX the K_M values are between 12.5-26 mmol, with V_{max} values between 0.59-318.2 s^{-1} being reported under slightly varying reaction conditions. It is noticeable that the values derived through our measurements are generally lower (up to 10 times) than those found in the literature. The same can be found for the reaction of D-alanine with DAAO, with the values in the database varying from 0.036-800 mmol for K_M and 0.000167-721 s^{-1} for V_{max} . As mentioned, the reasons for this can be of a different nature, like temperature or pH. One systematic reason however, could be the wrong assumption that the second reaction of the cascade can be neglected in the calculations. This would need further clarification in future experiments.

6.2.3. Introducing a competing enzyme

In this subsection the effect of a competing catalase (CAT), which disproportionates H_2O_2 to H_2O and O_2 , is introduced. For these experiments we choose to compare CAT with GOX at different CAT concentrations. In all experiments all but the CAT concentrations remain constant at: 0.1 mg/mL ABTS, pH 6, 0.25 $\mu\text{g}/\text{mL}$ HRP and 0.23 mM glucose.

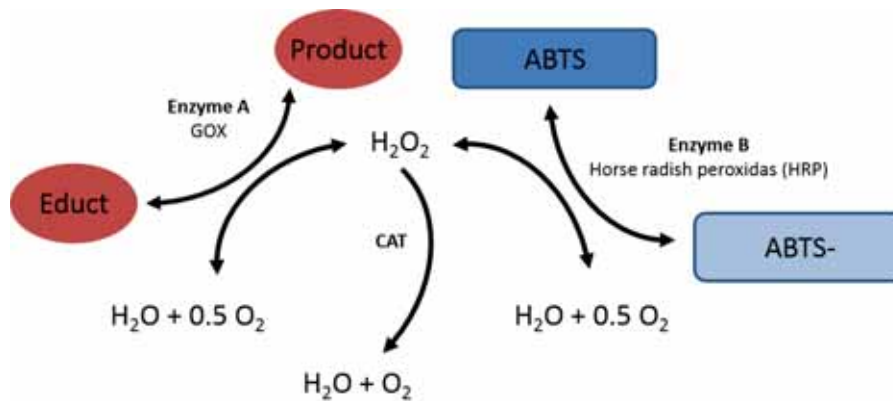


Figure 6.11.: Scheme of enzymatic cascade reaction with two enzymes competing for H_2O_2 , HRP and CAT.

Figure 6.11 shows the scheme for the enzymatic reactions happening in solution. In the first reaction GOX oxidizes glucose and H_2O_2 is created which then can react in two different ways. The first way is, again, the enzymatic reaction with HRP and ABTS, the other reaction (with CAT) competes with HRP, and depending on their enzyme activity and concentration different intensities of ABTS* will be measured.

Figure 6.12 shows time traces recorded with different CAT concentrations. At low concentration, almost no influence on the reaction is visible. Just above

concentrations of 0.015 mg/mL a significant reduction of ABTS production is observed. At this point the enzyme ratio of CAT and HRP is 6. Increasing the ratio finally leads to the complete suppression of the creation of ABTS* at a ratio of 120.

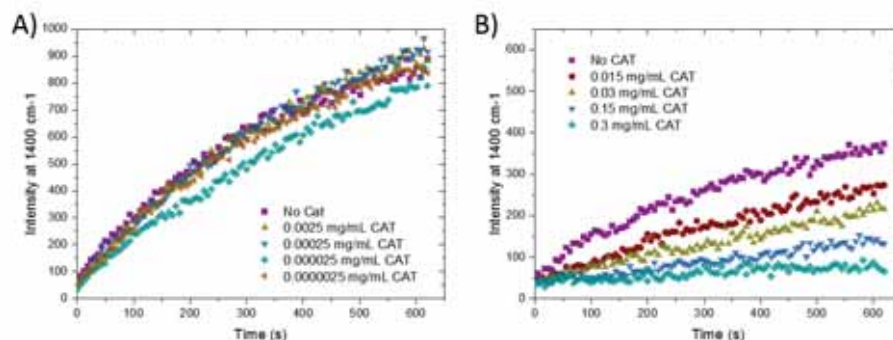


Figure 6.12.: Intensity of ABTS* over time with different CAT concentrations. Low concentrations up to 0.0025 mg/mL CAT (Graph A) show no significant effect on the ABTS* production. At higher concentrations from 0.015 mg/mL upwards (Graph B), the ABTS* production is reduced indicating that the competition with CAT became measurable

6.3. Catalysis in beads

A major advantage of Raman microscopy is the ability to map an excerpt of the field of view and get spectral information for each point. This was used to monitor the specific ABTS* intensities in a reaction environment where enzymes are immobilized in agarose beads. Throughout these experiments HRP will still be present in solution, whilst GOX is immobilized in agarose beads of low density (white in the microscope) and CAT is immobilized in agarose beads of high density (black beads in the microscope).

6. Enzymatic catalysis

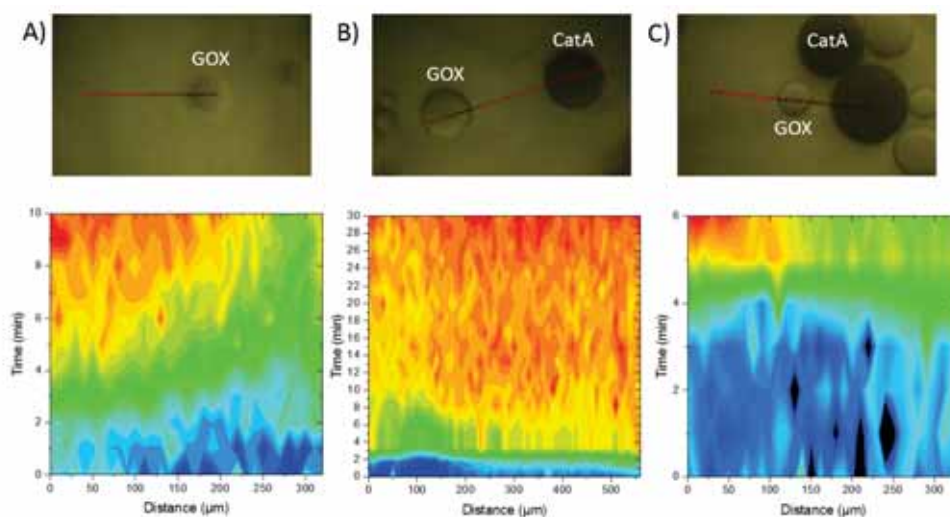


Figure 6.13.: Line scans of enzyme loaded beads in HRP solution and the corresponding increase of ABTS* signal (blue < red) for different arrangements of the beads. Pure beads of GOX (A), beads of GOX and CAT far away from each other (B) and beads of GOX and CAT in close proximity (C).

Figure 6.13 shows a line mapping of three different scenarios. In the first case only GOX beads were used and the signal measured over time (Figure 6.13A). The evolution of the signal shows a progressive increase over time within the line scan. Only the measuring points on the bead show a very slow increase. This is somewhat counterintuitive, as this point should be the highest turnover rate of ABTS, since GOX is needed for the creation of H_2O_2 . The reason for this anomaly could be of a technical nature. Due to the higher density of the bead, the focus point will be changed and the scattering of the agarose will lower the effective laser intensity.

In the second configuration (Figure 6.13B) CAT loaded beads were introduced and the signal was measured between two beads with a distance of several

6.4. Possible implementation of SERS

hundred micrometer to each other. In these cases the distance is too big and the signal increases evenly since the H_2O_2 will be consumed by the HRP in solution before it can diffuse to the CAT loaded bead.

Once the distance between the GOX and the CAT bead is reduced, GOX and CAT compete and less ABTS* is formed. Figure 6.13C shows a bead loaded with GOX with two very close CAT loaded beads on one side. In this configuration the ABTS* signal can be detected on the side pointing away from the CAT beads but in the void between the two beads very little to no ABTS is formed due to the competition of CAT. It must be noted that neither reaction will have reached a steady state, and once formed ABTS* will diffuse throughout the solution. Therefore it will be possible to eventually detect ABTS* everywhere.

6.4. Possible implementation of SERS

Finally, we aimed to extend the use of Raman spectroscopy towards SERS. For that purpose we used CTAC stabilized AuNPs of 70 nm in diameter, synthesized by Guillermo González-Rubio, and self assembled them on previously treated microscope slides.¹⁸⁶ The synthesis was not the focus of this work and initial experiments were done using a method previously reported in the dissertation of Andrea La Porta.¹⁸⁷ Briefly, glass slides were treated with 70% H_2SO_4 and subsequently immersed in a 6 μM solution of AuNPs

6. Enzymatic catalysis

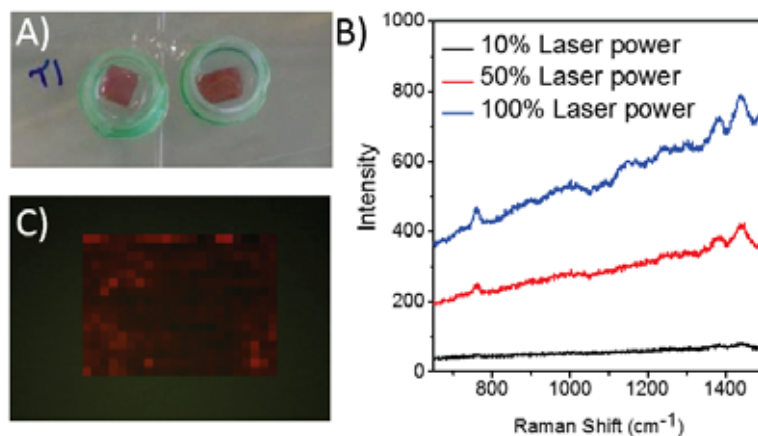


Figure 6.14.: A) Picture of the glass slide after treatment with AuNPs. The particles are immobilized on a glass slide which is then placed in a self-made container for roughly 500 μL of reaction solution. B) SERS background at different laser powers (785 nm) at 1s exposure time under 10x magnification. C) Mapping of the background shows homogeneous distribution of the signal. The signal is nominated to 1.

for 30 min. The residing AuNPs were washed off and the remaining AuNPs on the slide were used as SERS substrate (Figure 6.14A). The substrates generally showed a low background and an even distribution of the SERS signal as shown in Figure 6.14.

As a proof of concept we elected to use pyruvate kinase as the enzyme - examining the formation of benzaldehyde from benzyl amine whilst pyruvate reacts to form alanine (Figure 6.15A inset). This was conducted as a precursor to inclusion in a cascade reaction with a second enzyme to transform the aldehyde to an alcohol. However, to see if the detection of either benzyl amine, benzaldehyde or benzyl alcohol is possible, the SERS signal of each compound was recorded and plotted in Figure 6.15. All compounds show a SERS signal and indeed a difference can be detected. For the first reaction of

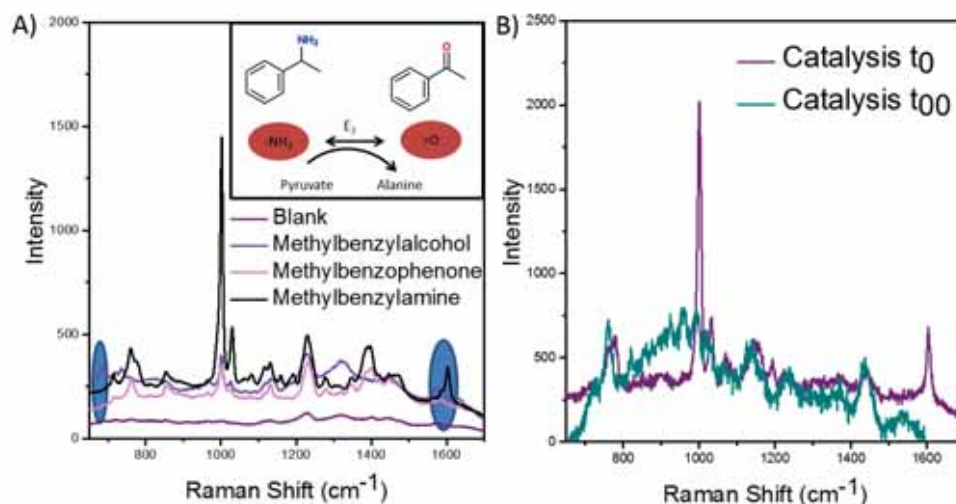


Figure 6.15.: A) SERS spectra of benzyl amine, benzyl alcohol, benzaldehyde. Inset: Enzymatic reaction under investigation. Pyruvate kinase will transform benzyl amine to benzaldehyde using pyruvate which reacts to form alanine. B) SERS spectra of the reaction mixture before (t_0) and after (t_∞).

the transformation of the amine to the aldehyde, the amine shows a unique band at 1600 cm^{-1} which could, in principle, be used to monitor the reaction. In the next step the reaction was run in a controlled environment and the mixture was checked before (t_0) and after (t_∞) to see if other compounds in the reaction mixture will interfere with the signal. Figure 6.15 shows both spectra before and after the reaction, indicating that the band at 1600 cm^{-1} can indeed be used to monitor the reaction in future experiments. This reaction is not a simple process and involves complicated reaction conditions. Therefore this work is presented here as a proof of concept with continuation required in order to develop a SERS sensor to follow the reaction set out in the future work section.

6.5. Conclusion

In this chapter it was shown that Raman spectroscopy can be used as a tool to monitor (quantitatively) enzymatic cascade reactions by following the intense Raman signal of ABTS*. ABTS*, which is created from ABTS in the presence of HRP and H₂O₂, is produced in a cascade reaction coupled to other enzymatic reactions of GOX or DAAO. The oxidation of glucose and D-alanine were observed through real time monitoring in both systems. The examination of the process at different concentrations ultimately led to a determination of the reaction rate at different substrate concentrations. Using these, we calculated the Michaelis Menten constant for both enzymes. The correlation between theory and results is not satisfying yet, which can be seen by the significant error for the fit. Additionally the same data was analyzed using the Lineweaver and Burk method which also gives values for K_M and V_{max} . The comparison of both fitting methods shows fairly good agreement of the values with a small discrepancy for all but one value. In future experiments, more measuring points for different substrate concentrations and reorganization of the setup could help to improve the results. Especially the delay between the start of the measurement and the mixing of the reactants should be minimized.

In a last set of experiments we extend the technique towards SERS and synthesized substrates with AuNPs on which enzymatic reaction could take place in solution. We tested the possibility to detect benzyl amine, benzalde-

hyde and benzyl alcohol. There was not enough time during this work to finish the experiments and thus this chapter only shows preliminary results. However the direction shown is very promising and shows great potential for future work. In a first set of experiments the enzymatic reaction could be monitored in real time over the substrate by monitoring the disappearance of the band at 1600 cm^{-1} . In a second step this reaction could be coupled to another enzyme to form the alcohol out of the aldehyde and again monitor this by SERS.

Ultimately we could imagine an extension of this work to immobilize the enzyme in beads again, look at the spatial distribution and load the beads with AuNPs as well. This could possibly give hints to the transition states of the substrate.

7 Chapter 7.

Conclusion and Outlook

Metal nanoparticle - polymer composite materials are widely used in many different forms and aspects to advance urgent questions in research. As briefly introduced in Chapter 2, the combination of metal nanoparticles with polymers offers a huge variety of options from nanoclusters, single nanoparticles covered and stabilized with polymers up to micron-sized polymeric structures functionalized with metal nanoparticles. The focus of this thesis has been on the combination of AuNPs with polymeric micro structures. In total, three different systems have been introduced:

- The first system was based on thermoresponsive nanogels attached with evenly distributed and in-situ grown AuNPs (Chapter 3). These AuNP impregnated nanogels have subsequently been investigated for applications as a delivery medium for two different anti-cancer drugs (Chapter 4), and also as a potential SERS sensor (Chapter 5).
- In a second system, the combination of PLGA microgels loaded with with hydrophobic AuNPs (Chapter 3) tested to examine their capability

7. Conclusion and Outlook

for SERS sensing (Chapter 5).

- The last particle system could not be completely embraced due to time constraints. The idea was to load agarose beads with enzymes and AuNPs for SERS studies (Chapter 6). The work in this thesis however, did not yet reach this task yet and dealt mainly with resonance Raman studies and an outlook to implement SERS measurements.

The thermoresponsive nanogels were synthesized using PEGMA based monomers to ensure bio-compatibility and to have the ability to fine tune the LCST. The nanogels were synthesized using a polymerization precipitation method and a new method was then developed to grow AuNPs in-situ. A mixture of HAuCl_4 and NaBr was used to grow previously synthesized small AuNPs with formaldehyde at high pH. This method was chosen to ensure a free gold surface (avoiding the possible influence of stabilizing ligands) for better drug delivery or SERS applications.

To examine the robust nature of the drug delivery system, two anti-cancer drugs were chosen which exhibited different physicochemical properties. For further functionalization, the nanogels were additionally wrapped with two different polyelectrolytes (alginate or poly-L-arginine). The polyelectrolytes offer further stability, alter the release profile and produce different modifications in the thermoresponsive nanogels. It was shown that pH, glutathione concentration, heat and NIR-light triggers the release and that the drug is successfully delivered to cells.

In addition, the nanogels were also examined as potential SERS substrates. It was shown that the nanogels can indeed be used to detect crystal violet and Doxo. However, the SERS intensity was not enough to follow the Doxo release inside cells. The signal, using the 633 nm laser as excitation was not sufficient enough to overcome the high fluorescence background and thus the signal to noise ratio was very poor. To improve the response, one possibility could be to vary the AuNP synthesis to improve the SERS enhancement factor, by example - using a modified procedure to produce AuNSs. As discussed previously, such particles may then offer improved enhancement with the 785 nm laser through greater resonant SERS with the particles and suppression of the auto fluorescence of the cells which would be less dominant at this wavelength.

To develop this procedure further, it would possible to modify the polymeric scaffold and add extra functionalities. Recent work by other groups has shown, for example, degradation upon pH changes or or changes of [GSH].¹⁰⁰ To the best of the authors knowledge, this systems have yet to be combined with metal nanoparticles. The implementation of such a system would not, however, be straightforward since nanoparticles inside the gel would most likely hinder the degradation process and maybe completely suppress it. That is not to say that it is not worthy of investigation, as exploitation of this field would lead to a variety of different systems and applications. Another significant question, raised by the work in this thesis, is the mech-

7. Conclusion and Outlook

anism of drug release using thermoresponsive microgels. Depending on the nature of the monomer, the mechanism and thus the path for the drug release will change drastically. PEGMA based monomers seem to favor a drug release upon heating, as shown in Chapter 4. The polymer collapses above the LCST and, much like a sponge, will then squeeze out the drug.^{35,107} Switching the monomer towards pNIPAM however seems to encapsulate the drug differently and favors release through diffusion below the LCST and encapsulate molecules above it.^{50,188} To my knowledge there is no study to compare both polymers in the context of drug delivery and it would be interesting to know more about it for the design of future experiments.

PLGA as a polymeric matrix was chosen due to its wide use in biomedical application. The polymer itself is of synthetic nature but still FDA approved and biodegradable. Due to these enticing properties it is widely used as a scaffold for tissue growth, and as microgels for drug delivery systems. In cooperation with the group of Prof. Lahann from the University of Michigan, mainly SERS encoded AuNSs, but also other particles, were implemented in high quantities using electro hydrodynamic co-jetting. The resulting multi-compartmental structures were analyzed using 3D-SERS tomography and tested on their long term stability under light. In contrast to fluorescence, these systems could be very interesting to monitor scaffold degradation in situ. The SERS signal is stable under UV-irradiation and additionally should

have a better penetration depth when using a 785 nm laser. Two scenarios are imaginable, one would be the labeling of the PLGA scaffold, the growth of a tissue, and the observation of the long term degradation of the scaffold. This could be realized in a controlled environment and then ultimately in animals. The second scenario would be additional labeling of the cells with SERS encoded AuNSs. It is well known that the microenvironment of tumor metastases plays a crucial role in the spread throughout the body. Especially the cell-cell interactions between tumor cells and associated fibroblast, which seems to be important for growth.¹⁸⁹ In this context, PLGA scaffolds could be used to simulate such an environment with SERS labeled cells to monitor their interaction and maybe changes in the micro-environment.

Finally enzymatic cascade reactions have been followed by resonance Raman spectroscopy in solution. This work has been conducted in collaboration with Dr. Fernando López-Gallego. ABTS reacts in the presence of H₂O₂ and HRP to form ABTS*, which shows a characteristic resonance Raman band at 1600 cm⁻¹. Under selected conditions this reaction can be used to follow an upstream connected enzyme reaction of GOX or DDO. Introduction of a third enzyme (CatA), which remains in concurrence to HRP, leads to inhibition of ABTS* production which was monitored as well. The concept was extended to enzymes immobilized in agarose beads. Finally, first steps towards including SERS were done, by testing SERS substrates

7. Conclusion and Outlook

with the proof of concept reaction of benzyl amine to benzyl alcohol with the intermediate of a benzaldehyde. Results show that it is possible to distinguish the three compounds. In future work, it would be interesting to follow the actual enzymatic reaction in situ. Furthermore, once the SERS system is established, it is easy to imagine that the concept could be expanded to more enzymes and substrates. Immobilization of AuNPs inside the agarose gel next to enzymes could also be interesting and reveal, in the best cases, insights about different transition states of either the enzyme or the substrate. The outcome of work in this direction is not clear since the enzyme - metal interaction could play an important role and maybe even prevent the system from working. However further work in this direction would be interesting and could lead to a new methods to monitor enzymatic reactions.

In a more general outlook, the knowledge gained throughout the work for this PhD would be useful and a good starting point for the development of new bio-imaging systems.¹⁹⁰ As mentioned previously, the use of three dimensional SERS imaging could be an interesting tool to monitor tissue degradation as well as cell migration in tumors. The method however, is not limited for biomedical applications and could be extended to a general method of monitoring catalysis or for polymer characterization. Another interesting aspect would be to work towards a more quantitative SERS system. In general, quantitative SERS measurements remain challenging but would

work great as sensing platform. Controlled aggregation and extensive use of statistics led to a variety of quantitative SERS measurements systems.¹⁹¹⁻¹⁹⁴ However, creating a quantitative sensing tool for in-situ measurements which could be used to study release kinetics of drugs or monitor biomolecule in real time would be a great goal to achieve.

A XPS measurements

XPS experiments were performed in a SPECS Sage HR 100 spectrometer with a non monochromatic X ray source (Mg $K\alpha$ line of 1253.6 eV energy and 250 W). The samples were placed perpendicular to the analyzer axis and calibrated using the $3d_{5/2}$ line of Ag with a full width at half maximum (FWHM) of 1.1 eV. An electron flood gun was used to compensate for charging during XPS data acquisition.

The selected resolution for the survey and high resolution spectra were 30 and 15 eV of Pass Energy and 0.5 and 0.15 eV/step, respectively. All measurements were made in an ultra high vacuum (UHV) chamber at a pressure below 5×10^{-8} mbar.

In the fittings, Gaussian Lorentzian functions were used (after a Shirley background correction), where the FWHM of all peaks were constrained while the peak positions and areas were set free.

A. XPS measurements

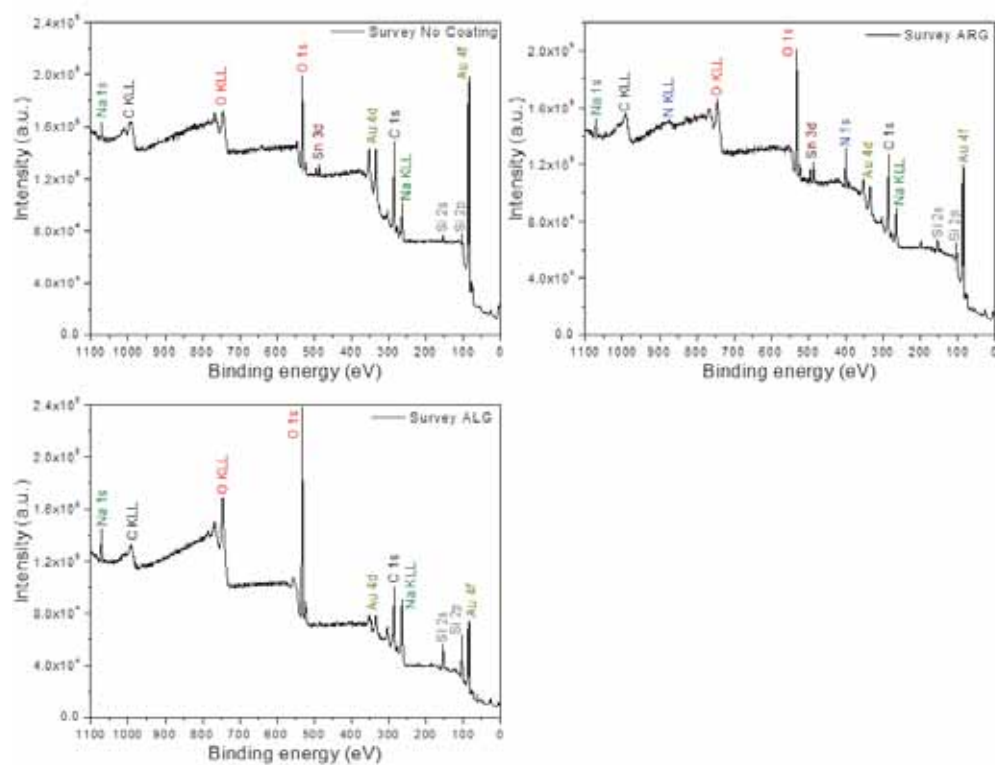


Figure A.1.: General survey spectra. The photoelectron and Auger peaks from sodium, carbon, oxygen, tin, nitrogen, silicon and gold were detected.

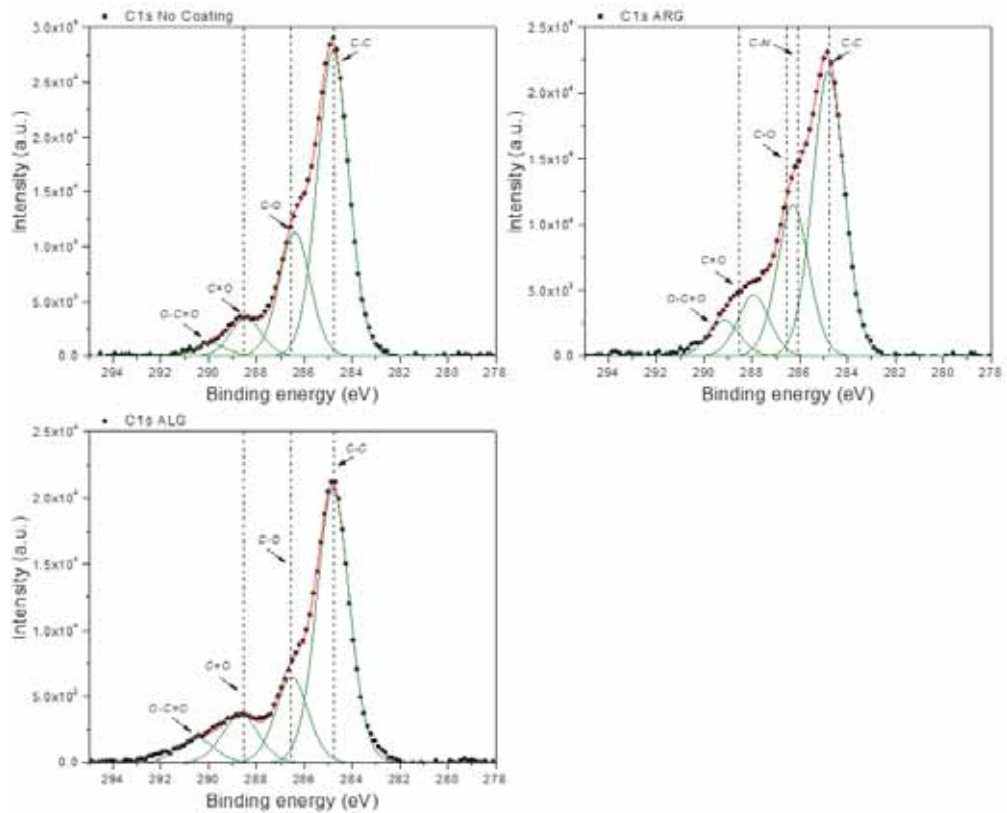


Figure A.2.: Shown in the spectra are the expected positions of the C C bonds at 285.0 eV, C N bonds at around 286.0 eV, and C-O, C=O and O-C=O bonds at around 286.5, 288.6 and 290.5 eV, respectively.

A. XPS measurements

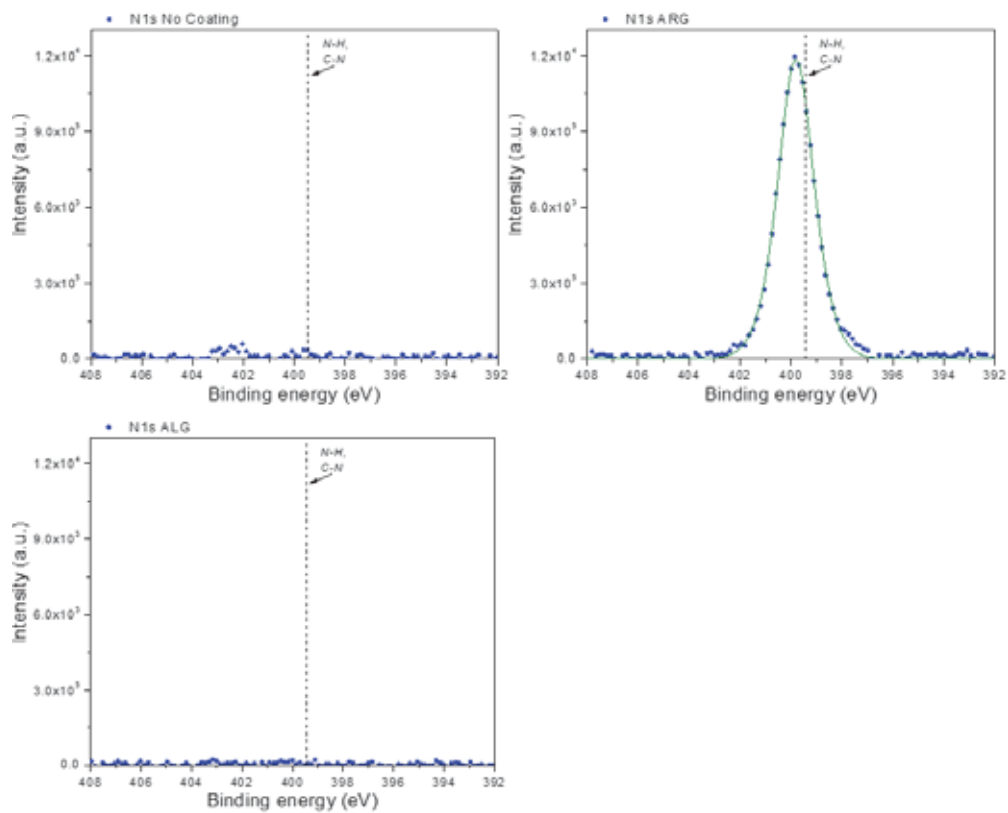


Figure A.3.: XPS spectra at the region where the N 1s signal is expected. Only the sample with poly-L-arginine showed nitrogen signal, with the N 1s peak position at around 399.7 eV, which is attributed to N-H, C-N bonds.

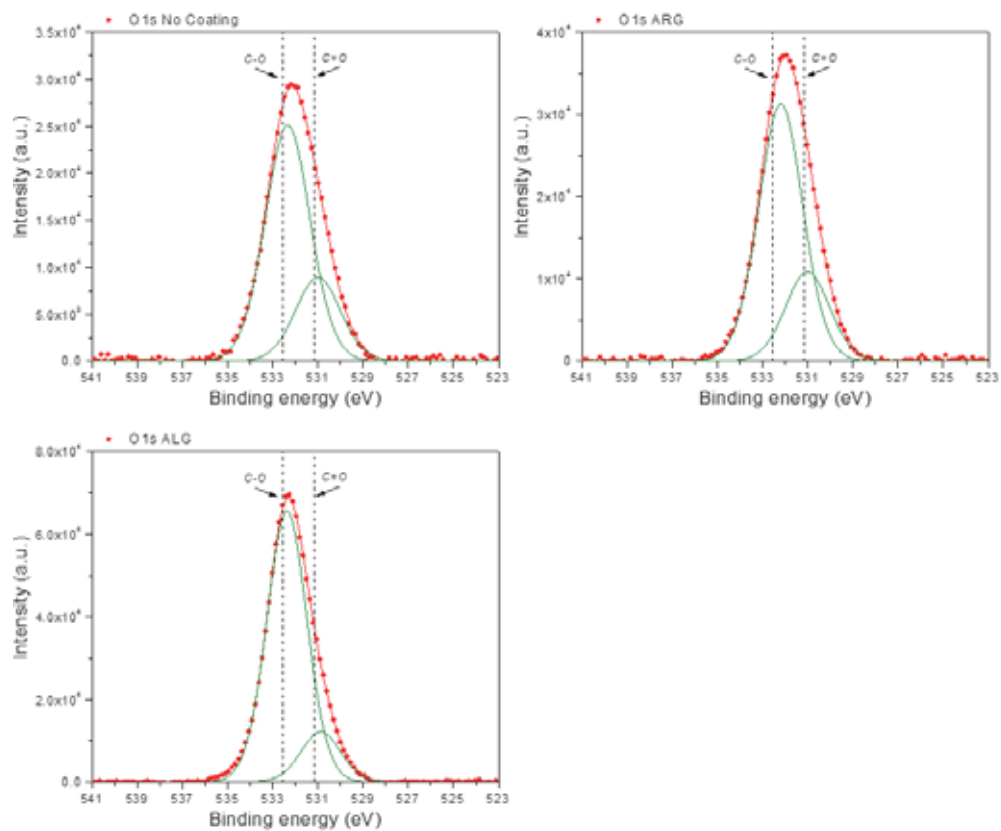


Figure A.4.: Shown in the spectra are the expected positions of the C=O bonds at around 531.2 eV and the C O bonds at around 532.5 eV.

B Publications and conference contributions

B.1. Publications

- **Spatial Analysis of Metal-PLGA Hybrid Microstructures Using 3D SERS Imaging**
M.S. Strozyk, D. Jimenez de Aberasturi, J.V. Gregory, M. Brust, J. Lahnann, L.M. Liz-Marzán
Adv. Funct. Mater. **2017**, *27*, 1701626
- **Biocompatible, Multiresponsive Nanogel Composites for Co-delivery of Anti-angiogenic and Chemotherapeutic Agents**
M.S. Strozyk, S. Carregal-Romero, M. Henriksen-Lacey, M. Brust, L.M. Liz-Marzán
Chem. Mater. **2017**, *29*, 2303-2313

B.2. Conferences

- **03/2017** NanoSpain 2017, San Sebastian (Spain)
Poster Title: Thermosensitive nanogels with multiple anti-tumour associated effects
- **11/2016** International Conference on 'Self-Assembly in Confined Spaces', San Sebastian (Spain)
Poster Title: 'SERS Encoded Particles with Antibody Labeling for advanced Cell Tracking'
- **10/2016** HYMADE project meeting, Vienna (Austria)
Workshop on Thin Films and Student Training: Entrepreneurship and Business Models
- **03/2016** Europt[r]ode XII, Graz (Austria)
Poster Title: 'Gold loaded microgels as SERS devices for biological applications'
- **03/2015** Fourth international conference on 'Multifunctional, Hybrid and Nanomaterials', Sitges (Spain)
Poster Title: 'Hydrogel supported Au and Au/Pd- clusters'

Bibliography

- [1] Matthias Karg and Thomas Hellweg. New "smart" poly(NIPAM) microgels and nanoparticle microgel hybrids: Properties and advances in characterisation. *Current Opinion in Colloid and Interface Science*, 14(6):438–450, 2009.
- [2] Xiaohua Huang and Mostafa A. El-Sayed. Gold nanoparticles: Optical properties and implementations in cancer diagnosis and photothermal therapy. *Journal of Advanced Research*, 1(1):13–28, 2010.
- [3] Roy Shenhar, Tyler B. Norsten, and Vincent M. Rotello. Polymer-mediated nanoparticle assembly: Structural control and applications. *Advanced Materials*, 17(6):657–669, 2005.
- [4] Krishnendu Saha, Sarit S. Agasti, Chaekyu Kim, Xiaoning Li, and Vincent M. Rotello. Gold nanoparticles in chemical and biological sensing. *Chemical Reviews*, 112(5):2739–2779, 2012.
- [5] Suljo Linic, Phillip Christopher, and David B. Ingram. Plasmonic-metal nanostructures for efficient conversion of solar to chemical energy. *Nature Materials*, 10(12):911–921, 2011.
- [6] P. V. Kamat. Meeting the clean energy demand: Nanostructure Architectures for Solar Energy Conversion. *Phys. Chem.*, 392:2834–2860, 2007.
- [7] John Turkevich, Peter Cooper Stevenson, and James Hillier. a Study of the Nucleation and Growth Processes IN the Synthesis of Colloidal Gold. *Discuss. Faraday Soc.*, 55:55–75, 1951.

Bibliography

- [8] Stacy Jones, Avijit Pramanik, Carrie Sweet, Anthony Keyes, Salma Begum, Aruna Vangra, Hongtal Yu, Peter P. Fu, and Paresh Chandra Ray. Environmental Carcinogenesis and Ecotoxicology Reviews Recent progress on the development of anisotropic gold nanoparticles : Design strategies and growth mechanism. *Journal of Environmental Science and Health, Part C*, 35(1):47–66, jan 2017.
- [9] Santosh Kumar Meena, Sirin Celiksoy, Philipp Schäfer, Andreas Henkel, Carsten Sönnichsen, and Marialore Sulpizi. The role of halide ions in the anisotropic growth of gold nanoparticles: a microscopic, atomistic perspective. *Phys. Chem. Chem. Phys.*, 18(19):13246–13254, may 2016.
- [10] Ana Sánchez-Iglesias, Naomi Winckelmans, Thomas Altantzis, Sara Bals, Marek Grzelczak, and Luis M. Liz-Marzán. High-yield seeded growth of monodisperse pentatwinned gold nanoparticles through thermally induced seed twinning. *Journal of the American Chemical Society*, 139(1):107–110, jan 2017.
- [11] Na Li, Pengxiang Zhao, and Didier Astruc. Anisotropic gold nanoparticles: Synthesis, properties, applications, and toxicity. *Angewandte Chemie - International Edition*, 53(7):1756–1789, 2014.
- [12] Sora Lim, Ji Eun Song, Ju A. La, and Eun Chul Cho. Gold nanospheres assembled on hydrogel colloids display a wide range of thermoreversible changes in optical bandwidth for various plasmonic-based color switches. *Chemistry of Materials*, 26(10):3272–3279, 2014.
- [13] Cheng An J Lin, Ralph A. Sperling, Jimmy K. Li, Ting Ya Yang, Pei Yun Li, Marco Zanella, Walter H. Chang, and Wolfgang J. Parak. Design of an amphiphilic polymer for nanoparticle coating and functionalization. *Small*, 4(3):334–341, 2008.
- [14] R. A. Sperling and W. J. Parak. Surface modification, functionalization and bioconjugation of colloidal inorganic nanoparticles. *Philosophical Transactions of the Royal Society A: Mathematical, Physical and Engineering*

- Sciences*, 368(1915):1333–1383, 2010.
- [15] Ana Sánchez-Iglesias, Marek Grzelczak, Thomas Altantzis, Bart Goris, Jorge Pérez-Juste, Sara Bals, Gustaaf Van Tendeloo, Stephen H. Donaldson, Bradley F. Chmelka, Jacob N. Israelachvili, and Luis M. Liz-Marzán. Hydrophobic interactions modulate self-assembly of nanoparticles. *ACS Nano*, 6(12):11059–11065, 2012.
- [16] Kyle W Smith, Hangqi Zhao, Hui Zhang, Ana Sánchez-Iglesias, Marek Grzelczak, Yumin Wang, Wei Shun Chang, Peter Nordlander, Luis M. Liz-Marzán, and Stephan Link. Chiral and Achiral Nanodumbbell Dimers: The Effect of Geometry on Plasmonic Properties. *ACS Nano*, 10(6):6180–6188, 2016.
- [17] Marek Grzelczak, Ana Sánchez-Iglesias, Hamed Heidari Mezerji, Sara Bals, Jorge Pérez-Juste, and Luis M. Liz-Marzán. Steric hindrance induces crosslike self-assembly of gold nanodumbbells. *Nano Letters*, 12(8):4380–4384, 2012.
- [18] Dorleta Jimenez De Aberasturi, Ana B. Serrano-Montes, Judith Langer, Malou Henriksen-Lacey, Wolfgang J. Parak, and Luis M. Liz-Marzán. Surface Enhanced Raman Scattering Encoded Gold Nanostars for Multiplexed Cell Discrimination. *Chemistry of Materials*, 28(18):6779–6790, 2016.
- [19] E Piskin, a Tuncel, a Denizli, and H Ayhan. Monosize microbeads based on polystyrene and their modified forms for some selected medical and biological applications. *Journal of biomaterials science. Polymer edition*, 5(5):451–471, 1994.
- [20] Rubén Ahijado-Guzmán, Paulino Gómez-Puertas, Ramón A. Alvarez-Puebla, Germán Rivas, and Luis M. Liz-Marzán. Surface-enhanced Raman scattering-based detection of the interactions between the essential cell division FtsZ protein and bacterial membrane elements. *ACS Nano*, 6(8):7514–7520, 2012.

Bibliography

- [21] Yunxing Li, Yunfei Pan, Lili Zhu, Zhaoqun Wang, Dongmeng Su, and Gi Xue. Facile and controlled fabrication of functional gold nanoparticle-coated polystyrene composite particle. *Macromolecular Rapid Communications*, 32(21):1741–1747, 2011.
- [22] Jian Gong, Xihong Zu, Wei Mu, and Yulin Deng. In situ self-assembly synthesis of gold nanoparticle arrays on polystyrene microspheres and their surface plasmon resonance. *Colloid and Polymer Science*, 291(1):239–244, 2012.
- [23] Ana B. Serrano-Montes, Judith Langer, Malou Henriksen-Lacey, Dorleta Jiménez De Aberasturi, Diego M. Solís, José M. Taboada, Fernando Obelleiro, Kadir Sentosun, Sara Bals, Ahmet Bekdemir, Francesco Stellacci, and Luis M. Liz-Marzán. Gold Nanostar-Coated Polystyrene Beads as Multifunctional Nanoprobes for SERS Bioimaging. *Journal of Physical Chemistry C*, 120(37):20860–20868, 2016.
- [24] Bernat Mir-Simon, Judit Morla-Folch, Patricia Gisbert-Quilis, Nicolas Pazos-Perez, Hai-nan Xie, Neus G Bastús, Víctor Puentes, Ramon A Alvarez-Puebla, and Luca Guerrini. SERS efficiencies of micrometric polystyrene beads coated with gold and silver nanoparticles: the effect of nanoparticle size. *Journal of Optics*, 17(11):114012, 2015.
- [25] Edwin Donath, Gleb B Sukhorukov, Frank Caruso, Sean a Davis, and Helmuth Möhwald. Novel Hollow Polymer Shells by Colloid Templated Assembly of Polyelectrolytes. *Angew Chem Int Ed Engl*, 37(16):2201–2205, 1998.
- [26] Zhifei Dai, Andreas Voigt, Stefano Leporatti, Edwin Donath, Lars Dähne, and Helmuth Möhwald. Layer-by-Layer Self-Assembly of Polyelectrolyte. *Advanced Materials*, 13(17):1339–1342, 2001.
- [27] F. Caruso, M. Spasova, V. Salgueiriño-Maceira, and L. M. Liz-Marzán. Multilayer assemblies of silica-encapsulated gold nanoparticles on decomposable colloid templates. *Advanced Materials*, 13(14):1090–1094,

- 2001.
- [28] Frank Caruso, Rachel A. Caruso, and Helmuth Möhwald. Nanoengineering of Inorganic and Hybrid Hollow Spheres by Colloidal Templating. *Science*, 282:1111–1114, 1998.
- [29] Markus Ochs, Susana Carregal-Romero, Joanna Rejman, Kevin Braeckmans, Stefaan C. De Smedt, and Wolfgang J. Parak. Light-addressable capsules as caged compound matrix for controlled triggering of cytosolic reactions. *Angewandte Chemie - International Edition*, 52(2):695–699, 2013.
- [30] Wen-Fei Dong, Gleb B Sukhorukov, and Helmuth Mohwald. Enhanced Raman imaging and optical spectra of gold nanoparticle doped microcapsules. *Physical Chemistry Chemical Physics*, 5(14):3003–3012, 2003.
- [31] Hirenkumar K. Makadia and Steven J. Siegel. Poly Lactic-co-Glycolic Acid (PLGA) as biodegradable controlled drug delivery carrier. *Polymers*, 3(3):1377–1397, 2011.
- [32] Joerg Lahann. Recent progress in nano-biotechnology: Compartmentalized micro- and nanoparticles via electrohydrodynamic co-jetting. *Small*, 7(9):1149–1156, 2011.
- [33] Malte S. Strozyk, Dorleta Jimenez de Aberasturi, Jason V. Gregory, Mathias Brust, Joerg Lahann, and Luis M. Liz-Marzán. Spatial Analysis of Metal-PLGA Hybrid Microstructures Using 3D SERS Imaging. *Advanced Functional Materials*, 27(33), 2017.
- [34] Dong Woo Lim, Sangyeul Hwang, Oktay Uzun, Francesco Stellacci, and Joerg Lahann. Compartmentalization of gold nanocrystals in polymer microparticles using electrohydrodynamic co-jetting. *Macromolecular Rapid Communications*, 31(2):176–182, 2010.
- [35] Manuel Pernia Leal, Andrea Torti, Andreas Riedinger, Rocco La Fleur, Daniela Petti, Roberto Cingolani, Riccardo Bertacco, and Teresa Pellegrino. Controlled release of doxorubicin loaded within magnetic

Bibliography

- thermo-responsive nanocarriers under magnetic and thermal actuation in a microfluidic channel. *ACS Nano*, 6(12):10535–10545, 2012.
- [36] Andrij Pich, Anne Tessier, Volodymyr Boyko, Yan Lu, and Hans-Juergen P. Adler. Synthesis and Characterization of Poly(vinylcaprolactam)-Based Microgels Exhibiting Temperature and pH-Sensitive Properties. *Macromolecules*, 39:7701–7707, 2006.
- [37] J. F. Lutz and Ann Hoth. Preparation of ideal PEG analogues with a tunable thermosensitivity by controlled radical copolymerization of 2-(2-methoxyethoxy)ethyl methacrylate and oligo(ethylene glycol) methacrylate. *Macromolecules*, 39(2):893–896, 2006.
- [38] R H Pelton and P Chibante. Preparation of aqueous latices with N-isopropylacrylamide. *Colloids and Surfaces*, 20(3):247–256, 1986.
- [39] Malte S. Strozyk, Munish Chanana, Isabel Pastoriza-Santos, Jorge Pérez-Juste, and Luis M. Liz-Marzán. Protein/polymer-based dual-responsive gold nanoparticles with pH-dependent thermal sensitivity. *Advanced Functional Materials*, 22(7):1436–1444, 2012.
- [40] Ming Qiang Zhu, Li Qiong Wang, Gregory J. Exarhos, and Alexander D Q Li. Thermosensitive Gold Nanoparticles. *Journal of the American Chemical Society*, 126(9):2656–2657, 2004.
- [41] Erik W. Edwards, Munish Chanana, Dayang Wang, and Helmuth Möhwald. Stimuli-responsive reversible transport of nanoparticles across water/oil interfaces. *Angewandte Chemie - International Edition*, 47(2):320–323, 2008.
- [42] Maria Molina, Mazdak Asadian-Birjand, Juan Balach, Julian Bergueiro, Enrico Miceli, and Marcelo Calderon. Stimuli-responsive nanogel composites and their application in nanomedicine. *Chemical Society Reviews*, 44(17):6161–6186, 2015.
- [43] Robina Begum, Khalida Naseem, and Zahoor H. Farooqi. A review of responsive hybrid microgels fabricated with silver nanoparticles:

- synthesis, classification, characterization and applications. *Journal of Sol-Gel Science and Technology*, 77(2):497–515, 2016.
- [44] Susana Carregal-Romero, Niklaas J. Buurma, Jorge Pérez-Juste, Luis M. Liz-Marzán, and Pablo Hervés. Catalysis by Au@pNIPAM nanocomposites: Effect of the cross-linking density. *Chemistry of Materials*, 22(10):3051–3059, 2010.
- [45] Jorge Pérez-Juste, Isabel Pastoriza-Santos, and Luis M. Liz-Marzán. Multifunctionality in metal@microgel colloidal nanocomposites. *Journal of Materials Chemistry A*, pages 20–26, 2013.
- [46] Rafael Contreras-Cáceres, Jessica Pacifico, Isabel Pastoriza-Santos, Jorge Pérez-Juste, Antonio Fernández-Barbero, and Luis M. Liz-Marzán. Au@pNIPAM thermosensitive nanostructures: Control over shell cross-linking, overall dimensions, and core growth. *Advanced Functional Materials*, 19(19):3070–3076, 2009.
- [47] Rafael Contreras-Cáceres, Isabel Pastoriza-Santos, Ramón A. Alvarez-Puebla, Jorge Pérez-Juste, Antonio Fernández-Barbero, and Luis M. Liz-Marzán. Growing Au/Ag nanoparticles within microgel colloids for improved surface-enhanced Raman scattering detection. *Chemistry - A European Journal*, 16(31):9462–9467, 2010.
- [48] Cristina Fernández-López, Carlos Pérez-Balado, Jorge Pérez-Juste, Isabel Pastoriza-Santos, Ángel R. de Lera, and Luis M. Liz-Marzán. A general LbL strategy for the growth of pNIPAM microgels on Au nanoparticles with arbitrary shapes. *Soft Matter*, 8(15):4165, 2012.
- [49] Nicolas Sanson and Jutta Rieger. Synthesis of nanogels/microgels by conventional and controlled radical crosslinking copolymerization. *Polymer Chemistry*, 1(7):965, 2010.
- [50] Ramon A. Álvarez-Puebla, Rafael Contreras-Cáceres, Isabel Pastoriza-Santos, Jorge Pérez-Juste, and Luis M. Liz-Marzán. Au@pNIPAM colloids as molecular traps for surface-enhanced, spectroscopic, ultra-

Bibliography

- sensitive analysis. *Angewandte Chemie - International Edition*, 48(1):138–143, 2009.
- [51] Matthias Karg, Isabel Pastoriza-Santos, Jorge Pérez-Juste, Thomas Hellweg, and Luis M. Liz-Marzán. Nanorod-coated PNIPAM microgels: Thermoresponsive optical properties. *Small*, 3(7):1222–1229, 2007.
- [52] Mallika Das, Nicolas Sanson, Dnniele Fava, and Eugenia Kumacheva. Microgels loaded with gold nanorods: Photothermally triggered volume transitions under physiological conditions. *Langmuir*, 23(1):196–201, 2007.
- [53] Garima Agrawal, Marco Philipp Schürings, Patrick van Rijn, and Andrij Pich. Formation of catalytically active gold–polymer microgel hybrids via a controlled in situ reductive process. *Journal of Materials Chemistry A*, 1(42):13244, 2013.
- [54] Gustav Mie. Beiträge zur Optik trüber Medien, speziell kolloidaler Metallösungen. *Annalen der Physik*, 330(3):377–445, 1908.
- [55] R. Gans. Über die Form ultramikroskopischer Silberteilchen. *Annalen der Physik*, 352(10):270–284, 1915.
- [56] Viktor Myroshnychenko, Enrique Carbó-Argibay, Isabel Pastoriza-Santos, Jorge Pérez-Juste, Luis M. Liz-Marzán, and F. Javier García de Abajo. Modeling the Optical Response of Highly Faceted Metal Nanoparticles with a Fully 3D Boundary Element Method. *Advanced Materials*, 20(22):4288–4293, 2008.
- [57] U. Kreibig and M. Vollmer. *Optical Properties of Metal Clusters*. Springer-Verlag Berlin Heidelberg, 25 edition, 1995.
- [58] Rubén Ahijado-Guzmán, Janak Prasad, Christina Rosman, Andreas Henkel, Lydia Tome, Dirk Schneider, Germán Rivas, and Carsten Sönnichsen. Plasmonic Nanosensors for Simultaneous Quantification of Multiple Protein-Protein Binding Affinities. *Nano Letters*, 14(10):5528–5532, oct 2014.

- [59] Irene Ament, Janak Prasad, Andreas Henkel, Sebastian Schmachtel, and Carsten Sönnichsen. Single Unlabeled Protein Detection on Individual Plasmonic Nanoparticles. *Nano Letters*, 12(2):1092–1095, feb 2012.
- [60] Ming Li, Scott K. Cushing, Nianqiang Wu, C. Ma, J. Li, Y. Li, M. Shi, W. Tan, R. Yang, B. Zhao, M. J. Natan, and K. H. Lee. Plasmon-enhanced optical sensors: a review. *The Analyst*, 140(2):386–406, dec 2015.
- [61] Leonardo Scarabelli, Marc Coronado-Puchau, Juan J. Giner-Casares, Judith Langer, and Luis M. Liz-Marzán. Monodisperse Gold Nanotriangles: Size Control, Large-Scale Self-Assembly, and Performance in Surface-Enhanced Raman Scattering. *ACS Nano*, 8(6):5833–5842, jun 2014.
- [62] P S Kumar, I Pastoriza-Santos, B Rodríguez-González, F J García de Abajo, and L M Liz-Marzán. High-yield synthesis and optical response of gold nanostars. *Nanotechnology*, 19:15606, 2008.
- [63] W. Andrew Murray and William L. Barnes. Plasmonic materials. *Advanced Materials*, 19(22):3771–3782, nov 2007.
- [64] Prashant K. Jain, Kyeong Seok Lee, Ivan H. El-Sayed, and Mostafa A. El-Sayed. Calculated absorption and scattering properties of gold nanoparticles of different size, shape, and composition: Applications in biological imaging and biomedicine. *Journal of Physical Chemistry B*, 110(14):7238–7248, 2006.
- [65] Guillaume Baffou and Romain Quidant. Thermo-plasmonics: using metallic nanostructures as nano-sources of heat. *Laser & Photonics Reviews*, 7(2):171–187, mar 2013.
- [66] Xiang-Qi Wang and Arun S Mujumdar. Heat transfer characteristics of nanofluids: a review. *International Journal of Thermal Sciences*, 46:1–19, 2007.
- [67] Stephan Link and Mostafa A. El-Sayed. Shape and size dependence of radiative, non-radiative and photothermal properties of gold nanocrystals.

Bibliography

- tals. *International Reviews in Physical Chemistry*, 19(3):409–453, 2000.
- [68] E Prodan, C Radloff, Naomi J Halas, and Peter Nordlander. A hybridization model for the plasmon response of complex nanostructures. *Science (New York, N.Y.)*, 302(5644):419–422, 2003.
- [69] P. Nordlander, C. Oubre, E. Prodan, K. Li, and M. I. Stockman. Plasmon hybridization in nanoparticle dimers. *Nano Letters*, 4(5):899–903, 2004.
- [70] M. Fleischmann, P. J. Hendra, and A. J. McQuillan. Raman spectra of pyridine adsorbed at a silver electrode. *Chemical Physics Letters*, 26(2):163–166, 1974.
- [71] David L. Jeanmaire and Richard P. Van Duyne. Surface raman spectro-electrochemistry: Part I. Heterocyclic, aromatic, and aliphatic amines adsorbed on the anodized silver electrode. *Journal of Electroanalytical Chemistry*, 84(1):1–20, 1977.
- [72] M. Grant Albrecht and J. Alan Creighton. Anomalously Intense Raman Spectra of Pyridine at a Silver Electrode. *Journal of the American Chemical Society*, 99(15):5215–5217, 1977.
- [73] Sebastian Schlücker. Surface-enhanced Raman spectroscopy: concepts and chemical applications. *Angewandte Chemie (International ed. in English)*, 53(19):4756–4795, 2014.
- [74] Ramón A. Alvarez-Puebla and Luis M. Liz-Marzán. SERS-based diagnosis and biodetection. *Small*, 6(5):604–610, mar 2010.
- [75] Daniela Drescher and Janina Kneipp. Nanomaterials in complex biological systems: insights from Raman spectroscopy. *Chemical Society reviews*, 41(17):5780–99, sep 2012.
- [76] C.V. Raman and K.S. Krishnan. A New Type of Secondary Radiation. *Nature*, 121(3048):501–502, 1928.
- [77] John R. Ferraro, Kazuo Nakamoto, and Chris W. Brown. Front Matter. In *Introductory Raman Spectroscopy*. Academic Press, London, 2 edition,

2003.

- [78] Ricardo. Aroca. *Surface enhanced vibrational spectroscopy*. Wiley, 2006.
- [79] Paul L. Stiles, Jon A. Dieringer, Nilam C. Shah, and Richard P. Van Duyne. Surface-Enhanced Raman Spectroscopy. *Annual Review of Analytical Chemistry*, 1(1):601–626, 2008.
- [80] J. A. Creighton. The resonance Raman contribution to sers: Pyridine on copper or silver in aqueous media. *Surface Science*, 173(2-3):665–672, aug 1986.
- [81] Joel I. Gersten, Ronald L. Birke, and John R. Lombardi. Theory of enhance I light scattering from molecules adsorbed at the metal-solution interface. *Physical Review Letters*, 43(2):147–150, jul 1979.
- [82] Y Xie, D Y Wu, G K Liu, Z F Huang, B Ren, J W Yan, Z L Yang, and Z Q Tian. Adsorption and photon-driven charge transfer of pyridine on a cobalt electrode analyzed by surface enhanced Raman spectroscopy and relevant theories. *Journal of Electroanalytical Chemistry*, 554-555(1):417–425, 2003.
- [83] Ken Bosnick, Mathieu Maillard, and Louis Brus. Single Molecule Raman Spectroscopy at the Junctions of Large Ag Nanocrystals. *The Journal of Physical Chemistry B*, 107(37):9964–9972, 2003.
- [84] Diego M. Solís, José M. Taboada, Fernando Obelleiro, Luis M. Liz-Marzán, and F. Javier García De Abajo. Optimization of Nanoparticle-Based SERS Substrates through Large-Scale Realistic Simulations. *ACS Photonics*, 4(2):329–337, 2017.
- [85] Olaf Hollricher and Wolfram Ibach. High-Resolution Optical and Confocal Microscopy. In *Confocal Raman Microscopy SE - 1*, volume 158, pages 1–20. Springer, Heidelberg Dordrecht London New York, 2011.
- [86] Andrea La Porta, Ana Sánchez-Iglesias, Thomas Altantzis, Sara Bals, Marek Grzelczak, and Luis M. Liz-Marzán. Multifunctional self-

Bibliography

- assembled composite colloids and their application to SERS detection. *Nanoscale*, 7(23):10377–10381, 2015.
- [87] Meikun Fan, Gustavo F S Andrade, and Alexandre G. Brolo. A review on the fabrication of substrates for surface enhanced Raman spectroscopy and their applications in analytical chemistry. *Analytica Chimica Acta*, 693(1-2):7–25, 2011.
- [88] Gustavo Bodelón, Verónica Montes-García, Vanesa López-Puente, Eric H. Hill, Cyrille Hamon, Marta N. Sanz-Ortiz, Sergio Rodal-Cedeira, Celina Costas, Sirin Celiksoy, Ignacio Pérez-Juste, Leonardo Scarabelli, Andrea La Porta, Jorge Pérez-Juste, Isabel Pastoriza-Santos, and Luis M. Liz-Marzán. Detection and imaging of quorum sensing in *Pseudomonas aeruginosa* biofilm communities by surface-enhanced resonance Raman scattering. *Nature Materials*, 15(11):1203–1211, 2016.
- [89] Lakshminarayana Polavarapu and Luis M. Liz-Marzán. Towards low-cost flexible substrates for nanoplasmonic sensing. *Physical Chemistry Chemical Physics*, 15(15):5288, 2013.
- [90] Ramon A. Álvarez-Puebla, Rafael Contreras-Cáceres, Isabel Pastoriza-Santos, Jorge Pérez-Juste, and Luis M. Liz-Marzán. Au@pNIPAM Colloids as Molecular Traps for Surface-Enhanced, Spectroscopic, Ultra-Sensitive Analysis. *Angewandte Chemie International Edition*, 48(1):138–143, 2009.
- [91] Bin Kang, Marwa M Afifi, Lauren A Austin, Mostafa A El-sayed, United States, Material Science, Oral Pathology, and Champillion St. Exploiting the Nanoparticle Plasmon Effect : Observing Drug Delivery Dynamics in Single Cells via Raman / Fluorescence Imaging Spectroscopy. *ACS Nano*, 7(8):7420–7427, 2013.
- [92] P. Couvreur. Nanoparticles in drug delivery: Past, present and future, jan 2013.
- [93] Theresa M. Allen and Pieter R. Cullis. Liposomal drug delivery systems:

- From concept to clinical applications. *Advanced Drug Delivery Reviews*, 65(1):36–48, 2013.
- [94] Yulin Li, Dina Maciel, João Rodrigues, Xiangyang Shi, and Helena Tomás. Biodegradable polymer nanogels for drug/ nucleic acid delivery. *Chemical Reviews*, 115(16):8564–8608, 2015.
- [95] Elvin Blanco, Haifa Shen, and Mauro Ferrari. Principles of nanoparticle design for overcoming biological barriers to drug delivery. *Nature Biotechnology*, 33(9):941–951, 2015.
- [96] Simona Mura, Julien Nicolas, and Patrick Couvreur. Stimuli-responsive nanocarriers for drug delivery. *Nature Materials*, 12(11):991–1003, 2013.
- [97] M B Yatvin, J N Weinstein, W H Dennis, and R Blumenthal. Design of liposomes for enhanced local release of drugs by hyperthermia. *Science (New York, N.Y.)*, 202(4374):1290–3, dec 1978.
- [98] Brandon Smith, Ilya Lyakhov, Kristin Loomis, Danielle Needle, Ulrich Baxa, Amichai Yavlovich, Jacek Capala, Robert Blumenthal, and Anu Puri. Hyperthermia-triggered intracellular delivery of anticancer agent to HER2+ cells by HER2-specific affibody (ZHER2-GS-Cys)-conjugated thermosensitive liposomes (HER2+ affisomes). *Journal of Controlled Release*, 153(2):187–194, jul 2011.
- [99] Ko Jie Chen, Hsiang Fa Liang, Hsin Lung Chen, Yucai Wang, Po Yuan Cheng, Hao Li Liu, Younan Xia, and Hsing Wen Sung. A thermoresponsive bubble-generating liposomal system for triggering localized extracellular drug delivery. *ACS Nano*, 7(1):438–446, jan 2013.
- [100] Jung Kwon Oh, Ray Drumright, Daniel J Siegwart, and Krzysztof Matyjaszewski. The development of microgels/nanogels for drug delivery applications, 2008.
- [101] Arif Gulzar, Shili Gai, Piaoping Yang, Chunxia Li, Mohd Bismillah Ansari, and Jun Lin. Stimuli responsive drug delivery application of polymer and silica in biomedicine. *J. Mater. Chem. B*, 3(44):8599–8622,

Bibliography

2015.

- [102] Soo Hyeon Lee, Seung Ho Choi, Sun Hwa Kim, and Tae Gwan Park. Thermally sensitive cationic polymer nanocapsules for specific cytosolic delivery and efficient gene silencing of siRNA: Swelling induced physical disruption of endosome by cold shock. *Journal of Controlled Release*, 125(1):25–32, jan 2008.
- [103] Tatsuaki Tagami, Warren D Foltz, Mark J Ernsting, Carol M Lee, Ian F Tannock, Jonathan P May, and Shyh Dar Li. MRI monitoring of intratumoral drug delivery and prediction of the therapeutic effect with a multifunctional thermosensitive liposome. *Biomaterials*, 32(27):6570–6578, sep 2011.
- [104] Hamilton Kakwere, Manuel Pernia Leal, Maria Elena Matera, Alberto Curcio, Pablo Guardia, Dina Niculaes, Roberto Marotta, Andrea Falqui, and Teresa Pellegrino. Functionalization of strongly interacting magnetic nanocubes with (thermo)responsive coating and their application in hyperthermia and heat-triggered drug delivery. *ACS Applied Materials and Interfaces*, 7(19):10132–10145, 2015.
- [105] Zhouqi Meng, Fang Wei, Ronghua Wang, Mengge Xia, Zhigang Chen, Huiping Wang, and Meifang Zhu. NIR-Laser-Switched in Vivo Smart Nanocapsules for Synergic Photothermal and Chemotherapy of Tumors. *Advanced Materials*, 28(2):245–253, 2016.
- [106] M.S. Strozyk, S. Carregal-Romero, M. Henriksen-Lacey, M. Brust, and L.M. Liz-Marzán. Biocompatible, Multiresponsive Nanogel Composites for Codelivery of Antiangiogenic and Chemotherapeutic Agents. *Chemistry of Materials*, 29(5), 2017.
- [107] Malte S. Strozyk, Dorleta Jimenez de Aberasturi, Jason V. Gregory, Mathias Brust, Joerg Lahann, and Luis M. Liz-Marzán. Spatial Analysis of Metal-PLGA Hybrid Microstructures Using 3D SERS Imaging. *Advanced Functional Materials*, 27(33):1–7, 2017.

- [108] Tong Cai, Manuel Marquez, and Zhibing Hu. Monodisperse thermoresponsive microgels of poly(ethylene glycol) analogue-based biopolymers. *Langmuir*, 23(17):8663–8666, 2007.
- [109] Jean François Lutz. Polymerization of Oligo(Ethylene Glycol) (Meth)Acrylates: Toward New Generations of Smart Biocompatible Materials. *Journal of Polymer Science Part A: Polymer Chemistry*, 46:3459–3470, 2008.
- [110] Zhibing Hu, Tong Cai, and Chenglin Chi. Thermoresponsive oligo(ethylene glycol)-methacrylate- based polymers and microgels. *Soft Matter*, 6:2115, 2010.
- [111] J. F. Lutz, Julien Andrieu, Senta Üzgün, Carsten Rudolph, and Seema Agarwal. Biocompatible, thermoresponsive, and biodegradable: Simple preparation of "All-in-one" biorelevant polymers. *Macromolecules*, 40(24):8540–8543, 2007.
- [112] Yukinori Okada and Fumihiko Tanaka. Cooperative hydration, chain collapse, and flat LCST behavior in aqueous poly(N-isopropylacrylamide) solutions. *Macromolecules*, 38(10):4465–4471, 2005.
- [113] Henna Vihola, Antti Laukkanen, Lauri Valtola, Heikki Tenhu, and Jouni Hirvonen. Cytotoxicity of thermosensitive polymers poly(N-isopropylacrylamide), poly(N-vinylcaprolactam) and amphiphilically modified poly(N-vinylcaprolactam). *Biomaterials*, 26(16):3055–3064, 2005.
- [114] Mark R Langille, Michelle L Personick, Jian Zhang, and Chad A Mirkin. Defining Rules for the Shape Evolution of Gold Nanoparticles. *Journal of the American Chemical Society*, 134:14542–14554, 2012.
- [115] Ralph Weissleder. A clearer vision for in vivo imaging Progress continues in the development of smaller , more penetrable probes for biological imaging . Toward the phosphoproteome. *Nature Biotechnology*, 19(4):316–317, 2001.

Bibliography

- [116] John E. Wong, Ana M.D. Ez-Pascual, and Walter Richtering. Layer-by-layer assembly of polyelectrolyte multilayers on thermoresponsive P(NiPAM-co-MAA) microgel: Effect of ionic strength and molecular weight. *Macromolecules*, 42(4):1229–1238, 2009.
- [117] Jochen Kleinen, Andreas Klee, and Walter Richtering. Influence of architecture on the interaction of negatively charged multisensitive poly(N-isopropylacrylamide)-co-methacrylic acid microgels with oppositely charged polyelectrolyte: Absorption vs adsorption. *Langmuir*, 26(13):11258–11265, 2010.
- [118] Candace C. Fleischer and Christine K. Payne. Secondary structure of corona proteins determines the cell surface receptors used by nanoparticles. *Journal of Physical Chemistry B*, 118(49):14017–14026, 2014.
- [119] Eudald Casals, Tobias Pfaller, Albert Duschl, Gertie Janneke Oostingh, and Victor Puntès. Time evolution of the nanoparticle protein corona. *ACS Nano*, 4(7):3623–3632, 2010.
- [120] Gerard W. Doorley and Christine K. Payne. Cellular binding of nanoparticles in the presence of serum proteins. *Chem. Commun.*, 47(1):466–468, 2011.
- [121] Ana B. Serrano-Montes, Dorleta Jimenez de Aberasturi, Judith Langer, Juan J. Giner-Casares, Leonardo Scarabelli, Ada Herrero, and Luis M. Liz-Marzán. A General Method for Solvent Exchange of Plasmonic Nanoparticles and Self-Assembly into SERS-Active Monolayers. *Langmuir*, 31(33):9205–9213, 2015.
- [122] Sahar Rahmani, Sumaira Ashraf, Raimo Hartmann, Acacia F. Dishman, Mikhail V. Zyuzin, Chris K. J. Yu, Wolfgang J. Parak, and Joerg Lahann. Engineering of nanoparticle size via electrohydrodynamic jetting. *Bioengineering & Translational Medicine*, 1(1):82–93, 2016.
- [123] Wan J. Li, Cato T. Laurencin, Edward J. Caterson, Rocky S. Tuan, and Frank K. Ko. Electrospun nanofibrous structure: A novel scaffold for

- tissue engineering. *Journal of Biomedical Materials Research*, 60(4):613–621, 2002.
- [124] Srijanani Bhaskar, Jonathon Hitt, Sei Won Laura Chang, and Joerg Lahann. Multicompartmental microcylinders. *Angewandte Chemie - International Edition*, 48(25):4589–4593, 2009.
- [125] Yan Geng, Paul Dalhaimer, Shenshen Cai, Richard Tsai, Manorama Tewari, Tamara Minko, and Dennis E Discher. Shape effects of filaments versus spherical particles in flow and drug delivery. *Nature nanotechnology*, 2(4):249–55, 2007.
- [126] Oktay Tacar, Pornsak Sriamornsak, and Crispin R. Dass. Doxorubicin: An update on anticancer molecular action, toxicity and novel drug delivery systems. *Journal of Pharmacy and Pharmacology*, 65(2):157–170, 2013.
- [127] C. Pisano, S. Cecere, and M. Di Napoli. Clinical trials with pegylated liposomal doxorubicin in the treatment of ovarian cancer. *J Drug Deliv*, 2013(898146), 2013.
- [128] Siteng Wang, Hongping Deng, Ping Huang, Pei Sun, Xiaohua Huang, Yue Su, Xinyuan Zhu, Jian Shen, and Deyue Yan. Real-time self-tracking of an anticancer small molecule nanodrug based on colorful fluorescence variations. *RSC Adv.*, 6(15):12472–12478, feb 2016.
- [129] Kerry K. Karukstis, Elizabeth H Z Thompson, Jennifer A. Whiles, and Robin J. Rosenfeld. Deciphering the fluorescence signature of daunomycin and doxorubicin. *Biophysical Chemistry*, 73(3):249–263, 1998.
- [130] Paul G. Richardson, Tomer M. Mark, and Martha Q. Lacy. Pomalidomide: New immunomodulatory agent with potent antiproliferative effects, 2013.
- [131] A A Chanan-Khan, A Swaika, A Paulus, S K Kumar, J R Mikhael, S V Rajkumar, A Dispenzieri, and M Q Lacy. Pomalidomide: the new immunomodulatory agent for the treatment of multiple myeloma. *Blood*

Bibliography

- cancer journal*, 3(9):e143, 2013.
- [132] Lesley J Scott. Pomalidomide: A review of its use in patients with recurrent multiple myeloma. *Drugs*, 74(5):549–562, 2014.
- [133] H Quach, D Ritchie, A K Stewart, P Neeson, S Harrison, M J Smyth, and H M Prince. Mechanism of action of immunomodulatory drugs (IMiDS) in multiple myeloma. *Leukemia*, 24(1):22–32, 2010.
- [134] Jonathan Welti, Sonja Loges, Stefanie Dimmeler, and Peter Carmeliet. Recent molecular discoveries in angiogenesis and antiangiogenic therapies in cancer, 2013.
- [135] Weitai Wu, Jing Shen, Probal Banerjee, and Shuiqin Zhou. Core-shell hybrid nanogels for integration of optical temperature-sensing, targeted tumor cell imaging, and combined chemo-photothermal treatment. *Biomaterials*, 31(29):7555–7566, 2010.
- [136] J. Siepmann and N. A. Peppas. Modeling of drug release from delivery systems based on hydroxypropyl methylcellulose (HPMC), 2001.
- [137] Mary E Anderson. 1998—Glutathione an overview of biosynthesis and modulation.pdf. *Chemico-Biological Interactions*, 112:1–14, 1998.
- [138] Guoyao Wu, Yun-zhong Fang, Sheng Yang, Joanne R Lupton, and Nancy D Turner. Recent Advances in Nutritional Sciences Glutathione Metabolism and Its Implications for Health 1. *Environmental Health*, 134(December 2003):489–492, 2004.
- [139] Alexander V. Kabanov and Serguei V. Vinogradov. Nanogels as pharmaceutical carriers: Finite networks of infinite capabilities, 2009.
- [140] Rui Hong, Gang Han, Joseph M. Fernández, Byoung Jin Kim, Neil S. Forbes, and Vincent M. Rotello. Glutathione-mediated delivery and release using monolayer protected nanoparticle carriers. *Journal of the American Chemical Society*, 128(4):1078–1079, 2006.
- [141] Cheng An J Lin, Ralph A. Sperling, Jimmy K. Li, Ting Ya Yang, Pei Yun

- Li, Marco Zanella, Walter H. Chang, and Wolfgang J. Parak. Design of an amphiphilic polymer for nanoparticle coating and functionalization. *Small*, 4(3):334–341, mar 2008.
- [142] By John L Wood. pH controlled Hydrogen-Bonding. *Biochem. J.*, 143:775–777, 1974.
- [143] Anna Li Volsi, Dorleta Jimenez de Aberasturi, Malou Henriksen-Lacey, Gaetano Giammona, Mariano Licciardi, and Luis M. Liz-Marzán. Inulin coated plasmonic gold nanoparticles as a tumor-selective tool for cancer therapy. *J. Mater. Chem. B*, 4(6):1150–1155, 2016.
- [144] Y Zhao, E B Butler, and M Tan. Targeting cellular metabolism to improve cancer therapeutics. *Cell death & disease*, 4(3):e532, mar 2013.
- [145] Xiao Yu Hu, Xin Liu, Wenyi Zhang, Shan Qin, Chenhao Yao, Yan Li, Derong Cao, Luming Peng, and Leyong Wang. Controllable Construction of Biocompatible Supramolecular Micelles and Vesicles by Water-Soluble Phosphate Pillar[5,6]arenes for Selective Anti-Cancer Drug Delivery. *Chemistry of Materials*, 28(11):3778–3788, 2016.
- [146] Yuanzhi Xia, Xiaoxia Wu, Jinshun Zhao, Zihou Li, Wenzhi Ren, Yuchen Tian, Aiguo Li, Zheyu Shen, Jing-Tai Zhao, and Aiguo Wu. Three dimensional plasmonic assemblies of AuNPs with overall size of sub-200 nm for chemo-photothermal synergistic therapy of breast cancer. *Nanoscale*, 8(3):18682–18692, 2016.
- [147] Yibing Xu, Jianwu Li, Gregory D. Ferguson, Frank Mercurio, Gody Khambatta, Lisa Morrison, Antonia Lopez-Girona, Laura G. Corral, David R. Webb, Brydon L. Bennett, and Weilin Xie. Immunomodulatory drugs reorganize cytoskeleton by modulating Rho GTPases. *Blood*, 114(2):338–345, 2009.
- [148] Sallouha Aidoudi, Kinga Bujakowska, Nelly Kieffer, and Andreas Bikfalvi. The CXC-chemokine CXCL4 interacts with integrins implicated in angiogenesis. *PLoS ONE*, 3(7), 2008.

Bibliography

- [149] Hossein Hosseinkhani, Mohsen Hosseinkhani, Ali Khademhosseini, Hisatoshi Kobayashi, and Yasuhiko Tabata. Enhanced angiogenesis through controlled release of basic fibroblast growth factor from peptide amphiphile for tissue regeneration. *27*:5836–5844, 2006.
- [150] Cristina Fernández-López, Lakshminarayana Polavarapu, Diego M. Solís, José M. Taboada, Fernando Obelleiro, Rafael Contreras-Cáceres, Isabel Pastoriza-Santos, and Jorge Pérez-Juste. Gold Nanorod- Sp-NIPAM Hybrids with Reversible Plasmon Coupling: Synthesis, Modeling, and SERS Properties. *ACS Applied Materials & Interfaces*, page 150407153946006, 2015.
- [151] Evtim V. Efremov, Freek Ariese, and Cees Gooijer. Achievements in resonance Raman spectroscopy. Review of a technique with a distinct analytical chemistry potential. *Analytica Chimica Acta*, 606(2):119–134, 2008.
- [152] Maria Vega Cañamares, Cat Chenal, Ronald L. Birke, and John R. Lombardi. DFT, SERS, and single-molecule SERS of crystal violet. *Journal of Physical Chemistry C*, 112(51):20295–20300, 2008.
- [153] L. Angeloni, G. Smulevich, and M. P. Marzocchi. Resonance Raman spectrum of crystal violet. *Journal of Raman Spectroscopy*, 8(6):305–310, 1979.
- [154] Anastasios C. Manikas, Giovanni Romeo, Antonio Papa, and Paolo a. Netti. Highly efficient surface-enhanced raman scattering substrate formulation by self-assembled gold nanoparticles physisorbed on poly(N -isopropylacrylamide) thermoresponsive hydrogels. *Langmuir*, 30(13):3869–3875, 2014.
- [155] Thomas Dieing, Olaf Hollricher, and Jan Toporski, editors. *Confocal Raman Microscopy*. Springer-Verlag Berlin Heidelberg, 2011.
- [156] Qi Zhang, Yih Hong Lee, In Yee Phang, Choon Keong Lee, and Xing Yi Ling. Hierarchical 3D SERS substrates fabricated by integrating pho-

- tolithographic microstructures and self-assembly of silver nanoparticles. *Small*, 10(13):2703–2711, 2014.
- [157] Sanpon Vantasin, Wei Ji, Yoshito Tanaka, Yasutaka Kitahama, Mengfan Wang, Kanet Wongravee, Harnchana Gatemala, Sanong Ekgasit, and Yukihiro Ozaki. 3D SERS Imaging Using Chemically Synthesized Highly Symmetric Nanoporous Silver Microparticles. *Angewandte Chemie - International Edition*, 55(29):8391–8395, 2016.
- [158] Qianru Jin, Ming Li, Beril Polat, Santosh K. Paidi, Aimee Dai, Amy Zhang, Jayson V. Pagaduan, Ishan Barman, and David H. Gracias. Mechanical Trap Surface-Enhanced Raman Spectroscopy for Three-Dimensional Surface Molecular Imaging of Single Live Cells. *Angewandte Chemie - International Edition*, 56(14):3822–3826, 2017.
- [159] Anne Marijke Leferink, Clemens van Blitterswijk, and Lorenzo Moroni. Methods of monitoring cell fate and tissue growth in three-dimensional scaffold-based strategies for in vitro tissue engineering. *Tissue Engineering Part B: Reviews*, 22(4):ten.TEB.2015.0340, 2016.
- [160] Gary A. Epling and Chitsan Lin. Photoassisted bleaching of dyes utilizing TiO₂ and visible light. *Chemosphere*, 46(4):561–570, 2002.
- [161] Freya Q. Schafer and Garry R. Buettner. Redox Environment of the Cell As Viewed Through the. *Free Radical Biology & Medicine*, 30(11):1191–1212, 2001.
- [162] Joseph R Casey, Sergio Grinstein, and John Orlowski. Sensors and regulators of intracellular pH. *Nature Reviews. Molecular Cell Biology*, 11(1):50–61, 2010.
- [163] Peter Mitchell. Turning the spotlight on cellular imaging. *Nature biotechnology*, 19(11):1013–7, 2001.
- [164] James B. Pawley, editor. *Handbook of Biological Confocal Microscopy. 3rd edition*. Springer Science + Business Media, New York, NY, 2006.

Bibliography

- [165] George M. Whitesides and Chi-Huey Wong. Enzyme in der organischen Synthese. *Angewandte Chemie*, 8(8):617–720, aug 1985.
- [166] Tomas Hudlicky. Introduction to enzymes in synthesis. *Chemical Reviews*, 111(7):3995–3997, jul 2011.
- [167] U. T. Bornscheuer, G. W. Huisman, R. J. Kazlauskas, S. Lutz, J. C. Moore, and K. Robins. Engineering the third wave of biocatalysis. *Nature*, 485(7397):185–194, may 2012.
- [168] Alle Bruggink, Eric C. Roos, and Erik de Vroom. Penicillin acylase in the industrial production of beta-lactam antibiotics. *Org. Proc. Res. Dev.*, 2(2):128–133, mar 1998.
- [169] Herfried Griengl, Helmut Schwab, and Martin Fechter. The synthesis of chiral cyanohydrins by oxynitrilases, jun 2000.
- [170] Toru Nagasawa, Tetsuji Nakamura, and Hideaki Yamada. Production of acrylic acid and methacrylic acid using *Rhodococcus rhodochrous* J1 nitrilase. *Archives of Microbiology*, 34(3):322–324, dec 1990.
- [171] J Muschiol, C Peters, N Oberleitner, M D Mihovilovic, U T Bornscheuer, and F Rudroff. Cascade catalysis—strategies and challenges en route to preparative synthetic biology. *Chem Commun (Camb)*, 51(27):5798–5811, 2015.
- [172] Nicholas J Turner. Directed evolution drives the next generation of biocatalysts. *Nature Chemical Biology*, 5(8):567–573, aug 2009.
- [173] Nicholas J Turner. Directed evolution of enzymes for applied biocatalysis, nov 2003.
- [174] Markus Baumann, Rainer Stürmer, and Uwe T. Bornscheuer. A high-throughput-screening method for the identification of active and enantioselective hydrolases. *Angewandte Chemie - International Edition*, 40(22):4201–4204, nov 2001.

- [175] Manfred T. Reetz, Klaus M. Kühling, Stephanie Wilensek, Heribert Husmann, Ulrich W. Häusig, and Marcus Hermes. A GC-based method for high-throughput screening of enantioselective catalysts. *Catalysis Today*, 67(4):389–396, jun 2001.
- [176] Manfred T. Reetz, Michael H. Becker, Klaus M. Kühling, and Arnold Holzwarth. Time-resolved IR-thermographic detection and screening of enantioselectivity in catalytic reactions. *Angewandte Chemie - International Edition*, 37(19):2647–2650, oct 1998.
- [177] Gérard Klein and Jean Louis Reymond. Enantioselective fluorogenic assay of acetate hydrolysis for detecting lipase catalytic antibodies. *Helvetica Chimica Acta*, 82(3):400–407, mar 1999.
- [178] Jianhua Guo, Jiangyue Wu, Gary Siuzdak, and M. G. Finn. Measurement of Enantiomeric Excess by Kinetic Resolution and Mass Spectrometry. *Angewandte Chemie International Edition*, 38(12):1755–1758, jun 1999.
- [179] Barry D Moore, Lorna Stevenson, Alan Watt, Sabine Flitsch, Nicolas J Turner, Chris Cassidy, and Duncan Graham. Rapid and ultra-sensitive determination of enzyme activities using surface-enhanced resonance Raman scattering. *Nature biotechnology*, 22(9):1133–8, sep 2004.
- [180] Cesar Mateo, Jose M. Palomo, Gloria Fernandez-Lorente, Jose M. Guisan, and Roberto Fernandez-Lafuente. Improvement of enzyme activity, stability and selectivity via immobilization techniques, may 2007.
- [181] Andreas Liese and Lutz Hilterhaus. Evaluation of immobilized enzymes for industrial applications. *Chemical Society Reviews*, 42(15):6236, 2013.
- [182] Ulf Hanefeld, Linqiu Cao, and Edmond Magner. Enzyme immobilisation: fundamentals and application. *Chemical Society Reviews*, 42(15):6211, 2013.

Bibliography

- [183] A. Garcia-Leis, D. Jancura, M. Antalík, J. V. Garcia-Ramos, S. Sanchez-Cortes, and Z. Jurasekova. Catalytic effects of silver plasmonic nanoparticles on the redox reaction leading to ABTS^{•+} formation studied using UV-visible and Raman spectroscopy. *Phys. Chem. Chem. Phys.*, 18(38):26562–26571, sep 2016.
- [184] H Gallati and I Pracht. [Horseradish peroxidase: kinetic studies and optimization of peroxidase activity determination using the substrates H₂O₂ and 3,3',5,5'-tetramethylbenzidine]. *J Clin Chem Clin Biochem*, 23(8):453–460, aug 1985.
- [185] BRENDA enzyme database.
- [186] Christoph Hanske, Guillermo González-Rubio, Cyrille Hamon, Pilar Formentín, Evgeny Modin, Andrey Chuvilin, Andrés Guerrero-Martínez, Lluís F. Marsal, and Luis M. Liz-Marzán. Large-Scale Plasmonic Pyramidal Supercrystals via Templated Self-Assembly of Monodisperse Gold Nanospheres. *Journal of Physical Chemistry C*, 121(20):10899–10906, may 2017.
- [187] Andrea La Porta. *Engineering The Morphology And Organization Of Gold Nanostructures For SERS Detection*. PhD thesis, Universidade de Vigo, 2016.
- [188] Dirk Schmaljohann. Thermo- and pH-responsive polymers in drug delivery. *Advanced Drug Delivery Reviews*, 58(15):1655–1670, 2006.
- [189] Katarzyna Kamińska, Cezary Szczylik, Zofia F Bielecka, Ewa Bartnik, Camillo Porta, Fei Lian, and Anna M Czarnecka. The role of the cell-cell interactions in cancer progression. *Journal of Cellular and Molecular Medicine*, 19(2):283–296, 2015.
- [190] Stacey Laing, Lauren E Jamieson, Karen Faulds, and Duncan Graham. Surface-enhanced Raman spectroscopy for in vivo biosensing. *Nature Reviews Chemistry*, 1(8):0060, 2017.
- [191] Joshua D. Weatherston, Nolan C. Worstell, and Hung-Jen Wu. Quantita-

- tive surface-enhanced Raman spectroscopy for kinetic analysis of aldol condensation using Ag@Au core-shell nanocubes. *The Analyst*, 141(21):6051–6060, 2016.
- [192] Chloe Westley, Yun Xu, Andrew J. Carnell, Nicholas J. Turner, and Royston Goodacre. Label-Free Surface Enhanced Raman Scattering Approach for High-Throughput Screening of Biocatalysts. *Analytical Chemistry*, 88(11):5898–5903, 2016.
- [193] Wei Shen, Xuan Lin, Chaoyang Jiang, Chaoyu Li, Haixin Lin, Jingtao Huang, Shuo Wang, Guokun Liu, Xiaomei Yan, Qiling Zhong, and Bin Ren. Reliable quantitative SERS analysis facilitated by core-shell nanoparticles with embedded internal standards. *Angewandte Chemie - International Edition*, 54(25):7308–7312, jun 2015.
- [194] Judith Langer, Isabel García, and Luis M. Liz-Marzan. Real-time dynamic SERS detection of galectin using glycan-decorated gold nanoparticles. *Faraday Discuss.*, 2017.

List of Figures

- 2.1. A) Schematic representation of the seeded growth method to grow nanoparticles in situ on a PS bead and representative SEM pictures for each stage. B-D) TEM pictures of PS beads decorated with different amounts of pre-synthesized gold nanostars. Figure A reproduced with permission from ref.[20] Copyright 2012, American Chemical Society. B-D reproduced with permission from ref.[23] Copyright 2016, American Chemical Society. 9
- 2.2. Upper panel: Schematic representation of different approaches for surface functionalization with vinyl groups: butenoic acid (A), polystyrene and vinylbenzene (B) and LbL with allylamine (C). Lower panel: Representative TEM images of Au spheres (D), octahedra (E), nanorods (F) and nanostars (G), encapsulated with pNIPAM using the LbL method. Reproduced with permission from ref.[45] Copyright 2013, Royal Society of Chemistry. 13

List of Figures

2.3. A) TEM pictures of nanorod assembly onto pNIPAM microgels. (B) Scheme and TEM pictures of in situ grown nanoparticle onto PEGMA microgels below and above the LCST. C) Gold nanoparticles grown inside a vinyl caprolactam microgel which was copolymerized with acetoacetoxyethylmethacrylate. Acetoacetoxyethylmethacrylate inside the gel reduces the gold in situ without additional reducing agent. Figure A reproduced with permission from ref.[1] Copyright 2009, American Chemical Society. Figure B reproduced with permission from ref.[53] Copyright 2013, The Royal Society of Chemistry 16

2.4. Scheme of the oscillating electrons under electromagnetic irradiation and corresponding UV-vis spectra for spherical particles and rodshaped particles. Scale bar in both pictures is 100 nm. 18

2.5. SEM images pNIPAM microgels decorated with AuNPs of different sizes below and above the LCST. Additionally the corresponding UV-vis spectra are shown. Reproduced with permission from ref.[12] Copyright 2014, American Chemical Society. 21

2.6. Jablonski Diagram of the different scattering modes. Rayleigh scattering, Stokes Scattering and Anti Stokes Scattering. For comparison IR absorption is also shown. 23

2.7. a) SERS enhancement dependent on substrate coverage for nanoparticles with different morphologies at 785 nm excitation wavelength. The dashed lines represent excitation at 633 nm for GNP and 900 nm for GNS. b) Corresponding simulations of the surface coverage. Defects were taken into account for this study. Reproduced with permission from ref.[84] Copyright 2017, American Chemical Society. 28

2.8. Principle setup of a confocal microscope. Picture taken from Witec Manual 30

2.9. Upper panel: Reference spectra of the difference SERS encoded nanoparticles in single cell cultures. B) and C) SERS spectra and particle assignment inside a cell co-culture. Reproduced with permission from ref.[18] Copyright 2016, American Chemical Society Lower panel: In one case the as a solution (D) and in the other case immobilized on PS beads (E). The intensity differs a lot showing an increased signal for the PS beads while keeping the AuNS concentration constant. Reproduced with permission from ref.[23] Copyright 2016, American Chemical Society 34

2.10. SERS signal of 1-naphtol as a function of temperature and heating cycle. (A) Starting at 4°C, heating up to 60 °C and cooling down back to 4 °C. (B) Starting at 60 °C cooling down to 4 °C and heating up back to 60 °C. Reproduced with permission from ref.[90] Copyright 2009, Wiley-VCH. 36

List of Figures

2.11. (a) Real-time monitoring of the doxo release measured by SERS (a) and fluorescence (b). The scale bar is 10 μm . Decrease of normalized Raman band intensities over time at 460 cm^{-1} (c) and the increase of the relative fluorescence intensity (d). Reproduced with permission from ref.[91] Copyright 2013, American Chemical Society	37
2.12. A) Schematic representation of doxo loaded polymer coated magnetic nanocubes under the influence of an magnetic field. On the right, the temperature profiles of the particles under a influence of a magnetic field and the release profile of doxorubicin. B) Release scheme of the doxo loaded polymer-CuS hybrid particle under the influence of laser irradiation. Figure B reproduced with permission from ref.[104] Copyright 2015, American Chemical Society. Figure B reproduced with permission from ref.[105] Copyright 2016, Wiley VCH.	40
3.1. a) Schematic representation of the in-situ growth of AuNPs in PEGMA nanogels. Small gold seeds were synthesized by reduction with NaBH_4 . Further growth was realized by introducing the nanogels with seeds in a growth solution containing NaBr and formaldehyde at high pH. The obtained nanogels were finally wrapped with a layer of polyelectrolytes. b) Representative TEM pictures of the nanogels during the different growth steps, as labeled. c) UV-Vis spectra of the corresponding particle colloids. Reproduced with permission from ref.[106] Copyright 2017, American Chemical Society.	46
3.2. a) TEM images of particles grown without initial seed growth step. b) Particles grown without NaBr in the second growth step. Reproduced with permission from ref.[106] Copyright 2017, American Chemical Society.	47

- 3.3. TEM pictures and corresponding UV-vis spectra of AuNGs synthesized with different amount of seeds. Seed concentrations decreases from 2000 μL (top left TEM image) to 10 μL (bottom right TEM image). Lower AuSeedsNG concentration leads to bigger nanoparticles inside the gel (250-500 μL AuSeedsNG). At very low concentration secondary nucleation occurs and gold forms a shell around the nanogels (50-10 μL AuSeedsNG). In all cases the gold salt concentration in the growth solution was constant at 0.5 mM. Insets share all the same scale bar of 100 nm. Reproduced with permission from ref.[106] Copyright 2017, American Chemical Society. 48
- 3.4. Growth of nanostars inside nanogels. Higher HAuCl_4 :AuSeedsNG ratio leads to better defined tips. TEM pictures from left to right show nanostars grown with 20, 50, 100 and 200 μL seed solution respectively. The concentration of HAuCl_4 was kept constant at 2.75 mmol/L for all samples. Scale bar is 200 nm for all insets. Reproduced with permission from ref.[106] Copyright 2017, American Chemical Society. 49
- 3.5. Au Nanostar decorated PEGMA nanogels and evolution of their UV-Vis spectra under heating and cooling cycles. The change of the spectra is irreversible due to reshaping. Reproduced with permission from ref.[106] Copyright 2017, American Chemical Society. 50
- 3.6. UV-VIS spectra of PEGMA nanogels in different media. Reproduced with permission from ref.[106] Copyright 2017, American Chemical Society. 52

List of Figures

- 3.7. AuNP loaded nanogels without coating (a) and with poly-L-arginine (b) and polyalginate coating (c) in water, cell media with 10% FBS-serum and glutathione (10 mM), after 1 week. Scale bar for close up pictures is 100 nm, for pictures with lower magnification 500 nm. Reproduced with permission from ref.[106] Copyright 2017, American Chemical Society. 54
- 3.8. Thermoresponsive behavior of nanogels (no Au NPs growth). Reproduced with permission from ref.[106] Copyright 2017, American Chemical Society 55
- 3.9. a) Schematic representation of the shrinking process and representative TEM pictures in collapsed and swollen states. b) Dynamic light scattering monitoring of the swelling ratio in AuNGs. c) UV-Vis spectra of the nanogels, alternating at 20 °C and 50 °C, plotted as solid and dashed lines, respectively. The insets show the LSPR maxima during each cycle. Reproduced with permission from ref.[106] Copyright 2017, American Chemical Society. 56

3.10. Fabrication of multicompartmental hybrid particles using electrohydrodynamic co-jetting. The size of the particles can be controlled by using different polymer molecular weights and varying solvent ratios, solvent polymer concentrations and composition. Images in A-F are representative for particles of different sizes and compositions. PLGA molecular weight was varied from 17 kDA (A,B) through 40 kDA (C,D) up to 50-75 kDA (E,F). These examples show various configurations with two (A,C-F) or three compartments (B), containing AuNs (A-F) and iron oxide nanoparticles (B). The particles also contain Poly[(m-phenylenevinylene)-alt-(2,5-dihexyloxy-p-phenylenevinylene)] as blue dye and Poly[tris(2,5-bis(hexyloxy)-1,4-phenylenevinylene)-alt-(1,3-phenylenevinylene)] as green dye, in different compartments. All scale bars are 500 nm. Reproduced with permission from ref.[107] Copyright 2017, American Chemical Society. 60

3.11. Large scale images of bicompartmental nanoparticles with two different Raman labeled Au NSs and two different dyes (blue and green) characterized by (A) SEM (B) TEM and (C) fluorescence confocal microscopy. Reproduced with permission from ref.[107] Copyright 2017, American Chemical Society. 62

List of Figures

- 3.12. (A) bicompartamental PLGA (40 KDa) particles containing 30 nm AuNSs labeled with 4-BPT and a green dye in one compartment, and AuNSs labeled with 4-BPT and a blue dye in the other compartment. (B) Fluorescence image of $\sim 4 \mu\text{m}$ particles showing that the dyes and hence the compartments are separated and distinguishable. (C) SERS mapping of a $\sim 7 \mu\text{m}$ particle, also showing two compartments. The signals from 4-BPT (red) and 2-Nat (green) are spatially separated. Reproduced with permission from ref.[107] Copyright 2017, American Chemical Society. 63
- 3.13. Examples of PLGA-based bicompartamental fibers prepared by electrohydrodynamic co-jetting and analyzed by fluorescence imaging (A) and SERS mapping (B). Reproduced with permission from ref.[107] Copyright 2017, American Chemical Society. 64
- 3.14. Additional particles can also be produce. Fluorescence images of (A) Particles including COOH in their surface to be modified with antibodies or other molecules (30% of 5.9 kDa of PLGA with COOH added) and (B) Cylinder shaped particles: Synthesized fibers can be cut to obtain cylinders of different sizes. Reproduced with permission from ref.[107] Copyright 2017, American Chemical Society. 65

3.15. (A) ~500 nm tricompartmental PLGA (17 KDa) particles containing 30nm AuNSs labeled with 4-BPT together with a blue dye in one compartment, 40 nm iron oxide nanoparticles with a red dye in a second compartment and a green dye in a thirds compartment. (B) TEM image where both nanoparticles can be observed. (C) Fluorescence image showing the three compartments differentiated by the 3 dyes. (D) Bicompartmental PLGA (55-75 KDa) particles ~8 μm containing 30 nm AgNPs labeled with 2-NAT together with a blue dye in one compartment and 30 nm AuNSs labeled with 2-NAT and with a green dye in a second compartment are shown. TEM images at different focus confirm that particles are embedded onto the PLGA particles and not only at the surface. Reproduced with permission from ref.[107] Copyright 2017, American Chemical Society. 67

4.1. Scheme of action for the application of the PEGMA nanogels as stimuli responsive drug delivering tool 74

4.2. a) Structure of doxorubicin. b) Excitation (black) and emission (red) spectra of doxorubicin under excitation at 470 nm. Figure B reproduced with permission from ref.[128] Copyright 2016, Royal Society of Chemistry 76

4.3. a) Structure of Pomalidomide. b) Schematic representation of Angiogenesis. Picture taken from <http://www.angioworld.com/DominiqueGarrel.h> October2017. 78

4.4. Typical calibration curves for doxorubicin (a) and pomalidomide (b). Reproduced with permission from ref.[106] Copyright 2017, American Chemical Society. 81

List of Figures

- 4.5. Increased release of Doxo (a) and Poma (b) between intracellular (pH=5.5, [GSH]= 5 mM) and extracellular conditions (pH=5.5, [GSH]= 1 μ M) with no trigger (control), heat and Laser. Reproduced with permission from ref.[106] Copyright 2017, American Chemical Society. 82
- 4.6. Release of pomalidomide over time at room temperature and 50 °C, monitored over 24 h. Reproduced with permission from ref.[106] Copyright 2017, American Chemical Society. 84
- 4.7. Relative release of doxorubicin (a) and pomalidomide (b) over time at room temperature and at 50 °C. The lines are the corresponding fitting curves according to Peppas model. Table (c) shows the values extracted from the fit for the release exponent (n). Reproduced with permission from ref.[106] Copyright 2017, American Chemical Society. 85

4.8. a) Temperature increase (open circles) of AuNG3 solution under NIR illumination (808 nm, 8.03 W/cm²) and the corresponding doxorubicin release (filled circles). b) Doxo release from AuNG3 upon heating and/or GSH addition and corresponding SERS spectra (inset). SERS spectra were recorded in solution at a concentration of 5 μg/mL(Au), $P_{laser} = 12\text{mW}$ for 633 nm and $t_{int}=20\text{s}$ with a 10x objective (NA=0.35). The assigned band at 1420 cm⁻¹ is highlighted with a gray background. c) pH influence on the release of Doxo at different [GSH]. d,e) Summary of the different Doxo release efficiencies comparing the delivery at room temperature (control) versus the delivery upon the application of external stimuli, NIR light and heat (50 °C) in solutions mimicking the extracellular (d) and intracellular environment (e). Reproduced with permission from ref.[106] Copyright 2017, American Chemical Society. 89

4.9. Increased release of Doxo (a) and Poma (b) when moving from extracellular environment (pH=7, [GSH]= 1 μM) to intracellular environment (pH=5.5, [GSH]= 5 mM) under the influence of no trigger (control), heat and laser illumination. Reproduced with permission from ref.[106] Copyright 2017, American Chemical Society. 90

List of Figures

- 4.10. a) Cellular uptake of free Doxo, AuNG2 and AuNG3 nanogels. A co-culture of HeLa (unstained) and HDF (blue stained) cells were exposed to Doxo and Doxo containing AuNG2 and AuNG3 for 2 h and uptake visualized using Doxo fluorescence (shown in red in main images or in white in inserts for clarity). Clear nuclear (left image) or endosomal staining (middle and right images) is seen after free or nanogel delivered Doxo, respectively. Scale bars are 100 μm . b) TEM images of HeLa cells exposed to AuNG2 and AuNG3 for 2 h and then processed the following day for TEM imaging. Magnified photos are shown in color coded boxes. Reproduced with permission from ref.[106] Copyright 2017, American Chemical Society. 92
- 4.11. MCF-7 breast cancer cells showing uptake of AuNG2 (a) and AuNG3 (b). Doxo (shown in red) is not released at this time, and therefore little to no cytotoxicity is observed. Free doxorubicin (c) causes high levels of cell death. Untreated control cells are shown in (d). Cells are DAPI stained. Scale bar is 50 μm . e) HeLa and HDF (stained blue) co-culture exposed to non-coated nanogels for 2 h; f) MCF-7 cells exposed to poly-L-arginine nanogels (AuNG2, without drugs) for approximately 18 h, and stained with DAPI. g) MCF-7 cells exposed to polyalginate nanogels (AuNG3, without drugs) for approximately 18 h, and stained with DAPI. h) Live/Dead staining of a HeLa and HDF cell co-culture exposed to non-coated nanogels for 2 h and then left for 4 days, with live cells imaged in the green fluorescence channel and dead cells using red fluorescence. Reproduced with permission from ref.[106] Copyright 2017, American Chemical Society. 93

- 4.12. TEM pictures showing AuNG3 and AuNG2 nanogel degradation inside cells after one week incubation time. HeLa cells were incubated with AuNGs for a week, followed by fixation, staining and embedding in a resin. The pictures show cross sections of thinly sliced cells with nanoparticles inside. The enlarged pictures highlight the presence of the nanogels. Reproduced with permission from ref.[106] Copyright 2017, American Chemical Society. 95
- 4.13. Cell viability of HeLa cells after incubation with different Poma concentrations. Cells were incubated with free Poma, free Doxo (same concentrations as the corresponding Doxo loaded AuNGs contained) and AuNG loaded with Poma alone and Doxo plus Poma. Cell viability was measured ca. 24 h later using the MTT assay. Reproduced with permission from ref.[106] Copyright 2017, American Chemical Society. 96
- 4.14. a) Live/Dead staining of HeLa/HDF co-cultures, ca. 4 days post initial exposure to free Doxo, or Doxo-containing AuNG2 and AuNG3. Live cells show green-channel fluorescence whilst dead cells uptake propidium iodide and are positive for red channel fluorescence. The predominant live population (green) are HDF cells which can be identified by their characteristic shape, whereas HeLa cells are the majority "dead" population. Scale bars are 200 μm . b) NIR-laser induced hyperthermia and photo-thermal-induced cytotoxicity of HeLa cells and c) cell viability of HeLa cells after lower NIR-laser irradiation without hyperthermia, showing exclusively enhanced drug release through NIR irradiation. Reproduced with permission from ref.[106] Copyright 2017, American Chemical Society. 98

List of Figures

- 4.15. Pomalidomide mediated inhibition of LPS-induced IL-6 from J774 murine macrophages. DMSO was also included as a solvent control, at the same final concentration as present in free Poma. Reproduced with permission from ref.[106] Copyright 2017, American Chemical Society. 99
- 4.16. a) The angiogenesis tube formation assay shows the ability of HUVEC cells to grow vessel-like interconnecting networks through the aid of growth factors present in the underlying gel. In cases where no nanogels were applied (a), established tube formation is seen within 6 h, yet with HUVEC cells pre-incubated with AuNG2 (c), or AuNG3 (d), or HUVEC cells incubated with free pomalidomide (b), poor or no tube-formation is seen. Control experiment with AuNG without coating and Poma show tube formation similar to no Poma (a). Each image (circle) is 4 mm in diameter DIC microscope image showing the whole well. Reproduced with permission from ref.[106] Copyright 2017, American Chemical Society. . . 100
- 4.17. HUVEC cells incubated with free Poma, AuNG2, AuNG3 or AuNG without Poma (control) for 4 h at a final Poma concentration of 10 μ M. Cells were washed, fixed and stained with DAPI and AF488-phalloidin to show the nucleus and actin fibers respectively. Scale bars are 50 μ m. c) Area and aspect ratio (AR) of cells described in (b), measured using ImageJ from at least 30 cells from 3 separate images. Mean \pm SD is shown. Reproduced with permission from ref.[106] Copyright 2017, American Chemical Society. 102

5.1. a) SERS spectra of CV using 633 nm excitation wavelength (1.19 mW) for nanogels with different sized AuNPs of ≈ 12 nm (1), ≈ 18 nm (2), ≈ 25 nm (3). b) SERS spectra of CV using 785 nm excitation wavelength (19.4 mW) for nanogels with different sized AuNPs. c) Representative TEM pictures of nanogels used for this experiment 114

5.2. SERS spectra and corresponding fluorescence spectra of Doxo without GSH and in a 2 mM GSH solution. 117

5.3. a)SERS spectra of Doxo below and above the LCST of the PEGMA nanogels b) UV-vis spectra of the corresponding nanogel at RT and 50 °C. The inset shows the LSPR maxima during each cycle 118

5.4. SERS mapping and a representative spectrum of J774 macrophages (a) and A594 cells (b) incubated with CV loaded nanogels. The contour plot was created using the SERS intensity at 1175 cm^{-1} 119

5.5. Intracellular and extracellular SERS spectra of A549 cells incubated with Doxo loaded nanogels after 3 hours of incubation (a) with the corresponding fluorescence microscopy picture (b). The same measurement was repeated after 6 hours and the SERS spectra (c) and fluorescence microscopy pictures were taken (d). In both cases is the contour plot created by using the SERS intensity at 1250 cm^{-1} . It has to be mentioned that the difference in signal is most likely due to a change of the background and not due to a different SERS intensity of Doxo. 121

List of Figures

5.6. Three-dimensional confocal Raman imaging of a single microgel particle. A) Z-stack showing the existence of separated compartments and the distribution of SERS labeled AuNSs within the particle. (B) Representative SERS spectra of BPT (red) and 2-NAT (green). The peaks marked with * indicate the specific signals used for mapping. (C,D) Three-dimensional reconstruction of the particle from two different perspectives. Reproduced with permission from ref.[107] Copyright 2017, American Chemical Society. 124

5.7. A large number (>100) of bicompartmental particles were immobilized on a glass substrate and both SERS and fluorescence signals were measured before (a) and after (b) exposing them to UV-light. Images 1-3 show that the SERS signal from both 4-BPT and 2-NAT SERS tags show no difference over time and remain active upon irradiation. The fluorescence signals of both blue and green dyes (4-6) however vanish after UV light exposure due to bleaching of the dye molecules. Reproduced with permission from ref.[107] Copyright 2017, American Chemical Society. 126

6.1. A Michaelis Menten curve for the reaction rate (ν) against the substrate concentration 134

6.2. Structural change of ABTS in presence of HRP and hydrogen peroxide. 136

6.3. a) Experimentally derived Raman spectrum of ABTS before and after the reaction (785 nm excitation wavelength). b) Scheme for the enzymatic reaction of ABTS 137

6.4. Time dependent Intensity of ABTS under different HRP concentrations. 138

- 6.5. Time dependent intensity of ABTS* at different pH's under otherwise constant conditions: 0.1 mg/mL ABTS, 10 mM H₂O₂, 2.5 μg/mL HRP. 139
- 6.6. Time dependent intensity of ABTS* at different H₂O₂ concentrations under otherwise constant conditions: 0.1 mg/mL ABTS, pH 6, 2.5 μg/mL HRP. 140
- 6.7. Schematically presentation of a cascade reaction using a first enzyme (GOX, DAAO) with a substrate to produce H₂O₂ which is then reacting with HRP and ABTS to form ABTS*. In our case the educt will be glucose, but in principle other substrates can be used. 141
- 6.8. A: Intensity of ABTS* over time at different glucose concentrations with GOX as the enzyme. B: From each dataset the first data-points where the increase of ABTS* is linear are separated. These data points follow a linear fit and can be used to determine the specific reaction rate for each glucose concentration. 144
- 6.9. A) Intensity of ABTS* over time at different XX concentrations with DAAO as the enzyme. B) From each dataset the first data-points where the increase of ABTS* is linear are separated. These data points follow a linear fit and can be used to determine the specific reaction rate for each glucose concentration. 145
- 6.10. A) Michaelis Menten plot with corresponding fitting values for V_{max} and k_M . B) Lineweaver Burk plot with corresponding values for V_{max} and K_M 146
- 6.11. Scheme of enzymatic cascade reaction with two enzymes competing for H₂O₂, HRP and CAT. 148

List of Figures

6.12. Intensity of ABTS* over time with different CAT concentrations. Low concentrations up to 0.0025 mg/mL CAT (Graph A) show no significant effect on the ABTS* production. At higher concentrations from 0.015 mg/mL upwards (Graph B), the ABTS* production is reduced indicating that the competition with CAT became measurable 149

6.13. Line scans of enzyme loaded beads in HRP solution and the corresponding increase of ABTS* signal (blue < red) for different arrangements of the beads. Pure beads of GOX (A), beads of GOX and CAT far away from each other (B) and beads of GOX and CAT in close proximity (C). 150

6.14. A) Picture of the glass slide after treatment with AuNPs. The particles are immobilized on a glass slide which is then placed in a self-made container for roughly 500 μ L of reaction solution. B) SERS background at different laser powers (785 nm) at 1s exposure time under 10x magnification. C) Mapping of the background shows homogeneous distribution of the signal. The signal is nominated to 1. 152

6.15. A) SERS spectra of benzyl amine, benzyl alcohol, benzaldehyde. Inset: Enzymatic reaction under investigation. Pyruvate kinase will transform benzyl amine to benzaldehyde using pyruvate which reacts to form alanine. B) SERS spectra of the reaction mixture before (t_0) and after (t_∞). 153

A.1. General survey spectra. The photoelectron and Auger peaks from sodium, carbon, oxygen, tin, nitrogen, silicon and gold were detected. 166

- A.2. Shown in the spectra are the expected positions of the C C bonds at 285.0 eV, C N bonds at around 286.0 eV, and C-O, C=O and O-C=O bonds at around 286.5, 288.6 and 290.5 eV, respectively. 167
- A.3. XPS spectra at the region where the N 1s signal is expected. Only the sample with poly-L-arginine showed nitrogen signal, with the N 1s peak position at around 399.7 eV, which is attributed to N-H, C-N bonds. 168
- A.4. Shown in the spectra are the expected positions of the C=O bonds at around 531.2 eV and the C O bonds at around 532.5 eV.169

Biocompatible, multiresponsive nanogel composites for co-delivery of anti-angiogenic and chemotherapeutic agents

Malte S. Strozyk,^{††} Susana Carregal-Romero,[†]

Malou Henriksen-Lacey^{†, //}, Mathias Brust[†], Luis M. Liz-Marzán^{*, †, ‡, //}

[†]Bionanoplasmonics Laboratory, CIC biomaGUNE, Paseo de Miramón 182, 20014 Donostia-San Sebastián, Spain

[†]Department of Chemistry, University of Liverpool, Liverpool L69 7ZD, United Kingdom

[‡]Ikerbasque, Basque Foundation for Science, 48013 Bilbao, Spain

^{//} CIBER de Bioingeniería, Biomateriales y Nanomedicina, CIBER-BBN, 20014 Donostia-San Sebastián, Spain

*e-mail: llizmarzan@cicbiomagune.es

Keywords:

ABSTRACT

Single therapy approaches are usually insufficient to treat certain diseases, due to genetic differences between patients or disease resistance. Therefore, such approaches are gradually replaced by combination therapies comprising two or more drugs. In oncology these include BRAF inhibitors, cytotoxic, anti-angiogenic or immunomodulatory agents, among others. We propose herein the use of multiresponsive nanogel composites for the co-delivery of a DNA intercalator (doxorubicin) and an anti-angiogenic and immunomodulatory agent (pomalidomide). We introduce a surfactant-free synthetic protocol to decorate biocompatible poly(ethylene glycol)methacrylate nanogels (PEGMA) with evenly distributed gold

nanoparticles and explore their ability to deliver drugs upon stimulation by various triggers such as heat, light and reducing agents present in the intracellular environment. We further demonstrate that an additional polymer coating on the nanogel surface can decrease uncontrolled drug leakage, and modulate cellular uptake and the drug release profile.

INTRODUCTION

Chemotherapy still prevails as the most common treatment for cancer. However, there is a rising demand for alternative therapies, which involve the use of anticancer drugs combined with other molecularly target agents toward the reduction of side effects and the enhancement of the treatment efficacy.^{1,2} The use of nanoparticles (NPs) for drug delivery is a well recognized method to control the delivery kinetics and biodistribution of the drug in question, as well as offering protection from biological conditions which can cause drug degradation.³⁻⁷ Furthermore, NP materials need not be limited to one sole material or be loaded with a single drug. In fact, this leads to many possibilities in terms of triggered, controlled, drug release and co-delivery that can be combined with multimodal imaging.⁸⁻¹¹ Regarding chemotherapy, NPs offer the possibility to improve treatment efficacy by delivering cytotoxic drugs to cancerous cells with minimal exposure to non-cancerous cells, thereby avoiding chemotherapy side effects.¹²⁻¹⁵ Tumors, however, are complex structures and their growth promotes angiogenesis in an autocrine manner, thereby allowing a constant supply of nutrients and oxygen to the cancerous cells.¹⁶⁻¹⁸ The suppression of tumor growth by action of anti-angiogenic agents is therefore an appealing method to target cancer.^{19,20} One of the most interesting aspects therefore of NPs is their ability to deliver a combination of drugs which can target different aspects of tumour growth and persistence. One such example of this is Doxil, a liposomal doxorubicin carrying NP system, which has been combined with dexamethasone and pomalidomide and is currently in clinical trials to treat Multiple Melanoma (MM) cancer (NCT01541332 from www.clinicaltrials.gov).

In this context, we propose the use of nanogels for combination therapy and controlled release of drugs. Nanogels are formed by crosslinked polymeric networks that possess a

large water content and open spaces with a characteristic mesh size. The mesh size governs the diffusion of drugs within the nanogel and the chemical interaction between the polymer structure determines the drug entrapment efficiency.^{21,22} Nanogels show several advantages over other drug carrier systems, which are related with the mild conditions of drug encapsulation, which allow entrapment of labile drugs (hydrophilic and hydrophobic), their excellent biocompatibility and the easy tailoring of their responsiveness toward triggers of drug release.^{23,24} In contrast, the main drawback is the uncontrolled leakage of drugs. The nanogel polymer chemistry can be designed to release cargo molecules upon different stimuli such as e.g. pH or heat.²⁵ By including gold (Au) NPs within the nanogel, near-infrared (NIR) illumination can be used to induce local heating at the AuNP surface, thereby providing a further trigger for drug release and offering NP-based hyperthermia.^{26,27} Importantly, the use of NIR illumination renders such a system suitable for use in biological tissues, due to the reduced absorption by tissue of light with wavelength between 650 and 950 nm.²⁸

In this proof of concept work we demonstrate that AuNP-containing thermosensitive nanogels, coated with an appropriate polyelectrolyte, are suitable platforms for the co-delivery of doxorubicin (Doxo) – a cytotoxic agent and DNA intercalator – and pomalidomide (Poma) – an anti-angiogenic and immunomodulatory agent.^{29–31} These drug delivery systems are preferentially cytotoxic to cancer cells *in vitro*, while also being efficient at inhibiting angiogenesis in tube-formation assays *in vitro*. Nanogels are a highly versatile system in which drug release profiles can be controlled *via* polyelectrolyte coating and/or various external stimuli, showing good biocompatibility and biodegradation *in vitro*. The final nanogels thus offer a stable platform that can be prepared by straightforward

production methods and used to deliver several drugs, with both hyperthermia and photothermal ablation therapy characteristics.

RESULTS AND DISCUSSION

Formation of polyelectrolyte coated AuNP decorated PEGMA nanogels

The thermoresponsive nanogels used for the loading and co-delivery of the two selected drugs were based on poly(ethylene glycol) methyl ether methacrylate (PEGMA), and formed by the well-established free radical polymerization method.^{32–34} PEGMA nanogels were chosen because of their easy-to-tailor lower critical solution temperature (LCST), ranging from room temperature up to 90 °C,^{35,36} and because their monomer constituents are non-toxic.³⁷ These are two major advantages, as compared *e.g.* to the widely used poly(N-isopropyl acrylamide) (pNIPAM).^{38,39} In the second step of the synthesis, a surfactant-free method was used to incorporate light responsive (plasmonic) AuNPs within the PEGMA nanogels, thereby avoiding potential toxicity of surfactants and keeping the AuNPs surface free to adsorb other molecules (**Figure 1a**). To this purpose, pre-made nanogels were immersed in a solution of HAuCl₄, followed by addition of a strong reducing agent, NaBH₄. The amino groups in the nanogels (present in the monomer 2-aminoethyl methacrylate hydrochloride) coordinate the gold precursor and small gold seeds of approximately 3 nm were formed upon NaBH₄ reduction. These seeds were subsequently grown by addition of HAuCl₄, sodium bromide and formaldehyde, which displays a pH-dependent reducing potential.⁴⁰ Sodium bromide helped in controlling AuNP growth due to the formation of a gold bromide complex with higher stability as compared to free HAuCl₄. When the process was carried out, in the absence of either Au seeds or sodium bromide, nanogels were obtained with particle

disparity, anisotropy and aggregation (**Figure S1**, Supporting Information). On the contrary, seeded growth produced nanogels with evenly distributed AuNPs with an average size of 23.2 ± 6.1 nm and a low proportion of anisotropic particles (**Figure 1b**). The nanogel containing AuNPs displayed a localized surface plasmon resonance (LSPR) band centered at 540 nm (**Figure 1c**), which is redshifted with respect to free AuNPs with similar sizes due to some anisotropy and plasmon coupling between the AuNPs in the gel. This two-step process allows a good level of control over the final AuNP size, which can range from 9 to 30 nm simply by tuning the amount of Au seed-loaded nanogels added to the growth solution (**Figure S2**). PEGMA nanogels were subsequently wrapped with biodegradable and biocompatible polyelectrolytes to modify the release profile of encapsulated drugs, and to add a coating that can easily bind other functional moieties (such as antibodies or dyes) for future applications.⁴¹ Functionalization was carried out by immersing AuNP-loaded nanogels in the appropriate polyelectrolyte solution followed by several washing steps to remove non-adsorbed polyelectrolytes. Samples with different surface compositions were named as follows: 1) AuNG1 had no coating, 2) AuNG2 was coated with poly-L-arginine and 3) AuNG3 was coated with polyalginate. We studied the influence of the two different coatings, *i.e.* the polypeptide poly-L-arginine and the polysaccharide polyalginate, on the physicochemical properties of the nanogels, and their drug loading and release profiles for both Doxo and Poma.

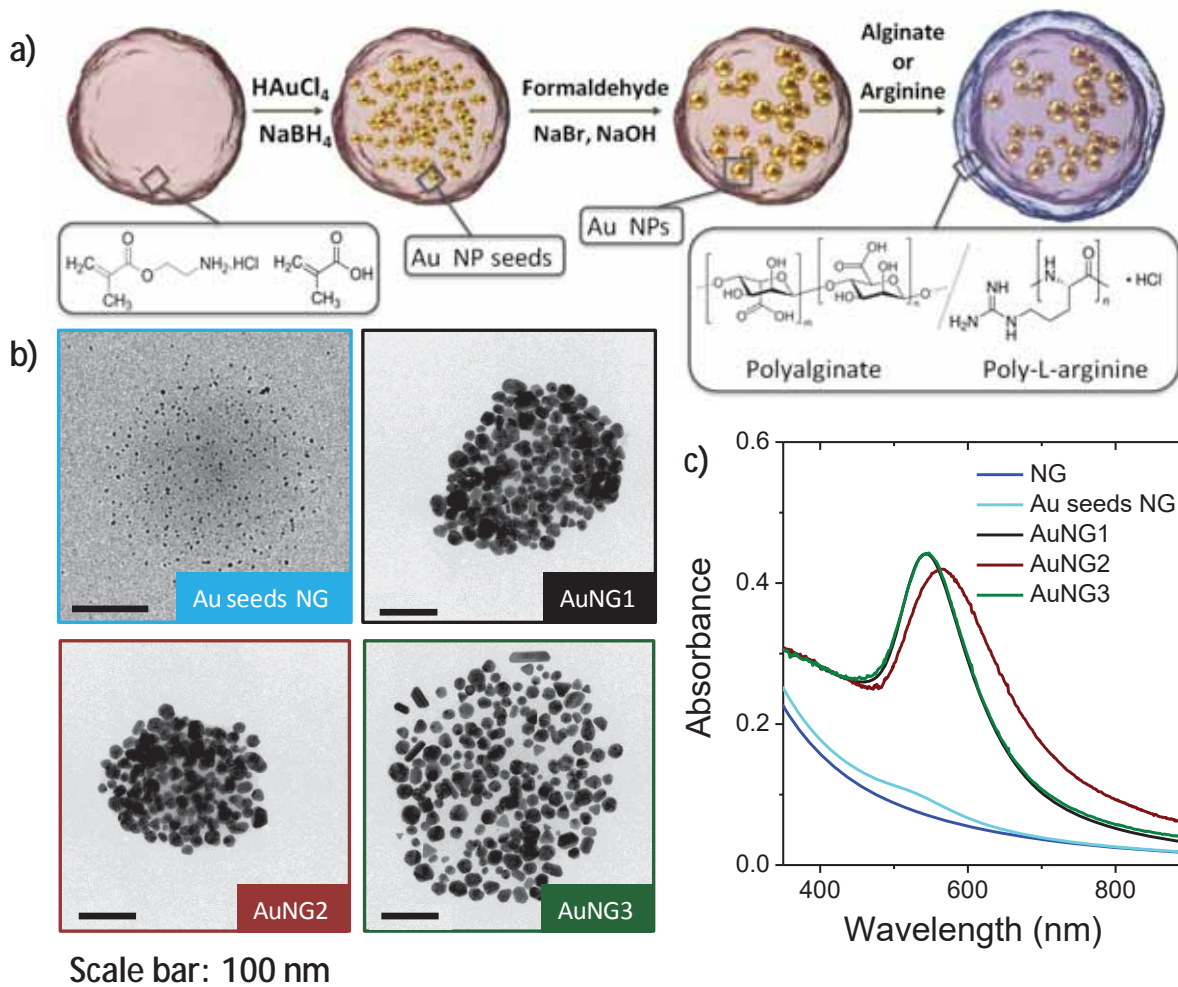


Figure 1. a) Schematic representation of the in-situ growth of gold nanoparticles in PEGMA nanogels. Small gold seeds were synthesized by reduction with NaBH₄. Further growth was realized by introducing the nanogels with seeds in a growth solution containing NaBr and formaldehyde at high pH. The obtained nanogels were finally wrapped with a layer of polyelectrolyte. b) Representative TEM pictures of the nanogels during the different growth steps, as labeled. c) UV-Vis spectra of the corresponding particle colloids.

Influence of polyelectrolyte coatings on the physicochemical properties of PEGMA nanogels

The presence of the polyelectrolytes on PEGMA nanogels was confirmed by X-ray photoelectron spectroscopy (XPS), zeta potential, LSPR and particle size analysis. XPS data showed a clear decrease in the amount of Au on the nanogel surface between coated and non-coated nanogels. Additionally, nitrogen was identified in sample AuNG2 due to

the amino groups in poly-L-arginine, whereas AuNG3 showed a higher amount of oxygen due to the hydroxyl and carboxyl groups in polyalginate, as compared with AuNG1. Changes in zeta potential, LSPR and particle size were also observed, as shown in **Table 1**. AuNG2 was found to become more compact upon polyelectrolyte addition, which in turn reduced the AuNP interparticle distance attached to the nanogels, resulting in stronger plasmon coupling and a LSPR red shift of 23 nm after functionalization (**Figure 1b,c**). The decrease in overall nanogel size observed in AuNG2 is due to the strong electrostatic interaction between the negatively charged nanogel and the positively charged polyelectrolyte causing the formation of a polyelectrolyte-gel complex.⁴² In some cases if the molecular weight of the coating molecule is low enough they can even penetrate the nanogel reducing the mesh size.⁴³ In contrast, functionalization with the anionic polyalginate did not modify the LSPR but caused slight swelling of the nanogel, presumably due to the weaker interactions between polyalginate and the nanogel.

Table 1. Differences in elemental composition, LSPR, zeta potential (ζ) and hydrodynamic diameter (D_h) of the coated and non-coated PEGMA nanogels.

Sample	N (at.%)	C (at.%)	O (at.%)	Au (at.%)	LSPR (nm)	ζ (mV)	D_h (nm)
AuNG1	0	64.3	24.8	10.9	544	-36.2 ± 0.2	274.1 ± 2.0
AuNG2	11.1	56.3	27	5.6	567	40.9 ± 0.3	223.8 ± 1.4
AuNG3	0	46.9	49.6	3.5	544	-34.5 ± 0.8	292.1 ± 4.4

In the context of physicochemical changes, it is worth highlighting the strong influence of polyelectrolyte coatings on the thermoresponsive behavior of PEGMA nanogels. Bare nanogels displayed a LCST above 30 °C (**Figure S11**) and the inclusion of AuNPs inside the nanogels did not hinder their ability to shrink or swell in response to heat changes (**Figure 2a**). In contrast, we noted significant differences in the swelling ratios (Q)

depending on the type of polyelectrolyte coatings. Q was defined as the ratio between the volume of the corresponding nanogel at a temperature T versus the volume at $70\text{ }^{\circ}\text{C}$ ($Q=V(T)/V(70\text{ }^{\circ}\text{C})$). **Figure 2b** illustrates the observed decrease in Q for coated PEGMA nanogels. The largest decrease of Q between coated and non coated nanogels was observed for AuNG2, which almost completely lost its thermoresponsiveness. This result is in agreement with the reduction in particle size upon coating with poly-L-arginine. Interestingly, the LCST increased from $32\text{ }^{\circ}\text{C}$ in AuNG1 to $36\text{ }^{\circ}\text{C}$ and $37\text{ }^{\circ}\text{C}$ for AuNG2 and AuNG3 respectively, closer to physiologically relevant temperatures.

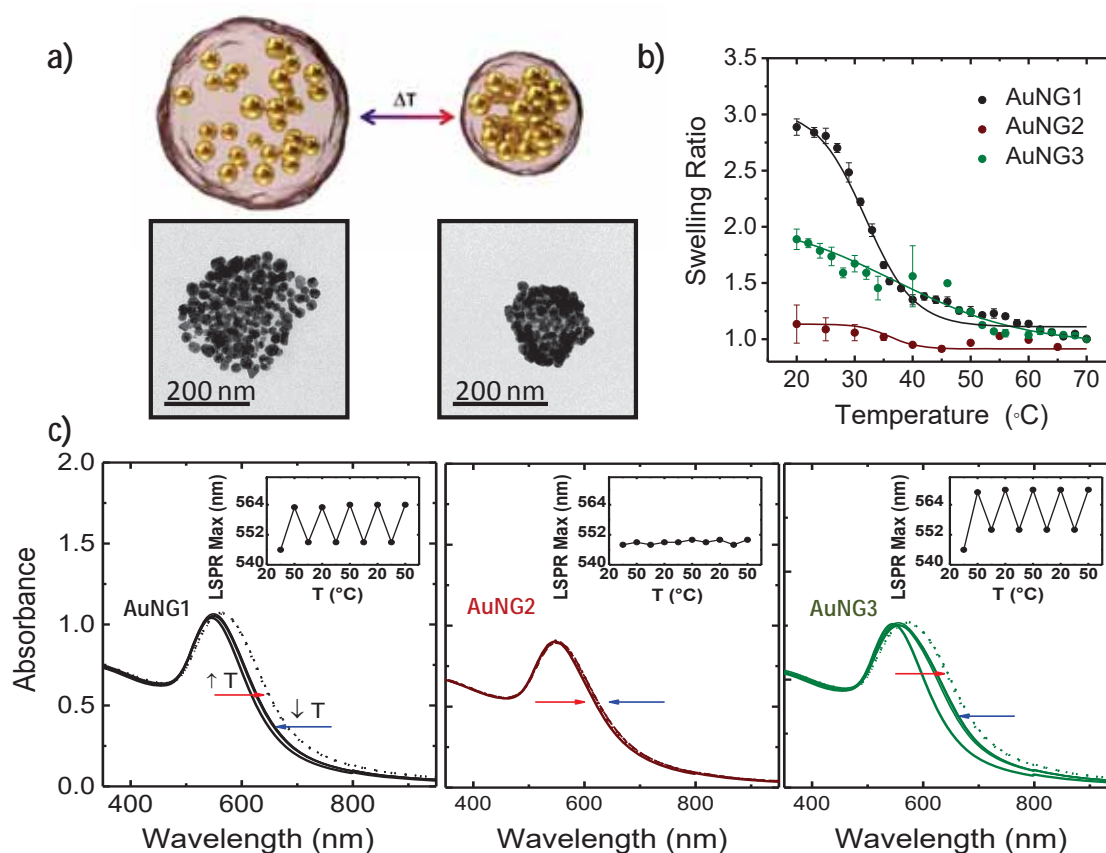


Figure 2. a) Schematic representation of the shrinking process and representative TEM pictures in collapsed and swollen states. b) Dynamic light scattering monitoring of the swelling ratio in AuNGs. c) UV-Vis spectra of the nanogels, alternating at $20\text{ }^{\circ}\text{C}$ and $50\text{ }^{\circ}\text{C}$, plotted as solid and dashed lines, respectively. The insets show the LSPR maxima during each cycle.

These results were confirmed with UV-Vis spectroscopy. As expected, the thermoresponsive decrease in the volume of the nanogel led to smaller inter-particle distances and hence to a red shift and broadening of the LSPR band. AuNG1 and AuNG3 behave similarly, with an approximate red shift of 14 nm between 20 and 50 °C. We verified the reversibility of the shift by carrying out multiple heating/cooling cycles. The shift was fully reversible over 5 temperature cycles (**Figure 2c, inset**). AuNG2, in contrast, shows no change of the LSPR, in accordance with the low Q value ($Q= 1.1$). Interestingly, the thermoresponsive behavior of coated PEGMA nanogels was observed to further change after encapsulation of drugs, in such a way that AuNG2 recovered its thermal responsiveness (**Figure 3a**). Further detailed information about the thermal behavior of different formulations of PEGMA nanogels has been included in the Supporting Information.

In addition to the described physicochemical differences, the colloidal stability between coated and non-coated PEGMA nanogels was studied by incubating them in different media of biological interest and analyzing the corresponding values of LSPR maxima and zeta potential.⁴⁴ AuNG3 displayed higher colloidal stability in non-supplemented cell culture media as compared with AuNG1 and AuNG2, which aggregated due to the high ionic strength, as previously reported for different polymer coated AuNPs. All PEGMA nanogels showed colloidal stability in cell culture media supplemented with serum due to protein adsorption (data shown in the Supporting Information).⁴⁵

Influence of polyelectrolyte coatings on stimulated drug delivery

Drug loading was achieved by immersing AuNP decorated PEGMA nanogels in an aqueous solution of drugs in basic conditions, and quantified by the decrease of drug

concentration in solution after loading. The maximum loading of Doxo was 0.33 mol/mg(Au) for AuNG1 and AuNG3, and 0.30 mol/mg(Au) for AuNG2. The encapsulation of Poma was less efficient with only 0.025 mol/mg(Au) for AuNG1, 0.019 mol/mg(Au) for AuNG2 and 0.020 mol/mg(Au) for AuNG3. For the sake of simplicity we discuss in the main text the loading and release behavior of Doxo alone, though a similar analysis was carried out for Poma and is discussed in the Supporting information. The entrapment of drugs was possible due to attractive interactions between Au decorated PEGMA nanogels and Poma and Doxo. Both electrostatic interactions and hydrogen bonding may be involved in the loading of the nanogels, due to the presence of carbonyl and ester groups in the nanogel and amino groups in both drugs.⁴⁶ In fact, a change in the zeta potential of the nanogels toward more positive values after drug encapsulation was observed, as previously reported for similar nanogels.⁴⁷ **Figure 3** shows the influence of polyelectrolyte presence on Doxo release from PEGMA nanogels, as a function of increasing temperature. Both polyelectrolytes shifted the thermal release to temperatures above 37 °C, as compared to the non-coated AuNG1 (**Figure 3a**). However, poly-L-arginine (AuNG2) hindered more the uncontrolled leakage of Doxo from the nanogel compared to polyalginate (AuNG3), but also made PEGMA nanogels less efficient at thermally triggered release. **Figure 3b** shows an 18-fold increase for AuNG3 but only a 5-fold increase for AuNG2, of released Doxo between room temperature and 50 °C.

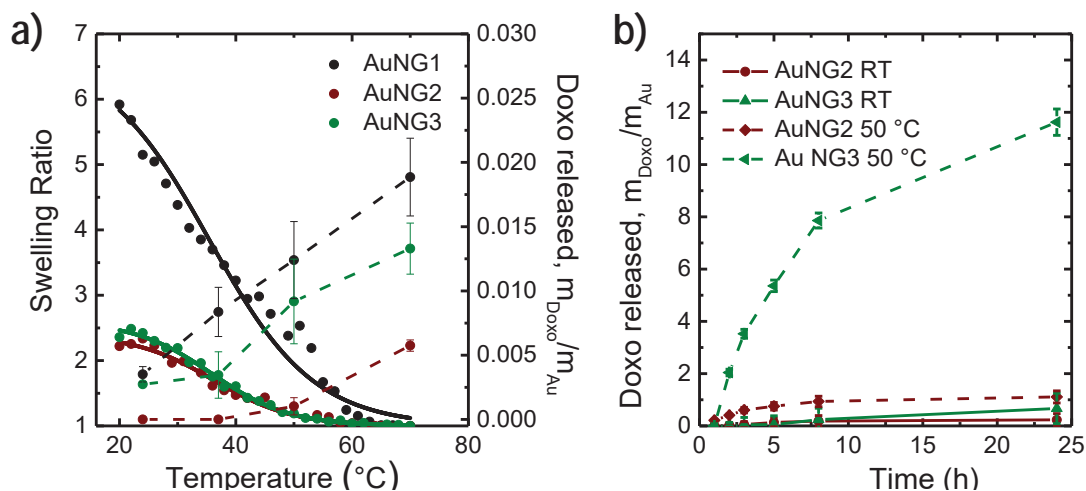


Figure 3. a) Dynamic light scattering measurements showing the correlation between the decrease in the swelling ratio (solid lines) of AuNG1, AuNG2 and AuNG3 and the increase in Doxo release (dashed lines) with the increase of temperature. b) Cumulative Doxo release over time at room temperature (solid lines) and at 50 °C (dashed lines).

Near-infrared (NIR) light, glutathione (GSH) and pH were also confirmed to trigger the release of drugs from AuNP decorated PEGMA nanogels, *via* different mechanisms (**Figure 4a-c**). The interaction of NIR light with AuNPs inside the nanogels led to shrinkage and in turn remotely controlled release of drugs due to the photothermal effect. Upon continuous NIR illumination (808 nm, 8.3 W/cm²), an initial increase in both the recorded temperature and Doxo release were noted, followed by a plateau in both measurements after ca. 10 minutes (**Figure 4a**).

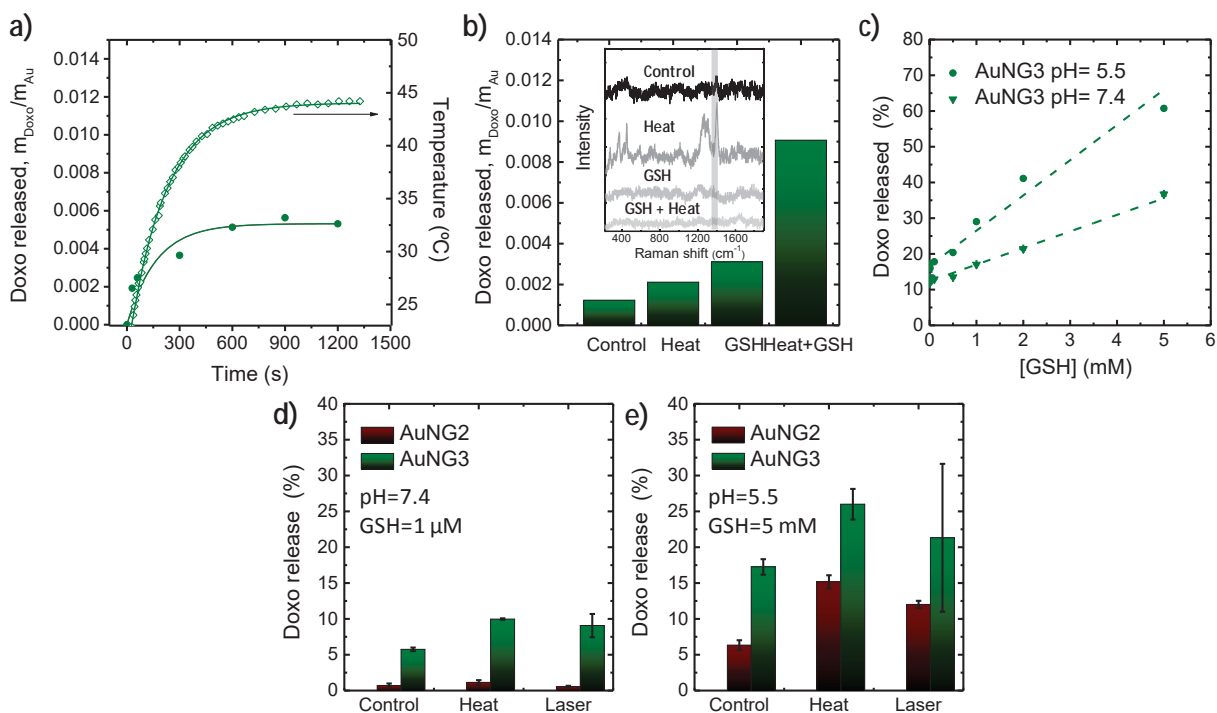


Figure 4. a) Temperature increase (open circles) of AuNG3 solution under NIR illumination (808 nm, 8.03 W/cm²) and the corresponding doxorubicin release (filled circles). b) Doxo release from AuNG3 upon heating and/or GSH addition and corresponding SERS spectra (inset). SERS spectra were recorded in solution at a concentration of 5 $\mu\text{g/mL}$ (Au), $P_{\text{laser}} = 12\text{mW}$ for 633 nm and $t_{\text{int}} = 20\text{s}$ with a 10x objective (NA=0.35). The assigned band at 1420 cm^{-1} is highlighted with a grey background. c) pH influence on the release of Doxo at different [GSH]. d,e) Summary of the different Doxo release efficiencies comparing the delivery at room temperature (control) versus the delivery upon the application of external stimuli, NIR light and heat (50 $^{\circ}\text{C}$) in solutions mimicking the extracellular (d) and intracellular environment (e).

The mechanism of drug release triggered by heating (including NIR light irradiation) and subsequent nanogel shrinkage can be related to the removal of hydrogen bonding between the drugs and the nanogel itself, but also to the decrease in the radius of the nanogel and shortening of the diffusion path for entrapped drugs. In contrast, drugs that are released through reduced temperature induced swelling of nanogels have been shown to diffuse faster when the mesh size of the hydrogel increases due to hydrogen bonding with water molecules.^{48,49} It should be noted that, realistically, the required temperature decrease is hard to achieve in biological systems. The release mechanism of Doxo and Poma at different temperatures from AuNG2 and AuNG3 was analyzed using the semi-empirical

Peppas model,⁵⁰ obtaining in both cases values of the release exponent n corresponding to the anomalous transport regime ($0.43 < n < 0.85$), which represents a mixture between diffusion-controlled release and other mechanisms (see Supporting Information).

GSH was also found to enhance drug release from AuNP decorated PEGMA nanogels. This trigger is of interest for intracellular drug delivery since its concentration is over 200 fold higher within cells (0.2-10 mM) than in the extracellular environment (2-20 μ M).^{51,52} To compare the GSH triggered Doxo release with that induced by heating, we exploited the ability of AuNPs to induce surface enhanced Raman scattering (SERS). SERS was used to identify Doxo within the AuNG3 nanogel after incubation with GSH, after heating and after both heating and GSH incubation, and the signals were compared to the corresponding fluorescence intensity of Doxo delivered to the supernatant from the nanogel. **Figure 4b** shows that both GSH and heat triggered the release of Doxo from the nanogel, and both triggers, acting in synergy, released 1.8 times more than the sum of the two triggers separately (30 min incubation time, $T = 50$ °C, [GSH] = 5 mM). The presence of Doxo was monitored using the characteristic SERS peak at 1420 cm^{-1} (corresponding to the C-O-H and C-H bending mode). The temperature increase enhanced the signal of Doxo as compared with the control experiment at room temperature, due to shortening of the inter-particle distances, which is known to induce a further enhancement of the Raman signal. However, upon application of both T increase and GSH, the Doxo signal vanished faster than by only heating. The release mechanism of GSH could be related to ion displacement,²³ since it is known that GSH adsorbs onto AuNPs and polymers and can trigger this kind of release mechanism intracellularly.^{53,54} In addition, we observed degradation and disassembly of the Au decorated PEGMA nanogels, both after GSH

exposure in solution and in *in vitro* experiments, which would subsequently enhance drug release (Supporting Information).

pH changes affect hydrogen bonding,⁵⁵ as well as charges on amino and carboxylic groups in the nanogels. As pH is also known to considerably decrease during the endocytotic pathway in cells, we studied the effect of pH on the release of Doxo from the nanogels. By exposing AuNG3 to pH 7.4 or pH 5.5, values that are representative of the extracellular and intracellular environment respectively, we noted a 2-fold increase in Doxo release. Additionally, the increased Doxo release at low pH was more pronounced in the presence of GSH at the usual concentrations in the intracellular environment (**Figure 4c**). We subsequently compared how all the aforementioned triggers can affect drug release in an environment mimicking both extracellular and intracellular conditions. **Figure 4d,e** shows that intracellular conditions enhance Doxo release induced by both heat and NIR illumination. Moreover, the polyelectrolytes on the nanogels surface caused significantly different drug release profiles, AuNG2 being more efficient in avoiding drug leakage, whereas all triggers enhanced drug release from AuNG3. We therefore conclude that AuNG3 appears to release higher amounts of Doxo, yet AuNG2 releases the same drug in a more controlled way under the effect of different triggers (**Figure S14**). A similar study was carried out for the release of Poma (**Figure S14**). In this case, release was more significantly affected at intracellular conditions (high [GSH] and low pH) than by the application of external stimuli. AuNG2 were more efficient in releasing Poma than AuNG3 and uncontrolled leakage was similar for both types of nanogels. The different release profiles shown in our work are key when selecting the appropriate carrier for a specific drug that could demand a faster release or which is very toxic and should be only released at the target cells.

Modulation of cellular uptake *in vitro*

Polyelectrolyte shells on AuNG2 (poly-L-arginine) and AuNG3 (polyalginate) were shown to affect nanogel uptake by both cancer and non-cancer cells, due to the different composition and surface charge of the nanogels. Taking into consideration that the increased metabolic activity of cancer cells compared with non-cancer cells can be exploited to improve nanogel uptake,⁵⁶⁻⁵⁸ we conducted a co-culture of HeLa cancer cells with healthy human dermal fibroblasts (HDF) to determine the differences in nanogel endocytosis. Using fluorescence microscopy and TEM we observed higher levels of endocytosis for AuNG2, as compared to AuNG3 (**Figure 5**). Flow cytometry determined the levels of AuNG2 and AuNG3 uptake in this co-culture, measured 24 h after a short 2 h incubation. The percentages of HDF cells positive for Doxo (used as a fluorescent label) were 75.6% and 33.7% for AuNG2 and AuNG3 nanogels, respectively, whereas the percentage of HeLa cells positive for Doxo were 99.4% and 75.6% for AuNG2 and AuNG3, respectively. This shows significant differences in cell specificity which can indeed be ascribed to the enhanced metabolic rates of cancer cells, as well as increased levels of AuNG2 uptake compared to AuNG3 due to the overall cationic charge of the AuNG2 system. Cationic nanoparticles and also molecules with overall positive charges (e.g cell penetrating peptides) are well known to associate with cell membranes to higher levels than their anionic counterparts. As expected, incubation of cells (both cancerous and healthy) with free Doxo resulted in rapid nuclear localization, whereas Doxo containing AuNG2 and AuNG3 were localized in endosomes (**Figure 5a,b**). Similar results were obtained with breast cancer MCF-7 cells (**Figure S19**), in agreement with previous

studies.⁵⁶ However, such increased levels of uptake in cancer cells did not correlate with higher drug release *in vitro* (Figure 6).

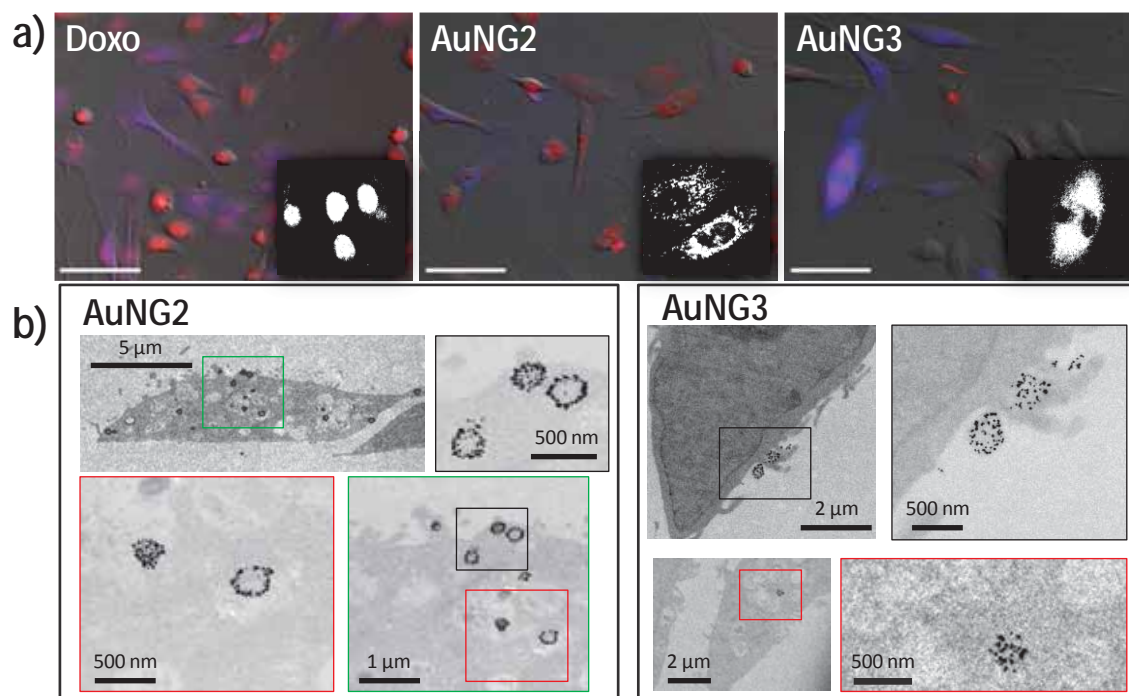


Figure 5. a) Cellular uptake of free Doxo, AuNG2 and AuNG3 nanogels. A co-culture of HeLa (unstained) and HDF (blue stained) cells were exposed to Doxo and Doxo containing AuNG2 and AuNG3 for 2 h and uptake visualized using Doxo fluorescence (shown in red in main images or in white in inserts for clarity). Clear nuclear (left image) or endosomal staining (middle and right images) is seen after free or nanogel delivered Doxo, respectively. Scale bars are 100 μm. b) TEM images of HeLa cells exposed to AuNG2 and AuNG3 for 2 h and then processed the following day for TEM imaging. Magnified photos are shown in color coded boxes.

Modulation of co-delivery *in vitro*

The effect of the two drugs Poma and Doxo was measured separately because they affect cells through different molecular mechanisms. We first verified that the increased levels of AuNG-PEGMA nanogel uptake by cancer cells compared to non-cancer cells resulted in downstream cell death. As seen in Figure 6a, whilst free Doxo resulted in cell death of both cancer and non-cancer cells in the co-culture system, exposure to Doxo-containing AuNG2 and AuNG3 caused predominate cytotoxicity to cancerous HeLa cells whilst HDF cells remained viable. The presence of Poma within the nanogels was verified as not

inducing any cytotoxic effects (**Figure S20**). The high levels of cytotoxicity noted in HeLa cells was slow, occurring ca. 4 days after the initial exposure of the cells to the AuNG-PEGMA nanogels. We subsequently investigated the use of NIR light as a method to improve Doxo release and subsequent cell death, compared to non-illuminated controls. NIR-light illumination of HeLa cells incubated with AuNG-PEGMA nanogels resulted in a significant decrease in the viability over the non-illuminated cells (**Figure 6b**). Non-Doxo loaded nanogels (AuNG*) were used as second control, showing that it was possible to induce hyperthermia with AuNP-PEGMA nanogels, which is interesting for combined therapy as previously reported for other drug delivery systems.⁵⁹ However, we verified that there exists an enhancement of Doxo release under NIR light illumination *in vitro* when lower power densities are applied, thereby avoiding hyperthermia (**Figure S21**).

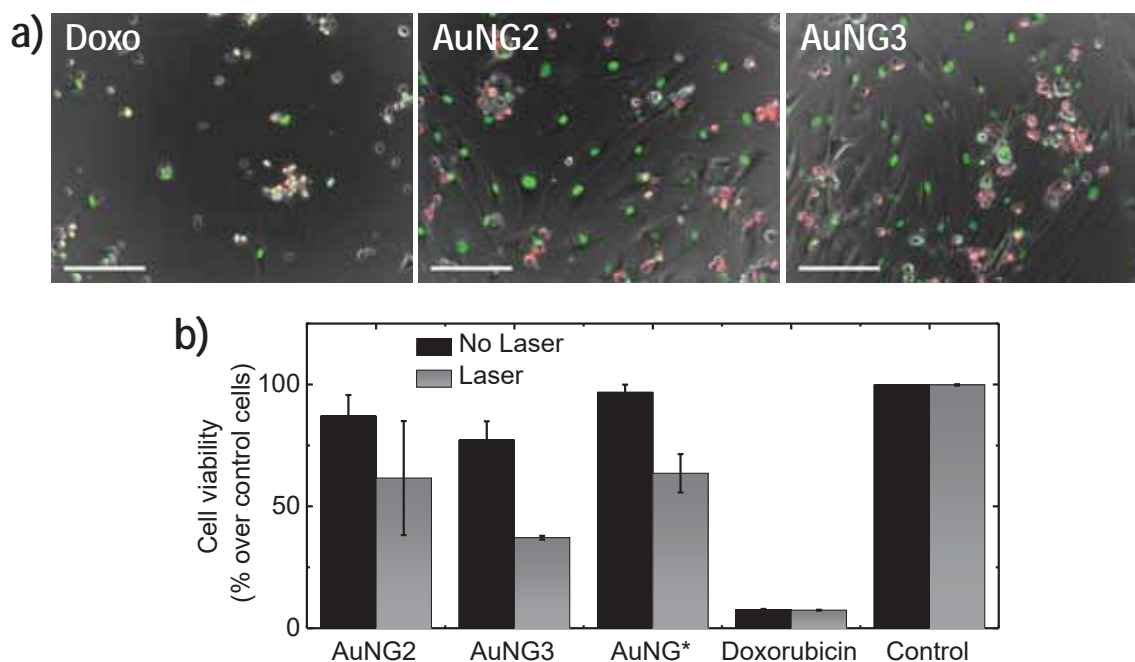


Figure 6. a) Live/Dead staining of HeLa/HDF co-cultures, ca. 4 days post initial exposure to free Doxo, or Doxo-containing AuNG2 and AuNG3. Live cells show green-channel fluorescence whilst dead cells uptake propidium iodide and are positive for red channel fluorescence. The predominant live population (green) are HDF cells which can be identified by their characteristic shape, whereas HeLa cells are the majority “dead” population. Scale bars are 200 μm . b) NIR-laser induced hyperthermia and photo-thermal-induced cytotoxicity of HeLa cells. HeLa cells were exposed to Doxo-containing AuNG2 and AuNG3, or non-Doxo control nanogels (AuNG*) for ca. 12h, followed by illumination with an

808 nm diode laser at 16 W/cm² for 20 minutes. Cell viability was measured the following day using the MTT assay (mean of triplicate wells +/- SD).

The drug Poma has been shown to be highly efficient at inhibiting angiogenesis,³¹ in addition to a wide variety of immune system modifying effects such as the inhibition of cytokine production in LPS-stimulated peripheral blood mononuclear cells (PBMCs),⁶⁰ thereby placing it in the group of immunomodulatory drugs (IMiDs).⁶¹ We took advantage of these immunomodulatory effects as a method to verify that Poma remained active after release from AuNG nanogels. In order to do so we exposed LPS-stimulated J774 murine monocyte-macrophage cells to AuNG2 and AuNG3, containing Poma alone or Doxo and Poma, and determined the levels of IL-6 cytokine produced. Compared to non-exposed controls, IL-6 levels were reduced by 90 %, similar to exposure to free Poma (**Figure S22**). No significant differences in the ability of AuNG2 and AuNG3 to inhibit LPS-induced IL-6 were observed, nor did the presence of Doxo in the formulations hinder Poma. We next investigated the ability of Poma containing nanogels to inhibit angiogenesis in an *in vitro* tube formation model. Due to the short time span of the assay (“tubes” form within hours and cells die naturally at approximately 24 h post planting), we pre-incubated HUVEC cells with Poma-containing nanogel formulations overnight, and the following day we planted the nanogel-containing HUVEC cells on the tube-inducing gel support. **Figure 7a** shows the effective inhibition of tube formation when healthy HUVEC cells, otherwise capable of tube formation, were pre-incubated with both Poma- containing AuNG2 or AuNG3, at a concentration equivalent to 10 μ M. On the contrary, HUVEC cells pre-incubated with Au decorated PEGMA nanogels without Poma were able to form tubes (**Figure S23**), as expected. In addition to Poma effects on HUVEC cells when grown under angiogenesis-

stimulating conditions, the cell surface area and the aspect ratio (AR) of HUVEC cells were significantly reduced upon exposure to Poma-containing nanogels when grown under “normal” tissue culture conditions (**Figure 7b,c**). IMiD compounds have been shown to activate GTPases, enzymes which are responsible for cellular cytoskeleton reorganization, cellular differentiation and movement.⁶² In fibroblasts, Poma has been shown to induce formation of actin stress fibers,⁶² and changes of cell area and aspect ratio have been documented upon exposure of cells to both anti- and pro-angiogenic molecules.^{63,64} Considering that the production of pro-angiogenic molecules such as VEGF and bFGF is inhibited by a cascade of signaling pathways due to pomalidomide’s ability to down-regulate cell adhesion molecules and reduce VEGF, bFGF and IL-6 secretion,⁶⁵ it is reasonable to assume that Poma will affect cell surface area. Exposure of HUVEC cells to Poma-containing nanogels resulted in a decrease in cell size, reducing the surface area by 1/3 – 2/3 of the original value. The decrease in cell surface area and aspect ratio was more pronounced for Poma-containing AuNG2 than for AuNG3, which can be correlated with an enhanced cell uptake of these nanogels, but also with the higher degree of Poma release observed in solution. Interestingly, we did not observe any similar effects upon exposure of HUVEC cells to free Poma, which suggests that these IMiD mediated changes in cell morphology are highly dependent on exposure time and subsequent Poma release from nanogel formulations.

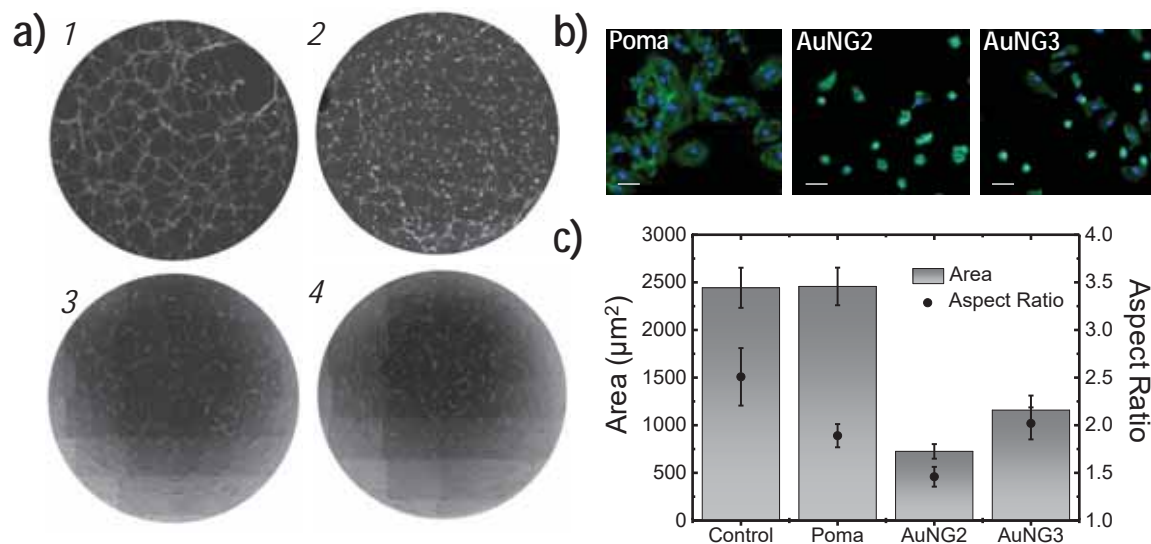


Figure 7. a) The angiogenesis tube formation assay shows the ability of HUVEC cells to grow vessel-like interconnecting networks through the aid of growth factors present in the underlying gel. In cases where no nanogels were applied (1), established tube formation is seen within 6 h, yet with HUVEC cells pre-incubated with AuNG2 (3), or AuNG3 (4), or HUVEC cells incubated with free pomalidomide (2), poor or no tube-formation is seen. Each image (circle) is 4 mm in diameter showing the whole well. b) HUVEC cells incubated with free Poma, AuNG2 or AuNG3 for 4 h at a final Poma concentration of 10 μ M. Cells were washed, fixed and stained with Dapi and AF488-phalloidin to show the nucleus and actin fibers respectively. Scale bars are 50 μ m. c) Area and aspect ratio (AR) of cells described in (b), measured using ImageJ from at least 30 cells from 3 separate images. Mean \pm SD is shown.

CONCLUSIONS

In summary we synthesized a versatile multiresponsive drug delivery system based on thermoresponsive nanogels containing gold nanoparticles for the co-delivery of doxorubicin and pomalidomide. The gold nanoparticles inside the nanogel were synthesized in a new two-step method to ensure even particle distribution throughout the gel and surfactant-free synthesis. The leakage of drugs was reduced by wrapping the nanogels with a polyelectrolyte shell. We studied two possible coatings: polyalginate and poly-L-arginine. These two coatings produced different modifications in the thermoresponsive behavior of the nanogels and other physicochemical properties that were characterized and influenced first, the stimuli responsive release of the two drugs and

second, their interaction with cells and their drug delivery *in vitro*. We showed that pH, glutathione concentration, heat and NIR-light can all trigger the release of drugs in an extent that was dependent on the chemical nature of the drug and the coating polyelectrolytes. Both coated nanogel systems showed enhanced uptake by cancer cells compared to non-cancer cells, due to their enhanced metabolism, but more specific uptake in cancer cells was seen for nanogels coated with positively charged polyalginate. Taking this into account and considering: 1) both polyelectrolyte coated PEGMA nanogels have low leakage and show a slow drug release profile, 2) the cytotoxic doxorubicin is released more efficiently by a remote controlled trigger (light) from AuNG3 than AuNG2 nanogels and 3) the release of pomalidomide was effective for the two nanogel formulations, we can conclude that polyalginate coated PEGMA nanogels can be considered as the more convenient drug delivery system for the remote controlled co-delivery of doxorubicin and pomalidomide.

METHODS

Materials. Milli-Q water (resistivity 18.2 M Ω ·cm) was used in all experiments. Hydrogen tetrachloroaurate trihydrate (HAuCl₄·3H₂O, \geq 99.9%), di(ethylene glycol) methyl ether methacrylate, poly(ethylene glycol) methyl ether methacrylate, poly(ethylene glycol) diacrylate, 2-aminoethyl methacrylate hydrochloride, methacrylic acid, formaldehyde (37 wt%), doxorubicin hydrochloride and poly-L-arginine hydrochloride (mol wt >70,000) were all purchased from Sigma-Aldrich. Pomalidomide was purchased from Abcam.

Alginic acid (sodium salt) was obtained from Fisher Scientific. All glassware was washed with aqua regia, rinsed 3 times with Milli-Q water and dried before use.

Synthesis of poly ethylene glycol methacrylate nanogel.

Nanogels were synthesized by purging a 300 mL Milli-Q water solution of 5.6 g di(ethylene glycol) methyl ether methacrylate, 2.4 g poly(ethylene glycol) methyl ether methacrylate, 160 mg poly(ethylene glycol) diacrylate, 297 mg methacrylic acid and 576 mg 2-aminoethyl methacrylate hydrochloride with argon for an hour at 70 °C. The reaction was then started by adding 120 mg of 2,2, azobis(2methylpropionamide)dihydrochloride dissolved in 2 mL of degassed Milli-Q water and run for 12 hours at 70 °C.

Synthesis of AuNP decorated nanogel.

After washing via centrifugation, 10 mL of nanogels were incubated with 50 μ L 0.1 M HAuCl₄ overnight before reduction of the gold occurs with addition of 100 μ L 0.1 M NaBH₄ solution. Small gold domains of about 3-4 nm were formed and stabilized by the amino group of 2-aminoethyl methacrylate hydrochloride. The nanogels were used as seeds for the growth of bigger gold particles without further purification. Further growth of AuNP was carried out with formaldehyde under basic conditions. A 100 mL growth solution with a final concentration of 1 mM HAuCl₄, 5 mM NaBr and different amounts of seeds was prepared followed by the addition of 500 μ L formaldehyde solution (37 wt%). The reduction was finally started by changing the pH to 11 through the addition of 750 μ L 1 M NaOH. The reaction was very slow due to the more stable gold-bromide complexes. After 15 minutes a color change was observed but the reaction was allowed to run overnight before particles were carefully washed via centrifugation and characterized (TEM and UV-Vis spectroscopy). By simply varying the amount of seeds, AuNP with different sizes were obtained.

Loading with Doxorubicin/Pomalidomide and addition of polyelectrolyte layer

Nanogels were loaded with drugs by immersing them in solutions of Doxo and/or Poma with a final concentration of 0.25 mM of each drug and a pH adjusted to ca. 8. The nanogels were incubated overnight and the addition of the polyelectrolyte layer was carried out without further purification. After mixing, the particles were gently shaken and the mixture was incubated for 30 min. Nanogels and polyelectrolytes were mixed in a 1:1 volume ratio. The solutions of polyelectrolytes were prepared with a concentration of 1 mg/mL poly alginate, 0.5M NaCl adjusted to pH=5 and 0.5 mg/mL poly-L-arginine and 0.5 M NaCl. Thereafter, nanogels were purified by centrifugation (6 times, 2240 g for 15 min) and the supernatants were collected to calculate the loading of every drug by fluorescence spectroscopy (Varioskan Flash from Thermo Scientific) and ultra performance liquid chromatography (Acquity).

Drug release via NIR-illumination

One hundred μ L of AuNG samples was placed in a 96-well transparent microplate and laser irradiation was carried out using a 808 nm fiber coupled laser diode with a maximum power of 4 W (Lumics). The spot size was chosen to illuminate the whole well at once (0.4 cm in diameter) and the power and time was adjusted to obtain the desired power density used for the experiments.

Co-culture and Live/Dead staining

Human dermal fibroblast (HDF; Invitrogen) cells were stained in suspension for 1 h, 37 °C, using Cell Tracker Blue CMF2HC (Invitrogen) at a final dilution of 1/100 in FBS free DMEM. Cells were washed and mixed 1:1 with unstained HeLa cells (a gift from Prof. Charles Lawrie, Biodonostia) and plated at a final cell number of 1×10^4 cells/well in a 96-well plate (Ibidi μ -plate 96-well). The following day media was replaced with doxorubicin

(4 $\mu\text{g}/\text{mL}$; Sigma Aldrich) and nanogel solutions (diluted 1/25, equivalent to 4 $\mu\text{g}/\text{mL}$ doxorubicin), 200 $\mu\text{L}/\text{well}$. PEGMA nanogels were incubated with cells for 2.5h, followed by washing with warm PBS (10 mM, pH 7.4) and replacement of the medium. Images were taken at various time points, after removal of nanogel solutions, using a 20 \times objective with DIC contrast and red and blue fluorescence channels for doxorubicin and Cell Tracker Blue (HDF cells) fluorescence respectively. A Zeiss Cell Observer microscope with AxioVision software was used.

The same cultures were used to analyze cell viability using Live/Dead (Abcam) staining after ca. 96 h. Media was replaced with 150 μL of warmed staining buffer containing 1/1000 dilutions of both “live” and “dead” fluorophores. Cells were left at 37 $^{\circ}\text{C}$ for 15 min and then imaged using a 10 \times objective with phase contrast and green and red fluorescence channels for “live” and “dead” staining respectively. Due to the late timepoint, HDF cells were no longer positive for Cell Tracker Blue and therefore visual comparison of cell morphology alone was used to differentiate between dead cell populations. A Zeiss Cell Observer microscope with AxioVision software was used.

Flow cytometry

Human dermal fibroblast cells were stained in suspension for 1 h, 37 $^{\circ}\text{C}$, using Cell Tracker Blue CMF2HC at a final dilution of 1/100 in FBS free DMEM. Cells were washed and mixed 1:1 with unstained HeLa cells and plated in a 24-well plate at 5×10^4 cells/well. The following day media was replaced with doxorubicin (4 $\mu\text{g}/\text{ml}$) and nanogel solutions (diluted 1/25, equivalent to 4 $\mu\text{g}/\text{ml}$ doxorubicin), 500 $\mu\text{L}/\text{well}$. PEGMA nanogels were incubated with cells for 2h30, followed by washing with warmed PBS (10 mM, pH 7.4) and replacement of the media. The following day cells were lifted up using trypsin-EDTA and

washed twice with ice-cold PBS. Samples were analysed in 1 % BSA/PBS on a BD Canto II flow cytometer using compensation. Cells were gated using the Pacific Blue channel (HeLa vs. CMF₂HC-stained HDF cells), and then the % of doxorubicin positive cells measured in the PE channel.

Cell viability; irradiation experiments

HeLa cells were plated in a 96-well TC-treated transparent plate at 5×10^4 cells/mL, 100 μ L/well. The following day media was replaced with doxorubicin (4 μ g/mL) and NP solutions (diluted 1/25, equivalent to 4 μ g/mL doxorubicin), 100 μ L/well. NPs were left overnight with cells (approx 18 h) followed by replacement of the cell media. Individual wells were irradiated using a 808 nm fiber coupled laser diode with a maximum power of 4 W (Lumics). The spot size was chosen to illuminate the whole well at once (0.4 cm in diameter) and the power and time was adjusted to obtain the desired power density used for the experiments. The following day cell viability was analysed using the MTT assay (Roche) and absorbance measured at 550 nm, showing both non-irradiated and irradiated wells.

Transmission electron microscopy of cells

HeLa cells were grown in 60 mm diameter tissue culture treated petri dishes, 1×10^6 cells/3 mL/dish. The following day, nanogels were added at a final dilution of 1/50, 3 ml/dish. PEGMA nanogels were incubated with cells for 2 h, followed by washing with warm PBS and replacement of the medium. The day after, cells were fixed in the dish using 2 % formaldehyde/2.5 % glutaldehyde in Sorensens buffer (initial fixation of 10 min at rt, followed by secondary fixation with fresh solution for 2 h at 4°C). Fixative was removed and cells washed using cold Sorensens buffer. A cell scraper was used to bring the cells into suspension. Cells were embedded in 2% agar, followed by further fixation and staining

with a 1% osmium tetroxide solution for 1h on ice. Samples were washed with Sorensens buffer and then water, and dehydrated in an ethanol series, followed by 2 final pure ethanol and then pure acetone washes. Samples were embedded in Spurr's resin and polymerized overnight at 65 °C. One hundred nm slices were cut using an ultramicrotome and viewed using TEM (JEOL JEM-1400PLUS , 40kV - 120kV).

LPS-induced IL-6 production from J774 cells

J774 macrophages were plated in a normal tissue culture treated 96-well plate at a concentration of 2×10^5 cells/ml, 100 μ l/well. The following day half the wells were pre-treated with LPS (Sigma Aldrich) at a final concentration of 1 μ g/ml, 100 μ l/well. After 1 h of LPS-stimulation, a further 100 μ l of NPs (1/5 diluted, equivalent to a final pomalidomide concentration of 10 μ M) were added. Controls including free pomalidomide (a final pomalidomide concentration of 10 μ M), DMSO (final dilution of 1/5000 equivalent to the volume present in 10 μ M pomalidomide), and pomalidomide free NPs were included. The final volume was 200 μ l/well. Cells were incubated for 24 h, following which supernatants were removed and frozen for subsequent IL-6 analysis. Supernatants were analysed for IL-6 using standard sandwich ELISA with TMB substrate detection.

Angiogenesis assays

Human umbilical vein endothelial cells (HUVEC) were plated in a normal tissue culture 96-well plate at 1×10^6 cells/ml, 100 μ L/well. The following day nanogels were added at a final concentration equivalent to 10 μ M pomalidomide. Cells were incubated with PEGMA nanogels for 2 h, followed by washing with warmed PBS and replacement of the media. The following day 10 μ L of Geltrex (Invitrogen) was placed in the lower wells of an angiogenesis slide (Ibidi μ -slide Angiogenesis) and left to solidify at 37 °C for approximately 30 min. HUVECs, previously incubated with nanogels, were uplifted using

Trypsin-EDTA (Invitrogen), counted, and adjusted to 2×10^5 cells/ml. Fifty μL of cells were added to each well (1×10^4 cells), taking care not to disturb the gel. Control wells without nanogel pre-incubation and with direct pomalidomide ($10 \mu\text{M}$) incubation were included. Cells were imaged approximately 6 h post seeding with a Zeiss Cell Observer microscope equipped with a x10 objective with phase contrast. AxioVision software with the “Mosaix” application was used to image the whole well (4 mm diameter).

Pomalidomide-induced cell morphological changes

HUVEC cells were plated in a 96-well plate (Ibidi μ -plate 96-well) at a concentration of 4×10^4 cells/well, $200 \mu\text{L}$ /well. The following day media was replaced with the corresponding nanogel solution, $200 \mu\text{L}$ /well, at a final concentration equivalent to $10 \mu\text{M}$ pomalidomide. Pomalidomide-free nanogels at an equivalent concentration, and pomalidomide alone were also included. After 4 h, wells were washed with warmed PBS and fixed using a 4% formaldehyde solution in PBS. Cells were stained using DAPI (Invitrogen) and AF488-phalloidin (Invitrogen) to show the nucleus and actin fibers respectively. Images were taken using an EC Plan-Neofluar x40 oil objective with DIC contrast and filters for green (AF488-phalloidin actin staining), red (doxorubicin staining) and blue (DAPI nuclear staining) fluorescence. Cell area and aspect ratio (AR) values were calculated using ImageJ, analyzing 10 cells from 3 separate compound images composed of 9 tiles (in total ca. 30 cells/formulation).

ACKNOWLEDGMENTS

Funding is acknowledged from the European Research Council (ERC Advanced Grant#267867 Plasmaquo) and MINECO (project MAT2013-46101-R). M.S. acknowledges a co-funded PhD fellowship from University of Liverpool and CIC

biomaGUNE. We thank Dr. Andrea La Porta for his support on image representation, Dr. Luis Yate for XPS measurements and Dr. Javier Calvo for ICP-MS and UPLC measurements.

REFERENCES

- (1) Webster, R. M. Combination Therapies in Oncology. *Nat Rev Drug Discov* **2016**, *15*, 81–82.
- (2) Tacar, O.; Sriamornsak, P.; Dass, C. R. Doxorubicin: An Update on Anticancer Molecular Action, Toxicity and Novel Drug Delivery Systems. *J. Pharm. Pharmacol.* **2013**, *65*, 157–170.
- (3) Sun, T.; Zhang, Y. S.; Pang, B.; Hyun, D. C.; Yang, M.; Xia, Y. Engineered Nanoparticles for Drug Delivery in Cancer Therapy. *Angew. Chemie - Int. Ed.* **2014**, *53*, 12320–12364.
- (4) Blanco, E.; Shen, H.; Ferrari, M. Principles of Nanoparticle Design for Overcoming Biological Barriers to Drug Delivery. *Nat. Biotechnol.* **2015**, *33*, 941–951.
- (5) Truong-Le, V.; Lovalenti, P. M.; Abdul-Fattah, A. M. Stabilization Challenges and Formulation Strategies Associated with Oral Biologic Drug Delivery Systems. *Adv. Drug Deliv. Rev.* **2015**, *93*, 95–108.
- (6) Anselmo, A. C.; Mitragotri, S. Nanoparticles in the Clinic. *Bioeng. Transl. Med.* **2016**, *55*, 10/29.
- (7) Kakwere, H.; Leal, M. P.; Materia, M. E.; Curcio, A.; Guardia, P.; Niculaes, D.; Marotta, R.; Falqui, A.; Pellegrino, T. Functionalization of Strongly Interacting Magnetic Nanocubes with (Thermo)responsive Coating and Their Application in Hyperthermia and Heat-Triggered Drug Delivery. *ACS Appl. Mater. Interfaces* **2015**, *7*, 10132–10145.
- (8) Topete, A.; Alatorre-Meda, M.; Villar-Alvarez, E. M.; Carregal-Romero, S.; Barbosa, S.; Parak, W. J.; Taboada, P.; Mosquera, V. Polymeric-Gold Nanohybrids for Combined Imaging and Cancer Therapy. *Adv. Healthcare Mater.* **2014**, *3*, 1309–1325.
- (9) Meng, H.; Wang, M.; Liu, H.; Liu, X.; Situ, A.; Wu, B.; Ji, Z.; Hyun Chang, C.; Nel, A. E. Use of a Lipid-Coated Mesoporous Silica Nanoparticle Platform for Synergistic Gemcitabine and Paclitaxel Delivery to Human Pancreatic Cancer in Mice. *ACS Nano* **2015**, *9*, 3540–3557.
- (10) Lee, D.-E.; Koo, H.; Sun, I.-C.; Ryu, J. H.; Kim, K.; Kwon, I. C. Multifunctional Nanoparticles for Multimodal Imaging and Theragnosis. *Chem. Soc. Rev.* **2012**, *41*, 2656–2672.
- (11) Kamaly, N.; Yameen, B.; Wu, J.; Farokhzad, O. C. Degradable Controlled-Release Polymers and Polymeric Nanoparticles: Mechanisms of Controlling Drug Release. *Chem. Rev.* **2016**, *116*, 2602–2663.
- (12) Kim, C. S.; Mout, R.; Zhao, Y.; Yeh, Y.-C.; Tang, R.; Jeong, Y.; Duncan, B.; Hardy, J. A.; Rotello, V. M. Co-Delivery of Protein and Small Molecule Therapeutics Using

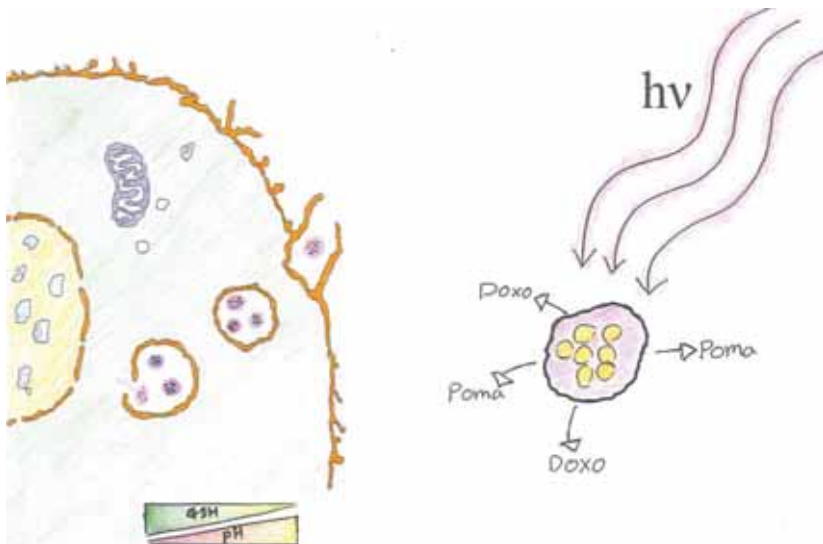
- Nanoparticle-Stabilized Nanocapsules. *Bioconjug. Chem.* **2015**, *26*, 950–954.
- (13) Torchilin, V. P. Multifunctional, Stimuli-Sensitive Nanoparticulate Systems for Drug Delivery. *Nat. Rev. Drug Discov.* **2014**, *13*, 813–827.
 - (14) Dhar S, Kolishetti N, Lippard SJ, F. O. Targeted Delivery of a Cisplatinprodrug for Safer and More Effective Prostate Cancer Therapy in Vivo. *Proc Natl Acad Sci U S A* **2011**, *108*, 1850–1855.
 - (15) Davis, M. E.; Chen, Z. G.; Shin, D. M. Nanoparticle Therapeutics: An Emerging Treatment Modality for Cancer. *Nat. Rev. Drug Discov.* **2008**, *7*, 771–782.
 - (16) Mackey, J. R.; Kerbel, R. S.; Gelmon, K. A.; McLeod, D. M.; Chia, S. K.; Rayson, D.; Verma, S.; Collins, L. L.; Paterson, A. H. G.; Robidoux, A.; *et al.* Controlling Angiogenesis in Breast Cancer: A Systematic Review of Anti-Angiogenic Trials. *Cancer Treat. Rev.* **2012**, *38*, 673–688.
 - (17) Welti, J.; Loges, S.; Dimmeler, S.; Carmeliet, P. Recent Molecular Discoveries in Angiogenesis and Antiangiogenic Therapies in Cancer. *J. Clin. Invest.* **2013**, *123*, 3190–3200.
 - (18) Wang, J.; Yang, Y.; Zhang, Y.; Huang, M.; Zhou, Z.; Luo, W.; Tang, J.; Wang, J.; Xiao, Q.; Chen, H.; *et al.* Dual-Targeting Heparin-Based Nanoparticles That Re-Assemble in Blood for Glioma Therapy through Both. **2016**.
 - (19) Gasparini, G. Combination of Antiangiogenic Therapy With Other Anticancer Therapies: Results, Challenges, and Open Questions. *J. Clin. Oncol.* **2005**, *23*, 1295–1311.
 - (20) Chu, K. F.; Dupuy, D. E. Thermal Ablation of Tumours: Biological Mechanisms and Advances in Therapy. *Nat. Rev. Cancer* **2014**, *14*, 199–208.
 - (21) Saxena, S.; Hansen, C. E.; Lyon, L. A. Microgel Mechanics in Biomaterial Design. *Acc. Chem. Res.* **2014**, *47*, 2426–2434.
 - (22) Sierra-Martin, B.; Retama, J. R.; Laurenti, M.; Fernández Barbero, A.; López Cabarcos, E. Structure and Polymer Dynamics within PNIPAM-Based Microgel Particles. *Adv. Colloid Interface Sci.* **2014**, *205*, 113–123.
 - (23) Kabanov, A. V.; Vinogradov, S. V. Nanogels as Pharmaceutical Carriers: Finite Networks of Infinite Capabilities. *Angew. Chemie - Int. Ed.* **2009**, *48*, 5418–5429.
 - (24) Li, J.; Mooney, D. J. Designing Hydrogels for Controlled Drug Delivery. *Nat. Rev. Mater.* **2016**, *1*, 16071.
 - (25) Li, Y.; Maciel, D.; Rodrigues, J.; Shi, X.; Tomás, H. Biodegradable Polymer Nanogels for Drug/nucleic Acid Delivery. *Chem. Rev.* **2015**, *115*, 8564–8608.
 - (26) Austin, L. A.; MacKey, M. A.; Dreaden, E. C.; El-Sayed, M. A. The Optical, Photothermal, and Facile Surface Chemical Properties of Gold and Silver Nanoparticles in Biodiagnostics, Therapy, and Drug Delivery. *Arch. Toxicol.* **2014**, *88*, 1391–1417.
 - (27) Huang, X.; Jain, P. K.; El-Sayed, I. H.; El-Sayed, M. A. Plasmonic Photothermal Therapy (PPTT) Using Gold Nanoparticles. *Lasers Med. Sci.* **2008**, *23*, 217–228.
 - (28) Weissleder, R. A Clearer Vision for in Vivo Imaging. *Nat. Biotechnol.* **2001**, *19*, 316–317.
 - (29) Dredge, K.; Marriott, J. B.; Todryk, S. M.; Muller, G. W.; Chen, R.; Stirling, D. I.; Dalglish, A. G. Protective Antitumor Immunity Induced by a Costimulatory Thalidomide Analog in Conjunction with Whole Tumor Cell Vaccination Is Mediated by Increased Th1-Type Immunity. *J. Immunol.* **2002**, *168*, 4914–4919.
 - (30) Reddy, N.; Hernandez-Ilizaliturri, F. J.; Deeb, G.; Roth, M.; Vaughn, M.; Knight, J.;

- Wallace, P.; Czuczman, M. S. Immunomodulatory Drugs Stimulate Natural Killer-Cell Function, Alter Cytokine Production by Dendritic Cells, and Inhibit Angiogenesis Enhancing the Anti-Tumour Activity of Rituximab in Vivo. *Br. J. Haematol.* **2008**, *140*, 36–45.
- (31) Lu, L.; Payvandi, F.; Wu, L.; Zhang, L. H.; Hariri, R. J.; Man, H. W.; Chen, R. S.; Muller, G. W.; Hughes, C. C. W.; Stirling, D. I.; *et al.* The Anti-Cancer Drug Lenalidomide Inhibits Angiogenesis and Metastasis via Multiple Inhibitory Effects on Endothelial Cell Function in Normoxic and Hypoxic Conditions. *Microvasc. Res.* **2009**, *77*, 78–86.
- (32) Sanson, N.; Rieger, J. Synthesis of Nanogels/microgels by Conventional and Controlled Radical Crosslinking Copolymerization. *Polym. Chem.* **2010**, *1*, 965–977.
- (33) Cai, T.; Marquez, M.; Hu, Z. Monodisperse Thermoresponsive Microgels of Poly(ethylene Glycol) Analogue-Based Biopolymers. *Langmuir* **2007**, *23*, 8663–8666.
- (34) Guarrotxena, N.; Quijada-Garrido, I. Optical and Swelling Stimuli-Response of Functional Hybrid Nanogels: Feasible Route to Achieve Tunable Smart Core@Shell Plasmonic@Polymer Nanomaterials. *Chem. Mater.* **2016**, *28*, 1402–1412.
- (35) Lutz, J. F. Polymerization of Oligo(ethylene Glycol) (Meth)acrylates: Toward New Generations of Smart Biocompatible Materials. *J. Polym. Sci. Part A Polym. Chem.* **2008**, *46*, 3459–3470.
- (36) Hu, Z.; Cai, T.; Chi, C. Thermoresponsive Oligo(ethylene Glycol)-Methacrylate-Based Polymers and Microgels. *Soft Matter* **2010**, *6*, 2115.
- (37) Lutz, J. F.; Andrieu, J.; Üzgün, S.; Rudolph, C.; Agarwal, S. Biocompatible, Thermoresponsive, and Biodegradable: Simple Preparation of “All-in-One” biorelevant Polymers. *Macromolecules* **2007**, *40*, 8540–8543.
- (38) Okada, Y.; Tanaka, F. Cooperative Hydration, Chain Collapse, and Flat LCST Behavior in Aqueous poly(N-Isopropylacrylamide) Solutions. *Macromolecules* **2005**, *38*, 4465–4471.
- (39) Vihola, H.; Laukkanen, A.; Valtola, L.; Tenhu, H.; Hirvonen, J. Cytotoxicity of Thermosensitive Polymers poly(N-Isopropylacrylamide), poly(N-Vinylcaprolactam) and Amphiphilically Modified poly(N-Vinylcaprolactam). *Biomaterials* **2005**, *26*, 3055–3064.
- (40) Langille, M. R.; Personick, M. L.; Zhang, J.; Mirkin, C. A. Defining Rules for the Shape Evolution of Gold Nanoparticles. *J. Am. Chem. Soc.* **2012**, *134*, 14542–14554.
- (41) Bodelón, G.; Montes-García, V.; Fernández-López, C.; Pastoriza-Santos, I.; Pérez-Juste, J.; Liz-Marzán, L. M. Au@pNIPAM SERRS Tags for Multiplex Immunophenotyping Cellular Receptors and Imaging Tumor Cells. *Small* **2015**, *11*, 4149–4157.
- (42) Wong, J. E.; Díez-Pascual, A. M.; Richtering, W. Layer-by-Layer Assembly of Polyelectrolyte Multilayers on Thermoresponsive P(NiPAM- Co -MAA) Microgel: Effect of Ionic Strength and Molecular Weight. *Macromolecules* **2009**, *42*, 1229–1238.
- (43) Kleinen, J.; Klee, A.; Richtering, W. Influence of Architecture on the Interaction of Negatively Charged Multisensitive poly(N-Isopropylacrylamide)-Co-Methacrylic Acid Microgels with Oppositely Charged Polyelectrolyte: Absorption vs Adsorption. *Langmuir* **2010**, *26*, 11258–11265.
- (44) Casals, E.; Pfaller, T.; Duschl, A.; Oostingh, G. J.; Puntès, V. Time Evolution of the

- Nanoparticle Protein Corona. *ACS Nano* **2010**, *4*, 3623–3632.
- (45) Zyuzin, M. V.; Honold, T.; Carregal-Romero, S.; Kantner, K.; Karg, M.; Parak, W. J. Influence of Temperature on the Colloidal Stability of Polymer-Coated Gold Nanoparticles in Cell Culture Media. *Small* **2016**, *12*, 1723–1731.
- (46) Wu, W.; Shen, J.; Banerjee, P.; Zhou, S. Core-Shell Hybrid Nanogels for Integration of Optical Temperature-Sensing, Targeted Tumor Cell Imaging, and Combined Chemo-Photothermal Treatment. *Biomaterials* **2010**, *31*, 7555–7566.
- (47) Meng, Z.; Wei, F.; Wang, R.; Xia, M.; Chen, Z.; Wang, H.; Zhu, M. NIR-Laser-Switched in Vivo Smart Nanocapsules for Synergic Photothermal and Chemotherapy of Tumors. *Adv. Mater.* **2016**, *28*, 245–253.
- (48) Huang, G.; Gao, J.; Hu, Z.; St. John, J. V.; Ponder, B. C.; Moro, D. Controlled Drug Release from Hydrogel Nanoparticle Networks. *J. Controlled Release* **2004**, *94*, 303–311.
- (49) Qian, J.; Wu, F. Thermosensitive PNIPAM Semi-Hollow Spheres for Controlled Drug Release. *J. Mater. Chem. B* **2013**, *1*, 3464–3469.
- (50) Siepmann, J.; Peppas, N. A. Modeling of Drug Release from Delivery Systems Based on Hydroxypropyl Methylcellulose (HPMC). *Adv. Drug Deliv. Rev.* **2001**, *48*, 139–157.
- (51) Anderson, M. E. Glutathione an Overview of Biosynthesis and Modulation. *Chem. Biol. Interact.* **1998**, *111–112*, 1–14.
- (52) Wu, G.; Fang, Y.; Yang, S.; Lupton, J. R.; Turner, N. D. Recent Advances in Nutritional Sciences Glutathione Metabolism and Its Implications for Health 1. *Environ. Heal.* **2004**, *134*, 489–492.
- (53) Hong, R.; Han, G.; Fernández, J. M.; Kim, B.; Forbes, N. S.; Rotello, V. M. Glutathione-Mediated Delivery and Release Using Monolayer Protected Nanoparticle Carriers. *J. Am. Chem. Soc.* **2006**, *128*, 1078–1079.
- (54) Lin, C.-A. J.; Sperling, R. A.; Li, J. K.; Yang, T.-Y.; Li, P.-Y.; Zanella, M.; Chang, W. H.; Parak, W. J. Design of an Amphiphilic Polymer for Nanoparticle Coating and Functionalization. *Small* **2008**, *4*, 334–341.
- (55) Wood, B. J. L. pH Controlled Hydrogen-Bonding. *Biochem. J.* **1974**, *143*, 775–777.
- (56) Li Volsi, A.; Jimenez de Aberasturi, D.; Henriksen-Lacey, M.; Giammona, G.; Licciardi, M.; Liz-Marzán, L. M. Inulin Coated Plasmonic Gold Nanoparticles as a Tumor-Selective Tool for Cancer Therapy. *J. Mater. Chem. B* **2016**, *4*, 1150–1155.
- (57) Zhao, Y.; Butler, E. B.; Tan, M. Targeting Cellular Metabolism to Improve Cancer Therapeutics. *Cell Death Dis* **2013**, *4*, e532.
- (58) Hu, X.-Y.; Liu, X.; Zhang, W.; Qin, S.; Yao, C.; Li, Y.; Cao, D.; Peng, L.; Wang, L. Controllable Construction of Biocompatible Supramolecular Micelles and Vesicles by Water-Soluble Phosphate pillar[5,6]arenes for Selective Anti-Cancer Drug Delivery. *Chem. Mater.* **2016**, *28*, 3778–3788.
- (59) Xia, Y.; Wu, X.; Zhao, J.; Li, Z.; Ren, W.; Tian, Y.; Li, A.; Shen, Z.; Zhao, J.-T.; Wu, A. Three Dimensional Plasmonic Assemblies of AuNPs with Overall Size of Sub-200 Nm for Chemo-Photothermal Synergistic Therapy of Breast Cancer. *Nanoscale* **2016**, 18682–18692.
- (60) Corral, L. G.; Haslett, P. a; Muller, G. W.; Chen, R.; Wong, L. M.; Ocampo, C. J.; Patterson, R. T.; Stirling, D. I.; Kaplan, G. Differential Cytokine Modulation and T Cell Activation by Two Distinct Classes of Thalidomide Analogues That Are Potent Inhibitors of TNF-Alpha. *J. Immunol.* **1999**, *163*, 380–386.

- (61) Chanan-Khan, A. A.; Swaika, A.; Paulus, A.; Kumar, S. K.; Mikhael, J. R.; Rajkumar, S. V; Dispenzieri, A.; Lacy, M. Q. Pomalidomide: The New Immunomodulatory Agent for the Treatment of Multiple Myeloma. *Blood Cancer J.* **2013**, *3*, 1–8.
- (62) Xu, Y.; Li, J.; Ferguson, G. D.; Mercurio, F.; Khambatta, G.; Morrison, L.; Lopez-Girona, A.; Corral, L. G.; Webb, D. R.; Bennett, B. L.; *et al.* Immunomodulatory Drugs Reorganize Cytoskeleton by Modulating Rho GTPases. *Blood* **2009**, *114*, 338–345.
- (63) Aidoudi, S.; Bujakowska, K.; Kieffer, N.; Bikfalvi, A. The CXC-Chemokine CXCL4 Interacts with Integrins Implicated in Angiogenesis. *PLoS One* **2008**, *3*, e2657.
- (64) Hosseinkhani, H.; Hosseinkhani, M.; Khademhosseini, A.; Kobayashi, H.; Tabata, Y. Enhanced Angiogenesis through Controlled Release of Basic Fibroblast Growth Factor from Peptide Amphiphile for Tissue Regeneration. *Biomaterials* **2006**, *27*, 5836–5844.
- (65) Richardson, P. G.; Mark, T. M.; Lacy, M. Q. Pomalidomide: New Immunomodulatory Agent with Potent Antiproliferative Effects. *Crit. Rev. Oncol. Hematol.* **2013**, *88*, S36–S44.

Table of Contents Graphic



Spatial Analysis of Metal–PLGA Hybrid Microstructures Using 3D SERS Imaging

Malte S. Strozyk, Dorleta Jimenez de Aberasturi, Jason V. Gregory, Mathias Brust, Joerg Lahann,* and Luis M. Liz-Marzán*

The incorporation of gold nanoparticles in biodegradable polymeric nanostructures with controlled shape and size is of interest toward different applications in nanomedicine. Properties of the polymer such as drug loading and antibody functionalization can be combined with the plasmonic properties of gold nanoparticles, to yield advanced hybrid materials. This study presents a new way to synthesize multicompartamental microgels, fibers, or cylinders, with embedded anisotropic gold nanoparticles. Gold nanoparticles dispersed in an organic solvent can be embedded within the poly(lactic-co-glycolic acid) (PLGA) matrix of polymeric microstructures, when prepared via electrohydrodynamic co-jetting. Prior functionalization of the plasmonic nanoparticles with Raman active molecules allows for imaging of the nanocomposites by surface-enhanced Raman scattering (SERS) microscopy, thereby revealing nanoparticle distribution and photostability. These exceptionally stable hybrid materials, when used in combination with 3D SERS microscopy, offer new opportunities for bioimaging, in particular when long-term monitoring is required.

1. Introduction

The 21st century is the era of modern nanomedicine, when nanotechnology and biotechnology converge into a new foundation that enables entirely novel modalities for diagnostics, sensing, and therapy.^[1,2] The development of new microscopic and spectroscopic techniques combined with the preparation of nanomaterials with a high degree of control is crucial

to the development of new drug carrier systems and therapeutic methods.^[3] One example is given by surface-enhanced Raman scattering (SERS), a ultrasensitive imaging tool, which, in combination with engineered particle systems, has already found a variety of applications.^[4,5] The ability to tune the excitation wavelength into the near infrared (NIR) range, the so-called biological transparency window (650–950 nm), leads to improved light penetration in living tissue, while the low Raman cross section of water and the potential for multiplexed measurements over long periods of time, render this technique ideal for nanomedicine applications.^[5–7] For example, Contag, Gambhir, and co-workers recently introduced a Raman spectrometer coupled to an endoscope for SERS-based endoscopy.^[8,9] Crucial for this and other applications

are nanoparticles functionalized with Raman active molecules (SERS-tags).^[5,10] A common strategy toward achieving stable, SERS active nanostructured materials, comprises the integration of both polymers and gold nanoparticles into hybrid materials. Recent examples have been reported for a variety of systems, where, e.g., a thin polymer shell acts as the particle stabilizer, the polymer itself being used as the SERS tag, or where gold particles are embedded in SERS tag-loaded

M. S. Strozyk, Dr. D. Jimenez de Aberasturi, Prof. L. M. Liz-Marzán
CIC biomaGUNE
Paseo de Miramón 182, Donostia-San Sebastián 20014, Spain
E-mail: llizmarzan@cicbiomagune.es


M. S. Strozyk, Prof. M. Brust
Department of Chemistry
University of Liverpool
Liverpool L69 7ZD, UK

Dr. D. Jimenez de Aberasturi, Prof. L. M. Liz-Marzán
CIBER de Bioingeniería, Biomateriales y Nanomedicina
CIBER-BBN
Donostia-San Sebastián 20014, Spain

Dr. J. V. Gregory, Prof. J. Lahann
Biointerfaces Institute Department of Chemical Engineering Materials
Science and Engineering
Biomedical Engineering Macromolecular Science and Engineering
B10-A175 NCRC University of Michigan
2800 Plymouth Road, Ann Arbor, MI 48109-2800, USA
E-mail: lahann@umich.edu

Prof. L. M. Liz-Marzán
Ikerbasque
Basque Foundation for Science
Bilbao 48013, Spain

© 2017 The Authors. Published by WILEY-VCH Verlag GmbH & Co. KGaA, Weinheim. This is an open access article under the terms of the Creative Commons Attribution-NonCommercial License, which permits use, distribution and reproduction in any medium, provided the original work is properly cited and is not used for commercial purposes.

 The ORCID identification number(s) for the author(s) of this article can be found under <https://doi.org/10.1002/adfm.201701626>.

DOI: 10.1002/adfm.201701626

hydrogels.^[6,11–13] These systems are often too specific and intrinsically limited to specific shapes, sizes, and surface functionalizations. Embedding metal nanoparticles in a biodegradable polymeric system, which can be modulated in shape and size, would offer more versatile alternatives for applications in nanomedicine. This kind of polymers can be easily used as anchor points for further functionalization with targeting molecules, as cavities for drug loading, or as smart polymers that are responsive to a specific stimulus.^[14,15] Interestingly, a simple modification of the size of a polymeric microgel can result in a different cell uptake mechanism.^[16] In this context, poly(lactic-co-glycolic acid) (PLGA) is a biocompatible (FDA approved)^[17] and biodegradable polymer, which is widely used to fabricate nanostructures like microgels, nanoparticles, fibers, or rods.^[18,19] PLGA can also be loaded with drugs and functional molecules for further surface functionalization.^[20,21] Additional complexity has also been imparted to PLGA nanostructures by implementing multicompartimental structures for highly specific applications, such as drug delivery systems containing two different drugs and distinct release profiles.^[22,23] Embedding metal nanoparticles in PLGA particles can be used to combine different optical, electrical, and magnetic features, thereby increasing the range of potential applications.^[24] Gold nanoparticles, in contrast to PLGA, are optically active and show interesting behavior upon laser irradiation, including local heating that can be exploited for thermoresponsive delivery methods, as well as the above-mentioned SERS activity, which can be used for imaging.^[25] These biological applications are favored for gold nanoparticles with shape anisotropy, such as gold nanostars (AuNSs), which absorb ≈ 800 nm, where tissue displays reduced absorption and, in turn, increased penetration depth.^[26] However, anisotropic nanoparticles are often grown in water or other solvents with high dielectric constants, which may hinder their encapsulation in polymers.^[27–29]

We present here a universal method to embed metal nanoparticles of various composition, shape and size, in PLGA nanomaterials by means of the so-called electrohydrodynamic (EHD) co-jetting process. This process has been well established for PLGA over the last decade and offers a high throughput method to synthesize PLGA microgels of different sizes and morphologies.^[19] Transfer of gold nanoparticles from water into chloroform (CHCl_3)^[6,30] was accomplished using hydrophobic SERS active molecules, which act as both capping agents and SERS labels. The resulting nanoparticles with high and reliable SERS signals can be embedded in selected compartments of the PLGA particles, while different fluorescent dyes were added to other compartments, thereby allowing us to expand the standard characterization methods (transmission electron microscopy (TEM), scanning electron microscopy (SEM), and fluorescence microscopy) and using 3D confocal SERS microscopy (3D-SERS) to identify the nanoparticle distribution inside the polymer. To avoid potential interferences arising from the fluorescence of the dyes, these were selected so that their absorption and emission were sufficiently far away from the laser excitation wavelength (785 nm in this case) used for SERS measurements. Even though 3D-SERS imaging offers powerful and complementary possibilities, it is still fairly undeveloped due to its complexity, as the weak nature of the Raman signal and its complicated scattering behavior require

finding a suitable compromise for the optimum pinhole size that ensures confocality as well as sufficiently high signal intensity.^[31] Recently, a few groups developed substrates to demonstrate Raman imaging with high spatial resolution in 3D.^[13,32,33] Especially Ozaki and co-workers recently showed the reconstruction of a 3D plasmonic structure using 3D-SERS.^[32] Promising applications for 3D SERS imaging would be, e.g., related to monitoring of implanted scaffolds for tissue regeneration, so as to control their degradation over time, in combination with tissue growth. This is commonly done by using invasive methods such as histology, which do not allow continuous monitoring, while noninvasive methods such as fluorescence microscopy are often limited in penetration depth, sensitivity, and long-term stability, as well as by photobleaching.^[34,35]

We introduce here the synthesis of PLGA–metal nanoparticle hybrid materials using EHD co-jetting. AuNSs labeled with different SERS active molecules were embedded in separate compartments of different polymeric structures (particles and fibers), and 3D-SERS imaging was used to monitor the distribution of the particles inside the polymer. We propose that these hybrid materials containing SERS labeled nanoparticles and thus allowing characterization by means of SERS imaging, offer significant advantages over existing fluorescence-based materials for bioimaging.

2. Results and Discussion

2.1. Synthesis of Bicompartimental PLGA Nanoparticles Loaded with SERS Encoded Nanoparticles in Separate Hemispheres

The preparation of hybrid multicompartimental PLGA–plasmonic microparticles is schematically illustrated in **Figure 1**. Nanoparticles synthesized in aqueous solution were transferred into CHCl_3 by means of a protocol previously reported by our group.^[30] A Raman active molecule was used as surfactant during this process to obtain highly stable and bright SERS tags. The resulting particle suspension was mixed with various amounts of PLGA and different fluorescent dyes: ((Poly[(*m*-phenylenevinylene)-*alt*-(2,5-dihexyloxy-*p*-phenylenevinylene)] as a blue dye or poly[tris(2,5-bis(hexyloxy)-1,4-phenylenevinylene)-*alt*-(1,3-phenylenevinylene)] as a green dye.

Gold nanostars were specifically selected for most of the experiments due to their strong absorbance in the NIR range (see TEM images and optical spectra in Figure S1, Supporting Information) and their outstanding performance as SERS tags, to conduct 3D SERS measurements. The Raman active molecules biphenyl-4-thiol (4-BPT) and 2-naphthalene-thiol (2-NAT) were used as ligands due to their strong binding affinity to gold surfaces and their characteristic and easily distinguishable Raman signals. The final particle size was influenced by the solvent composition and the molecular weight of PLGA.^[19] When using 17 kDa PLGA and 70:30 CHCl_3 :DMF, particles of ≈ 600 –800 nm were obtained, whereas 40 kDa PLGA in 70:30 CHCl_3 :DMF yielded particles of ≈ 1 –2 μm , and using 50–75 kDa PLGA and solvent ratios between 70:30 and 97:3 CHCl_3 :DMF, particles in the range of 3–8 μm could be produced.

In order to demonstrate universality of the method, we also prepared polymeric particles containing SERS-encoded 30 nm

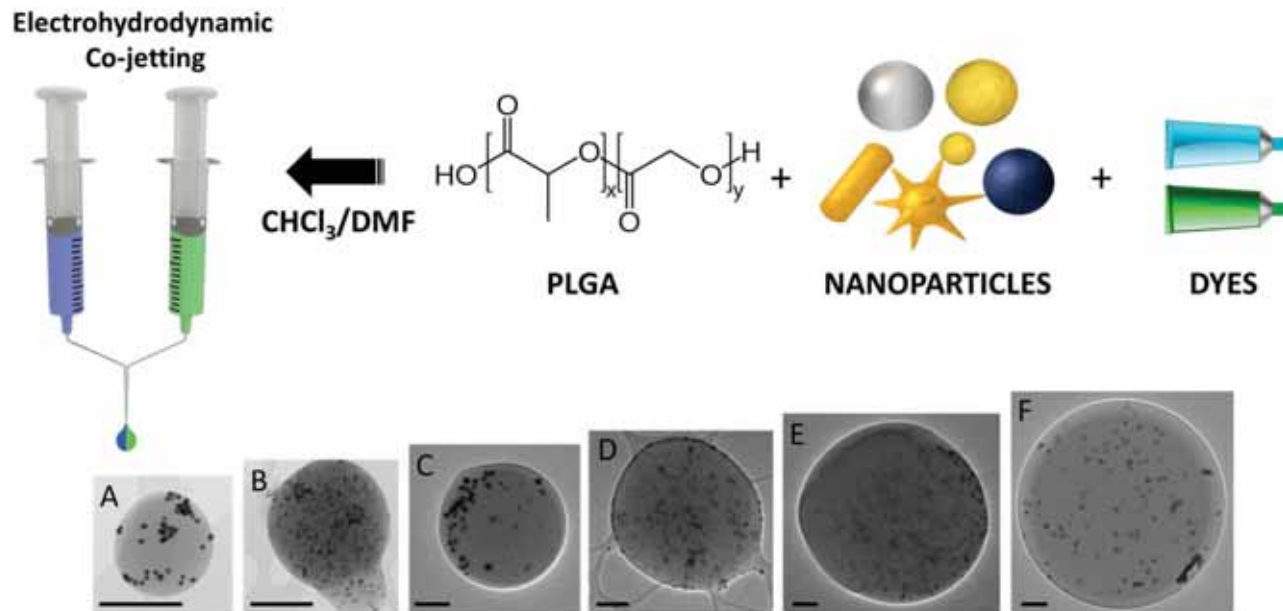


Figure 1. Fabrication of multicompartamental hybrid particles using electrohydrodynamic co-jetting. The size of the particles can be controlled by using different polymer molecular weights and varying polymer concentrations. TEM images in A–F are representative for particles of different sizes and compositions. PLGA molecular weight was varied from A,B) 17 kDa through C,D) 40 kDa up to E,F) 50–75 kDa. These examples show various configurations with two (A, C–F) or three (B) compartments, containing AuNSs (A–F) and iron oxide nanoparticles (B). The particles also contain poly[(*m*-phenylenevinylene)-*alt*-(2,5-dihexyloxy-*p*-phenylenevinylene)] as a blue dye and poly[tris(2,5-bis(hexyloxy)-1,4-phenylenevinylene)-*alt*-(1,3-phenylenevinylene)] as a green dye, in separate compartments. All scale bars are 500 nm.

AgNPs and 40 nm iron oxide particles (Figure 1; Figures S2 and S3, Supporting Information). AgNPs are ideal for SERS measurements at laser excitation wavelengths ≈ 500 –600 nm, whereas magnetic nanoparticles could be used to separate/collect the hybrid particles by magnetophoresis. In an additional experiment, the PLGA surface was functionalized with carboxylic acid groups, by adding 30% of 5050 DLG 1A polymer (5.9 kDa) to the initial PLGA/AuNSs mixture (Figure S4A, Supporting Information). For subsequent experiments, these can be useful as anchor points for further (bio) functionalization, e.g., with antibodies.

For EHD co-jetting, the polymer/particle/dye mixtures were flown in a laminar regime through parallel mounted metallic needles at 0.2 mL per hour. After a stable droplet was formed at the interface of the polymeric solutions, a voltage was applied between the droplet and a collector plate. The voltage created a polymeric jet from the tip of the droplet towards the collector and was sufficiently high to induce break-up of the jet into individual particles. Transmission electron microscopy (TEM), scanning electron microscopy (SEM), and fluorescence microscopy studies demonstrate that particles evenly formed over a large area (Figure S4, Supporting Information).

2.2. Stability of the Compartments

PLGA hybrid microgels showed high particle loading, regardless of the type of plasmonic particles used in the synthesis, as observed in TEM images (Figure 1A–F). However, TEM images alone could not resolve the different compartments within the particles. Therefore, the inner distribution and the preservation

of the different compartments after synthesis were characterized by means of fluorescence imaging (from blue and green dyes) and SERS imaging (from two different SERS-encoded AuNSs).

Once synthesized, polymeric particles were embedded in a ProLong™ gold matrix between two coverslips and initially examined by confocal fluorescence microscopy (Figure 2A). For SERS measurements, the particles were immobilized on a quartz glass slide to avoid the fluorescence background from standard glass and then examined under a WITec Alpha 300RS confocal Raman microscope, using a 785 nm diode laser as the excitation source. As a reference, we used the Raman bands at 1275 cm^{-1} for 4-BPT (C–C ring stretch) and 1375 cm^{-1} for 2-NAT (C–C ring stretch), so that the characteristic bands of both Raman reporters could be clearly distinguished (Figure 3B). In Figure 2B,C, both fluorescence and SERS images indicate the stability and preservation of the two initial compartments. Interestingly, no interference from the fluorescent dyes was observed, and as a result the shape of the compartments was clearly resolved by both techniques. The SERS images also allowed for differentiation of the compartments, but in contrast to fluorescence imaging, the SERS signal was not found to be evenly distributed throughout the entire particle. This is due to the distribution of AuNSs, which, in contrast to the dyes, may associate into clusters within the PLGA compartments, resulting in a distinct pattern with islands of higher intensity in the SERS maps. Figure 2C also shows a dominant signal from 4-BPT in this form of representation and reveals lack of information regarding the inner particle distribution. For this reason, 3D SERS imaging was conducted, focusing on obtaining spatial information in *x*, *y*, and *z* directions.

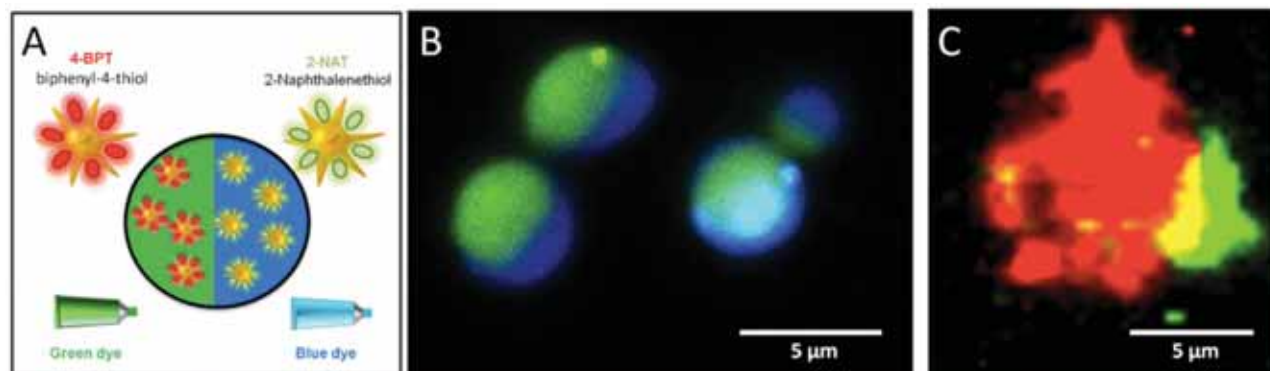


Figure 2. A) Bicompartmental PLGA (40 kDa) particles containing ≈ 50 nm AuNSs labeled with 4-BPT and a green dye in one compartment, and AuNSs labeled with 2-NAT and a blue dye in the other compartment. B) Fluorescence image of ≈ 4 μm particles showing that both dyes and compartments are well separated and distinguishable. C) SERS mapping of a ≈ 7 μm particle, also displaying two separate compartments. The signals from 4-BPT (red) and 2-NAT (green) are spatially separated.

The 3D distribution of SERS-encoded AuNSs inside the microgel particles was examined with high-resolution confocal Raman microscopy. We selected a 100×0.9 NA objective with a 50 μm pinhole that best met our requirements.^[31] One particle was scanned over a volume of $14 \times 14 \times 20$ μm^3 ($40 \times 40 \times 35$ points per line), with an integration time of 40 s per line (785 nm laser, 7 mW). The observed signal-to-noise-ratios were in general very high and the SERS spectra for both Raman tags were well resolved under these scanning conditions (Figure 3B). A series of slices (in z-direction) were imaged, in which both SERS tags (2-NAT, 4-BPT) could be resolved, indicating spatial separation within different compartments. Even though some degree of overlap (yellow–orange color) was observed, the compartments were found to be well separated from each other in most cases. Additional 3D reconstructions (Figure 3C,D) confirm these results and suggest that the compartments are not perfect hemispheres but rather have a “tennis ball” like structure, where

both compartments are wrapped around each other. In conclusion, we show that SERS labeled AuNSs are present throughout the microgel and their distribution can be resolved by confocal Raman microscopy. This 3D reconstruction especially helps to achieve information about nanoparticle distribution, which is not possible by conventional SERS measurements.

2.3. Labeled Fibers and Rods

One of the challenges related to monitoring the evolution and degradation of scaffolds during tissue growth is related to a low penetration depth when using fluorescence microscopy (usually with illumination and fluorescence in the visible). Since PLGA electrospun nanofibers have been reported as scaffolds for cell or tissue growth,^[36] we explored the possibility to synthesize PLGA fibers containing AuNSs, while preserving

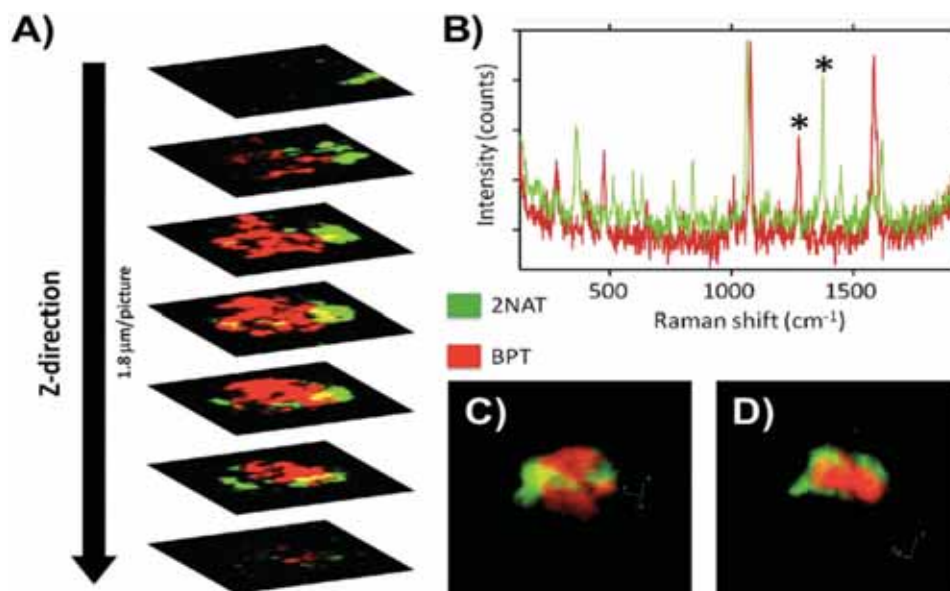


Figure 3. 3D confocal Raman imaging of a single microgel particle. A) Z-stack showing the existence of separated compartments and the distribution of SERS labeled AuNSs within the particle. B) Representative SERS spectra of BPT (red) and 2-NAT (green) labeled AuNSs measured inside PLGA particles. The peaks marked with * indicate the specific signals used for mapping. C,D) 3D reconstruction of the particle from two different perspectives.

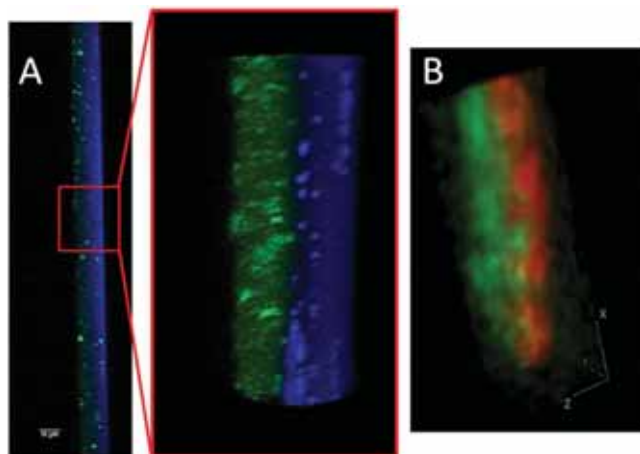


Figure 4. Examples of PLGA-based bicompartmental fibers containing SERS-encoded AuNSs, prepared by electrohydrodynamic co-jetting and analyzed by A) fluorescence imaging and B) SERS mapping.

their bicompartmental structure (Figure 4). We thus prepared fibers with a diameter of 10 μm , i.e., twice as large as the particles above, which would likely facilitate the resolution of the different compartments. SERS imaging indeed showed a distinct separation between the compartments filled with 4-BPT-coated AuNSs and 2-NAT-coated AuNSs (Figure 4B). The 3D reconstruction of the SERS data in Figure 4B confirms yet again that SERS is a useful tool to resolve the structure of our hybrid polymeric structures and the internal structure of the different compartments.

To further demonstrate the universal character of our synthesis protocol, the obtained fibers were cut into pieces, to obtain cylinders with different lengths (Figure S5, Supporting Information). Upon embedding the fibers in a Tissue-Plus matrix and using a cryosectioning instrument (see Experimental Section), it was possible to fabricate cylinders while keeping the two compartments stable.^[18] Cylinders are of interest since the shape of particles plays an important role in the modulation of cell uptake, as reported elsewhere.^[37]

2.4. Fluorescence versus SERS: Long-Term Experiments

Long-term stability is a key advantage of SERS, as compared to fluorescence, and can be exploited in labeled scaffolds or microgels as imaging tools in nanomedicine. During long-term experiments, the particles are exposed to a number of factors that lead to degradation and bleaching of organic molecules. The environments used for both in vitro and in vivo experiments are chemically aggressive, containing redox active molecules, enzymes, highly reactive radicals and pH changes.^[38–40] Additionally, exposure to light during microscopy observation often leads to photobleaching of organic dyes.^[41]

We analyzed the effect of photobleaching on our hybrid materials by measuring fluorescence and SERS signals from a large number of particles (>100) before (Figure 5A) and after (Figure 5B) UV-irradiation for 30 min. Prior to irradiation, the samples displayed fluorescence and SERS signals throughout the whole field of view. In contrast, after irradiation,

the fluorescence signal completely vanished, while the SERS signals remained basically unaltered. This experiment clearly illustrates the degradation of the dye over time upon exposure to light, whereas the SERS tags remain stable and active, in a demonstration that SERS is an attractive tool for long-term (bio)imaging experiments.

3. Conclusions

We have introduced a universal method for the synthesis of PLGA microgels of different sizes and shapes, loaded with dyes and metal nanoparticles with distinct electromagnetic properties. These particles offer a wide range of potential applications, in particular for biomedical imaging. Even though we focused here on PLGA (FDA approved polymer), the EHD co-jetting method facilitates the use of various other polymers (and their blends), including a wide range of synthetic polymers (PMMA, PAA, PEI, Dextran) and more recently crosslinked biopolymers such as proteins. We demonstrated that SERS encoded AuNSs, embedded within polymer microgels, can be used to resolve and reconstruct the shape of both particles and fibers. Importantly, co-loaded dyes do not interfere with the SERS signal or create a background, which is likely due to the high and reliable SERS signal originating from AuNSs densely covered with Raman tags. Finally, an important outcome of this study is the demonstration that the SERS signals from embedded AuNS, in contrast to that from fluorescent dyes, are not altered upon exposure to UV illumination, therefore offering the possibility for long-term imaging experiments. Since PLGA is a biocompatible and biodegradable polymer, potential applications of these hybrid materials can be foreseen, for example in combined drug delivery/imaging devices. In particular, microfibers functionalized with AuNSs may allow us to obtain new insights in the role of implanted scaffolds in regenerative medicine.

4. Experimental Section

Materials: Milli-Q water (resistivity 18.2 M Ω cm) was used in all experiments. Hydrogen tetrachloroaurate trihydrate (HAuCl₄·3H₂O, $\geq 99.9\%$), sodium citrate tribasic dihydrate ($\geq 98\%$), silver nitrate (AgNO₃, $\geq 99\%$), L-ascorbic acid (AA, $\geq 99\%$), O-[2-(3-mercaptopropionylamino)ethyl]-O'-methylpolyethylene glycol (PEG-SH, $M_w = 5\,000\text{ g mol}^{-1}$), 2-naphthalenethiol (2-NaT, 99%), biphenyl-4-thiol (4-BPT, 97%), chloroform ($\geq 99.8\%$), and 50–75 kDa PLGA, were purchased from Sigma-Aldrich. 17 kDa PLGA (#5002a) and 40 kDa PLGA (#5004a) were purchased from Corbion. 5050 DLG 1A polymer (#LX00560-130) was purchased from Lakeshore Biomaterials. ProLong™ gold matrix was purchased from Thermofisher Scientific. Quartz microscope slides were from Electron microscopy (#72250-01). 5 nm AuNPs and 40 nm iron oxide nanoparticles were purchased from Ocean Nanotech LLC. All glassware was washed with aqua regia, rinsed threefold with Milli-Q water and dried, prior to use.

For EHD co-jetting, a syringe pump (Fisher Scientific Inc., USA) and a power supply (DC voltage source, Gamma High Voltage Research, USA) were used.

Synthesis of Gold Nanostars: AuNSs were prepared using a seed-mediated growth method.^[42] Adding 5 mL of $34 \times 10^{-3}\text{ M}$ citrate solution to 95 mL of boiling $0.5 \times 10^{-3}\text{ M}$ HAuCl₄ solution under vigorous stirring and then maintaining boiling for 15 min, seed particles were formed. 50 nm AuNSs with an LSPR maximum at 750 nm, were prepared by adding 2.5 mL

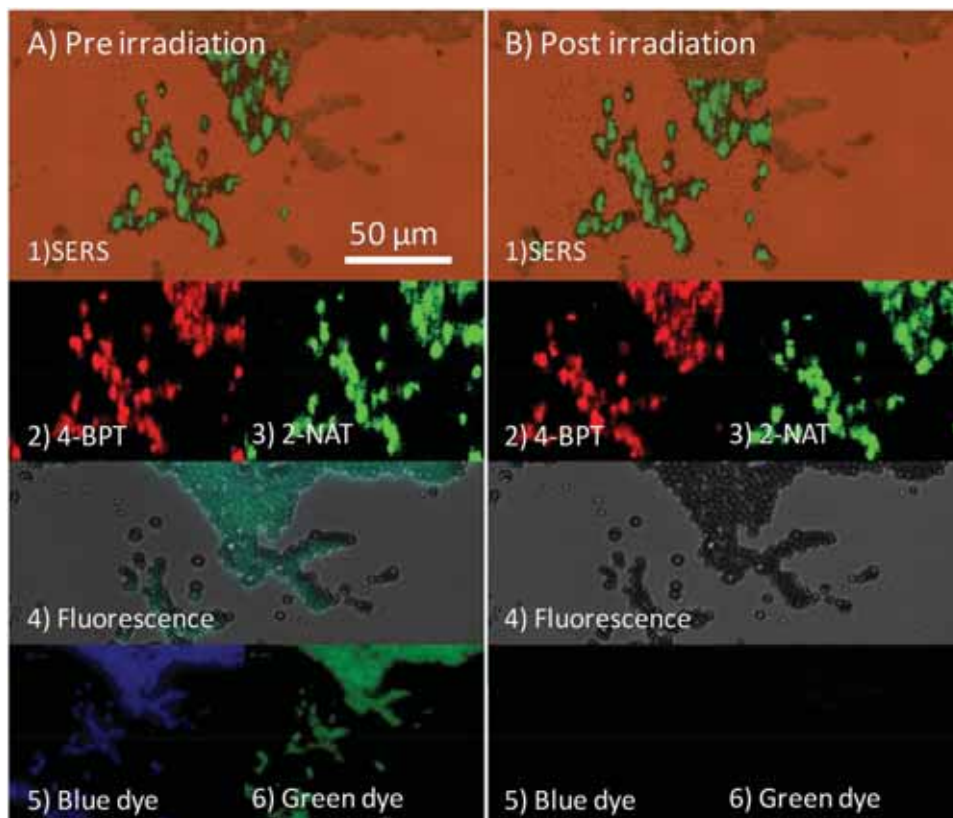


Figure 5. A large number (>100) of bicompartmental particles were immobilized on a glass substrate and both SERS and fluorescence signals were measured A) before and B) after exposure to UV-light. Images 1–3 demonstrate that the SERS signals from both 4-BPT and 2-NAT SERS tags show no difference over time and remain active upon irradiation. The fluorescence signals of both blue and green dyes (4–6) however, vanish after UV light exposure, due to photobleaching of the dye molecules.

of the citrate-stabilized seed solution to 50 mL of 0.25×10^{-3} M HAuCl_4 solution (containing 50 μL of 1 M HCl), in a 100 mL glass erlenmeyer at room temperature, under moderate stirring. Quickly, 500 μL of 3×10^{-3} M AgNO_3 and 250 μL of 100×10^{-3} M ascorbic acid were added simultaneously. The resulting AuNSs solution was mixed with 410 μL of PEG-SH 0.1×10^{-3} M, stirred for 15 min and washed by centrifugation at 1190 g, 25 min, 10°C , and subsequently redispersed in water.

Synthesis of Silver Nanoparticles: A modification of a previously reported approach was used to prepare 30 nm Ag NPs.^[43] 250 mL of Milli-Q water was heated under magnetic stirring, then 4 mL of trisodium citrate (0.1 M) and 0.32 mL of ascorbic acid (0.1 M) were added to the boiling water. Subsequently, 0.93 mL of AgNO_3 (0.1 M) was added and boiling was maintained for 1 h under stirring. The solution was cooled down and stored in the fridge.

Phase Transfer of Plasmonic Nanoparticles: All plasmonic particles were prestabilized with PEG (O-[2-(3-mercaptopropionylamino) ethyl]-O'-methylpolyethylene glycol),^[6,30] and subsequently transferred from water into CHCl_3 by vigorously stirring the colloids with a chloroform solution of the hydrophobic Raman active molecules. Both phases were mixed overnight, so that the particles would slowly diffuse from the aqueous into the organic phase. Afterwards, the aqueous phase was discarded and the organic phase centrifuged several times to remove excess of free ligand.

Bicompartmental PLGA Particles: Bicompartmental PLGA particles were synthesized using 50–75 kDa PLGA (#430471 Aldrich) and a solvent ratio of 97:3 for CHCl_3 and DMF. Briefly, in compartment (I) 0.0405 g of PLGA was mixed with 235 μL of green dye (1 mg mL^{-1} in CHCl_3) and 485 μL of SERS-Tag (4-BPT) AuNSs [$\text{Au}^0 = 3 \times 10^{-3}$ M] in CHCl_3 and 15 μL DMF. Compartment (II) was prepared by mixing 0.0405 g of PLGA with 235 μL of blue dye (1 mg mL^{-1} in CHCl_3) and

485 μL of SERS-Tag (2-NAT) AuNSs [$\text{Au}^0 = 3 \times 10^{-3}$ M] in CHCl_3 and 15 μL DMF.

Bicompartmental Fibers: Using a 50–75 kDa PLGA (#430471 Aldrich) and a solvent ratio of 97:3 for CHCl_3 and DMF, 10 μm fibers were obtained. In compartment (I) 0.15 g of PLGA was mixed with 54.55 μL of green dye (1 mg mL^{-1} diluted in CHCl_3) and 350 μL of SERS-Tag (4-BPT) AuNSs [$\text{Au}^0 = 3 \times 10^{-3}$ M] in CHCl_3 and 15 μL DMF. Compartment (II) was prepared by mixing 0.15 g of PLGA with 54.55 μL of blue dye (1 mg mL^{-1} in CHCl_3) and 350 μL of SERS-Tag (2-NAT) AuNSs [$\text{Au}^0 = 3 \times 10^{-3}$ M] in CHCl_3 and 15 μL DMF.

Bicompartmental Cylinders: Bicompartmental fibers were deposited in an aligned orientation on a tissue cryomold, and then embedded in a Tissue-Plus matrix. They were stored at -4°C for 24 h, after being cut using a Leica 3050S cryostat cryosectioning instrument. The obtained slides were collected in falcon tubes and washed several times by centrifugation and redispersion in water. Cylinders of 2, 5, and 10 μm were obtained, as defined by the cutting plane size.

SERS Measurements: SERS measurements (except bleaching experiment) were carried out using a WITec Alpha 300RS microscope with a $100\times$ 0.9 NA objective, a 600 g mm^{-1} diffraction grating and a 785 nm Laser source with a power of about 7 mW.

3D Reconstruction: For each z-height, a single point map was created by plotting the intensity of a selected band for each SERS tag (1275 cm^{-1} for 4BPT and 1375 cm^{-1} for 2-NAT), as a function of the position. The resulting maps were merged using ImageJ and 3D reconstructions were created using the ImageJ plugin 3D Viewer.

Bleaching Experiment: The microgel suspension was dropcast on a quartz glass slide and SERS maps were measured using a Renishaw inVia Raman microscope, equipped with a 1024×512 CCD detector, using a

785 nm excitation source and a 1200 g mm⁻¹ diffraction grating. Measurements were carried out using a 100× 0.85 NA objective in Streamline mode, with 2.1 mW laser power and an exposure time of 3.58 s. The slide was transferred to a Zeiss Cell Observer microscope, where fluorescence images under 20× magnification were obtained and then the LED diodes were used to illuminate the sample. In general, the samples were illuminated for 30 min with the 470 and 530 nm lasers, with powers of 11.6 and 2.3 mW, respectively. Fluorescence images and SERS measurements were repeated and processed under the exact same conditions.

Supporting Information

Supporting Information is available from the Wiley Online Library or from the author.

Acknowledgements

This work was funded by the European Union's Horizon 2020 Program under the Marie Skłodowska-Curie grant HYMADE, agreement n° 645686.

Conflict of Interest

The authors declare no conflict of interest.

Keywords

3D surface-enhanced Raman scattering imaging, gold nanostars, PLGA particles, SERS tags

Received: March 28, 2017

Revised: May 18, 2017

Published online: July 14, 2017

- [1] P. D. Howes, R. Chandrawati, M. M. Stevens, *Science* **2014**, *346*, 1247390.
- [2] R. Duncan, M. J. Vicent, *Adv. Drug Delivery Rev.* **2013**, *65*, 60.
- [3] R. Duncan, R. Gaspar, *Mol. Pharm.* **2011**, *8*, 2101.
- [4] E. C. Dreaden, A. M. Alkilany, X. Huang, C. J. Murphy, M. A. El-Sayed, *Chem. Soc. Rev.* **2012**, *41*, 2740.
- [5] Y. Wang, S. Kang, J. D. Doerksen, A. K. Glaser, J. T. C. Liu, *IEEE J. Sel. Top. Quantum Electron.* **2016**, *22*, 154.
- [6] D. Jimenez de Aberasturi, A. B. Serrano-Montes, J. Langer, M. Henriksen-Lacey, W. J. Parak, L. M. Liz-Marzán, *Chem. Mater.* **2016**, *28*, 6779.
- [7] G. McNay, D. Eustace, W. E. Smith, K. Faulds, D. Graham, *Appl. Spectrosc.* **2011**, *65*, 825.
- [8] E. Garai, S. Sensarn, C. L. Zavaleta, N. O. Loewke, S. Rogalla, M. J. Mandella, S. A. Felt, S. Friedland, J. T. C. Liu, S. S. Gambhir, C. H. Contag, *PLoS One* **2015**, *10*, e0123185.
- [9] C. L. Zavaleta, E. Garai, J. T. C. Liu, S. Sensarn, M. J. Mandella, D. Van de Sompel, S. Friedland, J. Van Dam, C. H. Contag, S. S. Gambhir, *Proc. Natl. Acad. Sci. USA* **2013**, *110*, E2288.
- [10] S. Kang, Y. Wang, N. P. Reeder, J. T. C. Liu, *PLoS One* **2016**, *11*, e0163473.
- [11] G. Bodelón, V. Montes-García, C. Fernández-López, I. Pastoriza-Santos, J. Pérez-Juste, L. M. Liz-Marzán, *Small* **2015**, *11*, 4149.
- [12] Y. Wang, B. Yan, L. Chen, *Chem. Rev.* **2013**, *113*, 1391.

- [13] Q. Zhang, Y. H. Lee, I. Y. Phang, C. K. Lee, X. Y. Ling, *Small* **2014**, *10*, 2703.
- [14] M. R. Aguilar, J. San Roman, *Smart Polymers and Their Applications*, Elsevier, Amsterdam, NL **2014**.
- [15] M. A. Cohen Stuart, W. T. S. Huck, J. Genzer, M. Müller, C. Ober, M. Stamm, G. B. Sukhorukov, I. Szleifer, V. V. Tsukruk, M. Urban, F. Winnik, S. Zauscher, I. Luzinov, S. Minko, *Nat. Mater.* **2010**, *9*, 101.
- [16] T. Sun, Y. S. Zhang, B. Pang, D. C. Hyun, M. Yang, Y. Xia, *Angew. Chem., Int. Ed.* **2014**, *53*, 12320.
- [17] <http://www.americanpharmaceuticalreview.com/Featured-Articles/188841-FDA-s-Regulatory-Science-Program-for-Generic-PLA-PLGA-Based-Drug-Products/> (accessed: March 2017, FDA's Regulatory Science Program for Generic PLA/PLGA-Based Drug Products).
- [18] S. Bhaskar, J. Hitt, S.-W. L. Chang, J. Lahann, *Angew. Chem. Int. Ed.* **2009**, *48*, 4589.
- [19] S. Rahmani, S. Ashraf, R. Hartmann, A. F. Dishman, M. V. Zyuzin, C. K. J. Yu, W. J. Parak, J. Lahann, *Bioeng. Transl. Med.* **2016**, *1*, 82.
- [20] F. Danhier, E. Ansorena, J. M. Silva, R. Coco, A. Le Breton, V. Préat, *J. Controlled Release* **2012**, *161*, 505.
- [21] H. K. Makadia, S. J. Siegel, *Polymers* **2011**, *3*, 1377.
- [22] S. Rahmani, A. M. Ross, T.-H. Park, H. Durmaz, A. F. Dishman, D. M. Prieskorn, N. Jones, R. A. Altschuler, J. Lahann, *Adv. Healthcare Mater.* **2016**, *5*, 94.
- [23] J. Lahann, *Small* **2011**, *7*, 1149.
- [24] D. W. Lim, S. Hwang, O. Uzun, F. Stellacci, J. Lahann, *Macromol. Rapid Commun.* **2010**, *31*, 176.
- [25] A.-I. Henry, B. Sharma, M. F. Cardinal, D. Kurouski, R. P. Van Duyne, *Anal. Chem.* **2016**, *88*, 6638.
- [26] R. Weissleder, *Nat. Biotechnol.* **2001**, *19*, 316.
- [27] N. Li, P. Zhao, D. Astruc, *Angew. Chem. Int. Ed.* **2014**, *53*, 1756.
- [28] J. Yang, J. Y. Lee, J. Y. Ying, *Chem. Soc. Rev.* **2011**, *40*, 1672.
- [29] M. Lista, D. Z. Liu, P. Mulvaney, *Langmuir* **2014**, *30*, 1932.
- [30] A. B. Serrano-Montes, D. Jimenez de Aberasturi, J. Langer, J. J. Giner-Casares, L. Scarabelli, A. Herrero, L. M. Liz-Marzán, *Langmuir* **2015**, *31*, 9205.
- [31] T. Dieing, O. Hollricher, J. Toporski, *Confocal Raman Microscopy*, Springer Science & Business Media, Berlin, Heidelberg **2011**.
- [32] S. Vantasin, W. Ji, Y. Tanaka, Y. Kitahama, M. Wang, K. Wongravee, H. Gatemala, S. Ekgasit, Y. Ozaki, *Angew. Chem. Int. Ed.* **2016**, *55*, 8391.
- [33] Q. Jin, M. Li, B. Polat, S. K. Paidi, A. Dai, A. Zhang, J. V. Pagaduan, I. Barman, D. H. Gracias, *Angew. Chem. Int. Ed.* **2017**, *56*, 3822.
- [34] A. M. Leferink, C. A. van Blitterswijk, L. Moroni, *Tissue Eng., Part B* **2016**, *22*, 265.
- [35] G. A. Epling, C. Lin, *Chemosphere* **2002**, *46*, 561.
- [36] W.-J. Li, C. T. Laurencin, E. J. Caterson, R. S. Tuan, F. K. Ko, *J. Biomed. Mater. Res.* **2002**, *60*, 613.
- [37] Y. Geng, P. Dalhaimer, S. Cai, R. Tsai, M. Tewari, T. Minko, D. E. Discher, *Nat. Nanotechnol.* **2007**, *2*, 249.
- [38] F. Q. Schafer, G. R. Buettner, *Free Radical Biol. Med.* **2001**, *30*, 1191.
- [39] J. R. Casey, S. Grinstein, J. Orłowski, *Nat. Rev. Mol. Cell Biol.* **2010**, *11*, 50.
- [40] P. Mitchell, *Nat. Biotechnol.* **2001**, *19*, 1013.
- [41] P. Vesely, *Scanning* **2007**, *29*, 91.
- [42] H. Yuan, C. G. Khoury, H. Hwang, C. M. Wilson, G. A. Grant, T. Vo-Dinh, *Nanotechnology* **2012**, *23*, 075102.
- [43] B. Mir-Simon, J. Morla-Folch, P. Gisbert-Quilis, N. Pazos-Perez, H. Xie, N. G. Bastús, V. Puentes, R. A. Alvarez-Puebla, L. Guerrini, *J. Opt.* **2015**, *17*, 114012.